# A STUDY ON THE CONSOLIDATION OF SULFIDE-BASED INFRARED OPTICAL CERAMICS

BY

YIYU LI

A THESIS

SUBMITTED TO THE FACULTY OF

ALFRED UNIVERSITY

IN PARTIAL FULFILLMENT OF THE REQUIREMENTS
FOR THE DEGREE OF

DOCTOR OF PHILOSOPHY

IN

CERAMIC ENGINEERING

ALFRED, NEW YORK

DECEMBER, 2018

A STUDY ON THE CONSOLIDATION OF SULFIDE-BASED

INFRARED OPTICAL CERAMICS

BY

YIYU LI

B.S. CENTRAL SOUTH UNIVERSITY (2010)

M.S. ALFRED UNIVERSITY (2015)

SIGNATURE OF AUTHOR _____

APPROVED BY _____
YIQUAN WU, ADVISOR

_____
S.K. SUNDARAM, ADVISORY COMMITTEE

_____
STEVEN C. TIDROW, ADVISORY COMMITTEE

_____
JUNJUN DING, ADVISORY COMMITTEE

_____
WILLIAM M. CARTY, CHAIR
ORAL THESIS DEFENSE

ACCEPTED BY_____
ALASTAIR N. CORMACK, DEAN
KAZUO INAMORI SCHOOL OF ENGINEERING

ACCEPTED BY_____
DR. W. RICHARD STEPHENS, JR
PROVOST AND VP FOR ACADEMIC AFFAIRS
ALFRED UNIVERSITY

# ACKNOWLEDGEMENTS

Two roads diverged in a wood, and I—
I took the one less traveled by,
And that has made all the difference.
— Robert Frost

One's life is usually created by making choices, so is mine. I am lucky to have made the choice to pursue my graduate studies in Ceramic Engineering at Alfred University I have benefited so much from so many people, who have so generously offered their precious help of various kinds.

First, I would like to express my sincere gratitude to my adviser, Prof. Yiquan Wu, for his longstanding guidance, support and insightful suggestions during my graduate study and research. Over the past years he has not only taught me how to acquire those fundamentals of scientific research, but has also given a lot of opportunities for me to attend multiple sorts of academic conferences. His well-informed knowledge of science and technology, his great enthusiasm for research, and his industriousness and science rigorousness set me a very good example, which will be quite fairly valuable for my future life career.

I am greatly indebted to my committee members, Prof. S.K. Sundaram, Prof. Steven Tidrow, and Prof. Junjun Ding, for their valuable and sagacious suggestions on my thesis work. From them I learned a lot on how to effectively perform a comprehensive study. Special gratitude goes to both Prof. Scott Misture and Prof. William Carty, for their instructions on characterization and ceramic processing, when I was a teaching assistant in their classes.

Thanks are due to Swavek Zdzieszynski, Gerald Wynick, Francis Williams, and James Thiebaud, for their patience and technical guidance on how to make best use of the instruments at Alfred University. Thanks to Prof. Ivar Reimanis, Michael Knight, Prof. Do Kyung Kim, Dr. Wook Ki Jung, Dr. Jiang Li, Dr. Chaoyu Li, Dr. Jian Zhang, Dr. Peng Liu, Hao Lu, Prof. Sergey Mirov, Dr. Vladimir Fedorov, Dr. Lihua Zhang and Dr. Kim Kisslinger, for their timely help on off-campus pressure-assisted sintering experiments and characterizations. I gratefully acknowledge the Office of Naval Research (Grant N00014-16-1-2404) for funding this research work under the guidance of Program Director Dr. Antti Makinen.

I should also thank my friends and colleagues, Dr. Yin Liu, Yan Yang, Dr. Wei Zhang, Dr. Yuxuan Gong, Dr. Peng Gao, Dr. Jie Yin, Dr. Xianqiang Chen, Dr. Wenxia Tan, Guangran Zhang, Iva Milisavljevic, Chao Liu, Dr. Shengquan Yu, Dr. Liaoyuan Wang, Thomas Olson, Dr. Dimple Pradhan, Sarah Whipkey, Sean Locker, Dr. Peter Metz, Trevyn Hey, Hyojin Lee, Max Modugno, Alec Ladonis, and Michael Alberga for their friendship and help on my research. Thanks are due to Laura Grove, Samantha Dannick, and Pat LaCourse as well, for the help in reviewing format and references of my thesis.

Last but not the least, I am so thankful to my dear wife, Dr. Yiming Li, who has rendered me constant love, care, encouragements, and considerateness. I am also grateful to my parents, my parents-in-law, and my grandparents, for their support, understanding, encouragement and love. This thesis is dedicated to them.

All these people have helped making my life so rich and different. I will remember them for good, so long as I can breathe or my life lasts. Thank you all!

# TABLE OF CONTENTS

# LIST OF TABLES

**Page**

# LIST OF FIGURES

**Page**

# ABSTRACT

Due to the favorable infrared transparency, zinc sulfide (ZnS) and calcium lanthanum sulfide ($CaLa_2S_4$) are both attractive sulfide-based candidates for infrared optical ceramics. In the current project, detailed studies were performed on the phase development, microstructural evolution, sintering behavior and grain growth kinetics of these sulfide-based ceramics under different pressure-assisted consolidation conditions, in order to process ZnS, $CaLa_2S_4$ and ZnS-$CaLa_2S_4$ infrared optical ceramics with improved optical and mechanical properties.

The phase transition behavior between sphalerite and wurtzite of ZnS infrared optical ceramics was investigated, by hot pressing and pressureless sintering of two different ZnS powders. This work revealed that, during sintering of ZnS, the phase transition behavior varied based on the starting powder particle size and magnitude of the applied pressure. It was demonstrated that smaller particle sizes led to the more phase transition from sphalerite to wurtzite at 1000 °C. Additionally, an applied uniaxial pressure during hot press sintering could promote a reverse phase transformation from wurtzite to sphalerite along with enhanced twining and densification, resulting in improved optical and mechanical performances of the ZnS ceramics.

Another study developed hot-pressed $Cr^{2+}$ doped ZnS ceramics for potential mid-infrared laser applications. Successful consolidation of $Cr^{2+}$ doped ZnS infrared transparent ceramics (maximum infrared transmittance of 67% at 11.6 μm) were achieved by vacuum hot pressing. Infrared absorption and photoluminescence measurements revealed that the $Cr^{2+}$ ions were tetrahedrally coordinated within the ZnS host lattice.

Different synthetic routes with and without high-temperature sulfurization were investigated and compared for optimization of the synthesis of $CaLa_2S_4$. It was found that $CaLa_2S_4$ with the cubic phase could be successfully synthesized, by using a wet chemistry method (single-source precursor method) followed by thermal decomposition, which demonstrated the possibility to synthesize $CaLa_2S_4$ without any hazardous sulfurization in $CS_2$ or $H_2S$.

$CaLa_2S_4$ infrared optical ceramics were sintered via different pressure-assisted sintering techniques (hot pressing and field-assisted sintering) at different temperatures.

Through densification curves and microstructural characterizations, densification behavior and grain growth kinetics of the $CaLa_2S_4$ ceramics were studied. Based on the established models, densification was determined to be controlled by various mechanisms depending upon temperature range. The infrared transmittance of the $CaLa_2S_4$ ceramics was observed to reach a maximum of 48.1% at 9.2 μm. Furthermore, it was revealed that the hardness was closely correlated with densification and grain growth.

In addition, ZnS and $CaLa_2S_4$ composite ceramics were consolidated via pressure-assisted sintering of 0.5ZnS-0.5$CaLa_2S_4$ (volume ratio) composite powders. The consolidated composite ceramics were identified to be composed of sphalerite ZnS, wurtzite ZnS and thorium phosphate-structured $CaLa_2S_4$. The sphalerite-wurtzite phase transition of ZnS was further demonstrated to be accompanied by formation of stacking faults and twins in the ceramics. Grain boundary diffusion was determined to be the main mechanism controlling grain growth for both phases within the composite ceramics. It was also found that the addition of the $CaLa_2S_4$ phase improved the indentation hardness of the ceramics relative to pure ZnS by homogeneous dispersion of ZnS and $CaLa_2S_4$ small grains. Further studies on decreasing grain size and impurity removal are critical to improving the infrared transmittance of the ZnS-$CaLa_2S_4$ ceramics.

# I. INTRODUCTION

## A. Infrared Optical Ceramics

### 1. Background on Infrared Optical Ceramics

Infrared optical ceramics refer to the ceramic materials employed in optical applications, particularly in the infrared wavelength range. Specifically, these ceramic materials correspond to infrared transparent polycrystalline ceramics as promising candidates for infrared windows/domes/lenses, infrared solid-state lasers, infrared sensors and thermal imaging devices.[1] In classical physics, light can be considered as a form of wavelike electromagnetic radiation. The electromagnetic radiation also includes heat, radar, radio waves, microwaves, x-rays and γ-rays.[2] A certain form of electromagnetic radiation has a certain specific wavelength range, corresponding to different photon energies according to Planck's equation. Figure 1 shows the spectrum of electromagnetic radiation ranging from radio waves to γ-rays. In terms of infrared light or infrared radiation, the wavelength ranges from 700 nm to 1 mm.

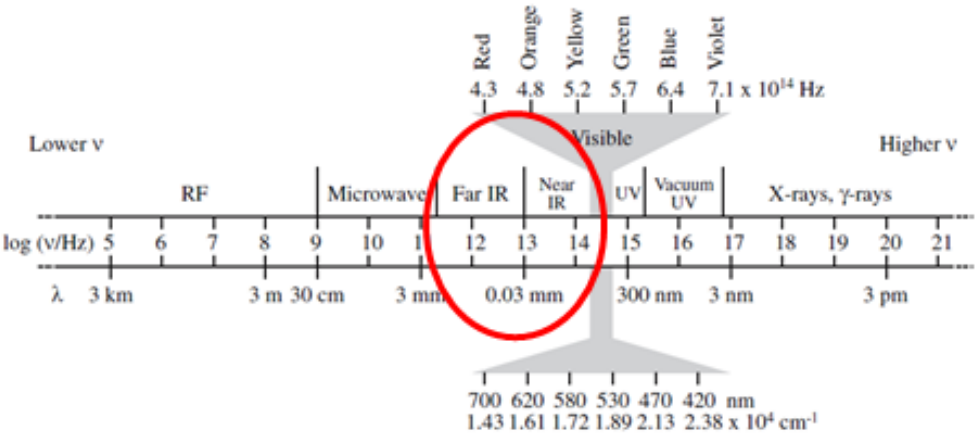


Figure 1. The spectrum of electromagnetic radiation, including wavelength ranges for the various colors in the visible light spectrum.[3] Reprinted with permission from Springer.

Several interactions, including absorption, reflection, and transmission, will occur to light when it travels between two different media. The radiation intensity of an incident light beam on the surface of a medium is equal to the sum of the intensities of the

transmitted, absorbed, and reflected beams. Thus, it is theoretically defined that materials that are able to transmit light with relatively little reflection and absorption are transparent materials.[2] In addition, low scattering loss is also crucial to achieving clear optical transparency, especially for ceramics.[3-5] The transparency of different materials is closely correlated with the basic structural characteristics of materials. Due to the difference in electron energy band structure and elastic vibration, absorptions of various materials are different, which in turn leads to the differences in theoretical transmission wavelength ranges, such as ultra-violet range, visible range and infrared range.[3] Moreover, based on different infrared transmission ranges of host materials, infrared optical materials are further divided into such categories as near infrared, short-wavelength infrared, mid-wavelength infrared, long-wavelength infrared and far infrared optical materials, on which their application fields are dependent.[6]

Similar to visible transparent materials, traditional infrared optically transparent materials also primarily include glass and single crystal. Glass materials can be engineered to possess desirable transmittance, through the systematic variation of glass compositions, the selection of appropriate glass-melting techniques, and the utilization of specialized post heat treatments, which makes them favorable candidates for optical applications in different wavelength ranges.[7] Single crystal is a crystalline solid for which the periodic and repeated atomic pattern extends throughout its entirety without interruption. Therefore, single crystal has little scattering loss sources, such as pores, defects and grain boundaries, which in turn allow single crystals to have comparable transparency with glass in visible and infrared wavelength ranges. In addition, compared with glass, with an amorphous structure, single crystals with a crystalline structure have superior mechanical strength, more stable physiochemical property and better thermal stability. Thus, single crystals are attractive candidates for optically transparent materials, especially for the applications in harsh environments. However, even though single crystals have been tried to be fabricated via various growth techniques, including Czochralski method, Bridgman method, edge-defined film-fed growth method, and floating zone method, it is still very challenging to process single crystals with large volumes and complex shapes. Additionally, all these techniques need very complicated facilities, making the growth of single crystals expensive and time-consuming. Moreover, the low concentration and inhomogeneity of doped laser-

active ions within single crystals also limit their applications, particularly in solid-state laser gain media applications.[5,8,9]

With the rapid development of ceramic science and engineering, polycrystalline ceramics with excellent optical transmittance have emerged as alternatives of optical materials with expanded capabilities, in order to overcome the technological and economical issues of glass and single crystal optical materials.[8] Optical ceramics have been demonstrated to possess the advantages of favorable mechanical properties, cost-effectiveness, large volume production, and viability of controllable shapes. They are extensively employed in various optical applications in different wavelength ranges, such as windows, domes, lenses, lighting, armors, solid-state lasers, scintillators, and transparent electro-optic devices.[5,10,11]

With regard to the optical ceramics applied in infrared wavelength range, the specific infrared transmission wavelength range is highly dependent on the host material in ceramics, due to the difference in absorptions caused by elastic vibrations. It is acknowledged that most oxide ceramic materials have the cut-off wavelength only up to near infrared and short-wavelength infrared region. In contrast, due to the low phonon energy, ceramics that are composed of nonoxides, including fluoride, nitride, halide, phosphide, and chalcogenide, have longer intrinsic infrared absorption edges.[1,12] Among them, chalcogenide optical ceramics have the broadest transmission wavelength range up to long-wavelength infrared region, rendering them uniquely suitable for optical applications in both infrared wavelength ranges of 3-5 μm and 8-14 μm.[13,14]

## 2. Research and Development of Infrared Optical Ceramics

It is well acknowledged that one of the most significant objectives of most research on infrared optical ceramics is to achieve favorbale optical transmittance in infrared wavelength range of polycrystalline ceramics. Infrared optical transparency in different regions is a critical factor to determine practical applications of infrared optical ceramics. As aforementioned, light transmission is not only related to absorption and reflection but also extremely correlated with scattering. Due to the natural characteristics of polycrystalline ceramics, possible scattering sources include residual pores, second phase, grain boundaries, double refraction, inclusions, and surface roughness, all of which will in turn contribute to the transmission loss. Figure 2 displays a brief schematic of the

microstructure of conventional polycrystalline ceramics with different labeled possible scattering sources.[15,16] Among them, the porosity within grains and grain boundaries of ceramics is the most crucial factor to affect in-line transmittance by increasing the attenuation of incident light, which is mainly attributed to the dramatic difference in refractive index between pores and ceramics. Large-sized pores or even a small number of pores will effectively scatter light through refraction and reflection, which will lead to the opacity of ceramics.[17] Also, due to difference in optical behaviors between main phase and second phase, the presence of second phase (at grain boundaries or inclusions) is another main aspect contributing to scattering losses.[3,4] In addition, surface roughness also affects optical transmission because of the diffusive reflection. Based on Beer-Lambert Law, transmittance is also influenced by the thickness of ceramics.

It is important to note that the selection of material systems is of importance for the research and development of infrared optical ceramics. The difference in natural characteristics, including refractive index, band gap, and vibration frequency, leads to different transmission wavelength values and ranges. In addition, crystal structure of ceramic materials plays a critical role in determining if a material system is suitable for infrared optical ceramics. It is determined that the materials possessing a cubic, isotropic crystal structure are more appropriate than those with an anisotropic crystal structure. As shown in Figure 2, the birefringence or double refraction, on grain boundaries of the ceramics with an anisotropic crystal structure, can also scatter light, resulting in a decrease in the in-line transmittance. Figure 3 shows a diagram of different responses for ceramics with anisotropic and isotropic crystal structures when light travels through. Ceramics are usually composed of randomly oriented grains. Due to the difference in refractive index of different directions of an anisotropic crystal structure, light will be refracted when it travels through random oriented grains, which affect the transmission as a result.[18] In contrast, the ceramics with an optically isotropic cubic crystal structure do not have the scattering loss caused by double refraction.

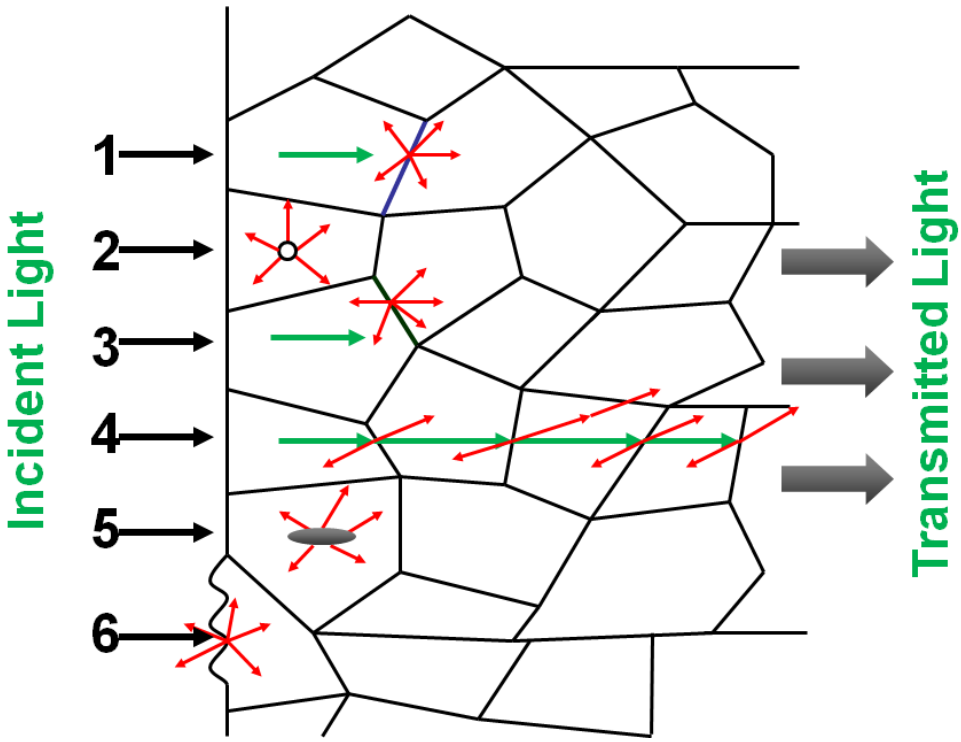


Figure 2. Schematic showing the microstructure of conventional transparent optical ceramics, light scattering and the attenuation of input power through the ceramic body. Various sources of scattering loss owing to (1) grain boundary, (2) residual pores, (3) second phase, (4) double refraction, (5) inclusions and (6) surface roughness in ceramics lead to the decrease in transmittance and prohibit applications in optics.[15] Reprinted with permission from Springer Nature.

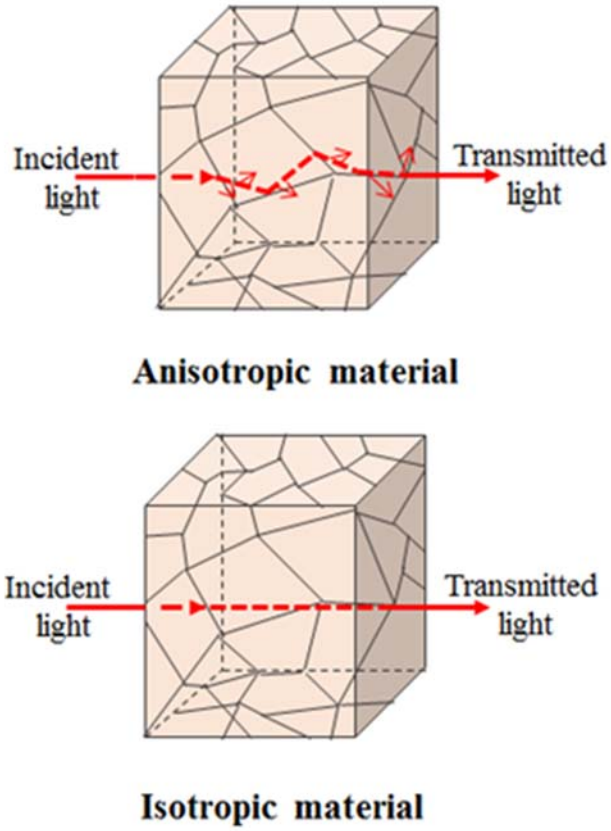


Figure 3. Diagram of different responses for ceramics composed of randomly oriented grains, with anisotropic and isotropic crystal structures when light travels through.[18] Reprinted with permission from OSA Publishing.

In order to attain excellent infrared transmittance of the infrared optical ceramics, tremendous studies on the optimization of ceramics processing have been performed to avoid, minimize, or eliminate light scattering within the ceramics. Generally, processing of infrared optical ceramics includes raw powder synthesis, green body forming, ceramic sintering, and post treatment. As previously discussed, second phases and impurities within ceramics can scatter light and affect the optical behavior. Therefore, it is required that the raw powders need to be synthesized with high purity to avoid scattering losses due to the presence of second phases or impurities. In addition, the microstructure and morphology of the synthesized raw powders are closely correlated with sintering properties, and thus very crucial for the subsequent sintering. Fine powders with favorable sintering properties are beneficial for sufficient densification and efficient pore removal, which will in turn contribute to the enhancement of optical transmittance. Various synthetic routes have been

investigated to process raw powders for infrared optical ceramics, including solid-state reaction method, co-precipitation, sol-gel method, combustion synthesis, hydrothermal synthesis, and flame spray pyrolysis. Compared with conventional solid-state reaction methods, wet-chemistry methods have attracted more extensive research interests, due to the capability of synthesizing highly pure, sinterable powders with controllable size, microstructure, and morphology, which aid in the fabrication of infrared optical ceramics with enhanced optical and machinal properties.

As the intermediate processing step between powder synthesis and sintering of ceramics, green body forming is usually employed to compact ceramic powders with a packing density. A high packing density can be of help for further densification and pore removal during the sintering process of infrared optical ceramics. Cold isostatic pressing, capable of loading equal hydrostatic high pressures simultaneously from all directions, is a common forming route to achieve a higher initial packing density for infrared optical ceramic green bodies. Plastic deformation and casting techniques (tape casting, gel casting, and slip casting from slurries or suspensions) are also employed in the forming process to reasonable packing densities, by adjusting rheological properties.[19] In addition, as the casting methods are capable of forming ceramic green bodies with complex shapes, researchers have performed extensive studies on casting of infrared optical ceramics, to meet the demands for infrared optical ceramics with more complicated shapes for various applications.

Sintering is extremely important for the processing of infrared optical ceramics. Through grain growth and grain boundary movement during the sintering process, ceramics can be consolidated at elevated temperatures, and pores can thus be eliminated. Due to the high demand for sufficient densification and low porosity, the sintering methods for infrared optical ceramics commonly require some additional conditions, including external pressure and atmosphere, to achieve better optical properties of various infrared optical ceramics. Pressure-assisted sintering techniques including hot pressing and field assisted sintering technique are extensively used in the sintering of infrared optical ceramics. By simultaneous application of uniaxial pressure and heat, pressure-assisted sintering can facilitate particle rearrangement and plastic flow between particles, which leads to more densified microstructures with small grains and efficient pore removal in

ceramics. Field assisted sintering technique (FAST), known as spark plasma sintering (SPS), is a rapid current-activated sintering route for consolidation, which can reduce sintering time, lower sintering temperature, facilitate mass transport, accelerate the rate of superplastic deformation, and retard grain growth.[20] It has recently been researched for the fabrication of various infrared optical ceramics because of its efficiency of accomplishing enhanced densification. Some special atmospheres (inert, vacuum, hydrogen, oxygen, etc) have also been applied during pressure-assisted sintering or convention sintering, to attain high purity, present oxidation, promote densification, and eliminate defects, for the optimization of optical properties of infrared optical ceramics. In addition, processing routes including microwave sintering, chemical vapor deposition, ceramization, and solid-state single crystal conversion have been investigated and utilized for consolidating infrared optical ceramics. Concurrently, in order to further promote consolidation and lower sintering temperature, various sintering additives are added to achieve liquid phase sintering for the ceramics. Post treatments of infrared optical ceramics usually include hot isostatic pressing (HIPing) and annealing. By employing a gas isostatic pressure that can compress as-sintered samples from all directions at elevated temperatures, HIPing can provide further densification and pore removal, so as to improve the infrared or even visible transmittance of optical ceramics. Annealing is used for the restoration of transparency by eliminating vacancies within infrared optical ceramics.

The past half-century has witnessed an increasing engagement in the research and development of various infrared optical ceramics. In 1950s and 1960s, with the expanding needs for infrared optical materials with larger scales, more complex shapes, and enhanced optical/mechanical characteristics for military and commercial instruments, researchers and scientists in various companies and research institutes started to explore the possibilities to fabricate infrared optical polycrystalline ceramics. Researchers from Kodak successfully managed to apply the hot pressing technique (in vacuum or inert atmosphere) on powders with high purities, for the purpose of fabricating series of non-oxide, including magnesium fluoride ($MgF_2$), zinc sulfide (ZnS), zinc selenide (ZnSe), and calcium fluoride ($CaF_2$) polycrystalline ceramics with sufficient densification and good visible/infrared transmittance for applications in infrared windows and domes.[21-27] Also, they further developed vacuum-hot-pressed $Dy^{2+}$ doped $CaF_2$ optical ceramics for laser

applications.[28,29] Furthermore, it was revealed that this hot pressing route was able to be extensively employed in the processing of more infrared optical ceramic materials including magnesium oxide (MgO), lanthanum fluoride ($LaF_3$), strontium fluoride ($SrF_2$), cadmium telluride (CdTe), cadmium sulfide (CdS), zinc oxide (ZnO), titanium dioxide ($TiO_2$), and cadmium selenide (CdSe).[25,30-36] At the same time, D. Buckner et al. from Bausch & Lomb company performed s detailed study on the hot pressing of $MgF_2$ polycrystalline ceramics applied in infrared optical application.[37] It was concluded that the optimum condition was sintering at 650 ℃ under a pressure of 207 MPa for 15 minutes, and physical properties of the obtained $MgF_2$ infrared optical ceramics demonstrated the capability of withstanding severe environments. W. Stoller et al.[38] from RCA Laboratories also reported the gallium arsenide (GaAs) optical ceramics with acceptable infrared transparency, fabricated by hot pressing in vacuum, at 1000 ℃ under 298 MPa. By conducting a study on the densification behaviour of the ceramics, they further found two main overlapped densification mechanisms (plastic flow and diffusion) that occurred during the hot-pressing process of the GaAs ceramics.[38] Moreover, it was claimed by M. Benecke et al. from the University of California, Berkeley that MgO infrared optical ceramics could be fabricated from fine MgO powder mixed with lithium fluoride (LiF) as the sintering additive, via vacuum hot-pressing at 775-975℃ under 3.9-27.6 MPa for 1-5 hours and post heat-treatment at 1300 ℃ for 3 hours in air.[39] Researchers from Global Electric, Sandia Laboratory, Army Materials and Mechanics Research Center, and Lehigh University also managed to apply conventional sintering, hot forging, hot pressing, and press forging to achieve desirable infrared transparency for yttrium oxide ($Y_2O_3$) ceramics.[40-43] In addition, R. Coble from Global Electric first demonstrated the feasibility of fabricating polycrystalline optical ceramics of aluminum oxide ($Al_2O_3$), which can be applied as an infrared window material, with an anisotropic crystal structure instead of an isotropic crystal structure. Through doping with the sintering additive MgO combined with sintering at temperatures higher than 1700 ℃ in vacuum and hydrogen, the $Al_2O_3$ ceramics were reported to be translucent in the visible region and transparent in the infrared region, which was attributed to the elimination of pores within the ceramics.[44]

Starting in the 1970s, as more and more studies were performed on sintering of various infrared optical ceramics, polycrystalline optical ceramics composed of ternary

compounds were also developed and researched. D. Roy et al. from Coors Porcelain Company reported the preparation of highly dense cubic magnesium aluminate ($MgAl_2O_4$) spinel ceramics for infrared windows, by calcining the mixture of $Al_2O_3$ and MgO and subsequent sintering with the sintering additive LiF in reducing atmosphere at 1600-1900 °C.[45] Also, K. Mazdiyasni et al. from the Air Force reported the fabrication of yttria-stabilized cubic zirconia (6mol%$Y_2O_3$•$ZrO_2$; 6YSZ) infrared optical ceramics with enhanced thermal stability, sintered via hot pressing of wet-chemistry processed powder.[46-48] A study on the phase diagram in the region of aluminum oxynitride (ALON) solid solubility region was performed by J. McCauley et al.[49] from Army Materials and Mechanics Research Center. Then, by referring to this newly determined phase diagram, they further developed fully dense, single-phase ALON spinel optical ceramics via reactive sintering of γ-$Al_2O_3$ and aluminum nitride (AlN) in a nitrogen atmosphere.[49] Concurrently, it was shown by scientists from Raytheon Company that the chemical vapor deposition method followed by HIPing could result in ZnS and ZnSe optical ceramics with highly improved visible and infrared optical performance. The development of these techniques demonstrated the viability of using alternative processing routes for non-oxide infrared optical ceramics.[50,51]

In the 1980s, by employing hot pressing and pressureless sintering of AlN, with CaO as the sintering aid, N. Kuramoto et al.[52] succeeded in preparing AlN optical ceramics with the maximum transmittance of ~40% in the infrared region, and reemphasized that the purity and sinterability were essential to produce optical non-oxide ceramics.[52] Similarly, M. Mitomo et al. developed the translucent β-SiAlON ($Si_{6-n}Al_nO_nN_{8-n}$; n=0-4.2) ceramics with the maximum transmittance of ~40% at 4.5 μm, reactively sintered via hot pressing at 1700-1800 °C under 9.8-29.4 MPa.[53] In order to develop ceramics for infrared windows with higher mechanical strength and broader transmission, a group of rare-earth alkaline-earth ternary sulfide materials were researched by scientists from Royal Signals and Radar Establishment.[54] Later, K. Saunders et al. from Raytheon Company proved that calcium lanthanum sulfide ($CaLa_2S_4$) optical ceramics with desirable infrared transmittance and resistance to rain erosion could be fabricated by sintering of sulfurized powder in an atmosphere of hydrogen sulfide ($H_2S$), followed by HIPing.[55] It was also demonstrated by G. de With et al. that translucent yttrium aluminum oxide ($Y_3Al_5O_{12}$,

YAG) with nearly full density could be processed via vacuum sintering of YAG powders with $SiO_2$ and MgO as the sintering aids.[56] Then, in the year of 1995, A. Ikesue et al. applied solid-state reaction in vacuum sintering (at 1800 ℃ for 5 hours) of high purity $Al_2O_3$ and $Y_2O_3$ powders to develop YAG optical ceramics, with nearly equivalent optical transmittance compared with single crystal in visible and infrared regions.[57] Additionally, they first demonstrated that the processed $Nd^{3+}$ doped YAG highly-transparent ceramics, possessing laser outputs with reasonable efficiencies, could be suitable for laser grain media applications,[58] which paved the way for extensive research on ceramic laser materials in various wavelength ranges.

Up till now, more materials including oxides and non-oxides with more complexed composition have also been investigated, to explore the feasibility of the application as cutting-edge infrared optical ceramics with innovative and attractive functional properties. To meet the demands in commercial and military applications under varying environments, extensive studies have been performed on powder synthesis, ceramic green body forming, ceramic consolidation, and post treatment of infrared optical ceramics, for improving optical, mechanical, and thermal characteristics. Moreover, fundamental studies on scientific issues including sintering behaviour, microstructural evolution, and phase transition have also been conducted to further elucidate and understand the correlation between processing, microstructure, and properties of infrared optical ceramics.

A. Bertrand et al.[59] developed a ceramization route for $12.5Bi_2O_3$-$12.5Nb_2O_5$-$75TeO_2$ glass, by glass melting at 850 ℃ for 30 min and subsequent crystallization at 510 ℃ for 90 min, to fabricate an innovative $Bi_{0.8}Nb_{0.8}Te_{2.4}O_8$ tellurite infrared optical ceramic, which exhibited high transparency in the near infrared range up to 5.5 μm.[59] In addition to the excellent infrared optical transmittance, this cost-effective and rapid ceramization process also resulted in good mechanical properties (hardness of 448 HV; Young's modulus of 79.5 ± 0.7 GPa), high refractive index (2.24 ± 0.05 at 1064 nm) and low coefficient of thermal expansion ($11.9 \times 10^{-6}$ $K^{-1}$). This glass-crystallization-ceramization process was shown to be promising for the processing new optical ceramics with tailored shapes.[59] More recently, it was further demonstrated that the $Nd^{3+}$-doped $Bi_{0.8}Nb_{0.8}Te_{2.4}O_8$ ceramics with desirable laser properties could also be processed via this technique, which broadened their applications in laser gain media.[60] In addition, by the

ceramization of single crystals at 1100 ℃ for 6 hours under 100 MPa in vacuum, Y. Jiang et al. succeeded in fabrication of $Nd^{3+}$-doped $Sr_9GdF_{21}$ infrared optical ceramics (average grain size of 18 μm), with excellent mid- and far-infrared transparency (up to 9 μm), and high fracture toughness.[61]

It was proposed by A. Gallian et al.[62] that the hot-pressed (hot pressing of ZnSe-CrSe mixtures at 1127-1227 ℃ under 30-35 MPa) $Cr^{2+}$-doped ZnSe polycrystalline infrared optical ceramics with an optical quality was sufficient for the first demonstration of gain-switched lasing in the mid-infrared. The ceramic laser yielded 2 mJ of output energy at a slope efficiency of up to 5%. The study further suggested that the mid-infrared laser system, based on hot-pressed polycrystalline ceramics, had a promising future.[62]

N. Nishitama et al.[63] developed transparent cubic silicon nitride (γ-$Si_3N_4$) ceramics with a spinel structure via a special synthetic route under high pressure at 15.6 GPa and at high temperatures between 1600-1800 ℃.[63] It was pointed out that the combination of ultrahigh pressure and high sintering temperature significantly contributed to densified nanostructured (~150 nm) $Si_3N_4$ ceramics, with phase transformation of hexagonal α-$Si_3N_4$ to cubic γ-$Si_3N_4$ (at 1800 ℃), which resulted in good transmittance in visible and near infrared wavelength ranges. More importantly, the reported superior mechanical properties of the ceramics showed the possibility of their potential applications under extreme conditions.[63]

The researchers from Naval Research Laboratory synthesized $MgAl_2O_4$ spinel raw powders via co-precipitation method using high-purity metal chloride or nitrate precursors under base conditions. Chemical treatments, such as acid washing, were further investigated and applied for purification of the $MgAl_2O_4$ spinel powders. $MgAl_2O_4$ infrared optical ceramics with different sizes and shapes were then processed by different sintering routes for infrared window applications. In particular, it was revealed that the hot pressing with nonreactive material spacers was beneficial for forming near-net-shape spinel ceramics without any sintering additives.[64,65] Moreover, silicon carbide (SiC) powders were also prepared via the carbothermic reduction of a carbon containing a dried sol-gel $SiO_2$ precursor, and then sintered via FAST. The resulting β-SiC translucent infrared ceramics indicated the potential of developing infrared ceramic window materials with much higher mechanical strength than the traditionally applied materials.[66]

J. Cheng et al. studied the densification behaviors of AlON ceramics consolidated via microwave sintering at 1700, 1750, and 1800 ℃ for 1 h at a heating rate of approximately 100 ℃/min in a nitrogen atmosphere.[67] They found that the densification was enhanced, and the grain size increased apparently from 1-2 μm to 40-50 μm, as the sintering temperature increased. Additionally, it was further claimed that the ALON ceramic sintered at 1800 ℃ had the best optical performance (~60% in infrared region at 2.5 μm), which demonstrated that microwave sintering could lower sintering temperatures and shorten sintering time, compared with traditional sintering processes for ALON infrared optical ceramics.[67]

It was reported by X. Mao et al.[68] that the visible and infrared transmittances of $Al_2O_3$ ceramics (doped with MgO as the sintering additive) could be significantly improved, by using a magnetic-field-assisted slip casting method, followed by sintering in $H_2$. The MgO doped $Al_2O_3$ suspension with 30 vol% solids was slip-casted in a 12 T magnetic field, to orient the slurry along the optical axes. Then the ceramics were sintered at 1850 ℃ in a $H_2$ atmosphere for 3 h, which led to improved transmittance compared with randomly orientated sample.[68] The study provided a new concept for fabricating the optical ceramic materials that possess anisotropic crystal structures. The grains within ceramics could be aligned to a single direction, where the refractive index for each grain is consistent. In this way, the influence of the birefringence can be significantly minimized.[68]

In addition, it has also been demonstrated that nanograins (much smaller than the light wavelength) can be helpful for the optimization of optical properties for the infrared optical ceramics that are composed of materials possessing anisotropic crystal structures. Based on Rayleigh–Gans–Debye light-scattering, R. Apetz et al. further developed a light scatting model for ceramics consisting of birefringent crystals, and concluded that the nanograins in fully dense ceramics could effectively decrease the scattering efficiency.[69] It was found by D. Jiang et al. that spark plasma sintering of high-purity $Al_2O_3$ powder with an average particle size of 200 nm, at 1300 ℃ for 5 min under 90 MPa, could lead to nanostructured, highly infrared transparent $Al_2O_3$ ceramics for short-wavelength infrared window applications, due to the combination of small grains and enhanced densification.[70] Furthermore, S. Grasso et al. performed a modification on the dies used in spark plasma sintering, by using WC instead of graphite, which enabled the loading of high pressure

during the sintering process. Then, they developed fully dense $Al_2O_3$ nanoceramics with no considerable grain growth (average grain size of ~200 nm) and improved in-line transmittance, by sintering at much lower temperatures (1000 ℃ or 950 ℃) under 500 MPa with less sintering time.[71] Tetragonal $ZrO_2$ infrared transparent ceramics[72] and hexagonal strontium fluoride phosphate ($Sr_5(PO_4)_3F$) laser ceramics[73] with nanograins were demonstrated by applying the similar methods and mechanism. In addition to the improvement in optical performance of non-cubic ceramics, the infrared optical nanoceramics including $MgAl_2O_4$, sintered under ultrahigh pressure up to several GPa, were revealed to possess better mechanical hardness.[74-76]

In order to improve the mechanical properties without affecting the excellent optical transmittance for the 3-5 μm mid-wave infrared window for demanding aero-thermal applications, researchers from Rutgers University and Raytheon fabricated submicron-grained infrared transparent 50vol%$Y_2O_3$-50vol%MgO composite ceramics.[77] Plasma melting technique was applied to process the composite powders. Then, they employed cold isostatic pressing (under 200 MPa) and HIPing (at 1400 ℃ for 2 h under 200 MPa) to consolidate the composite optical ceramics, with the maximum infrared transmittance of 55% at 6 μm and enhanced fracture toughness.[77] The optical transmittance was further improved in the 50vol%$Y_2O_3$-50vol%MgO nanocomposite ceramics, demonstrating that scattering could be minimized or eliminated in composite ceramics, as long as the grain size of the individual phases is significantly smaller than the wavelength of light passing through.[78]

K. Morita et al.[79] performed a study on the discoloration of the $MgAl_2O_4$ spinel optical ceramics sintered via spark plasma sintering through spectroscopies and transmission electron microscopy. The discoloration, which affects the optical transmittance of the ceramics, was explained by the combined effect of carbon contamination and color centers ($F^+$). Carbon contamination was determined to be attributed to $CO_3$ and the evaporation of graphite foil/die, which were correlated with the sintering conditions. Based on the ESR analysis, $F^+$-centers were shown to be related to the oxygen vacancies, which were dependent on the rate of sintering/deformation. The concentration of the F+-center was enhanced with the heating rate, and reduced with the sintering temperature.[79]

I. Reimanis et al.[80] summarized fundamental studies on the densification mechanisms and the microstructural development for spinel optical ceramics processed by free sintering. It was concluded that the complex final-stage sintering of transparent spinel proceeded by a number of mechanisms, where the stoichiometry and concentration of oxygen vacancies played an important role. As a sintering additive, LiF resulted in a liquid phase formation at lower temperatures (up to ~ 1000 ℃), which strongly promoted grain-boundary mobility and densification. It was also revealed that LiF could alter the stoichiometry and concentration of oxygen vacancies during densification. In addition, LiF might react with impurities trapped at grain boundaries such as carbon and sulfide to form volatile fluoride species, making the ultimate removal of excess LiF important for achieving high visible and infrared transparency.[80]

## B. Sulfide-Based Infrared Optical Ceramics

Due to the intrinsic weak chemical bonds and resulting low vibrational frequencies, sulfides have longer infrared transmittance wavelength ranges than most oxides and fluorides, making the sulfide-based optical ceramics suitable for the infrared optical applications in both mid-wavelength infrared (3-5 μm) and long-wavelength infrared (8-14 μm) regions, such as the two-color infrared windows.[1,81] Among all the sulfide-based ceramic materials, ZnS and $CaLa_2S_4$ infrared optical ceramics are most widely investigated.

### 1. ZnS Infrared Optical Ceramics

As a well-known wide bandgap II-VI semiconductor, ZnS has been extensively employed in various applications, such as infrared windows/lenses, mid-infrared lasers, phosphors, electroluminescence, sensors and photocatalysts, because of its unique physical and chemical properties. In particular, due to its desirable infrared transparency in 8-12 μm and acceptable mechanical/thermal properties, ZnS has been researched as an attractive candidate for the infrared optical ceramics in commercial and military applications.[51,82]

#### a ZnS Crystal Structures and Phase Transition

It is well-acknowledged that ZnS has two primary crystal structures: sphalerite (zinc blende, β-ZnS) with the face center cubic (FCC) structure and wurtzite (α-ZnS) with

the hexagonal close-packed (HCP) structure. In addition, it has been reported that ZnS sphalerite can transform to another cubic, metastable ZnS phase with a rocksalt structure under pressures of 15.0-24.5 GPa.[83-86] Figure 4 displays the two well-characterized crystal structures of ZnS. Sphalerite belongs to the cubic space group $F\bar{4}3m$, with the prototype of B-3 structure, while wurtzite belongs to the hexagonal space group $P6_3mc$, with the prototype of B-4 Structure. The two crystal structures of ZnS are both close-packed structures with an atomic packing factor of 0.74. The zinc atoms and sulfur atoms are tetrahedrally coordinated with a coordination number of 4 for both phases. However, the atoms stacking patterns within the two crystal structures are different. ZnS sphalerite has the close-packed atomic arrangement of ABCABC pattern on the {111} plane along the [110] axis, while wurtzite has the close-packed atomic arrangement of the ABABAB pattern on the {0001} plane along the $[11\bar{2}0]$ axis.[87]

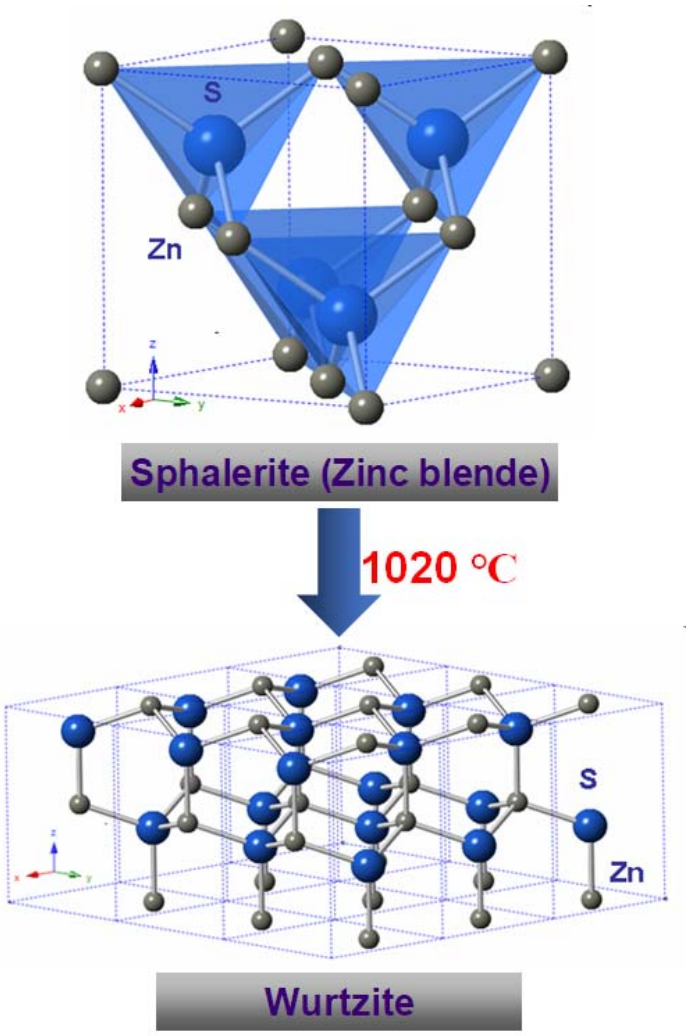


Figure 4. Two well-characterized crystal structures of ZnS (ZnS, in mineral form at ambient pressure, experiences a phase transition at 1020 ºC from the cubic sphalerite phase to the hexagonal wurtzite phase).

Since the two structures are very similar, ZnS sphalerite and wurtzite can often easily transform to each other. The reversible ZnS phase transition between sphalerite and wurtzite is believed to be martensitic, accompanied by the involvement of deformation faults (twinning) in closed-packed planes.[88,89] It is widely acknowledged that, in a mineral form at ambient pressure, ZnS experiences a phase transition from cubic sphalerite to hexagonal wurtzite at 1020 ºC, as shown in Figure 4.[90] The phase transition temperature of the natural sphalerite ZnS minerals can be shifted by variations in stoichiometry (by changing sulfur fugacity) and metal impurities.[91,92] It has also been reported that the application of external stresses or deformation to ZnS minerals and single crystals can lead

to a reverse phase transition at room temperature, from wurtzite to sphalerite, through the introduction of stacking faults.[93-96]

Also, the trivial difference in ZnS two main crystal structures leads to difference in optical and electronic properties, resulting in different preference between the two ZnS phases in different applications. Experiments and simulations indicate that the two phases of ZnS are both semiconductors with direct band gaps. The ZnS sphalerite phase has a band gap of ~3.72 eV, while wurtzite has a higher band gap as ~3.77 eV.[97] In terms of the properties desired for electronic and optoelectronic applications, wurtzite is a more attractive phase than sphalerite due to its wider intrinsic band gap. Thus, in applications where wurtzite is the desired phase, its stability can be increased by decreasing particle size to the nanometer-scale, which lowers the effective transition temperature at which ZnS transforms from sphalerite to wurtzite.[98-100] Moreover, surface area, morphology and doping can be adjusted to promote the formation of the wurtzite during different syntheses.[101-106] However, for infrared optical ceramic applications, cubic sphalerite is preferred, as it is optically isotropic. The presence of wurtzite in primarily sphalerite ZnS reduces transparency, due to the difference in refractive index and the anisotropic nature of the hexagonal structure of wurtzite. Thus, the processing of high-quality ZnS infrared optical ceramics not only requires the high purity of raw powders and sufficient consolidation of ceramics, but also needs the preservation of sphalerite phase in the ZnS ceramics.

### b Research and Development of ZnS Infrared Optical Ceramics

In the 1950s, scientists from Kodak started to apply hot pressing technique to develop ZnS infrared optical ceramics, as an alternative to ZnS single crystals for infrared windows. This work resulted in the commercialization of ZnS infrared optical ceramics, named IRTRAN® 2.[51] It was claimed that the ZnS polycrystalline optical ceramics with high relative density (higher than 99%) were fabricated via hot pressing of ZnS powder, with the particle size of less than 5 μm. The specular transmission in the visible and infrared region of the electromagnetic spectrum of the processed yellow ZnS ceramics could be achieved.[23,24] E. Carnall (Kodak) then further reported a positive logarithmic trend of the relative density of ZnS ceramics sintered via hot pressing at 750 ℃ (using Mo-alloy dies for 20 min) versus increased applied pressure. Extensive twinning was then confirmed

through the photomicrograph observation of the optically transparent ZnS sample sintered under 289.5 MPa, and Carnall claimed that the densification of ZnS proceeded primarily by twinning in the studied pressure-temperature range, but provided no further detailed evidence.[25]

In the 1970s, Raytheon Company began using a dynamic chemical vapor deposition (CVD) method to process ZnS polycrystalline transparent materials. ZnS was grown via the reaction of Zn and $H_2S$ gas at high temperatures in a mandrel.[50,51] To achieve better optical properties of the CVD-processed ZnS infrared optical ceramics, post HIPing was then employed to perform further densification and pore removal, which in turn led to improved visible transmittance. Due to the capability of producing large pieces of high-purity ZnS with lower optical scattering losses, the CVD-processed ZnS optical ceramics gradually replaced hot-pressed ZnS ceramics.[107]

Researchers have conducted many studies on CVD processed ZnS infrared optical ceramics. It was revealed by Z. Fang et al. that the CVD technique using simple substances of Zn and S could also effectively fabricate ZnS optical ceramics with desirable infrared transmittance (average transmittance of 75% in the range of 8-10 μm).[108] Y. Drezner investigated the correlation between microstructure, composition and optical transparency of CVD-processed ZnS. They found that the increase in deposition temperature led to improved transparency, due to the reduction of residual pores. The density of pores decreased with increasing vertical distance from the substrate until a steady state was reached, due to a decrease of the effect of substrate on the thermal conductivity and heat capacity of the growing film.[109] It was suggested by P. Biswas et al. that the hot isostatic press (HIP) process resulted in a preferred crystallographic orientation along the (111) plane of ZnS sphalerite, based on X-ray diffraction (XRD) analysis. The HIP process was demonstrated to be effective for removing the Zn-H absorption band and enhancing near-infrared and visible transmittances.[110]

E. Karaksina et al.[111] further investigated the recrystallization behavior during the HIP process of CVD-processed ZnS. They found that the recrystallization process followed a diffusion mechanism at low HIP temperatures (810-985 °C), while the diffusion mechanism was accompanied by plastic deformation at high temperatures (985-1100 °C).[111] J. McCloy et al.[112] performed a detailed study on the CVD-processed ZnS after the

HIP process, through investigating the effects of temperature, pressure, and metal promotor on the recrystallized microstructure and optical transmission. It was revealed that the presence of metal foils could promote the HIP-induced recrystallization at low HIP temperatures. The HIP process, with the simultaneous combination of temperature and isotropic pressure, led to crystallographic texture change and reduction in hexagonality, which in turn contributed to improved optical performance.[112] According to the microstructural analysis via EBSD, T. Zscheckel et al.[113-115] observed twining with $\Sigma 3$ twin boundaries in the CVD-processed ZnS crystals. The lamellar twining disappeared during the recrystallization induced by HIP. In addition, they discovered that this recrystallization resulted in a notable grain coarsening, and a change in the grain orientation as well as the texture of the processed ZnS infrared optical ceramics.[113-115]

Although the CVD process for fabricating ZnS infrared optical ceramics is highly effective, it is very costly and time-consuming. In addition, HIP causes a decrease in mechanical strength and hardness due to recrystallization and grain growth. Thus, with the rapid development of chemical synthesis of diverse nanostructured ZnS materials,[97,116] researchers and scholars have been attempting to use various facile wet-chemistry-based (solution-based) approaches to synthesize single-phase ZnS particles with controllable sizes and microstructures, in order to achieve better sintering properties. Then, they again began applying pressure-assisted sintering techniques to consolidate different ZnS powders to form ZnS infrared optical ceramics. Extensive studies have been performed to elucidate the correlation between processing, phase composition, microstructure, and property of the sintered ZnS infrared optical ceramics.

In the late 1980s and early 1990s, A. Celikkaya et al.[117] conducted an investigation into the synthesis of uniform spherical ZnS submicron-sized particles, via the solution-based reaction of zinc ion sources (zinc acetate, zinc sulfate, zinc chloride and zinc nitrate) with a sulfur ion source (thioacetamide, TAA) in an acidic condition. Hot water bath and post quenching were applied to control the particle size of ZnS. By characterizing the homogeneously precipitated ZnS powders synthesized using different zinc ion sources, they postulated that the ZnS particles, synthesised in nitrate solutions, had superior characteristic than others, including bimodal or continuous size distribution, good phase purity and easily-controlled morphology.[117] It was further discussed that the mechanism of

the ZnS particle formation followed a two-step process, nucleation and aggregation. The particle size distribution was believed to be controlled by two competing processes, rate of sulfide ion generation and rate of growth of agglomerates.[118] Furthermore, the authors made a following-up study on hot pressing of the process ZnS powders. It was demonstrated that ZnS translucent ceramics with high relative densities and uniform submicron grains could be fabricated via hot pressing of synthesised monodispersed powders. The Power-law creep model was the dominate mechanism during the initial densification stage, while boundary diffusion dominated the final stage.[119,120]

In addition, by observing the sintering behaviour of ZnS powders during pressureless sintering in argon at 900-1250 °C, Y. Kim et al.[121] found that the monodispersed ZnS powders showed a high sinterability, compared with other agglomerated or aggregated ZnS powders, and ZnS powders with particle size of 0.1 μm could be densified to above 98% of relative density, by pressureless sintering at 1000 °C. Concurrently, the phase transition from sphalerite to wurtzite was also observed at sintering temperatures higher than 1000 °C.[121]

It was proposed by L. A. Xue et al.[122] that the ZnS infrared optical ceramics could be successfully processed, via hot pressing of high-purity commercial ZnS powder at 900-1130 °C under 200 MPa (using a die made of Ti-Zr-Mo alloy) for 15-480 min in an atmosphere of He + 4% $H_2$. They further investigated the ZnS sphalerite-wurtzite phase transition during hot pressing, by quantitatively plotting content of ZnS wurtzite versus sintering temperature. It was revealed that ZnS phase transition occurred apparently at temperatures above 1020 °C, and the presence of the ZnS wurtzite was detrimental to the optical transmittance of the ZnS ceramics due to the difference in refractive index between the two phases. They further concluded that higher hot pressing temperature (at above 1020 °C) led to higher contents of wurtzite and larger grain sizes, which resulted in more significant scattering losses, as illustrated in Figure 5.[122] Furthermore, they investigated the deformation-dependent phase transition in hot-pressed ZnS ceramics in the temperature range of 900 °C to 1150 °C, near the phase transition temperature (1020 °C). The researchers proposed that the *in situ* deformation resulted in the strain-dependent phase transition from wurtzite to sphalerite, at temperatures lower than the transition temperature,

and the high strain rate and flow stress would promote phase transition from sphalerite to wurtzite.[123,124]

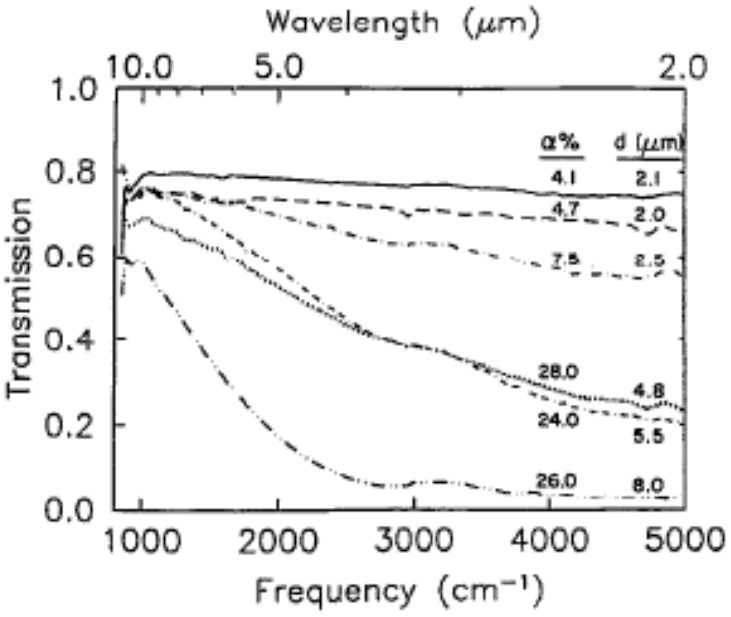


Figure 5. Influence of content and grain size on infrared transmission spectra of ZnS (thickness of 1mm).[122] Reprinted with permission from AIP Publishing.

Years later, a research group from CNRS/University of Rennes carried out some systematic studies on ZnS infrared optical ceramics, from powder synthesis to ceramics consolidation. S. Zhu et al.[125] applied three wet-chemistry methods to synthesize ZnS nanopowders, and to examine the influence of synthetic routes on the resulting ZnS particles. Then, homogeneous and find ZnS powder, synthesized via fast homogeneous precipitation method using TAA as the sulfur source, was sintered via hot pressing at 950-1200 ℃ under 25 MPa. Sodium sulfide ($Na_2S$), as a sintering aid, was also added to decrease the sintering temperature and prevent the phase transition. The ZnS ceramics have the relatively low infrared transmittance (maximum infrared transmittance of ~40%, thickness of 0.4 mm), due to the presence of wurtzite and impurities induced by $Na_2S$.[125]

Chilique et al. performed a comparative study on the sintering of two types of ZnS powders, synthesized and commercial, by using hot uniaxial pressing and spark plasma sintering.[126] It was revealed by them that the degree of optical scattering was dependent on

the presence of the second phase (wurtzite), the ceramic grain size, and the graphite contamination during the experiments, independent of powder used. The ZnS ceramic sintered via hot uniaxial pressing using the commercial powder exhibited the best optical performance (near 70%) in the range of 8-12 μm. In addition, it was also demonstrated that SPS can lead to the densification of ZnS at a lower sintering temperature as 750 ℃ due to the inhibition of grain growth and the maintenance of the initial powder granulometry.[126]

Then, they conducted some follow-up research on the hot pressing of ZnS ceramics with high transmittance using the synthesized monodisperse ZnS nanopowders.[127] They developed a more efficient wet-chemistry synthesis procedure (using $ZnCl_2$ as the zinc source and TAA as the sulfur source) and post treatment for the precipitated powders, which greatly improved the chemical purity and the size distribution of the precursor powders. By hot-pressing of the ZnS powders at 950°C for 2 h under a pressure of 50 MPa, the ZnS ceramics (composed of both sphalerite and wurtzite) with homogeneous microstructure, smooth grain boundaries, and an excellent infrared transmission of about 70% in the 11 μm region were fabricated, as shown in Figure 6. It was observed that the infrared transmittance of the ZnS ceramics was improved with the increase in dwell time during hot pressing, which might be attributed to the decrease in the amount of the optically anisotropic ZnS wurtzite, due to the prolonged heating under the applied pressure.[127]

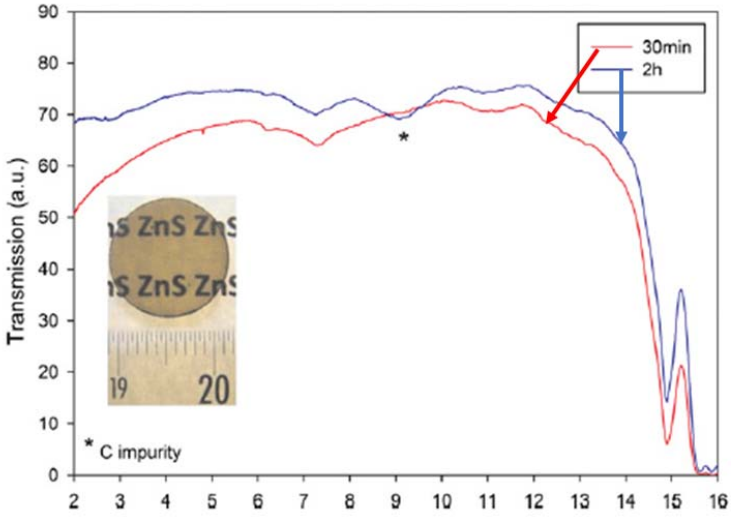


Figure 6. Infrared transmission of ZnS hot-pressed ceramics (950°C, 30 min and 2 h, 50 MPa) from synthesized powders (thickness: 1 mm), and photograph of ZnS ceramic processed for 2 h.[127]

Concurrently, researchers from different commercial companies performed several processing studies on ZnS infrared optical ceramics. D. Gao et al. from Nanocerox Inc. reported the fabrication of ZnS optical ceramics with excellent visible and infrared transmittance.[128] The ceramics were consolidated in an inert atmosphere, by using ZnS nanopowders synthesized via aqueous synthesis techniques, to achieve a relative density of approximately 95% and closed porosity. After post treatment via HIP, the ZnS infrared optical ceramics were shown to have comparable optical and mechanical properties with the commercially available CVD-processed ZnS.[128]

K. Rozenburg et al.[129] from Schott Corporation pointed out that highly infrared transparent ZnS ceramics with improved mechanical strength were prepared, by consolidating ZnS powders with compromising particle sizes. The particle needed to be fine enough to promote sintering but coarse enough to prevent the early phase transition from sphalerite to wurtzite at low temperatures. The ZnS optical ceramics with fine grains were reported to be processed via uniaxial hot pressing at 900-1000 ℃ under 40-60 MPa, followed by HIPing at 900-1000 ℃ under 180-230 MPa.[129]

By using powder metallurgical technology, T. Ueno et al.[130] developed a processing route consisting of sintering and net-shape molding process, to precisely fabricate economical ZnS ceramic lens with spherical, aspherical and diffractive optical element lens

shapes. The developed ZnS ceramic lens exhibited excellent optical characteristics for thermal camera applications, including desirable infrared transmittance in 8-12 μm and remarkable modulation transfer function performance.[130]

Additionally, it was claimed by D. Ravichandran et al.[131] from Texas Biochemicals Inc. that the ZnS ceramics, with nanograins and pure sphalerite phase, could be sintered via spark plasma sintering of ZnS synthesized nanopowders at low temperatures (600-750 ℃). Different zinc sources and sulfur sources were used to synthesize ZnS monodispersed nanopowders via homogeneous precipitation.[131] Moreover, they proposed that the hot pressing (at 1000 ℃) and vacuum sintering (at 800-1010 ℃, followed by HIP) of ZnS green bodies, which were formed by cold isostatic pressing of ZnS nanopowders, could also result in ZnS infrared optical nanoceramics and different shapes, for various infrared optical applications.[132]

As spark plasma sintering method was extensively investigated and employed more intensely in the field of infrared optical oxide ceramics, its capability in processing of ZnS infrared optical ceramics was also widely explored. Y. Chen et al.[133] investigated the spark plasma sintering of ZnS ceramics using heat treated ZnS commercial powder. They concluded that the ZnS samples sintered at 840 ℃ at a heating rate of 5 ℃/min had the optimized optical performance reaching ~65% in the wavelength range of 5.0-12.0 μm. Figure 7 shows the photos and infrared transmittance curves of the ZnS samples. Through the study on the effect of heating rate on the processed ZnS ceramics consolidated via SPS, it was revealed that the relative density increased, and the content of wurtzite reduced, as the heating rate decreased from 100 ℃/min to 5 ℃/min.[133]

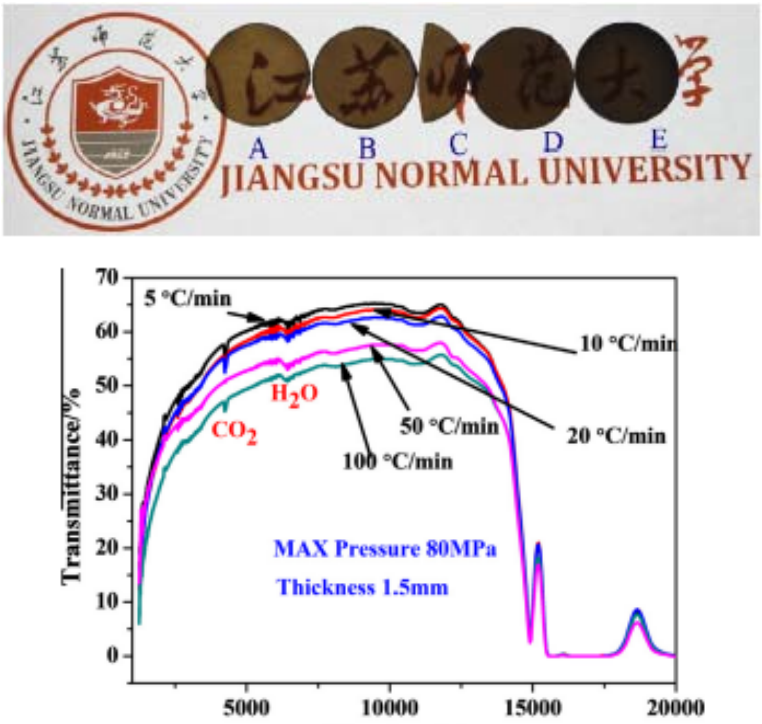


Figure 7. Appearance and transmission plots of the mirror-polished specimens sintered with different heating rates ((A) 5 °C/min, (B) 10 °C/min, (C) 20 °C/min, (D) 50 °C/min, and (E) 100 °C/min).[133] Reprinted with permission from Elsevier.

Also, M. Isogai et al.[134] recently reported the fabrication of ZnS infrared optical ceramics by optimizing sintering conditions during SPS. Different commercially available ZnS powders were pre-heat-treated to remove outgassing at 400 °C. It was also found that lower heating rate and longer soaking time were beneficial for densification. The ZnS ceramics experienced at sphalerite-wurtzite phase transition at 800 °C, which was assumed to be driven by the deformation faults in raw powder. The sample sintered at 900 °C under optimized conditions had high infrared transmittance and good mechanical properties.[134]

By using the ZnS nanopowder processed through mechanochemical synthesis, H. Ahn et al.[135] applied SPS to sinter ZnS infrared optical ceramics with sintering additives. The ZnS ceramics, sintered at 920 °C for 10 min under 50 MPa, using the optimized ZnS powder added with LiF, were shown to have the best optical properties (maximum infrared transmittance of ~ 55%) and most sufficient densification (99.8% of relative density) The high degree of the sphalerite-wurtzite phase transition and large grain sizes were reported to be due to the actually high SPS temperature applied on the sample.[135]

Y. Li et al. performed a processing study on the wet-chemistry synthesis of ZnS nanopowders using various sulfur sources under different pH conditions. It was revealed that the colloidal processing method, including precipitation and subsequent water baths, was beneficial for obtaining homogenously-distributed spherical ZnS particles with controllable sizes. ZnS infrared optical ceramics were then sintered via SPS and hot pressing using the synthesized powders, to study and compare consolidation behaviors.[136] The ZnS powders with homogeneous spherical particles were shown to have a favorable sinterability. It was also demonstrated that the hot pressing method was a more effective way to process ZnS optical ceramics. Although particle size-induced early phase transition from sphalerite to wurtzite was partially observed, the hot-pressed ZnS ceramic sintered using the spherical particles still exhibited excellent infrared optical transmittance (as shown in Figure 8(a)), due to the enhanced densification.[137] In addition, the sintered ZnS ceramics exhibited photoluminescent characteristics, with a weak blue emission peak and strong green emission band. It was postulated that the blue emission was due to the zinc vacancies, while the green photoluminescence was attributed to sulfur defects and elemental sulfur species.[137,138] However, as J. McCloy et al. discussed in the photoluminescence study on CVD-processed ZnS, the photoluminescence data suggested an extremely complicated picture of electronic defects, with copper defects or oxygen complexes likely responsible for the dominant green photoluminescence.[139,140]

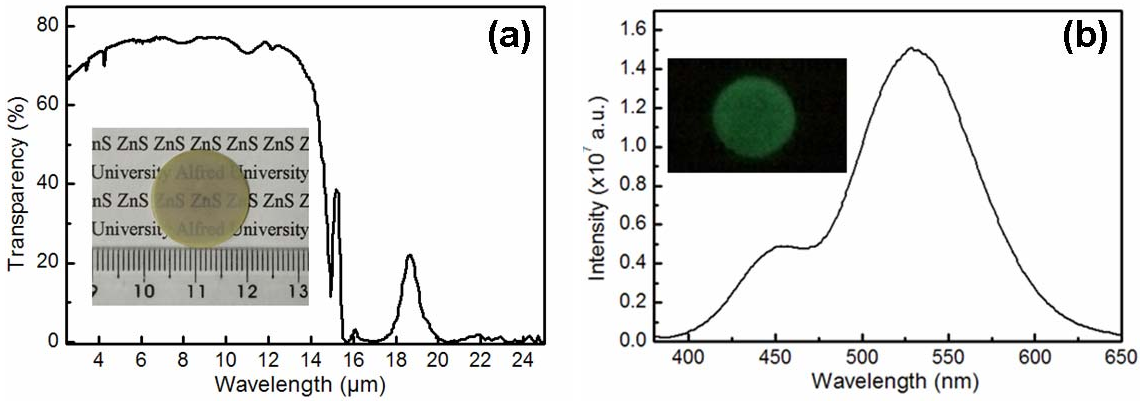


Figure 8. (a) Infrared transmittance spectrum of the hot-pressed ZnS ceramic (sintered at 1000 ℃ under 50 MPa for 3 hours) and a photograph of the ZnS pellet (inset) with a diameter of 18.75 mm and a thickness of 0.60 mm; (b) Photoluminescence emission spectrum for the hot-pressed ZnS ceramic with an excitation wavelength of 365 nm and a photograph of a ZnS pellet after UV light exposure (inset).[137]

C. Li et al. studied the densification, phase transition and preferred orientation of ZnS infrared optical ceramics.[141] ZnS nanopowders were synthesized via a precipitation method to be prepared for consolidation. It was reported that transparent ZnS ceramics with maximum densification could be fabricated via hot pressing of heat-treated synthesized ZnS powder composed of pure wurtzite, at 900 ℃ under a high pressure of 250 MPa (using tungsten dies). They also observed a reverse phase transition from ZnS wurtzite back to ZnS sphalerite as the sintering temperature increases in the range of 750-900 ℃. In addition, it was found that the presence of wurtzite orientation along [0001] direction was beneficial for the reduction of the scattering loss caused by secondary phase scattering and birefringence.[141] Moreover, by adopting a similar processing method combined with the post HIP process, they succeeded in fabricating $Fe^{2+}$ doped ZnS infrared optical ceramics, with the maximum in-line infrared optical transmittance of 65% at 4.5 μm.[142] Alternatively, they applied a route with a combination of wet-chemical precipitation and solvothermal synthesis to fabricate ZnS nanopowders, for subsequent hot pressing of ZnS infrared optical ceramics. It was emphasized that the solvothermal treatment was useful for controlling phase composition and removing impurities, which in turn led to the improvement of infrared transmittance.[143]

Recently, K. Lee et al.[144] and S. Yeo et al.[145] conducted processing studies on hot pressing of ZnS infrared optical ceramics, by using ZnS nanopowders synthesized via hydrothermal method.[144,145] It was proposed in both studies that the appropriate pre-heating treatment of the as-synthesized ZnS powder was of great importance for the removal of impurities (carbon and sulfate) and the sufficient densification of ZnS ceramics. The resulting hot-pressed ZnS ceramics were reported to have the maximum transmittance of 60%-70% in the mid-infrared wavelength range.

Researchers also demonstrated the feasibility of applying hot pressing to process ZnS optical ceramics with complex shapes. X. Mao et al. modified the hot- pressing die into a dome shape for the production of ZnS infrared ceramic domes. The powders were cold-isostatically pressed under 200 MPa, and then hot-pressed at 750-950 ℃ under 200-400 MPa for 30-120 min. The ZnS ceramic domes exhibited desirable, uniform infrared optical properties, which could be further improved by using HIP.[146]

Apart from the ZnS infrared optical ceramics for their applications in infrared windows/domes, ZnS polycrystalline materials doped with transition metals (Cr and Fe) are excellent candidates for mid-infrared laser grain media. S. Mirov et al. conducted tremendous research on the lasing performances of $Cr^{2+}$:ZnS and $Fe^{2+}$:ZnS materials.[147-152] It was reported that they applied CVD or chemical vapor transport (CVT) methods followed by thermal diffusion to fabricate $Cr^{2+}$:ZnS and $Fe^{2+}$:ZnS transparent ceramics with desirable mid-infrared lasing performances. CVD combined with HIP was also used to prepare polycrystalline ZnS host ceramics prior to the thermal diffusion of $Cr^{2+}$ ions. The processed ZnS infrared optical ceramics doped with $Cr^{2+}$ and $Fe^{2+}$ exhibited unique spectroscopic (absorption and emission) characteristics of mid-infrared region, due to the $^5E \leftrightarrow {}^5T_2$ transitions in the tetrahedral crystal field of ZnS ceramics.

### 2. $CaLa_2S_4$ Infrared Optical Ceramics

Due to its favorable optical performance and mechanical properties, the rare earth and alkaline earth ternary refractory sulfide compound $CaLa_2S_4$, crystallizing in the cubic thorium phosphate ($Th_3P_4$) crystal structure, has received intense research interest as a promising candidate for infrared optical ceramics.[54,153,154] It has been reported that $CaLa_2S_4$ not only displays a broad infrared transmittance range of 8-14 um, but also has superior hardness and better rain erosion resistance compared with conventional infrared ceramic

materials such as ZnS and ZnSe, suggesting that it has the potential as an advanced infrared optical ceramic.[55,155,156] Table I shows a comparison of some physical properties of $CaLa_2S_4$ and ZnS. It is demonstrated that $CaLa_2S_4$ has better mechanical properties than those of ZnS.

Table I. Some Physical Properties of $CaLa_2S_4$ and ZnS.[155,157,158]

| | $CaLa_2S_4$ | ZnS |
|---|---|---|
| Flexural Strength (MPa) | 86-106 | 60-103 |
| Young's Modulus (GPa) | 95.8 | 74.6-87.6 |
| Poisson's Ratio | 0.26 | 0.29 |
| Knoop Hardness (GPa) | 5.59 | 2.45 |
| Thermal Expansion ($10^{-6}$/K) | 14.7 | 7.4 |
| Thermal Conductivity (Cal/cm·sec·ºC) | 0.006 | 0.041 |
| Refractive Index | 2.70 | 2.35 |
| Absorption coefficient, at 10.6 μm ($cm^{-1}$) | 0.2 | 0.1 |

**a Crystal Structure of $CaLa_2S_4$**

The crystal structure of $CaLa_2S_4$ bears a strong resemblance to that of γ-lanthanum sesquisulfide (γ-$La_2S_3$), which exhibits a cubic-defect $Th_3P_4$ structure; a variation of the $Th_3P_4$ structure, but with a small fraction of metal vacancies. Figure 9 shows the crystal structures of $La_2S_3$ with the cubic-defect $Th_3P_4$ structure, and $CaLa_2S_4$ with the ideal $Th_3P_4$ structure. The $La_2S_3$ unit cell is composed of 16 sulfur atoms and $10\frac{2}{3}$ lanthanum atoms, with metal vacancies being randomly arranged in such a way that every ninth position is vacant. It has been reported that the addition of small amounts of large divalent cations (such as $Ca^{2+}$) into the metal vacancy sites of the $La_2S_3$ lattice stabilizes the cubic structure by producing a near-ideal cation-to-anion ratio, which is 3:4 for the $Th_3P_4$ structure.[159] In this ideal $Th_3P_4$ structure, calcium and lanthanum atoms occupy the twelve point sites corresponding to Site Symmetry 4, while the sulfur atoms fully occupy the sixteen point sites corresponding to Site Symmetry 3. Thus, $CaLa_2S_4$ has the stabilized cubic structure

with $Ca^{2+}$ ions occupying the metal vacancies and a portion of La sites in the $Th_3P_4$ structure.[160]

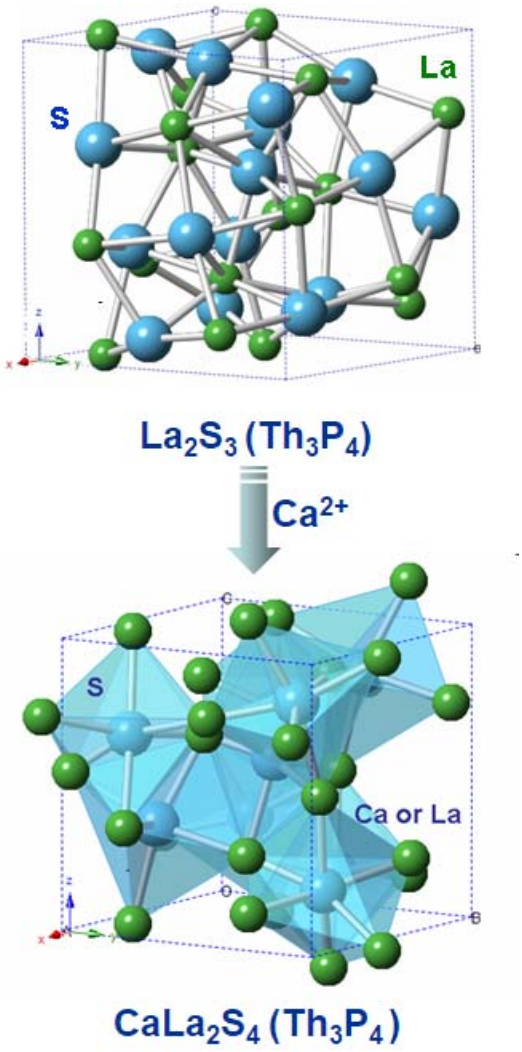


Figure 9. Crystal structures of $La_2S_3$ with the cubic-defect $Th_3P_4$ structure and $CaLa_2S_4$ with the ideal $Th_3P_4$ structure.

### b Research and Development of $CaLa_2S_4$ Infrared Optical Ceramics

In the 1980s, to find suitable airborne ceramic window materials for 8-12 μm thermal systems resistant to harsh environmental conditions, including aerodynamic heating, thermal shock, and rain erosion, a family of alkaline rare earth ternary sulfide ($AB_2S_4$), which could offer the potential for exhibiting better thermal and mechanical properties than ZnS, was investigated to ascertain its feasibility for the application.[54] The

refractory compound $CaLa_2S_4$ with the cubic $Th_3P_4$ structure attracted much research interest, due to its enhanced mechanical hardness and extended infrared transmission range.[161]

Since then, many studies have been performed on $CaLa_2S_4$, mainly focusing on the preparation of $CaLa_2S_4$ powders and consolidation of $CaLa_2S_4$ infrared optical ceramics. In general, the $CaLa_2S_4$ pure powders were reported to be synthesized through long-time and high-temperature sulfurization of $CaLa_2S_4$ precursors in $H_2S$ or $CS_2$ atmosphere, which were previously prepared with various processing variables via different routes including carbonates coprecipitation, alkoxide method, evaporative decomposition of solutions and mixed oxide/carbonate/hydroxide method. The as-synthesised, single-phase $CaLa_2S_4$ powders were subsequently consolidated via different pressure-assisted sintering techniques to form $CaLa_2S_4$ infrared optical ceramics.

In the United Kingdom, K. Lewis et al. and J. Beswick et al. explored the processing methods for the $CaLa_2S_4$ synthesis and consolidation.[153,162] They first applied the slow evaporation of Ca/La nitrates at 900 ℃ for 24 hours to form oxides, followed by sulfurization in $H_2S/N_2$ at 1150-1350 ℃. However, the relatively high sulfurization temperature resulted in partially sintered powders with 5-20 μm grains, and this method led to non-uniformity in composition and color. Then, four improved synthetic routes, including oxalate route, organic route, rapid decomposition of solution, and evaporative decomposition of solution, were developed to successfully synthesize the $CaLa_2S_4$ precursors for sulfurization at lower temperatures (900-1000 ℃). Hot pressing at 1100-1500 ℃ was used for consolidation of the ceramics, and the effect of sintering aids ($PbLa_2S_4$ and LiF) was also later investigated. It was revealed that the $CaLa_2S_4$ sample sintered at 1346 ℃ (or 1350 ℃) could achieve the theoretical density, but it exhibited dark black color with no infrared transparency, due to the sulfur loss and deficiency during the hot-pressing process. Thus, the post-annealing process in $H_2S$ considerably improved the infrared transmittance of $CaLa_2S_4$ ceramics (with a maximum infrared transmittance of ~60%; thickness of 0.33 mm). Nevertheless, broad absorption peaks were evidently observed in 9-11 μm region of the infrared transmittance curve, due to the presence of $SO_3^{2-}$ and $SO_4^{2-}$. Another consolidation method, a combination of pressureless sintering in $H_2S$ followed by HIPing, was demonstrated to be more promising for the fabrication of

$CaLa_2S_4$ infrared optical ceramics with both favorbale transmittance and hardness.[155] In addition, through a study on the $CaLa_2S_4$-$La_2S_3$ solid solution system, J. Savage et al. managed to fabricate CaS45mol%-$La_2S_3$55mol% ceramics, with the elimination of oxygen impurity induced absorptions and enhanced infrared transmittance.[155,163]

Concurrently, researchers in the United States also performed tremendous processing studies on $CaLa_2S_4$ infrared optical ceramics. W. White et al.[164] synthesized $CaLa_2S_4$ powders by reacting carbonates of the alkaline earth elements with either oxides or hydroxides of the lanthanide elements at 1050-1100 ºC in flowing $H_2S$ for 3-7 days. It is found that it was difficult to achieve the exact stoichiometry. CaS was also detected as an impurity in the processed powder, but it could be removed by washing, and the powder needed to be sulfurized again at 800 ºC. Two sintering routes were investigated and applied to consolidate the milling-processed synthesized $CaLa_2S_4$ powders. Sintering in flowing $H_2S$ at 1500 ºC for 300 min could lead to the maximum densification of 95%. In contrast, with the assistance applied pressure, hot pressing at 1450 ºC under 20-40 MPa for 30 min could result in the $CaLa_2S_4$ with high densification of 99.9%. However, hot pressing was limited by the tendency of $CaLa_2S_4$ to drift off stoichiometry, which would in turn affect the optical properties. The $CaLa_2S_4$ ceramics exhibited the best infrared optical transmittance of ~50% at ~13 μm, with a pronounced absorption feature at ~10.6 μm due to oxygen impurities. Post HIPing of hot-pressed samples was demonstrated to result in theoretically dense $CaLa_2S_4$ ceramics with high Vickers hardness.[164] Alternatively, they employed an improved processing route to prepare oxide precursors for subsequent sulfurization, by the evaporative decomposition (spray pyrolysis) of nitrate salt solutions.[165] The resulting $CaLa_2S_4$ powders with smaller grain size were shown to have better sinterablities, which in turn led to denser $CaLa_2S_4$ and $CaLa_2S_4$-$La_2S_3$ ceramics.[166,167]

K. Saunders et al.[55] from Raytheon used an aqueous carbonate co-precipitation method using nitrate salts and ammonium carbonate, to synthesize carbonate precipitates as $CaLa_2S_4$ precursors. Then, the carbonates were subsequently sulfurized at 900-1000 ℃ in flowing $H_2S$ for 1-20 hours to prepare $CaSO_4$/$La_2O_2S$ or $CaLa_2S_4$. After being ball milled to break the necking formed during the high-temperature sulfurization process, the powder was cold isostatic pressed under 172 MPa and normally sintered at 1050-1150 ℃ in a $H_2S$ atmosphere. The as-sintered ceramics composed of single-phase $CaLa_2S_4$ were found to

have approximately 95% of relative density with isolated closed porosity. Fully dense $CaLa_2S_4$ ceramics were achieved using HIP at 990 ℃ under 172-200 MPa in argon for 3 hours and the absorption coefficient at ~10.6 um was significantly decreased. Since $CaLa_2S_4$ and $La_2S_3$ could form a complete series of solid solutions, non-stoichiometry was commonly found in the processed $CaLa_2S_4$ ceramics. The researchers further investigated the correlation between chemical compositions and optical properties of the $CaLa_2S_4$ ($CaLa_2S_4$-$La_2S_3$) infrared optical ceramics. It was revealed that the sample with a La/Ca ratio of 2.7 had the best infrared optical performance, as shown in Figure 10. In addition, the $CaLa_2S_4$ ceramics (La/Ca ratio: 2.7) were measured to have superior mechanical harness and water drop impact resistance but inferior thermal properties than ZnS ceramics.[55,168-170]

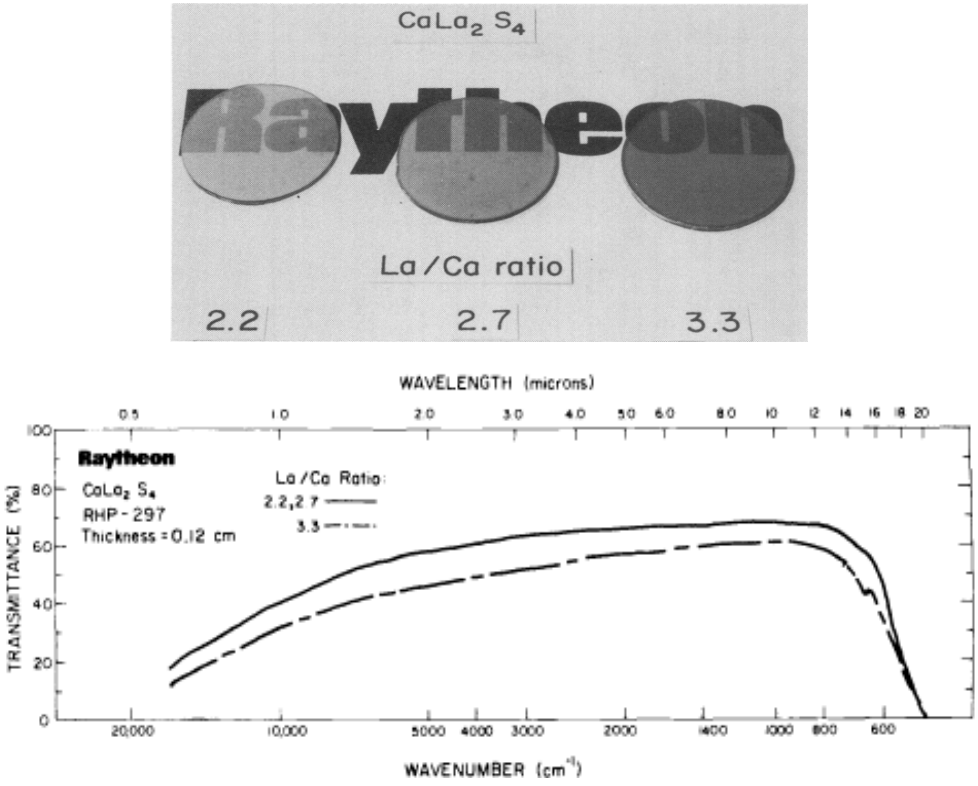


Figure 10. Photo and in-line transmittance curves of the $CaLa_2S_4$ samples with varying La/Ca ratios.[55] Reprinted with permission from SPIE Press.

Researchers from Naval Weapons Center developed another synthetic route to prepare $CaLa_2S_4$. A stoichiometric mixture of calcium and lanthanum nitrates was either

mixed with acetone to form a paste or dissolved in concentrated nitric acid. Then the materials were evaporated to dryness in a vacuum oven. The grinded mixed nitrates were sulfurized at 900 °C in $H_2S$ to form $CaLa_2S_4$. They applied two sintering procedures (hot pressing in vacuum or $H_2S$; sintering in $H_2S$ followed by HIPing in argon) to consolidate the $CaLa_2S_4$ infrared optical ceramics. A detailed investigation was conducted to determine the cause of the remaining extrinsic absorptions, in order to further optimize the optical properties of the ceramics. The presence of CaS, rhombic-sited $Fe^{3+}$, and octahedral-sited $Mn^{2+}/Cr^{3+}/V^{2+}$ was demonstrated by using electron paramagnetic resonance and excitation/emission spectroscopies. In addition, the calcium deficiency in $CaLa_2S_4$ could lead to the formation of $La_3S_4$ due to the sulfur loss of $La_2S_3$, which resulted in the observed infrared absorptions.[171,172]

In the 1990s, Y. Han et al. performed a processing study on the preparation of $CaLa_2S_4$ powders via sulfurization of methoxides of calcium and lanthanum.[173] Alkoxide mixtures of various La/Ca ratios (2.4-3.1) dispersed in methanol were reacted with $H_2S$ at 25-85 °C, and the amorphous gels obtained after the removal of methanol were heat treated in $H_2S$ for sulfurization at 200-950 °C for 5-10 h. It was found that single-phase $CaLa_2S_4$ powders were obtained with the La/Ca ratios of 2.41 and 2.68 in the temperature range of 650-750 °C, where the formation of cubic $LaS_2$ promoted the formation of $CaLa_2S_4$. Tetragonal $La_2S_3$ was detected as a secondary phase in the $CaLa_2S_4$ powders with higher La/Ca ratios. Infrared spectra did not show any significant absorption features, indicating that synthesized $CaLa_2S_4$ powders were free of oxygen contamination.[173]

L. Wang et al.[174-176] also applied a similar synthetic route for fabricating stoichiometric submicron $CaLa_2S_4$ powders with high sinterability, by high-temperature sulfurization of metal alkoxides (modified metal methoxides) in $H_2S$. The synthesized $CaLa_2S_4$ powders were then densified via normal sintering followed by HIP/annealing in $H_2S$. It was shown that 1050 °C was the optimum sulfurization temperature to obtain $CaLa_2S_4$ powders with less impurities and resulting ceramics with higher near-infrared transmittance. Furthermore, by conducting several processing studies, they demonstrated that 1400 °C was the optimum sintering and HIP temperature for fabricating highly dense $CaLa_2S_4$ infrared optical ceramics (with the maximum infrared transmittance ranging from 55%-60%).[174-176]

Concurrently, they also made several further investigations into the synthesis of $CaLa_2S_4$ via decomposition and sulfurization of carbonates precipitates. Various processing conditions, including stoichiometric ratio of La/Ca, pH value of the solvent, solvent type, titration rate, decomposition atmosphere, drying conditions, were investigated to form and to optimize $CaLa_2S_4$ powders with better homogeneity and sinterability.[177-179] It was revealed that the optimized powders could lead to translucent $CaLa_2S_4$ infrared optical ceramics (62% at 13 μm; thickness of 0.55 mm) in thin sections, via sintering, HIP treatment, and annealing in a $H_2S$ atmosphere at 1400 °C.[179] In addition, an acetate route was developed to synthesize $CaLa_2S_4$ precursors. The resulting densified $CaLa_2S_4$ ceramic sintered using the sulfurized powders was shown to achieve theoretical density, with the infrared transmittance of 40% at 13 μm (thickness: 0.45 mm).[180]

Through a study on the powder (via sulfurization of carbonate precipitates) and ceramic fabrication of $CaLa_2S_4$-$PbLa_2S_4$ solid-solution, L. Wang et al.[182,183] succeeded in the fabrication of $Pb_{0.1}Ca_{0.9}La_2S_4$ infrared optical ceramics, with the infrared transmittance of 50% at 13 μm (thickness: 0.47 mm). It was concluded that the limited addition of Pb could eliminate the CaS second phase, lower the sulfurization temperature, and improve the transmittance and reproducibility, due to low melting and high diffusivity.[181] Later, B. Tsay et al. from the same group employed the alkoxide sulfurization method to synthesize $Pb_{0.1}Ca_{0.9}La_2S_4$ (Pb:Ca:La=0.1:0.9:12) powders in different sulfurizing atmospheres including $CS_2$ and $H_2S$. The sample (thickness of 0.86 mm) sintered via normal sintering followed by HIPing (200 MPa) and annealing at 1350 °C in $H_2S$ exhibited the best infrared transmittance of 60% at 14 μm. The characteristic absorption bands of sulfate and sulfite at 9.2 μm and 11 μm were reduced by eliminating the oxygen content in the sulfide ceramics, using powders with optimized sulfurization conditions.[182,183]

M. Tsai et al.[184,185] studied the effects of sulfurizing agent (atmosphere) and La/Ca stoichiometric ratio on the formation of $CaLa_2S_4$, synthesised via sulfurization of carbonate precipitates. It was determined that $CS_2$ was beneficial for decreasing the temperature and soaking time for sulfurization of pure $CaLa_2S_4$ with uniform particles, as the cubic binary sulfide $LaS_2$ was the intermediate phase, while higher temperature and longer time were needed for sulfurization when sulfur or $H_2S$ was used as the sulfurizing agent, due to the presence of intermediate phase of oxysulfide $La_2O_2S$. In addition, the formation

temperature of $CaLa_2S_4$ increased as the La/Ca ratio increased.[184,185] Then, hot pressing followed by annealing in $CS_2$ was applied to consolidate the synthesized $CaLa_2S_4$ powders with different La/Ca ratios (2 and 15) to form $CaLa_2S_4$ infrared optical ceramics. The ceramic sample with the La/Ca ratio of 15 hot pressed at 1050 ℃ was shown to exhibit better infrared optical transmittance. However, the presence of extrinsic impurities including $CO_3^{2-}$, $SO_4^{2-}$, and C-S bond resulted in apparent absorption peaks, affecting the optical performance.[186,187]

Recently, O. Merdrignac-Conanec et al.[188] developed a novel patented method to synthesize $CaLa_2S_4$ powders in a shorter time, by sulfurization (in $H_2S$ at 1000 ℃) of precursors processed via solution combustion of metal nitrates and TAA. It was revealed that the powder with the La/Ca ratio of 2.7 could lead to the pure phase of $CaLa_2S_4$, while the ratios of 5 and 9 would contribute to the presence of β-$La_2S_3$ as the second phase, which might be attributed to a less efficient stabilization of the cubic $CaLa_2S_4$ phase by lowering Ca content. Pressureless sintering and hot pressing were applied for consolidation, and different sintering variables were investigated to achieve more densified ceramics with favorable optical transmittance. The most densified sample (99.8%, thickness of 1.2 mm) sintered at 1350 ℃ for 12 in $H_2S$ followed by hot pressing a BN powder bed at 1000 ℃ for 6h exhibited the infrared transmission of 51% in the 12-14 μm range. The $CaLa_2S_4$ compounds were shown to be very sensitive to oxygen contamination and stoichiometry deviation, which were dependent on different processing conditions.[188]

By using different methods for the preparation of $CaLa_2S_4$ precursors, researchers from Naval Research Laboratory managed to process fine powders of $CaLa_2S_4$ with high Brunauer–Emmett–Teller (BET) surface areas.[189] It was proposed that co-precipitation and separate precipitation could be used to prepare precursors through reactions of calcium/lanthanum nitrates with different sources including ammonium bicarbonate and ammonium oxalate. Alternatively, flame spray pyrolysis was employed to synthesize $CaLa_2O_4$ nanopowders as the precursor. The precursor high-temperature sulfurization in $H_2S$ at 900 ℃ for 24 hours to form $CaLa_2S_4$ nanopowders. The researchers also performed a study on $Pr^{3+}$ doped $CaLa_2S_4$ infrared optical ceramics, which demonstrated the potential of rare earth doped $CaLa_2S_4$ as a promising mid-infrared laser gain material.[190,191] The synthetic route from Naval Weapons Center was used for the powder synthesis, and the

ceramics were densified using hot pressing followed by HIPing. The $Pr^{3+}$ doped $CaLa_2S_4$ ceramics exhibited desirable broad infrared transmittance, but the absorption at about 9.5 μm was observed, indicative of the presence of oxygen impurities. The strong and broad emission at 4.5 μm with the lifetime of 9.7 ms, corresponding to the $^3H_5 \rightarrow {}^3H_4$ transition, was not only favorble for tunable CW pulsed laser operation, but also for ultrashort pulse lasing in the mid-infrared.[190,191]

### 3. Sulfide-Based Composite Infrared Optical Ceramics

It is well acknowledged that nanocomposite ceramics can offer improved mechanical properties over those of singe-phase materials or micro-crystalline composite ceramics. Significant enhancements of mechanical properties have been observed in different systems of structural nanocomposite ceramics, including $SiC/Al_2O_3$, $Al_2O_3/ZrO_2$, SiC/MgO, and $SiC/Si_3N_4$, due to different possible strengthening mechanisms.[78] For infrared optical composite ceramics, in recent years, several studies have focused on MgO-$Y_2O_3$ nanocomposite infrared optical ceramics, to improve mechanical strength and hardness through toughening. The 50vol% MgO-50vol% $Y_2O_3$ nanocomposite ceramics, sintered via various pressure-assisted sintering methods using various lab-processed powders, were shown to have superior mechanical properties than the two individual materials without expense of the infrared optical performance.[77,78,192-198] It was proposed that the grain size needed to be much smaller than the wavelength (less than about λ/20 or λ/30) to attain more favorable optical transmittance, which could reduce the scattering induced by the difference in refractive indices between the two phases.[199] In addition, strengthening in optically transparent spinel/$Si_3N_4$ nanocomposite ceramics was demonstrated by A. Gledhill et al. The composite ceramics were shown to possess >70% infrared transmittance in 3-4.5 μm, with enhanced average strength and indentation toughness.[200]

As discussed previously, despite their superior infrared transmittance suitable for infrared window applications, due to their intrinsically weak chemical bonds and poor mechanical properties, ZnS infrared optical ceramics have low durability and resistance to erosion caused by rain and sand exposure, which limits their application as infrared windows and domes in harsh environments.[156] Thus, some attempts have been made to enhance the mechanical properties of ZnS infrared optical ceramics, similarly by

introducing a second phase with a similar refractive index and better mechanical properties, to form ZnS-based composite materials.

Fundamental investigations of the partial equilibrium phase diagrams of ZnS-$Ga_2S_3$ (700-900 ℃) and ZnS-CdS (700-950 ℃) were conducted by B. Dunn et al. via phase analysis using XRD.[201,202] A eutectoid reaction occurred at 818±5 °C, where wurtzite (16±1 mol%) decomposed to sphalerite (9±1 mol%) and thiogallate (40±1 mol%). The solubility of $Ga_2S_3$ in ZnS was shown to increase with increasing temperature below the eutectoid temperature.[201] It was determined that the solubility of CdS in ZnS was extensive in both the sphalerite and wurtzite phases, with CdS stabilizing the wurtzite phase.[202] Furthermore, the researchers developed ZnS-$Ga_2S_3$ (8, 12, and 16 vol% of $Ga_2S_3$) ceramic composites sintered via hot pressing at 900 ℃ under 138 MPa in vacuum. The incorporation of $Ga_2S_3$ into ZnS enhanced both the hardness and fracture toughness of ZnS. The hardness was observed to increase as the grain size decreased for all the composite and pure ceramics, which was consistent with the Hall-Petch relation.[203]

R. Raj et al. performed a comprehensive study on ZnS-diamond composite infrared optical ceramics.[204-208] It was suggested that the addition of 10 wt% diamond particles to the hot-pressed ZnS ceramics improved the mechanical properties, and the fracture toughness was most significantly, approximately doubled, which was explained by elastic interaction of the crack-tip stress field with the dispersed stiff diamond particles. The infrared transmittance of the ZnS-diamond ceramics depended significantly on the quality of diamond dispersion, which was closely correlated with the green state processing conditions. They found that a combination of ultrasonic, shear mixing and freeze milling of the ZnS-diamond powders was beneficial for effective diamond dispersion and preservation of favorable infrared optical properties.[204] Hot-pressing parameters were also optimized to refine the grain size of ZnS-diamond and to reduce the hexagonal ZnS wurtzite to minimize scattering. The hot pressing at 900-1000 ℃ under 200 MPa for 30 min could lead to the ZnS-10wt%diamond micro-grain ceramics with good long-wave infrared transmittance at 10 μm comparable to pure ZnS. EMA model was used to explain the absorption in the two phase media, based on the microstructure observation, displaying that grains of the two phases were similarly interconnected in the composite ceramics.[208]

Also, A. Fujii et al.[209] reported that the hot-pressed ZnS-diamond composite ceramics with increased hardness, fracture strength and Young modulus could improve the durability against rain erosion for the ZnS infrared optical ceramics. Transmittance tended to decrease as diamond content increased. It was confirmed that two-layer constructed diamond-ZnS composites were improved in mechanical properties while maintaining effective optical property, suggesting that a multi-layer structure and/or gradient content structure would be desirable practically for ZnS-diamond composite infrared optical ceramics.[209]

M. Akinc's group investigated the chemical synthesis of chemical synthesis of ZnS/GaP nanocomposite powders. Two synthetic routes, flash pyrolysis and chemical vapor transport, were used to impregnate GaP nanoparticles into to ZnS powders with uniform, spherical, and submicrometer particles, which were synthesized via homogenous precipitation.[210,211] Densified by cold isostatic pressing followed by hot isostatic pressing at 900 ℃ under 207-276 MPa, the composite ceramics showed increases in both indentation hardness and fracture toughness, compared with pure ZnS. The increase in the hardness was postulated to be due to the addition of reinforcing harder phase GaP. The presence of nanosized dispersoids might deflect crack propagation or plastic deformation, which in turn led to the increase in fracture toughness.[212]

Moreover, J. Wahl et al.[213] uniformly mixed ZnS and $CaLa_2S_4$ nanopowders by ball milling, and applied pressureless sintering at 1100 ℃ for 6 hours, followed by HIPing at 990 ℃ for 12 hours, to consolidate the layered (thickness of 0.1 mm) 74vol%ZnS-26% $CaLa_2S_4$ nanocomposite material. Microstructural analysis showed that the $CaLa_2S_4$ phase incorporated into the ZnS matrix was needle-like. The nanocomposite exhibited a maximum transmittance of 45% in the long-wave infrared wavelength range and had evidently improved hardness. In addition, they also applied magnetron radio frequency sputtering to generate nanocomposite coatings of ZnS-$Y_2S_3$ with enhanced hardness and durability, while preserving the relevant optical properties. These ZnS-based composites showed potential for long-wave infrared optical window and coating applications.[213]

## C. Goals and Organization of the Thesis

Tremendous numbers of studies have been performed on the fabrication of sulfide-based infrared optical ceramics, mainly on ZnS and $CaLa_2S_4$. However, few studies have been systematically conducted to propose rational discussions to fundamentally elucidate the correlation between the processing, phase composition, microstructure and properties of the pressure-assisted sintered sulfide-based infrared optical ceramics, which will be of significance to effectively process these sulfide based optical ceramics with improved performances for future demanding applications.

The primary goal of the proposed project is to develop both individual and composite sulfide-based infrared optical ceramics with favorable optical properties and enhanced mechanical properties. To achieve this goal, this study aims to acquire an enhanced understanding of the phase development, microstructural evolution, sintering behavior and grain growth kinetics of sulfide-based ceramics under different pressure-assisted sintering conditions. In this work, wet chemistry methods will be used to synthesize ZnS and $CaLa_2S_4$. ZnS-$CaLa_2S_4$ composite powders will also be obtained using high-energy ball milling of commercial $CaLa_2S_4$ powders together with lab-processed ZnS powders. Then, pressure-assisted sintering techniques (hot pressing and field assisted sintering) will be applied to consolidate the powders into sulfide-based ceramics. Various characterization techniques will be employed to qualify and quantify the phase composition, microstructure, and property of the sulfide-based ceramics.

In this thesis, Chapter I has introduced the basic background information of infrared optical ceramics, including unique characteristics, processing requirements, development, and cutting-edge research, with a specific emphasis on the literature review of sulfide-based (ZnS and $CaLa_2S_4$) infrared optical ceramics.

The author's master thesis work discusses the synthesis of ZnS nanopowders via different wet chemistry methods, sintering behaviors of ZnS infrared optical ceramics sintered via hot pressing and field-assisted sintering, using different lab-processed and commercial powders, and photoluminescent characteristics of the as- sintered ZnS ceramics.[136] Thus, Chapter II of this thesis investigates the phase transition behavior between sphalerite and wurtzite of ZnS infrared optical ceramics, based on phase composition and microstructure analyses using XRD, scanning electron microscopy (SEM)

and electron backscatter diffraction (EBSD). The influence of microstructural features of starting particles and applied pressure during hot pressing on the ZnS phase transition is evaluated to provide discussions on the correlation between the control of phase composition and resulting optical/mechanical properties of ZnS ceramics.

Chapter III explores the possibility of the processing of hot-pressed chromium doped ZnS infrared optical ceramics for potential mid-infrared laser applications. Successful consolidation of highly dense $Cr^{2+}$ doped ZnS infrared transparent ceramics is demonstrated, through hot pressing of colloid-processed ZnS powder mixed with $Cr_2S_3$ powder. The location sites of the incorporated $Cr^{2+}$ within ZnS host lattice is determined using infrared absorption and photoluminescence spectra.

Chapter IV is a processing study on the synthesis of $CaLa_2S_4$ powders. Different synthetic routes with and without high-temperature sulfurization are investigated and compared, to develop a time-saving, cost-effective, and environmentally friendly method for the synthesis of $CaLa_2S_4$. The phase composition, crystallization behavior, and microstructural features of the heat-treated precursors are studied via XRD and SEM, in order to unveil the reaction mechanisms associated with different employed synthesis routes, chelating agents, and sulfur sources. Spectroscopic characterizations are employed to correlate the optical properties to the inherent characteristics of the processed oxysulfates, oxysulfides, and sulfides.

In Chapter V, consolidation of $CaLa_2S_4$ infrared optical ceramics via pressure-assisted sintering (field assisted sintering and hot pressing) is discussed. Microstructural features of the $CaLa_2S_4$ ceramics sintered via different sintering routes are compared. Densification behavior and grain growth kinetics of the samples sintered via field assisted sintering are systematically studied through densification curves and microstructural characterizations through applying established models. The infrared optical transmittance and mechanical indentation hardness is correlated with the microstructural properties and densification of the $CaLa_2S_4$ ceramics.

Chapter VI investigates the phase transition and consolidation of ZnS-$CaLa_2S_4$ ceramics sintered via pressure-assisted sintering of 0.5ZnS-0.5 $CaLa_2S_4$ (volume ratio) composite powders. XRD and transmission electron microscopy (TEM) are applied to study the sphalerite-wurtzite phase transition of ZnS within the composite ceramics. Based

on microstructure observation and sintering curve measurements, densification and grain growth of the composite ceramics sintered via field-assisted sintering are discussed, as a function of temperature to determine the sintering stages and grain growth mechanism. The infrared optical transmittance and indentation hardness of the ZnS-$CaLa_2S_4$ ceramics are characterized and compared with the individual ZnS and $CaLa_2S_4$ infrared optical ceramics.

# II. PHASE TRANSITION BETWEEN SPHALERITE AND WURTZITE IN ZnS OPTICAL CERAMIC MATERIALS

## A. Introduction

ZnS, a II-VI semiconductor with a wide band gap, has been widely investigated and utilized in many applications. As previously discussed, ZnS has two main crystal structures: cubic sphalerite and hexagonal wurtzite. The ZnS phase transition between sphalerite and wurtzite is believed to be martensitic, accompanied by the involvement of deformation faults (twinning) in closed-packed planes. In mineral form at ambient pressure, the phase transition from the cubic sphalerite to hexagonal wurtzite occurs at 1020º C,[90] and this temperature is the well-acknowledged phase transition temperature for the sphalerite-wurtzite phase transition at normal conditions.

The phases of ZnS are closely correlated with its potential applications. In terms of the properties desired for electronic and optoelectronic applications, wurtzite is a more attractive phase than sphalerite, due to its wider intrinsic band gap. Thus, in applications where wurtzite is the desired phase, its stability can be increased by decreasing particle size to nanometer-scale, which lowers the effective transition temperature at which ZnS transforms from sphalerite to wurtzite. Various researchers have performed extensive experimental and simulation-based studies on the influence of particle size on the ZnS phase transition during various nanosynthesis processes. S. B. Qadri et al. first proposed that reducing particle size could significantly lower the phase transition temperature of ZnS,[100] which led to numerous investigations into low-temperature syntheses of nanoscale wurtzite. F. Huang et al. developed a new model to account for the size-dependent sphalerite-wurtzite phase transition kinetics in hydrothermally synthesized nanocrystalline ZnS, based on the collective movement of atoms across sphalerite-wurtzite crystallite interfaces.[98] In addition, S. Li et al. and C. S. Tiwary et al. explained the effects of particle size and pressure on the ZnS phase transition, by considering the energetic contributions of surface energy, surface stress and external pressure to total Gibbs free energy, in a thermodynamic analysis of the phase transition.[214,215] In addition to the effect of particle size, *in situ* XRD measurements have demonstrated that pressure (ranging from 0.5 GPa to

11.5 GPa, dependent on the particle size) can also induce the phase transition from wurtzite back to sphalerite in both ZnS nanocrystals and nanobelts.[85,99,101] Moreover, the adjustments of surface area, morphology, and doping can also promote the formation of wurtzite during different synthesis processes.[101-106]

For infrared transparent ceramic applications, the cubic sphalerite phase is preferred, as it is crystallographically (and thus optically) isotropic. The presence of wurtzite in primarily sphalerite ZnS reduces transparency, due to the difference in refractive index between the two phases and the anisotropy of the hexagonal wurtzite structure. Since researchers at Kodak first demonstrated in the 1950s that highly dense ZnS infrared transparent ceramics could be achieved through hot pressing of ZnS powders, the method has become the desirable processing method for fabricating optical-grade ZnS ceramics for infrared applications.[216] With the simultaneous application of heat and pressure, hot pressing (in a vacuum or inert atmosphere) is capable of consolidating ZnS optical ceramics at relatively low temperatures.[119,127] Alternatively, another fabrication route, involving CVD followed by HIPing, has also seen significant exploration, which could produce ZnS ceramics with excellent transmittance in both the visible and infrared regions.[51,107]

Scholars have performed tremendous studies on the phase transition in ZnS optical ceramics processed via different routes. L. Xue et al. reported that the fraction of ZnS wurtzite formed during hot pressing was a function of sintering temperature. They observed that the phase transition from sphalerite to wurtzite occurred apparently at temperatures above 1020 ℃, and concluded that the increase in hot pressing temperature (>1020 ℃) led to higher wurtzite fractions and larger grain sizes, both of which resulted in more significant scattering losses.[122] They also investigated the deformation-dependent phase transition behavior of the hot-pressed ZnS ceramics, reheated in the temperature range of 900-1150 ℃ (near the sphalerite-wurtzite transition temperature: 1020 ℃). It was proposed that *in situ* deformation resulted in a strain-dependent phase transition from wurtzite to sphalerite, at temperatures lower than the typical transition temperature, with the high strain rate and flow stresses promoting the phase transition from sphalerite to wurtzite.[123,124] J. McCloy et al. studied the CVD-processed ZnS followed by HIP, and they further postulated that the strain-assisted recrystallization induced by HIP provided additional driving force for the reduction in hexagonality (martensitic transformation) and

crystallographic texture change (plastic deformation) of CVD-ZnS, both of which were beneficial for the improvement of optical transmittance as a result.[107,112] In addition, Chen et al. investigated SPS of ZnS ceramics using heat-treated commercial ZnS powder. Through examination of the effect of heating rate on the properties of the end ZnS ceramics, it was revealed that optical transmittance and relative density were improved, and wurtzite content was reduced, as the heating rate decreased from 100 °C/min to 5 °C/min.[133] A later study by C. Li et al. reported that transparent ZnS ceramics with maximum densification could be fabricated via hot pressing at 900 °C under a high applied pressure of 250 MPa. They also observed a reverse phase transition from wurtzite back to sphalerite, as the sintering temperature increased from 750 to 900 °C.[122,141,142] Through XRD and TEM analyses, our previous studies on ZnS optical ceramics processed via hot pressing and SPS have also indicated an "early" phase transition from sphalerite to wurtzite during sintering, which was attributed to the small particle size of the employed colloid-synthesized ZnS powders. To summarize, the phase transition between ZnS sphalerite and ZnS wurtzite has been extensively observed and investigated in various processing studies of ZnS infrared optical ceramics. Nevertheless, few studies have been conducted with an emphasis on the influence of starting particle size and hot pressing pressure on the phase transition behavior of ZnS optical ceramics.

In this chapter, the phase transition behavior of ZnS during both pressureless and hot press sintering of two different ZnS powders was investigated by using XRD, SEM and EBSD analyses. In detail, the effects of starting particle size and sintering pressure on the phase transition between 3C-sphalerite and 2H-wurtzite transition of ZnS were studied. Optical and mechanical properties of the ZnS ceramics were also characterized to correlate to microstructural features induced by sintering and phase transition. The current report is intended to serve as a thorough reference and interpretation of the phase transformation behavior of ZnS ceramics processed via pressure-assisted and pressureless sintering methods.

## B. Experimental Procedures

Two ZnS powders with different particle sizes and morphologies were employed in this work. Commercial ZnS powder (Sigma Aldrich, 99.99%) was used as received without

additional purification. ZnS powder was also synthesized through a colloidal synthetic route via precipitation in a hot water bath under acidic conditions, using zinc nitrate hexahydrate (≥99.0%, Sigma Aldrich) as zinc source and thioacetamide (TAA, Sigma Aldrich, ≥99.0%) as sulfur source, as reported in our previous study.[137] Both the commercial and synthesized ZnS powders were first heat treated at 1000 ºC for 4 hours in flowing argon in a fused silica tube for impurity removal. The annealed ZnS powders were then sintered via hot pressing at 1000 ºC for 2 hours at a heating rate of 5 ºC/min under an applied uniaxial pressure of 50 MPa. To make a controlled comparison with ceramics sintered without pressure, both ZnS powders were dry pressed and subsequently sintered at 1000 ºC for 2 hours at a heating rate of 5 ºC/min in flowing argon. In order to examine the effect of applied pressure on phase transition behavior, the colloid-synthesized ZnS powder was also sintered under 10 MPa pressure for 2 hours at 1000 ºC. In all cases, the samples were allowed to cool to room temperature at an uncontrolled rate after the dwelling process.

The phase composition of the ZnS powders and bulk ceramics was determined via XRD (D2 PHASER, Bruker) equipped with a CuKα radiation (30 kV, 10 mA), with the microstructural features of the powders characterized with SEM (Quanta 200, FEI). A Tristar II 3020 system (Micromeritics) was employed to measure the surface area of the ZnS powders using the BET method. The powders were degassed at 25 ºC for 10 min and at 150 ºC for 1 hour prior to measurement. In order to prevent preferred orientation effects from interfering with phase composition analysis of the sintered ceramic pellets, the ceramics were ground into fine powders prior to XRD measurements for quantitative analysis. Quantitative phase analysis was performed by Rietveld refinement using Topas XRD analysis software (version 4.2, Bruker), with the Pseudo-Voight function method used to fit the measured patterns. EBSD measurement of the sample's surface was carried out by tilting the polished sample at 70° towards an EDAX Hikari Plus EBSD camera (EDAX, Inc., Mahwah, NJ, USA), equipped in a JEOL JSM-7800F field emission scanning electron microscope (JEOL USA Inc., Peabody, MA, USA). All the EBSD data were collected from the polished surfaces of the ZnS ceramic samples. EBSD patterns were collected at an accelerating voltage of 15 kV in high vacuum, and analyzed using TSL OIM DC 7 EBSD analysis software, which automatically indexed the measured patterns to the

hexagonal and cubic *.bmt files. The files were compiled from the crystallographic information on ZnS in the International Center for Diffraction Data (ICDD) database. The Archimedes method was adopted to measure the density of the as-sintered ZnS ceramics, with relative density subsequently calculated based on the quantitative phase composition analysis. Fourier transform infrared spectroscopy (FTIR, Nicolet 6700, Thermo Fisher) was applied to measure the infrared transmittance of the polished ZnS ceramic pellets. Vickers hardness measurements were performed on a micro-hardness test apparatus (HMV-200, Shimadzu) with an applied load of 0.05 kgf and loading time of 10 s.

## C. Results and Discussion

SEM micrographs of the two ZnS powders employed in this study are shown in Figure 11. The commercial powder is observed to be composed of separate, inhomogeneous, micron-scale agglomerates that consist of smaller, submicron/micron-scale ZnS particles. In contrast, the ZnS powder prepared by the colloidal synthesis consists of monodispersed, spherical, submicron-scale agglomerates of ZnS nanoparticles, as shown in the inset of Figure 11 (b). The use of both hot and cold water baths during the colloidal synthesis process allows for better control over the particle growth, which results in the observed homogeneous morphology. Figure 12 shows the SEM images of the ZnS powders after heat treatment at 1000 ℃ in flowing argon for 4 hours. Both powders exhibit apparent coarsening after heat treatment, with the heat-treated commercial powder remaining larger in particle size. In addition, necking between adjacent particles can also be observed, indicative of the onset of sintering, which is very likely attributed to the relatively high temperature of the heat treatment. As detailed in Table II, which includes data on the specific surface area of the ZnS powders before and after heat treatment, the powder with a smaller average size in SEM measurements have a larger BET surface area. A larger surface area usually corresponds to higher surface energy, which will be beneficial during the sintering processes. Additionally, it is noted that an apparent decrease in the samples' specific surface area is caused by the necking and particle growth induced by the heat treatment.

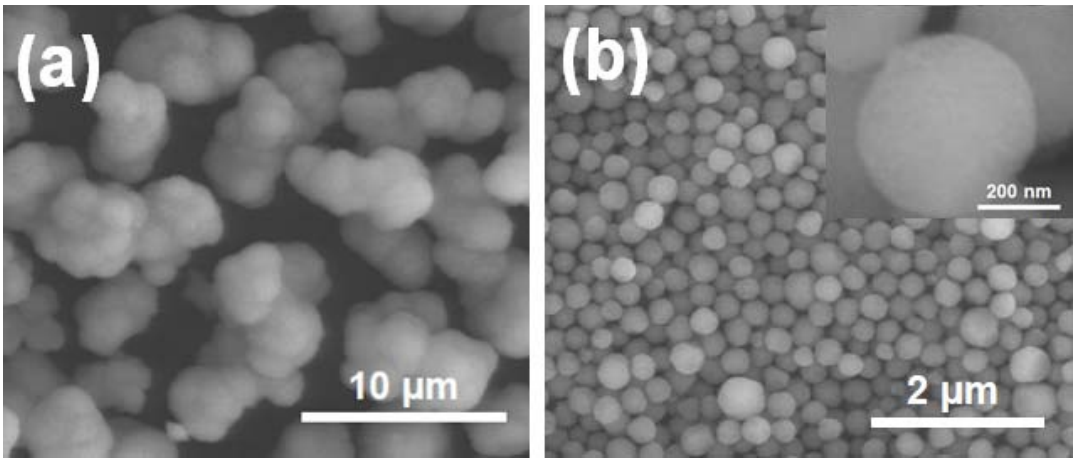


Figure 11. SEM images of the (a) commercial ZnS powder and (b) colloid-synthesized ZnS powder used in this study.

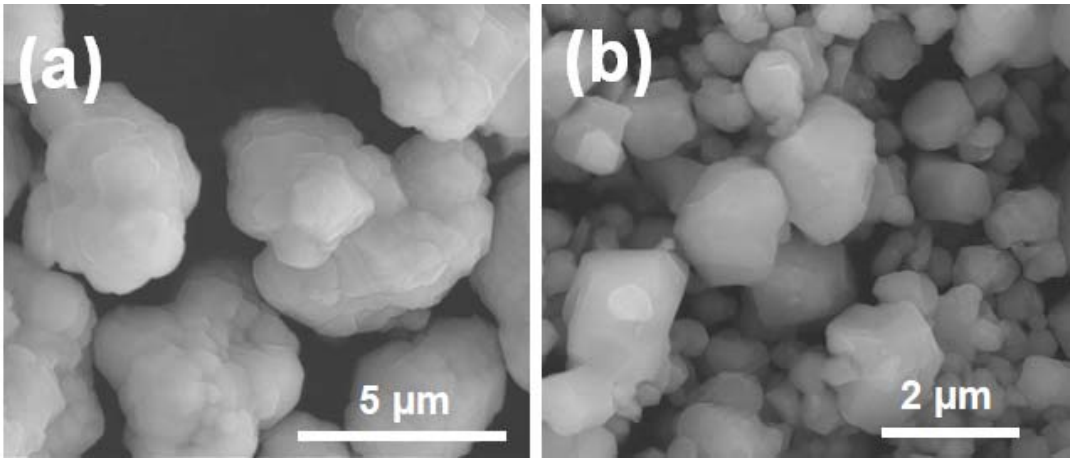


Figure 12. SEM images of the (a) commercial and (b) colloid-synthesized ZnS powders after heat treatment at 1000 ℃ for 4 hours in flowing argon.

Table II. BET Specific Surface Area Data of the Commercial and Colloid-Synthesized ZnS Powders before and after Heat Treatment.

| Sample | BET surface area ($m^2/g$) | Estimated standard deviation ($m^2/g$) |
|---|---|---|
| Commercial | 19.76 | 0.03 |
| Commercial, post heat treatment | 0.16 | 0.02 |
| Colloid-synthesized | 59.53 | 1.36 |
| Colloid-synthesized, post heat treatment | 4.59 | 0.28 |

Figures 13-14 display the XRD patterns of the commercial and colloid-synthesized ZnS powders before and after heat treatment. Significant peak broadening is apparent in the XRD pattern of the colloid-synthesized powder, which results from the small crystallite size of the powder. Peak broadening occurs as crystallite size decreases, according to the Scherrer Equation:

$$L = \frac{0.9\lambda}{\mathrm{B}\cos\theta} \quad (1)$$

where $L$ is the crystallite size, λ is the wavelength of the incident X-ray radiation, B is the full width at half maximum (FWHM) of a peak, in units of radians, and $\theta$ is the Bragg angle of a peak.[217] The observed peak broadening corresponds qualitatively to the broadening expected from the nano/submicron-scale particles observed by SEM. While the pronounced peak broadening is apparent in the XRD patterns of the starting powders, this broadening disappears after the heat treatment, as particles grow and coarsen to larger ones, resulting in a much narrower peak FWHM.

XRD phase composition analysis of the powders determines that the colloid-synthesized ZnS consists of single-phase sphalerite. However, a small amount (~6.43 wt%) of wurtzite ZnS is detected in the commercial ZnS powder. After the heat treatment at 1000 ℃ for 4 hours in argon, the powders are both composed of a mixture of cubic sphalerite (ICDD no: 04-001-6857; $F\bar{4}3m$; a=5.400 Å) and hexagonal wurtzite (ICDD no: 04-008-7254; $P6_3mc$; a=3.823 Å, c=6.261 Å). As noted previously, the annealing temperature is 1000 ºC, which is below the reported temperature (1020 ºC) for the sphalerite to wurtzite phase transition in bulk ZnS.[124] Therefore, the XRD results suggest a phase transition occurring earlier during the heat treatment process, at lower temperature, which is attributed to the significantly reduced particle size of the ZnS powders relative to the typical grain size of bulk ZnS. It has been proposed by multiple authors that the activation energy for the sphalerite to wurtzite phase transition is dependent on particle size.[98,218,219] It's also likely that the kinetic mechanism by which the phase transition occurs during the sintering of powders with small particle sizes is different from that for bulk ZnS. In addition, the surface Gibbs free energy difference, which contributes to the energetic favorability of a phase transition, has also been reported to be dependent on particle size.[101,220] The energetic barrier for the propagation of a phase transition is very small when

particle size is small. Thus, the increased surface energy of nano/submicron-scale ZnS powder facilitates the phase transition from sphalerite to wurtzite, which in turn renders the transition to occur at lower temperatures.[98] Furthermore, qualitative assessment of phase content, performed by examining the relative intensities of the (100) peak of wurtzite, clearly indicates that the colloid-synthesized ZnS with smaller particles shows a greater degree of transformation from sphalerite to wurtzite after heat treatment. This provides further evidence that the phase transition is particle size dependent, and that smaller particles will facilitate the nucleation and growth of the wurtzite phase during the heat treatment process.

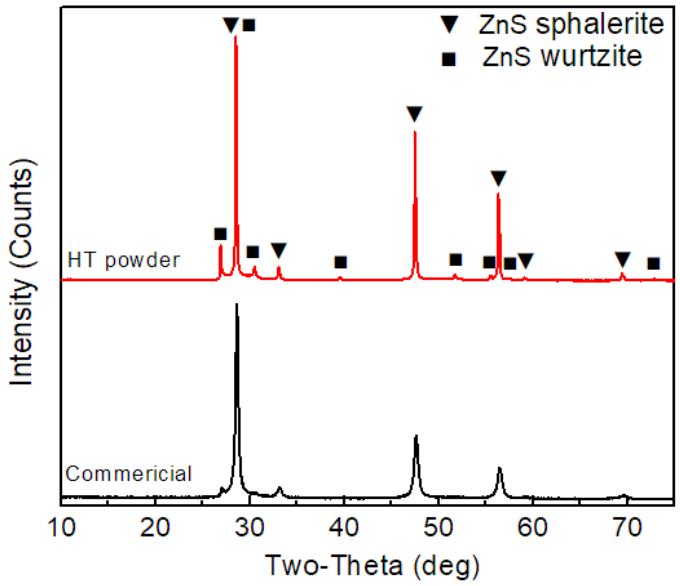


Figure 13. XRD patterns of the commercial ZnS powder before and after heat treatment at 1000 ℃ for 4 hours in flowing argon.

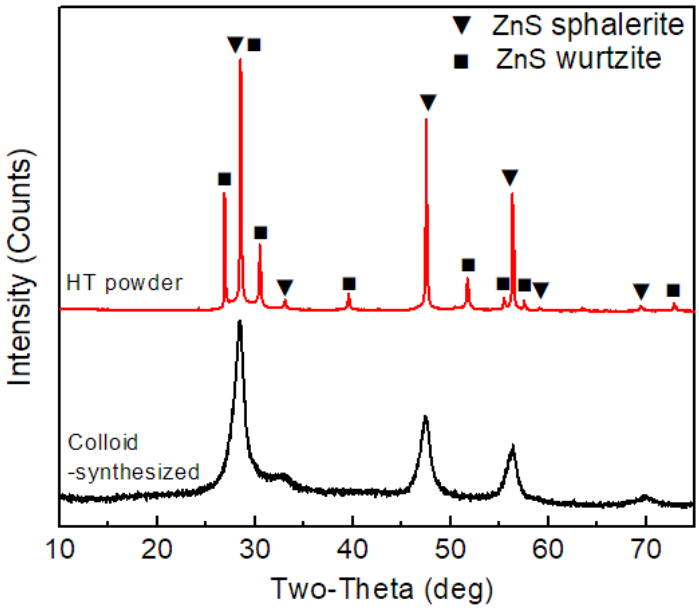


Figure 14. XRD patterns of the colloid-synthesized ZnS powder before and after heat treatment at 1000 ℃ for 4 hours in flowing argon.

The XRD patterns of the ZnS ceramics sintered via both pressureless sintering and hot pressing using the two heat-treated powders are shown in Figures 15 and 16. The XRD patterns of the ZnS powders after heat treatment are also included in the figures, to allow for direct comparison between the phase compositions of the powders being sintered and corresponding ceramics. Same with the heat-treated powders, the sintered ZnS ceramics are determined to be also biphasic, with the phases indexed to sphalerite ZnS and wurtzite ZnS. Qualitative assessment of phase content by observing the relative peak intensities of the two phases indicates that the relative levels of the two phases vary for different samples, suggesting a difference in the phase transition behavior. Rietveld refinement was performed to quantify phase contents of the powders and consolidated ceramics, with the results shown in Table III. The analysis reveals that the pressurelessly-sintered ceramics have a quantitative composition similar to that of the corresponding heat-treated powders used for sintering, with only a small increase in the wurtzite fraction, which is assumed to be due to the early phase transition during sintering at 1000 ℃. In contrast, both hot-pressed samples sintered under a uniaxial pressure of 50 MPa experience a reverse phase transition, from wurtzite to sphalerite, as the sintered ceramics exhibit a lower wurtzite content than the starting heat-treated powders. The reduction in hexagonality observed after hot pressing

is similar to other authors' reports of ZnS optical ceramics fabricated via hot pressing[141] and ZnS fabricated through CVD and subsequent HIPing.[112] Based on the stark difference in phase composition between the powders and ceramics sintered with and without pressure, it is concluded that applied pressure promotes the reverse wurtzite-sphalerite phase transition during the hot pressing process. Additionally, Rietveld analysis reveals that greater degrees of phase transition between sphalerite and wurtzite occur in the ceramic samples sintered using colloid-synthesized powder with smaller particle size. As discussed in the aforementioned analysis, this is likely due to the differences in both surface energy and the energy barrier for phase transformation propagation for powders with different particle sizes. It can be postulated from these results that the degree of transformation between sphalerite and wurtzite during sintering is closely correlated to particle size and applied pressure.

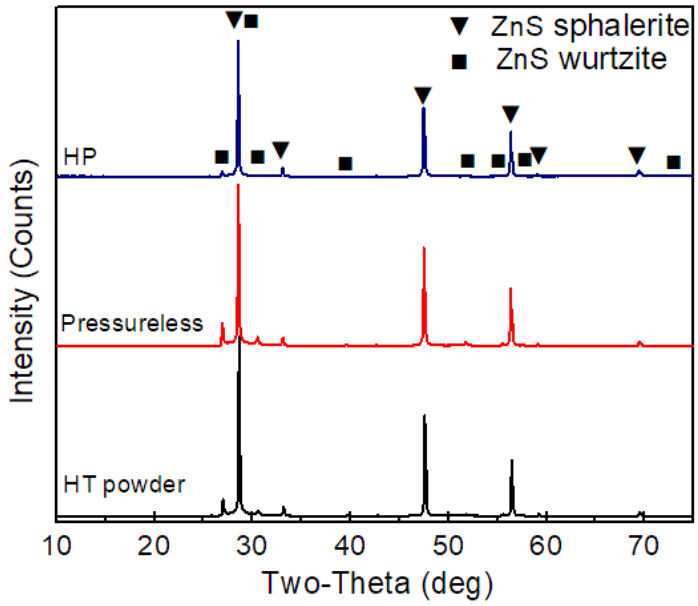


Figure 15. XRD patterns of the heat-treated commercial ZnS powder, and the resulting ceramics sintered without pressure and via hot-pressing under 50 MPa.

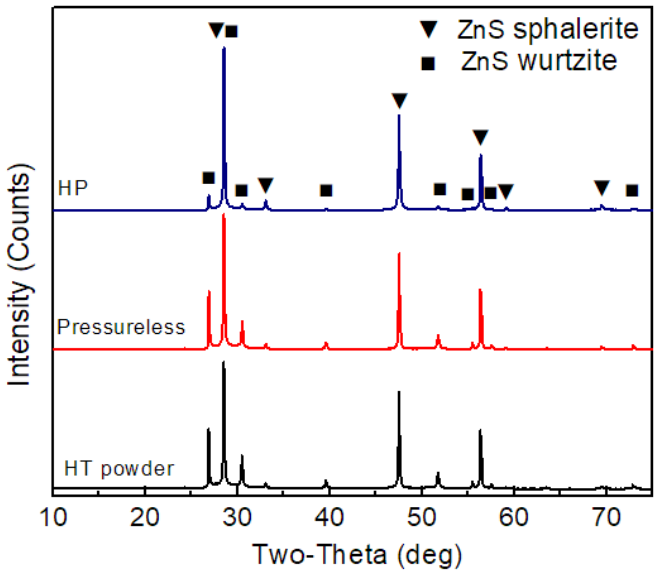


Figure 16. XRD patterns of the heat-treated colloid-synthesized ZnS powder, and the resulting ceramics sintered without pressure and via hot-pressing under 50 MPa.

Table III. Rietveld Refinement Results of the Phase Composition of the Heat-Treated ZnS Powders and Corresponding ZnS Ceramics Consolidated via Pressureless and Hot Press Sintering.

| Sample | Sphalerite (wt%) | Wurtzite (wt%) | Estimated standard deviation (wt%) |
|---|---|---|---|
| Commercial (post heat treatment) | 88.24 | 11.76 | 0.36 |
| Commercial (pressureless sintering) | 87.02 | 12.98 | 0.62 |
| Commercial (hot pressing, 50 MPa) | 93.21 | 6.79 | 0.43 |
| Colloid-synthesized (post heat treatment) | 78.62 | 21.38 | 0.52 |
| Colloid-synthesized (pressureless sintering) | 75.76 | 24.24 | 0.46 |
| Colloid-synthesized (hot pressing, 50 MPa) | 89.27 | 10.73 | 0.63 |

SEM and EBSD analyses were employed to characterize the microstructure of the sintered ZnS ceramics and gain further insight into the phase transition. Figure 17 shows the SEM image of the ZnS ceramics sintered without pressure at 1000 ℃ for 2 hours in flowing argon, using different heat-treated ZnS powders. EBSD phase maps with a grayscale image quality (IQ) map overlay and the corresponding inverse pole figure (IPF) maps of the ZnS ceramics sintered via hot pressing under 50 MPa using the two different ZnS powders are shown in Figures 18 and 19, respectively. It can be observed that both ZnS ceramics sintered via pressureless sintering are poorly densified, with the presence of large amounts of residual pores. The sintered ceramic using heat-treated commercial powder exhibits larger grains than that sintered using heat-treated synthesized powder, which is likely attributed to the larger starting particle size of the heat-treated commercial powder. In contrast, as can be observed from the EBSD phase+IQ maps in Figures 18 (a) and 19 (a), both hot-pressed ZnS ceramics are sufficiently consolidated with little residual porosity and smaller grains, compared with the samples sintered without pressure, which may be due to the effect of applied pressure. The phase+IQ maps qualitatively further illustrate that both the hot-pressed ceramics are primarily composed of sphalerite ZnS as the major phase and wurtzite ZnS as the minor phase, which is in agreement with the Rietveld refinement analysis based on XRD.

Detailed observations of the hot-pressed ZnS ceramics reveal five typical different types of grain microstructures, which are indicated by the circled regions labeled 1-5 in Figure 19 (b). As shown in areas 1 and 2, the grains are composed of pure sphalerite and pure wurtzite, respectively, suggesting that some entire grains remain as cubic sphalerite throughout the heat treatment and hot pressing processes, while some other grains fully transform to hexagonal wurtzite. Other grains, shown in areas 3 and 4, contain a mixture of both sphalerite and wurtzite, indicating partial conversion between sphalerite and wurtzite in the ZnS grains. It is interesting to note that in biphasic grains, the wurtzite phases exist as lamellae, with thicknesses ranging from submicron to micron-scale. The grain in area 4 is selected for more detailed analysis, with the phase+IQ and IPF maps shown in Figures 19 (c) and (d), respectively. In this type of grain, lamellae of both wurtzite and sphalerite are present, intersecting the ZnS grain. Additionally, lamellae of sphalerite

show two different two colors, indicative of the presence of two orientations of sphalerite within the grain. According to the EBSD data, the misorientations between the wurtzite and the sphalerite lamellae are both calculated to be 56.6°. Moreover, the lamellar structure with two different orientations is also observed in grains composed solely of sphalerite (area 5). The angle between the two orientations in sphalerite is determined to be approximately 60° (56.6°), with the two orientations sharing a parallel {111} plane, which is the close-packed plane of sphalerite ZnS. This discovery provides further evidence for the notion that these sphalerite lamellae are the result of twinning, with the boundaries between the lamellae being ∑3 twin boundaries.[115] Due to the difference in stacking sequence of sphalerite and wurtzite, a change in stacking sequence is associated with the phase transition between the two phases, which results in the formation of stacking faults.[92] The subsequent expansion of stacking faults during the phase transition between sphalerite ZnS and wurtzite ZnS can lead to the formation of twins in the sphalerite phase, as shown in the lamellar structure revealed by EBSD mapping. The types of grain observed in areas 2, 3, and 4 seems to indicate that some sphalerite twins can further transform to wurtzite, which in turn leads to the evolution to either entire wurtzite grains or wurtzite lamellae in ZnS biphasic grains, depending on the degree of phase transition that the grain undergoes.

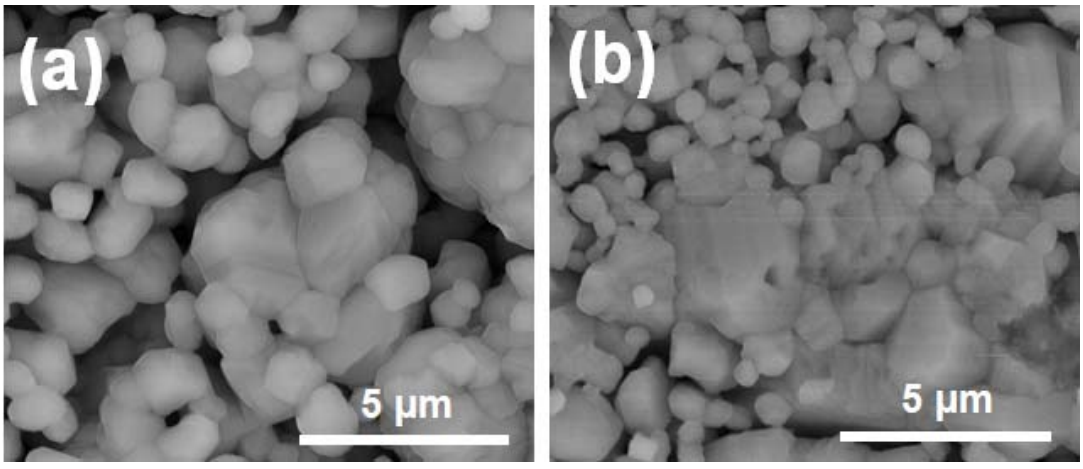


Figure 17. SEM images of the ZnS ceramics sintered without pressure at 1000 °C for 2 hours in flowing argon using (a) heat-treated commercial powder and (b) and heat-treated colloid-synthesized powder.

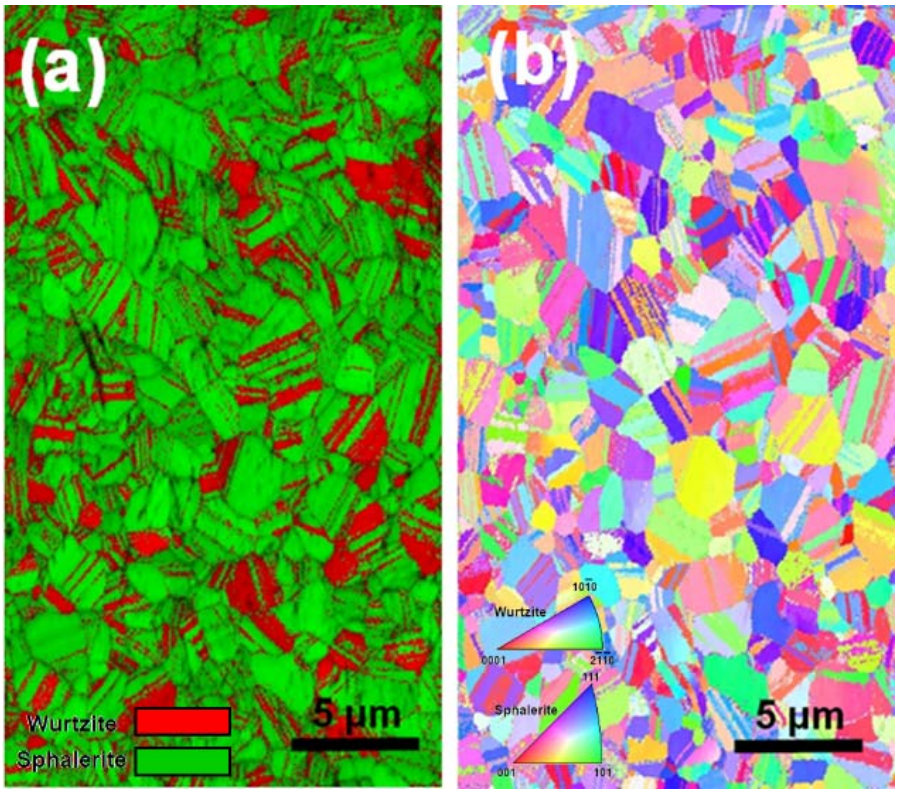


Figure 18. (a) EBSD phase map with a grayscale IQ map overlay and (b) corresponding IPF map of the ZnS ceramic sintered via hot pressing at 1000 ℃ for 2 hours under 50 MPa, using the heat-treated commercial ZnS powder. The two ZnS phases can be identified from the EBSD phase+IQ map, with the green areas corresponding to sphalerite and the red areas corresponding to wurtzite.

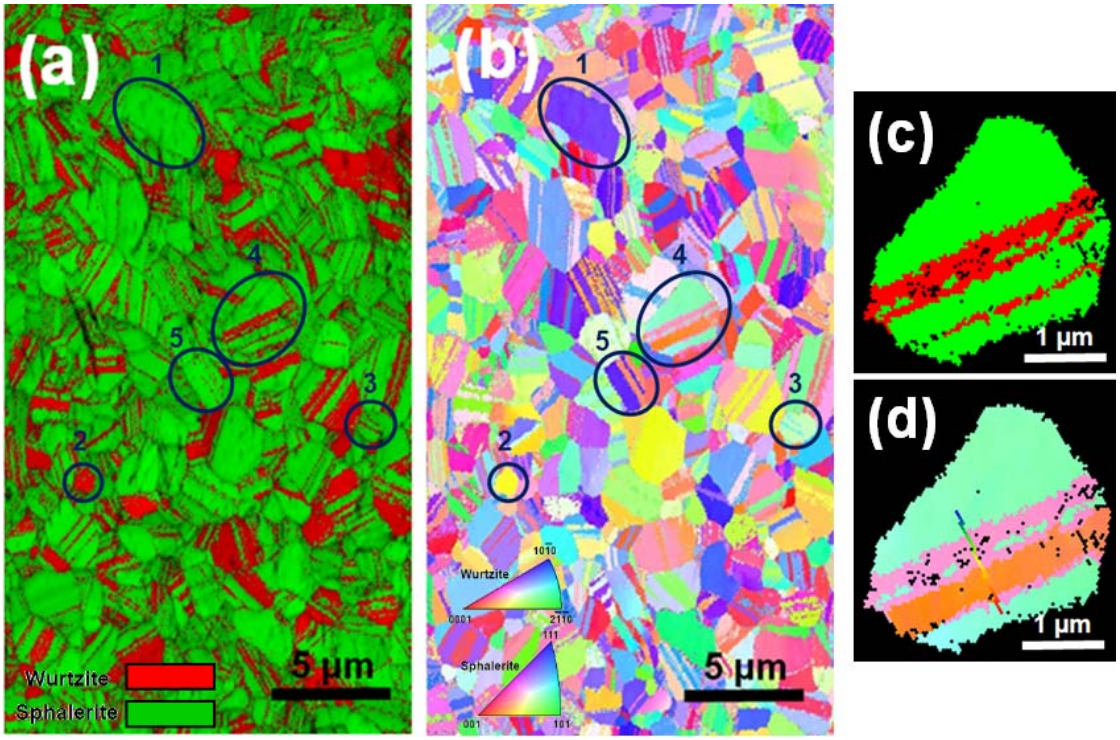


Figure 19. (a) EBSD phase map with a grayscale IQ map overlay and (b) corresponding IPF map of the ZnS ceramic sintered via hot pressing at 1000 °C for 2 hours under 50 MPa, using the heat-treated colloid-synthesized ZnS powder. The regions designated by the circles labeled 1-5 represent the five typical types of grain microstructures and phase compositions observed in the hot-pressed ZnS ceramic. An EBSD phase map and the corresponding IPF map of the grain in area 4 are shown in (c) and (d), respectively.

In order to further investigate the influence of pressure on the ZnS phase transition, the heat-treated colloid-synthesized ZnS powder was sintered via hot pressing at 1000 °C for 2 hours under 10 MPa, for comparison with the previous sample sintered under the same conditions but under 50 MPa. Figure 20 shows the results of XRD, SEM, and EBSD analyses of the sample. Rietveld refinement based on XRD reveals that the sample is composed of 84.59±0.17 wt% sphalerite and 15.41±0.17 wt% wurtzite, and this composition that is intermediate to the quantitative phase compositions of the ceramics sintered via pressureless sintering and by hot pressing under 50 MPa. As can be observed from the SEM image and EBSD maps, the sample is well-densified, but with some residual pores remaining at grain boundaries, resulting in an overall lower densification compared with the ceramic sintered under 50 MPa. EBSD mapping of the sample further reveals similar grain microstructures to those observed in the other ceramics consolidated via hot

pressing. However, it is interesting to note that the average grain size is larger than the sample sintered under 50 MPa. Additionally, the phase+IQ map suggests an increased wurtzite fraction relative to the analogous material sintered under 50 MPa, which is consistent with the phase composition analysis based on XRD results. It is thus further postulated that the application of uniaxial pressure during hot pressing induces the reverse phase transition from wurtzite to sphalerite. Thus, the higher sintering pressure is beneficial not only, in the conventional sense, for suppressing grain growth, producing reduced grain sizes, achieving pore removal, and increasing densification in the ZnS ceramics, but also for promoting the ZnS wurtzite-to-sphalerite phase transition.

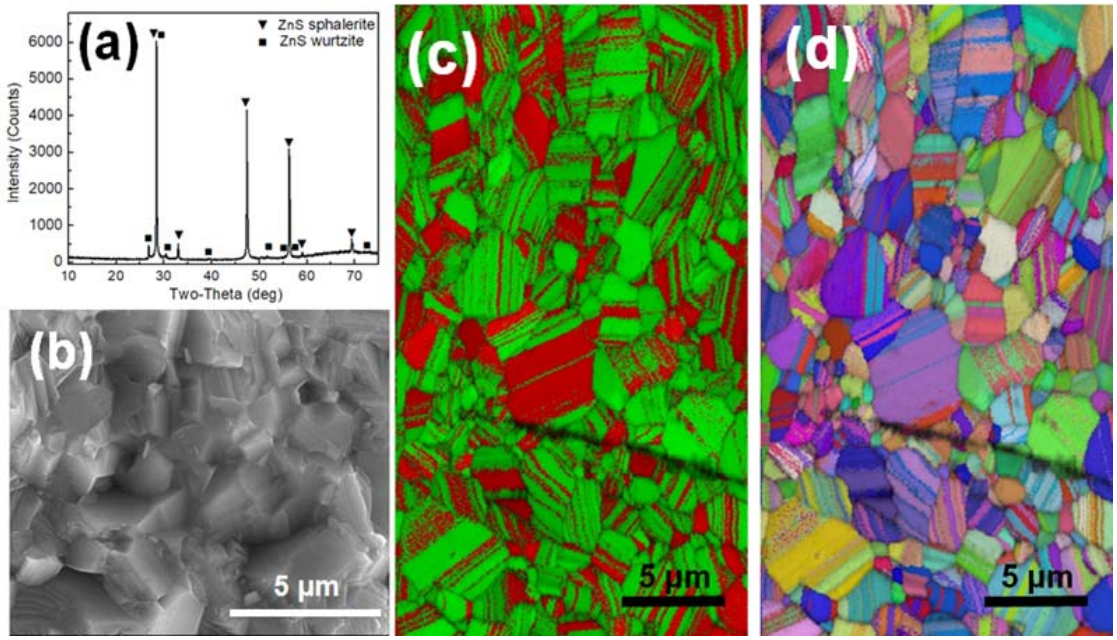


Figure 20. (a) XRD pattern, (b) SEM image, (c) EBSD phase map with IQ map overlay, and (d) corresponding IPF map of the ZnS ceramic sintered via hot pressing at 1000 °C for 2 hours under 10 MPa, using the heat-treated colloid-synthesized ZnS powder.

EBSD analysis of the hot-pressed ZnS ceramics also reveals that the ZnS wurtzite grains have preferred orientation on the surfaces of the samples, while the ZnS sphalerite grains on the surfaces are randomly oriented, as depicted in Figures 18-20. Figure 21 shows the {0001} pole figures of the wurtzite phases within the hot-pressed ZnS ceramics sintered under different pressures using different starting heat-treated powders. Certain preferred

orientation regions on the close-packed plane {0001} of ZnS wurtzite are observed in all the ceramics consolidated via hot pressing, which is attributed to the fact that the growth and movement of grains on the close packed atomic planes of the surface perpendicular to the stress direction are more energetically favorable, especially with the assistance of applied pressure, such as during hot pressing. In addition, based on comparison of the pole figures of different samples, it can be further suggested that the extent of texturing increases with the increase in hot pressing pressure.[141,221,222] As discussed in aforementioned phase composition analysis of hot-pressed and pressureless-sintered ZnS ceramics, higher uniaxial sintering pressure can lead to more reverse phase transition from wurtzite to sphalerite. Bearing in mind that the sphalerite grains in the ZnS ceramics are randomly oriented, it is hypothesized that a specific sequence of events may be involved in the development of preferred orientation on the {0001} plane of ZnS wurtzite, during the pressure-assisted reverse phase transition from wurtzite to sphalerite. As the applied sintering pressure increases, ZnS wurtzite grains with some certain orientations will first transform to ZnS sphalerite grains, leading to the observed preferred orientation in untransformed ZnS wurtzite. Further research on the pole figures of the hot-pressed ZnS ceramics consolidated under a wider range of applied pressure values is required to confirm the hypothesis concerning the sequence, by which the texture develops during the phase transition process.

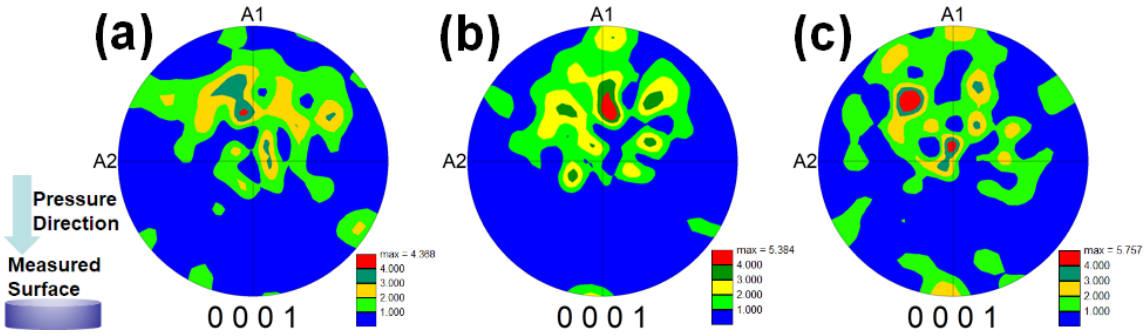


Figure 21. {0001} pole figures of the wurtzite phases within the hot-pressed ZnS ceramics sintered under different pressures using different powders: (a) under 50 MPa using heat-treated commercial powder; (b) under 50 MPa using heat-treated synthesized powder; and (c) under 10 MPa using heat-treated synthesized powder.

As previously discussed within the introductory literature review and the experimental results presented herein, the application of pressure during sintering has a significant effect on the ZnS phase transition. Figure 22 shows a schematic view of the crystal structure transformation that occurs during the ZnS phase transition between sphalerite and wurtzite. It is known that both the cubic sphalerite and hexagonal wurtzite forms of ZnS are close-packed structures, with sphalerite possessing the close-packed ABCABC atomic arrangement on the {111} plane along the [110] axis, and wurtzite possessing the ABABAB pattern on the {0001} plane along the $[11\bar{2}0]$ axis.[87] For the solid state phase transition between sphalerite and wurtzite, glide-induced stacking faults, which exist between these two different stacking sequences, are necessary to alter the stacking sequence.[92] During the phase transformation, the stacking faults will further evolve to form twins, with the ZnS phase transformation completed by the expansion of stacking faults and twins. It has been reported that the stacking faults and twinning that occur during the ZnS phase transition between sphalerite and wurtzite are deformation faults and deformation twinning,[88,89,107] which can be induced by thermal and mechanical stresses, such as those induced by heating/cooling and uniaxial pressure during the hot pressing process.[223] According to the aforementioned XRD results, the sintering of ZnS ceramics without applied pressure at the temperature of 1000 ℃ leads to a minor increase in wurtzite content, suggesting that the thermal stress applied during hot pressing at 1000 ℃ may be enough to promote the early phase transition from sphalerite to wurtzite, through the induction of deformation faults. In contrast, the wurtzite content apparently decreases with increasing uniaxial pressure from 0 to 50 MPa (0, 10 and 50 MPa), indicating that the reverse phase transition from wurtzite to sphalerite can be driven by pressure. As the ZnS phase transition between sphalerite and wurtzite is described as martensitic (displacive and diffusionless), driven by reduction of bulk-free energy per unit volume with additional shear and dilatational stress components,[107,224] the ZnS phase transition can be induced by applied pressure. Here, it has already been demonstrated by the current report that the application of pressure is more favorable for the wurtzite to sphalerite phase transition in ZnS, rather than the sphalerite to wurtzite phase transition, which is consistent with previous reports. This is assumed to be due to the relatively low stacking fault energy required to form sphalerite deformation faults/twinning from wurtzite, induced directly by

mechanical stress.[225-227] However, further research involving *in-situ* characterizations is required to advance this hypothesis, and to determine the type of stacking faults and twins induced by heating/cooling and applied pressure during the sintering process. In addition, sphalerite ZnS has a smaller specific volume ($V_s < V_w$) and a denser structure compared with wurtzite ZnS, as illustrated in Figure 22. The phase transition from ZnS wurtzite to ZnS sphalerite produces a lattice contraction that manifests itself macroscopically as volumetric contraction. It is thus appropriate to conclude that the application of pressure, which will presumably cause contraction of the ZnS lattice, will increase the favorability of forming the sphalerite phase, by promoting the wurtzite-sphalerite phase transition. Additionally, according to a study that modeled the thermodynamics of the ZnS phase transition by taking into consideration the combined effects of temperature, pressure and particle size on the Gibbs free energy difference between the two ZnS phases, phase transition temperature will decrease with decreasing starting particle size, and the phase transition from wurtzite ZnS to sphalerite ZnS can be driven by the application of external pressure.[214]

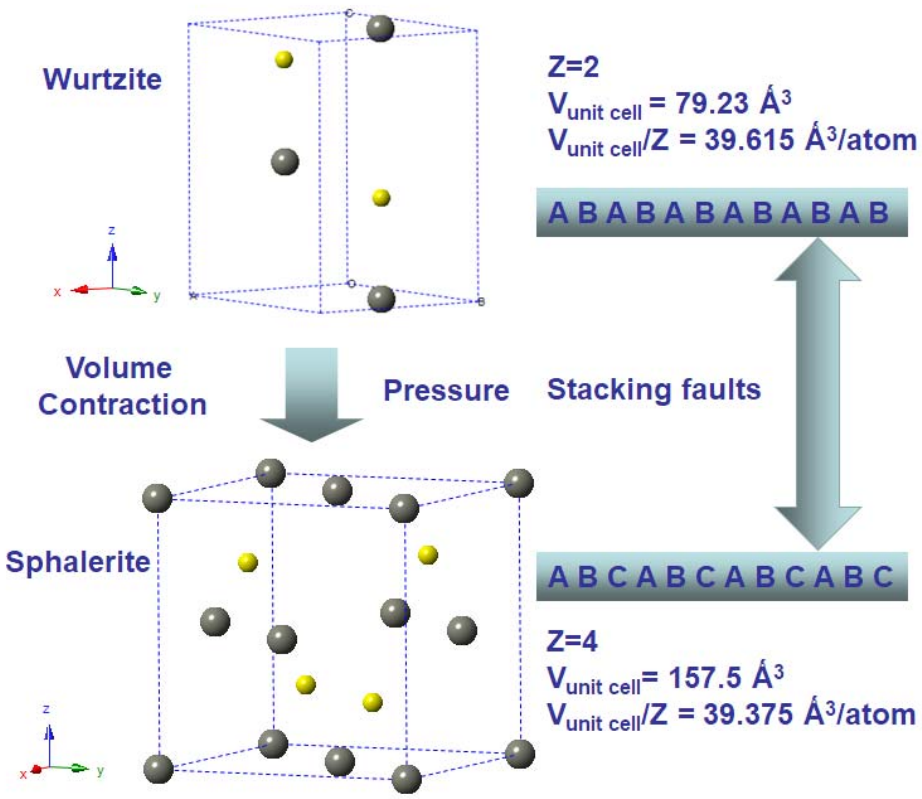


Figure 22. Schematic diagram depicting the crystal structure transformation during the ZnS phase transition between sphalerite and wurtzite.

The hot-pressed ZnS ceramics were measured using FTIR to investigate the infrared optical transmittance. Figure 23 shows the in-line infrared transmittance spectra of the two ZnS ceramics sintered via hot pressing at 1000 ℃ for 2 hours under 50 MPa, using various starting heat-treated powders. It is shown that both ceramics exhibit excellent optical transmittance in the near- and mid-infrared wavelength ranges, with maximum transmittances of 74.8% at 6.76 μm for the sample using the heat-treated colloid-synthesized powder, and 68.6% at 9.78 μm for the sample using the heat-treated commercial powder, due to sufficient densification. The overall spectra of the two hot-pressed ZnS ceramics are similar, indicative of similar vibrational bondings in the two samples. Absorption peaks observed at 3.4 μm and 4.2 μm correspond to atmospheric absorptions of $H_2O$ and $CO_2$, respectively, while the absorptions at 15.2 μm, 16.7 μm and 18.1 μm correspond to Zn-S characteristic vibrations. It is important to note that a small degree of carbon contamination may be present in the hot-pressed ZnS ceramics, which

manifests itself as weak absorptions located at 7.9 μm, 11.0 μm and 12.2 μm.

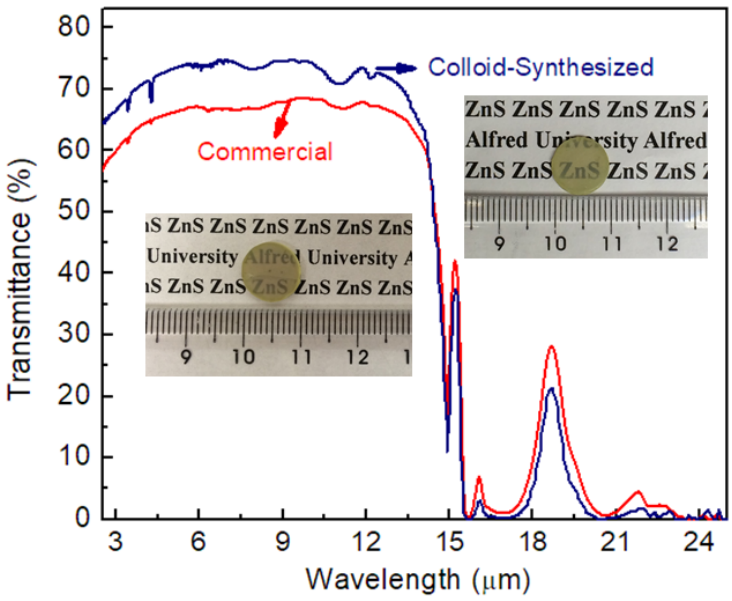


Figure 23. Infrared transmittance spectra and photos of the ZnS ceramics sintered via hot pressing at 1000 ℃ for 2 hours under 50 MPa, using heat-treated commercial and colloid-synthesized powders.

Comparison of the spectra of the two hot-pressed ceramics shows that the infrared optical transmittance of the ceramic sintered using the heat-treated commercial powder is inferior to that of the ceramic sintered using the heat-treated colloid-synthesized powder. This can be attributed to the slight difference in densification of the two samples (98.3% of relative density for the commercial powder ceramic vs 99.5% of relative density for the colloid-synthesized powder ceramic), an artifact of the different particle sizes and correspondingly different sinterabilities of the powders. Higher densification corresponds to lower porosity, which in turns leads to higher transmittance of the ZnS ceramic, through a reduction in the scattering loss caused by the difference in refractive index between ZnS and air. A similar reduction in transmittance is caused by the scattering loss induced by the difference in refractive index between phases possessing different refractive indices, such as between the primary sphalerite phase and secondary wurtzite phase of ZnS. In this study, the scattering loss in the ZnS consisting of two phases can be described as follows:[122,141]

$$Q_s = \frac{8k^4 r^4 \,\mathrm{Re}\left(\frac{n_s^2 - n_m^2}{n_s^2 + 2n_s^2}\right)^2}{3} \quad (2)$$

where $Q_s$ is the scattering efficiency, $k$ is the wave vector that is inversely proportional to the wavelength (λ) of incident radiation, $r$ is the average radius of the second phase, and $n_s$ and $n_m$ are the refractive indices of the matrix (sphalerite ZnS) and the embedded second phase (wurtzite ZnS), respectively. Thus, to minimize the scattering effect induced by the second phase wurtzite, the grain size of the second phase needs to be significantly less than the wavelength of incident light. In addition, the reduction in the grain size of the wurtzite phase with an anisotropic hexagonal crystal structure will also be beneficial for minimizing the scattering loss induced by the difference in refractive index of varying direction of the anisotropic crystal structure. In the current study, it is determined from XRD results that both ceramic samples include a measurable amount of wurtzite. Moreover, EBSD characterization reveals that ZnS wurtzite exists as both entire grains and grains that have partially transformed to wurtzite lamellae. Figure 24 shows the grain size distribution histograms of ZnS wurtzite in the hot-pressed ZnS ceramics sintered under 50 MPa, as obtained from EBSD analysis. The analysis suggests that in both samples, more than 95% of the wurtzite grains have an average diameter less than 325 nm. Therefore, the infrared transmittance of the hot-pressed ZnS ceramics sintered under 50 MPa will not be significantly affected by the second phase wurtzite, while the transmittance in the visible region, which has smaller wavelengths, may greatly be affected. The inferior visible transmittance of the hot-pressed ceramics can be observed by the naked eye in the photos of the samples shown in the insets of Figure 23, which is likely due at least in part to the effect of the wurtzite second phase. In addition, due to the lamellar structure of ZnS wurtzite, the larger value of length of the wurtzite lamellae may also affect the visible transmittance of the hot-pressed ZnS ceramics in other ways. According to the aforementioned analysis of phase transition behavior, the application of sintering pressure is demonstrated to lead to a reduction in wurtzite content through the facilitation of the wurtzite- sphalerite phase transition. Thus, it is reasonably expected that higher sintering pressures will result in ceramics with improved optical properties.

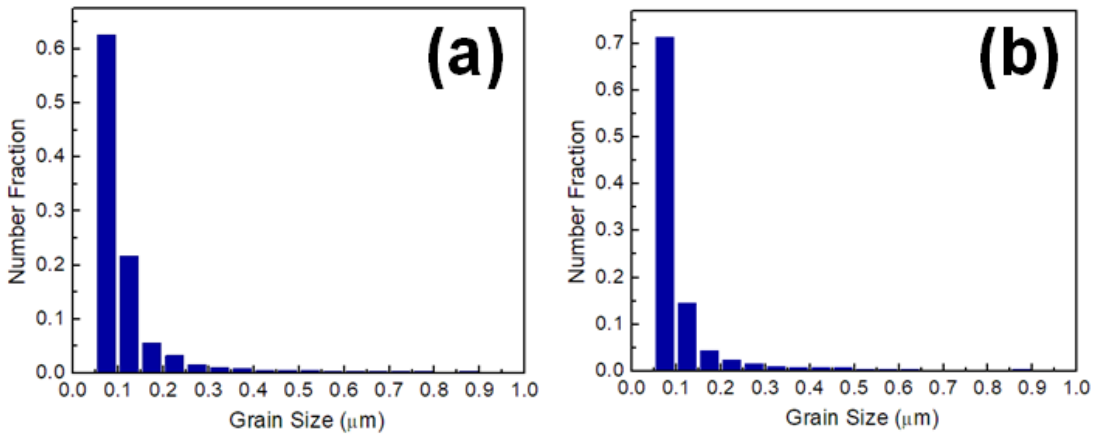


Figure 24. Grain size distribution histograms of ZnS wurtzite within the hot-pressed ZnS ceramics sintered under 50 MPa pressure, obtained from EBSD analysis: (a) using heat-treated commercial powder; (b) using heat-treated colloid-synthesized powder.

The mechanical property of the hot-pressed ZnS ceramics was also investigated by measuring the Vickers hardness of the ceramics using indentation tests. The sample sintered using the commercial powder has a hardness of 2.96 ± 0.30 GPa, while the sample sintered using the colloid-synthesized powder exhibits a hardness of 3.06 ± 0.26 GPa. Both ceramics have higher mechanical hardnesses than the value (1.5-2.6 GPa) reported for commercial ZnS optical ceramics.[228] This is likely a result of the enhanced densification and small grain size imparted by pressure-assisted sintering (hot pressing). In addition, the twinning induced by the pressure-promoted phase transition from wurtzite to sphalerite during hot pressing may contribute to the enhanced hardness through deformation strengthening.[229] It is expected that further studies, such as sintering conducted under appropriate ultra-high pressures, are promising to lead to more enhanced densification and promoted phase transition from wurtzite to sphalerite, which will in turn further improve the optical and mechanical properties of ZnS optical ceramics.

## D. Conclusions

A thorough investigation of the effects of starting particle size and sintering pressure on the phase transition behavior between sphalerite and wurtzite of ZnS ceramics was performed. Qualitative and quantitative phase composition analysis of the pressurelessly-sintered and hot-pressed ZnS ceramics revealed that the ZnS phase

transition behavior was closely related to the starting particle size of powder being sintered and the applied pressure during sintering. The ceramics fabricated from smaller starting particle sizes underwent an “earlier” phase transition at lower temperatures, which was attributed to both the increased surface energy and the smaller energetic barrier for the propagation of phase transition associated with decreasing particle size. Due to the expansion of sphalerite deformation faults/twinning and the compressive effect on the crystal lattice, the phase transition from wurtzite to sphalerite was promoted by the application of uniaxial pressure during hot pressing. Furthermore, the application of uniaxial pressure during sintering was demonstrated to promote the wurtzite-to-sphalerite phase transition, along with enhanced densification and twinning, which contributed to the improved optical and mechanical properties of the ZnS ceramics.

# III. HOT-PRESSED $Cr^{2+}$ DOPED ZnS INFRARED TRANSPARENT CERAMICS

## A. Introduction

As an extensively characterized II-VI wide bandgap semiconductor, zinc sulfide has been of significant interest for a long time due to its promising applications in various fields, including optical ceramics, phosphors, quantum dots, photocatalysts, and sensors.[1,97,230,231] When doped with transition metals and rare earth elements, ZnS can exhibit a wide range of luminescence behaviors in the visible and infrared regions.[232-236] In addition, due its exceptional performance as a material for room-temperature tunable solid state laser gain media in the mid-infrared region, transition metal doped ZnS has inspired a tremendous amount of interest for researchers within past decades.

In 1996, researchers at Lawrence Livermore National Laboratory demonstrated the potential of divalent transition metal doped zinc chalcogenides as materials for mid-infrared laser applications.[237] Various divalent transition metals ($Co^{2+}$, $Ni^{2+}$, $Fe^{2+}$ and $Cr^{2+}$) were doped into ZnS/ZnSe/ZnTe hosts, and their room temperature mid-infrared lasing performances were examined. It was determined that the tetrahedral substitution sites, rather than the octahedral sites, are more favorable doping sites for transition metals in the zinc chalcogenides. The tetrahedral coordination of dopants might contribute to the observed intense low-energy transitions, due to small crystal field splitting. Among the Zn chalcogenides, $Cr^{2+}$ doped ZnS/ZnSe showed exceptionally strong room-temperature absorption and emission in the mid-infrared region. In addition, temperature-dependent lifetime measurements indicated that these materials revealed high (close to 80 and 100% for Cr:ZnS and Cr:ZnSe, respectively) luminescence quantum yield at room temperature due to weak non-radiative relaxation process.[147,237] It was demonstrated that $Cr^{2+}$ doped ZnS/ZnSe crystals were the most promising candidates for room-temperature tunable mid-infrared laser applications. Since then, chromium doped ZnS has attracted more and more extensive attention.

Mirov et al. have conducted tremendous investigation into the lasing performances of $Cr^{2+}$:ZnS materials.[147-150] It has been reported that they applied chemical vapor transport (CVT) methods followed by thermal diffusion to fabricate $Cr^{2+}$:ZnS transparent ceramic

microchips with desirable lasing performances (optical and slope efficiency).[238] It was also demonstrated by Wang et al. that $Cr^{2+}$:ZnS thin films with promising properties for mid-infrared applications could be prepared by pulsed laser deposition.[239] In addition, Martyshkin et al. investigated and demonstrated the effective photoluminescence and lasing properties of $Cr^{2+}$:ZnS nanoparticles in the mid-infrared region.[240] Meanwhile, by using Cr:ZnS single crystals , Tolstik et al. obtained Kerr-Lens passive mode-locked Cr:ZnS femtosecond lasers, with distinguished pulse duration and energy.[241,242] The output characteristics of Kerr-lens-mode-locking were significantly improved with the use of Cr:ZnS polycrystalline gain media.[243-245] Besides studying the lasing performance of $Cr^{2+}$:ZnS, a significant amount of research has been conducted towards understanding the material, including the theory surrounding its crystal field splitting and local structure, as well as its potential applications in other fields such as cathodoluminescence and solar cell applications.[246-249]

The most commonly reported method to fabricate $Cr^{2+}$:ZnS transparent materials for laser applications is CVT method followed by thermal diffusion.[152] In addition, based on the method employed to process ZnS transparent ceramics, CVD combined with HIP has also been used to prepare polycrystalline ZnS host ceramics prior to the thermal diffusion of $Cr^{2+}$ ions.[250] However, these methods are expensive and time-consuming, and have poor repeatability. As a common consolidation method, it is well known that hot pressing has been proven to be an effective and a viable way to prepare various optically transparent non-oxide and oxide ceramics, such as ZnS, $CaF_2$, $Y_2O_3$, $Lu_2O_3$, and $MgAl_2O_4$.[41,64,127,137,251-254] It has also been demonstrated that $Cr^{2+}$:ZnSe transparent ceramics with suitable properties for laser applications can be fabricated via hot pressing.[62] However, few studies have been reported on the hot pressing of $Cr^{2+}$:ZnS transparent ceramics.

In the present chapter, $Cr^{2+}$:ZnS infrared transparent ceramics were fabricated via high vacuum hot pressing (VHP) using homogeneous ZnS powders synthesized using a wet chemical precipitation route, which were subsequently mixed with commercially sourced $Cr_2S_3$ powders. It was determined that the sintered $Cr^{2+}$:ZnS ceramics were primarily composed of cubic sphalerite phase, with hexagonal wurtzite as a minor phase. The ceramics were studied using SEM, and found to be well-consolidated and highly dense.

The spectroscopic properties of the material were characterized to investigate the mid-infrared absorption and photoluminescence behavior induced by doping with $Cr^{2+}$.

## B. Experimental Procedures

The synthesis of ZnS powders was performed through a facile colloidal processing method, which was reported in our previous studies.[137] Aqueous solutions of thioacetamide (TAA, ≥99.0%, Sigma Aldrich) and $Zn(NO_3)_2 \cdot 6H_2O$ (≥99.0%, Sigma Aldrich) with stoichiometric ratios of Zn:S were mixed together by stirring, and $HNO_3$ (70%, Sigma Aldrich) was added to the mixed solution to adjust pH to 2. The solution was then heated in a hot water bath to encourage particle growth. After sufficient time, the suspension of ZnS colloids was cooled in an ice water bath to halt particle growth. The precipitates were then washed by both DI water and ethanol (Reagent alcohol, 100%, Decon) to remove reaction residues, and then dried in an oven in air. The precipitates were then finely ground and mixed with an addition of 0.1 mol% $Cr_2S_3$ (99%, Alfa Aesar) in an agate mortar and pestle. The mixed powders were then heat treated at 900 ºC for 4 hours in flowing argon to prepare for sintering. The ceramic samples were prepared for VHP by loading the powders into a graphite die with a diameter of 10 mm, with layers of graphite foil (thickness of 0.5 mm) used to separate the sample powders from the punches. The powders were consolidated at 1000 ºC for 2 hours under a uniaxial pressure of 50 MPa under a vacuum of $10^{-5}$ mbar (OTF-1200X-VHP4, MTI).

The phase composition of the sintered $Cr^{2+}$:ZnS ceramics was determined using XRD (Bruker D2 PHASER) with a Cu$K\alpha$ ($\lambda$= 0.154 nm) radiation at a voltage of 30 kV and a current of 10 mA. Measurement conditions of 0.03 º2θ step size and 0.2s count time were employed over a measurement range of 10-75 º2θ. The morphological and structural features of the Cr:ZnS powders and sintered ceramics were investigated using SEM (FEI Quanta 200) at an accelerating voltage of 20 kV. Archimedes's method density measurements were adopted to determine the density of the as-sintered ceramics. The infrared transmittance of the polished pellet was measured using FTIR (Nicolet 6700, Thermo Fisher). Photoluminescence spectra and kinetics characterizations were performed using an acousto-optically Q-switched Er:YAG laser under an excitation at 1.645 μm with ~60 ns pulse duration. Photoluminescence spectra were collected by using a

monochromator (Acton Research ARC-300i). A Thorlabs PDA 20H PbSe detector, in addition to a fast PVI-3TE-5 (HgCdTe, VIGO systems) detector with a response time of ~200 ns were employed for signal detection. A polycrystalline $Cr^{2+}$:ZnS sample with a chromium concentration of $8 \cdot 10^{18}$ $cm^{-3}$, fabricated by a post-growth thermal diffusion method,[148] was used for the comparison of optical properties with the $Cr^{2+}$:ZnS ceramics.

## C. Results and Discussion

Figure 25 (a) shows the SEM image of the synthesized ZnS powders mixed with a 0.1 mol% addition of $Cr_2S_3$ powders. The powders appear to be composed of well-dispersed, homogenous, spherical particles with a size of approximately 100-200 nm, the small size of which is attributed to the use of both hot and cold water baths to achieve better control of particle growth during colloidal processing. The microstructure of the thermally etched surface of the polished $Cr^{2+}$:ZnS ceramics is shown in Figure 25 (b). It can be observed that the VHP-consolidated ceramics have an average grain size of about 1-2 μm and is highly dense, likely due to the homogenous morphology of the raw powders and the effectiveness of applied VHP technique. The relative density was measured to be 98.8%, which is in agreement with SEM observations of a highly consolidated microstructure. Figure 25 (c) displays the XRD pattern of the $Cr^{2+}$:ZnS ceramics consolidated via VHP. The sample is composed of a mixture of mainly cubic sphalerite (JCPDS no: 65-5476; $F\bar{4}3m$; a=5.40 Å) with a small amount of hexagonal wurtzite (JCPDS no: 02-1310; P63mc; a=3.82 Å, c=6.25 Å). In addition, no $Cr_2S_3$ impurity peaks can be detected in the XRD measurement, likely because of the low added level of $Cr_2S_3$. Due to the high surface energy of the small particles of the raw powders, during consolidation the $Cr^{2+}$:ZnS ceramics experience an early phase transition from the cubic phase to hexagonal phase at 1000 ºC, which is lower than the reported phase transition temperature of 1020 ºC.

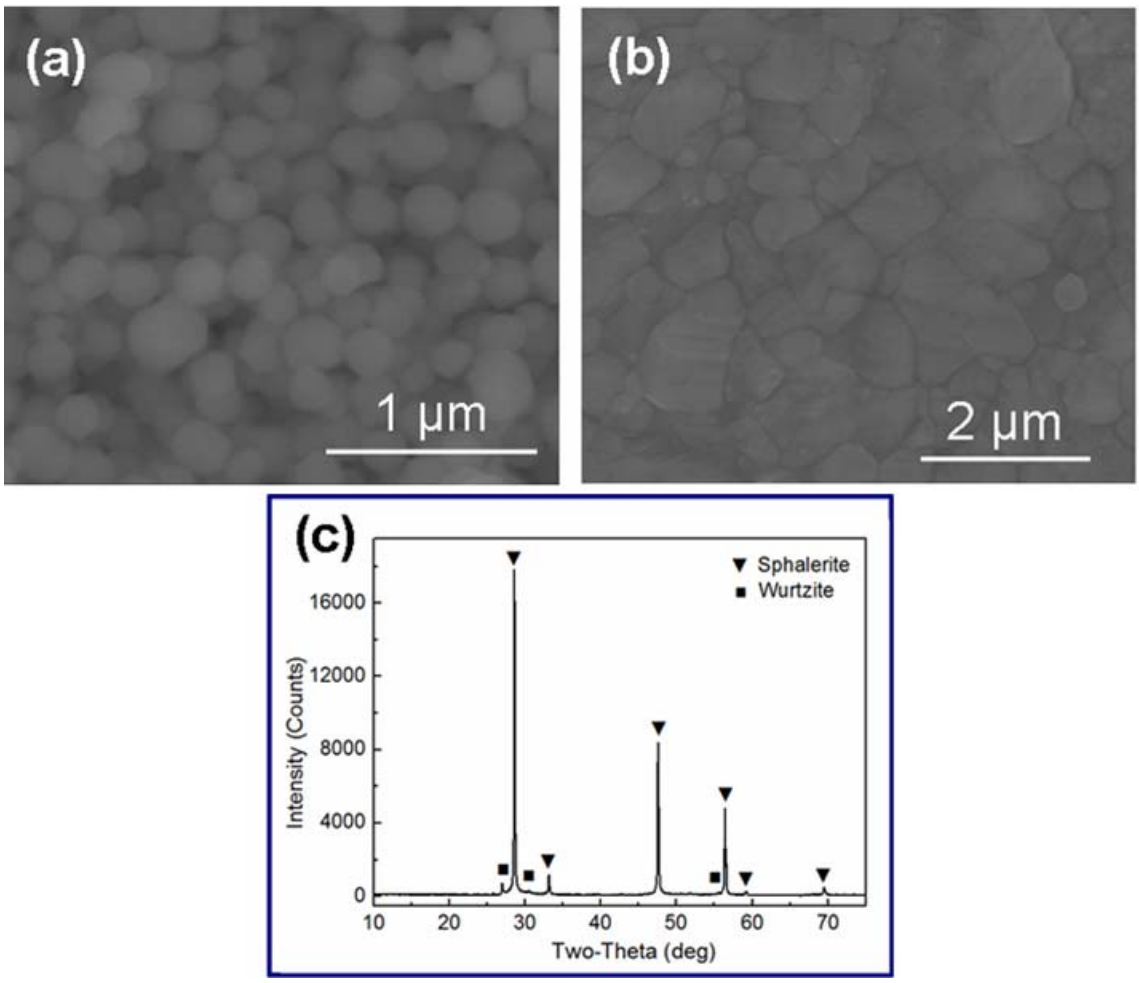


Figure 25. (a) SEM image of the synthesized ZnS powders mixed with 0.1 mol% $Cr_2S_3$ powders. (b) SEM image of the thermally etched surface of the VHP-sintered $Cr^{2+}$:ZnS ceramics. (c) XRD pattern of the $Cr^{2+}$:ZnS ceramics consolidated via VHP.

Figure 26 (a) shows the infrared transmittance curve of a polished $Cr^{2+}$:ZnS ceramic pellet, obtained by FTIR measurement over a wavelength range of 2.5-16.0 μm. Due to the effective consolidation via VHP, the $Cr^{2+}$:ZnS polycrystalline ceramic sample exhibits high transmittance in the infrared region, with a maximum transmittance of 67% at 11.6 μm, while the theoretical maximum transmittance according to the Fresnel's equations is 75% in the infrared range. It is important to note that the transmission curve shape near the infrared edge is very similar for the VHP-consolidated ceramic sample and the polycrystalline sample fabricated via the post-growth thermal diffusion method. The reduced transmission observed in the VHP-consolidated ceramic sample in the near-

infrared spectral range is likely due to scattering effects within the ceramic. As can been observed from the inset photo, the sample is translucent even in the visible region, with the green color of the sample believed to result from the incorporation of $Cr^{2+}$ ions into the ZnS lattice. Based on comparison of spectra from measurement of the samples and measurement of the ambient atmosphere, it is determined that the absorption peaks in the 3.2-7.0 μm range are due to atmospheric absorptions. Specifically, the absorption bands between 3.4, 3.5 and 6.2 μm are attributed to water adsorbed from the atmosphere, and the small peaks at 4.2, 5.7, and 7.0 μm correspond to the C=O stretching modes of $CO_2$ adsorbed from the ambient atmosphere. ZnS characteristic vibrations lead to the band at 15.2 μm.[236] In addition, the absorption peak at 9.1 and 10.9 μm can be probably attributed to ZnS precursor residuals in the colloidal processing route or carbon contamination from graphite during the VHP process.[127,137]

The near-infrared transmittance curve of the sample is shown in Figure 26 (b). Dotted line shows the baseline from the FTIR measurement of the ambient atmosphere. As can be determined from the transmittance plot, the VHP-sintered ceramic sample features a very strong scattering effect. It is important to note that the broad band at 1690 nm corresponds to the $^5T_2 \rightarrow {}^5E$ absorption band from the split ground state $^5D$ of $Cr^{2+}$, which confirms that some $Cr^{2+}(3d^4)$ is incorporated into the lattice of the ZnS host in a site with tetrahedral coordination.[255] In addition, the $Cr^{2+}$ concentration of the $Cr^{2+}$:ZnS ceramic can be estimated from the absorption peak at 1690 nm. First, the active absorption coefficient at 1690 nm can be obtained according to Beer Lambert Law:

$$\alpha = -Ln(T) / d \qquad (3)$$

where $\alpha$ is the active absorption coefficient, $T$ corresponds to the normalized transmittance ratio, and $d$ is the thickness of the sample (0.07 cm). Here, we can estimate $T$ to be 0.88, based on comparison of the actual measured transmittance at 1690 nm with the estimated baseline of the transmittance curve between 1400 nm and 2000 nm. After obtaining the active absorption coefficient at 1690 nm, the concentration of $Cr^{2+}$ can be estimated by the following relation:

$$N = \alpha / \sigma \qquad (4)$$

where $N$ is the concentration of the ion, and $\sigma$ refers to the absorption cross-section. It has been reported that the absorption cross-section of $Cr^{2+}$:ZnS at 1690 nm is $1.0\times10^{18}$ $cm^2$.[151] Thus, the $Cr^{2+}$ concentration can be calculated as $1.8\cdot10^{18}$ $cm^{-3}$ (sufficient for laser materials). However, the concentration is much smaller than the total concentration of Cr originally introduced into the material, which suggests that the incorporated Cr ions may have different valence states other than 2+. Due to the reducing nature of the high vacuum and carburizing environment due to the presence of graphite in the VHP chamber, some $Cr^{3+}$ ions from the added $Cr_2S_3$ are reduced to $Cr^{2+}$ ions, which are then incorporated into the ZnS host lattice, but a portion of the $Cr^{3+}$ ions from the $Cr_2S_3$ may still persist in the material. In addition, it is also revealed by a preliminary X-ray photoelectron spectroscopy characterization that there are some mixed valence states of Cr ions including 2+ and 3+ within the VHP-sintered ceramic. Future research is required to determine the location and valence states of the chromium ions in VHP-sintered Cr:ZnS ceramics.

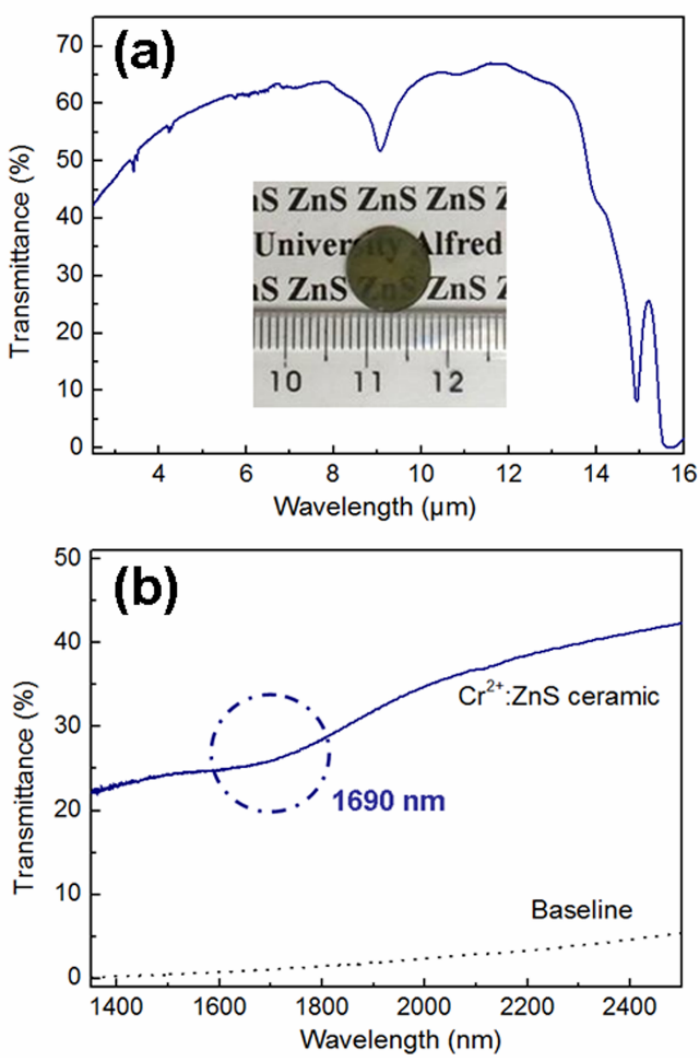


Figure 26. (a) Room-temperature infrared transmittance spectrum of the mirror-polished Cr:ZnS ceramic, with a photograph of the sample (inset) with a diameter of 10 mm and a thickness of 0.7 mm. (b) Room-temperature near-infrared transmittance spectrum of the Cr:ZnS ceramic.

Further characterization of the VHP-sintered $Cr^{2+}$:ZnS ceramic sample's mid-infrared optical behaviors was performed to investigate the infrared photoluminescence emission and corresponding emission kinetics of the $Cr^{2+}$:ZnS. Figure 27 (a) shows the room-temperature non-calibrated infrared photoluminescence spectrum of the VHP-sintered ceramic under 1645 nm excitation. The sample exhibits the characteristic $Cr^{2+}$ infrared photoluminescence band from 2000 nm to 2200 nm, which is attributed to the $^5E \rightarrow {}^5T_2$ electronic transition, as a result of the cubic tetrahedral crystal splitting of the 3d-levels of $Cr^{2+}$ ($3d^4$) in ZnS.[256] In addition, as discussed in the aforementioned XRD analysis, both

the cubic ZnS sphalerite phase and the hexagonal ZnS wurtzite phase are present in the ceramic. The difference in crystal structure and symmetry of these two phases may lead to polarization dependence of fluorescence,[257] which in turn results in the asymmetric photoluminescence band shown in the emission spectrum.[258,259] Figure 27 (b) shows the infrared photoluminescence kinetics of the VHP-sintered $Cr^{2+}$:ZnS sample measured at room temperature under 1645 nm excitation. The red curve shows the detector response time measured at the excitation wavelength for comparison. From the blue fit (Equation (5)) exponential decay curve shown in the spectrum, it is revealed that the sample exhibits a single exponential decay process with a lifetime of $\tau$=5.5 μs, which is consistent with previously reported decay times of the $Cr^{2+}$ $^5E \rightarrow {}^5T_2$ electronic transition in $Cr^{2+}$:ZnS.[255]

$$I(t) = A\exp(-t / \tau) \tag{5}$$

where *I(t)* refers to the time-dependent luminescence intensity, *A* is a pre-exponential weight factor, and *t* corresponds to the actual time, and $\tau$ is the decay time. This further demonstrates that the $Cr^{2+}$ ions are tetrahedrally coordinated in the VHP-sintered $Cr^{2+}$:ZnS ceramic.

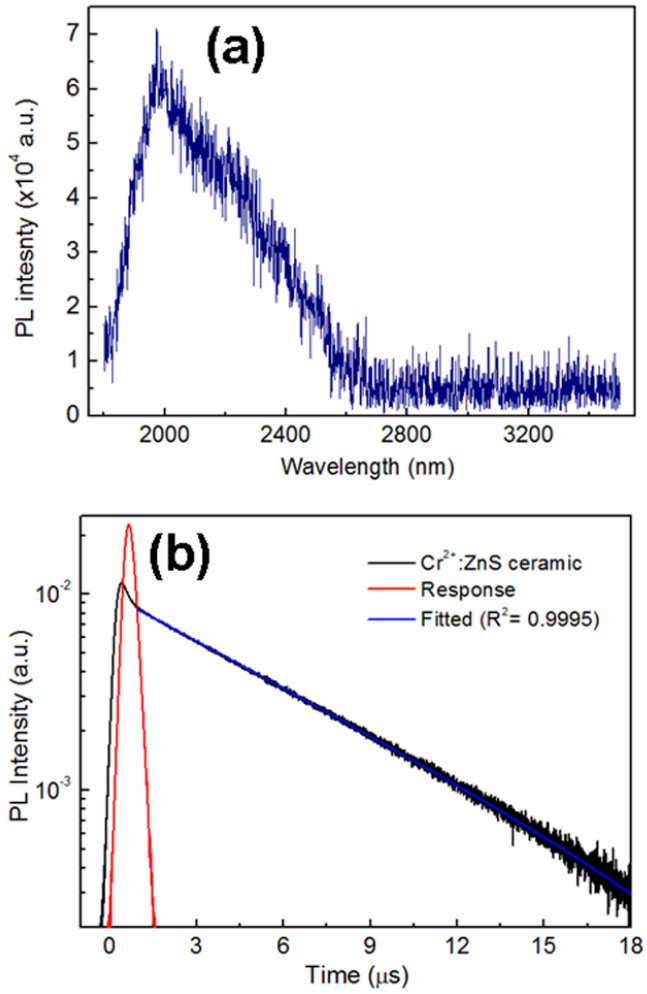


Figure 27. (a) Room-temperature infrared photoluminescence spectrum and (b) room-temperature infrared photoluminescence kinetics of the VHP-sintered $Cr^{2+}$:ZnS ceramic sample excited under 1645 nm excitation.

## D. Conclusions

In summary, $Cr^{2+}$:ZnS infrared transparent ceramics (67% transmittance at 11.6 μm) was successfully fabricated via vacuum hot pressing by consolidating colloidally processed ZnS powders mixed with commercially sourced $Cr_2S_3$ powders. The $Cr^{2+}$:ZnS ceramics were determined to be primarily composed of cubic ZnS sphalerite phase, with hexagonal ZnS wurtzite as a minor phase. It was demonstrated that the well-dispersed and homogenous morphology of the raw powders combined with the effects of VHP led to highly effective consolidation of the $Cr^{2+}$:ZnS powders into high-transparency ceramics. infrared absorption analysis demonstrated that $Cr^{2+}$ ions were incorporated into the ZnS

lattice, and the concentration of $Cr^{2+}$ in the VHP-sintered $Cr^{2+}$:ZnS ceramic was estimated to be $1.8 \cdot 10^{18}$ $cm^{-3}$. Characterization of the infrared photoluminescence emission and kinetics of the VHP-sintered ceramic revealed the corresponding $^5E \rightarrow {}^5T_2$ characteristic bands of $Cr^{2+}$ in ZnS, and further confirmed the existence of tetrahedrally coordinated $Cr^{2+}$ within the ZnS host lattice. Further studies focused on decreasing scattering effects in VHP-sintered $Cr^{2+}$:ZnS are required to improve the optical performance of the material to increase its suitability for mid-infrared laser applications.

# IV. SYNTHESIS AND CHARACTERIZATION OF $CaLa_2S_4$ NANOPOWDER

## A. Introduction

Due to its favorable optical performance and mechanical properties, $CaLa_2S_4$ (CLS) crystallizing in the cubic $Th_3P_4$ crystal structure, has been extensively studied as a promising candidate for infrared optical ceramics.[54,153] Since the 1980s, researchers have developed various methods to synthesize CLS powders. It has been reported that the CLS synthesis procedures employ different preparation routes, including evaporative decomposition of solutions, alkoxide method, carbonates coprecipitation, and mixed oxide methods, to prepare CLS precursors, which is typically followed by high-temperature sulfurization in a sulfur-containing atmosphere of $H_2S$ or $CS_2$, for long time periods.[165,173-175,181,183,185-187,189] It has been reported that optical-quality CLS powders can be synthesized via an alkoxide method followed by the sulfurization of precursors at high temperature in an atmosphere of $H_2S$ or $CS_2$.[173-175,183] Alternately, by adopting a carbonate precipitation route, M. Tsai et al. fabricated CLS powders via $CS_2$ sulfurization, and subsequently investigated the influence of varying the Ca/La stoichiometric ratio on the phase composition of the CLS powders.[181,185-187] W. White et al. developed an evaporative decomposition of solution (EDS) route for producing CLS, consisting of spraying an aqueous solution of Ca and La nitrates into a hot furnace and heating the resulting oxide powder in flowing $H_2S$.[165] Through flame spray pyrolysis of calcium and lanthanum nitrates, followed by sulfurization at elevated temperatures in $H_2S$, researchers from the Office of Naval Research have developed another method to fabricate CLS powders with large BET specific surface area and high purity.[189] In addition, single-phase CLS powders have recently been successfully prepared, by a novel solution-based combustion method with a La/Ca molar ratio of 2.7 for the starting La/Ca nitrates, followed by sulfurization in $H_2S$ at 1000 ºC. In summary, the previously investigated CLS synthesis procedures have mainly employed different methods to prepare the calcium lanthanum precursors, followed by sulfurization at elevated temperatures in an atmosphere of $CS_2$ or $H_2S$. However, sulfurization is a very slow and time-consuming process, which requires the use of highly

toxic and flammable gases such as $CS_2$ and $H_2S$, rendering it a costly and environmentally harmful route for synthesizing CLS.

In contrast, wet chemistry methods have been employed to synthesize high-quality metal sulfide nanomaterials with controllable morphologies and sizes over the past years.[260,261] The application of wet chemistry methods can allow for direct wet chemical precipitation or pyrolysis of the sulfur-containing precursors in protective atmospheres, either of which suggests the potential for the synthesis of sulfide materials without high-temperature sulfurization. Different sulfur sources and sulfur-containing precursors, such as organometallic compounds, dithiocarbamate salts, trithiocarbonate salts, xanthate salts, and metal dialkyldithiophosphates have been employed to chelate metal ions with sulfur ions during wet chemical processes, with the corresponding sulfides subsequently obtained by pyrolysis of the precursors.[262] However, few studies have reported the synthesis of CLS through the use of a wet chemistry method followed by thermal decomposition.

In this chapter, two general processing routes were employed in an attempt to synthesize CLS powders: the high-temperature sulfurization (in an atmosphere of $CS_2$/Ar) of oxygen-containing precursors produced by wet chemistry processing, and the thermal decomposition (in an atmosphere of Ar) of sulfur-containing precursor materials prepared via wet chemistry methods. The phase composition, crystallization behavior, and microstructural features of the heat-treated precursors were investigated and observed in order to unveil the reaction mechanisms associated with different employed synthesis routes, chelating agents, and sulfur sources. Spectroscopic characterizations were also performed to correlate the optical properties with the microstructural, morphological, and phase composition characteristics of the resulting oxysulfate, oxysulfide, and sulfide product materials.

## B. Experimental Procedures

All the chemicals employed in this study were of analytical grade and were used as received without any purification. For the first approach with high-temperature sulfurization, oxygen-containing precursors were first synthesized via different wet chemistry routes, including coprecipitation, carbonate precipitation, and combustion. Figure 28 shows the schematic of the synthesis process via wet chemistry methods and

subsequent sulfurization. 2.5 mmol calcium nitrate tetrahydrate ($Ca(NO_3)_2 \cdot 4H_2O$, 99%, Alfa Aesar) and 5 mmol lanthanum nitrate hexahydrate ($La(NO_3)_3 \cdot 6H_2O$, 99.9%, Alfa Aesar) were first dissolved in separate 100 ml deionized (DI) water (Millipore Automatic Sanitization Module), respectively. Next, the aqueous solutions of calcium and lanthanum nitrates were mixed by vigorous stirring. For the coprecipitation method, 7.5 mmol ethylenediaminetetraacetic acid (EDTA, ACS reagent, 99.4-100.6%, Sigma-Aldrich) was added to 100 ml DI water, with ammonium hydroxide ($NH_4(OH)$, ACS reagent, 28.0-30.0% $NH_3$ basis, Sigma-Aldrich) subsequently added to change the pH value to 9-10, in order to dissolve the EDTA. The EDTA solution was then added dropwise into the mixed solution of lanthanum and calcium nitrates under stirring, yielding white precipitates. After 1 hour of reaction, the precipitates were washed and centrifuged (Allegra X-12 Centrifuge, Beckman Coulter) three times with DI water and anhydrous ethanol (Reagent alcohol, 100%, Decon), and then dried in air at 55 °C for 24 hours. For the carbonate precipitation method, 7.5 mmol ammonium carbonate ($(NH_4)_2CO_3$, puriss., meets analytical specification of NF, Ph. Franc., Sigma-Aldrich) was dissolved in 100 ml DI water. Subsequently, the aqueous $(NH_4)_2CO_3$ solution was added to the mixed solution of lanthanum and calcium nitrates, under stirring. After 1 hour of reaction, the resulting white precipitates were washed and centrifuged three times with DI water and anhydrous ethanol, and then dried in air at 55 °C for 24 hours. For the combustion method, 7.5 mmol citric acid (ACS reagent, ≥ 99.5%, Sigma-Aldrich) was dissolved in 100 ml DI water. The citric acid solution was then added to the mixed solution of lanthanum and calcium nitrates under stirring, yielding a colorless and transparent solution. The solvent in the solution was then evaporated by heating on a hot plate at approximately 150 °C under vigorous stirring, until a sol (cation-polymer complex) was formed. The temperature was then elevated to approximately 300 °C to initiate the combustion reaction. For all three of the aforementioned wet chemistry methods, the resulting precursor materials were then calcined in a muffle oven at 600 °C for 2 hours in air. Finally, the heat-treated precursors were sulfurized in a $CS_2$/Ar atmosphere at 1000 °C for 8 hours.

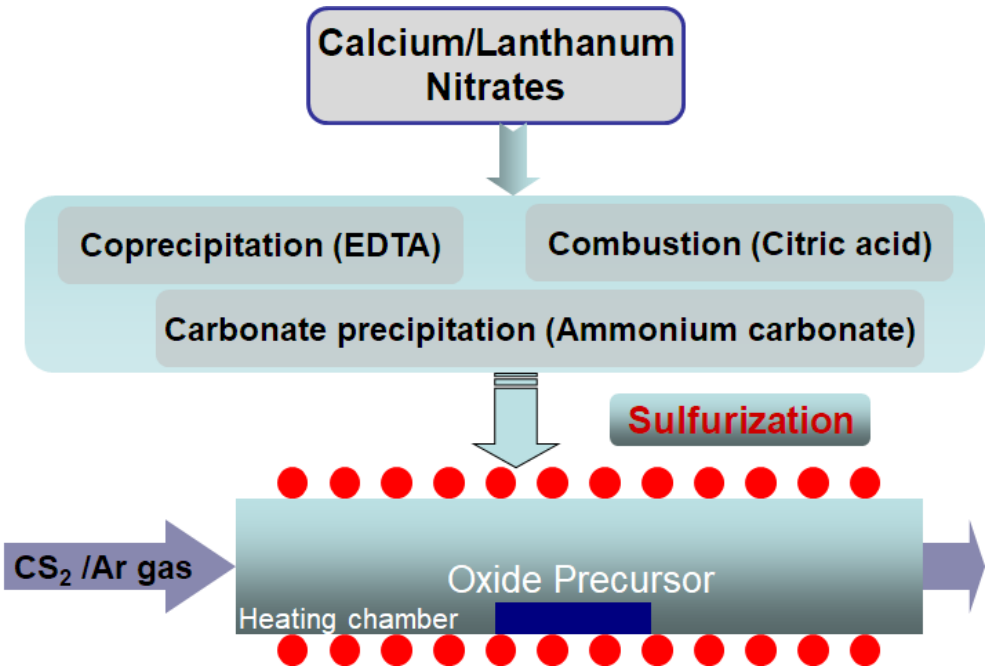


Figure 28. Schematic of the synthesis process via wet chemistry methods and subsequent sulfurization.

For the second method, the thermal decomposition/non-sulfurization approach, two wet chemistry methods, including wet-chemical precipitation and single-source precursor method, were applied to synthesize the sulfur-containing precursor for subsequent thermal decomposition. Figure 29 displays the schematic of the synthesis process via wet chemistry methods and subsequent thermal decomposition.

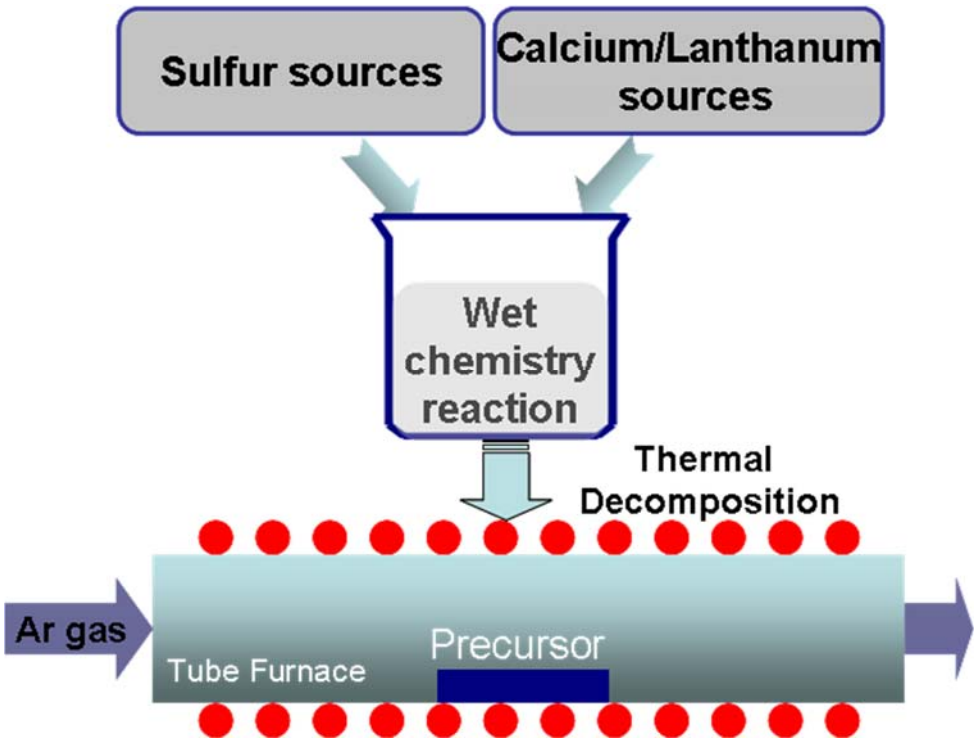


Figure 29. Schematic of the synthesis process via wet chemistry methods and subsequent thermal decomposition of sulfur-containing precursors.

For the wet chemical precipitation, 2.5 mmol calcium chloride dihydrate ($CaCl_2 \cdot 2H_2O$, 99%, Alfa Aesar) and 5 mmol lanthanum chloride heptahydrate ($LaCl_3 \cdot 7H_2O$, 99%, Alfa Aesar) were first dissolved in separate 100 ml volumes of anhydrous ethanol (Reagent alcohol, 100%, Decon), respectively. The alcoholic solutions of calcium and lanthanum chlorides were then mixed together by vigorous stirring. Four different reagents, thioacetamide (TAA), thiourea, sodium sulfide (Na2S), and ammonium sulfide ($(NH_4)_2S$) were employed as sulfur sources. 10 mmol TAA (≥99.0%, Sigma Aldrich) was first dissolved in 100 ml anhydrous ethanol. The same solution preparation procedure was employed with 10 mmol thiourea (ACS reagent, ≥99.0%, Sigma Aldrich), 10 mmol sodium sulfide nonahydrate ($Na_2S \cdot 9H_2O$, ACS reagent, ≥98.0%, Sigma Aldrich), and 10 mmol $(NH_4)_2S$ (20 wt. % in $H_2O$, Sigma-Aldrich). Ammonium hydroxide was subsequently added to the TAA and thiourea solutions to adjust the pH value to 9-10. Next, the mixed solution of calcium and lanthanum chlorides was added dropwise to each solution of sulfur source, while being stirred and yielding precipitates that were washed and centrifuged three times with anhydrous ethanol, and then dried in air at 55 °C for 24

hours. Finally, the dried precursors were heat treated at 1000 °C for 5 hours in flowing argon to achieve thermal decomposition.

For the single-source precursor method, 20 mmol sodium diethyldithiocarbamate trihydrate (Na(Ddtc)·3$H_2O$, Sigma-Aldrich) and 20 mmol 1,10-phenanthroline trihydrate ((Phen)·3$H_2O$, ≥ 99%, Sigma-Aldrich) were first dissolved in separate 100 mL anhydrous ethanol (Reagent alcohol, 100%, Decon), respectively. The alcoholic solutions of Na(Ddtc) and Phen were then mixed by vigorous stirring. In addition, 5 mmol lanthanum chloride heptahydrate ($LaCl_3$·7$H_2O$, 99%, Alfa Aesar) and 2.5 mmol calcium chloride dihydrate ($CaCl_2$·2$H_2O$, 99%, Alfa Aesar) were also dissolved in separate 100 ml anhydrous ethanol, respectively. Next, the lanthanum and calcium chlorides solutions were added dropwise into the mixed solution of Na(Ddtc) and Phen, while being stirred and yielding a yellowish solution. Thioglycolic acid (TGA, ≥ 98%, Sigma-Aldrich) of 2 mL was dissolved into 10 mL of anhydrous ethanol, and then added into the previously mixed yellowish alcoholic solution as a capping agent. After 1 hour of reaction, the resulting yellow precipitates were washed and centrifuged (Allegra X-12 Centrifuge, Beckman Coulter) several times with anhydrous ethanol and then dried in air at 55 °C for 24 hours. Finally, the dried precursor material was heat treated at 1000 °C for 5 hours in flowing argon to achieve thermal decomposition and reaction.

The phase compositions of the sulfurized and thermally decomposed precursors were determined using XRD with Cu Kα (λ= 0.154 nm) radiation (Bruker D2 PHASER) operated at a voltage of 30 kV and current of 10 mA. Measurement conditions of 0.03 °2θ step size and 0.2 s count time were employed over a measurement range of 10-75 °2θ. MDI Jade 9 integrated with ICDD database was employed for phase composition analysis. The morphological and microstructural features of the as-synthesized precursors and heat-treated precursors were investigated by SEM (FEI Quanta 200) with an acceleration voltage of 20 kV and TEM (JEOL 2100F) with an acceleration voltage at 200 kV. A Tristar II 3020 system (Micromeritics) was employed to measure the surface area and adsorption-desorption curve of the synthesized CLS powder using BET and Barrett-Joyner-Halenda (BJH) methods, respectively. The powder was degassed at 25 °C for 10 min and at 150 °C for 1 hour prior to the measurement. Thermogravimetry (TG) and differential thermal analysis (DTA) (SDT Q600, TA Instruments) were conducted in a nitrogen ($N_2$)

atmosphere at a heating rate of 10 °C/min from room temperature to 1100 °C, with α-$Al_2O_3$ as reference. The band gap of the materials was determined using an ultraviolet-visible (UV-Vis) spectrophotometer (Perkin-Elmer Lambda 900) to measure UV-Vis diffuse reflectance spectra, which were collected at 25 °C. FTIR (Nicolet 6700, Thermo Fisher) was applied to obtain information regarding the functional groups present in the precursors. Photoluminescence was investigated using photoluminescence spectra measurements (Jobin Yvon Fluorolog-3, Horiba) collected at 25 °C with a xenon lamp as the light source.

## C. Results and Discussion

### 1. Synthesis with High-Temperature Sulfurization

The SEM images of the as-synthesized oxygen-containing precursors obtained via different wet chemistry routes are displayed in Figure 30. It is observed that the coprecipitated precursor is composed of needle-like nanoparticles. The precursor synthesized via coprecipitation exhibits the smallest particle size of all three samples, which can be attributed to the dispersion effect of EDTA. The precursor fabricated via carbonate precipitation is composed of micron-scale particles with a plate-like morphology, while the combustion synthesis method generates the precursor with a floccule-like morphology, which is likely due to the formation of a cation-polymer complex resin. During the combustion synthesis, upon removal of excess water a solid polymeric resin forms, consisting of metal atoms bonded through oxygen to organic radicals, thus interconnecting the reactive species. It is readily apparent that the different synthesis methods and chelating agents generate precursors with significantly different morphologies and microstructures.

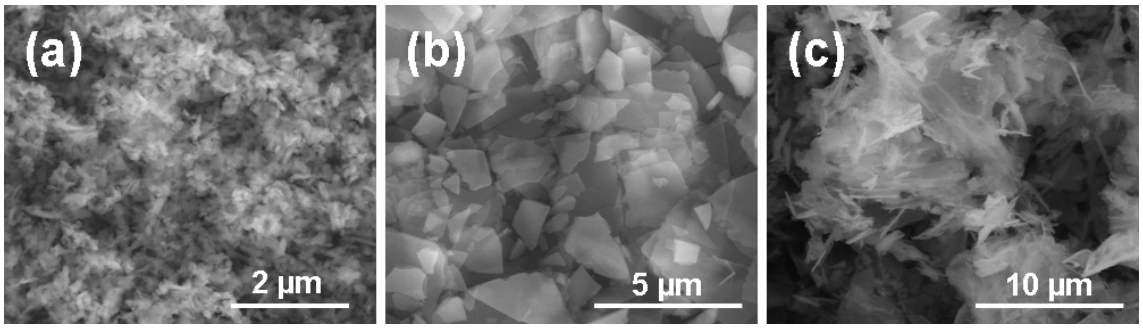


Figure 30. SEM images of the as-synthesized precursors obtained via various wet chemistry routes: (a) coprecipitation, (b) carbonate precipitation, and (c) combustion.

Figure 31 displays the SEM images of the sulfurized CLS precursors processed via different wet chemistry routes. It can be observed that all three samples consist of micron-scale and submicron-scale agglomerates, which undergo growth during high-temperature sulfurization. For the precursors synthesized via coprecipitation and carbonate precipitation, the morphologies remain almost unchanged after sulfurization, while the morphology of the sample synthesized via the combustion method changes from floccule-like to particle-like after sulfurization. During the sulfurization process, the polymeric resin is broken down by thermal decomposition of the polymers that compose the resin, which in turn leads to the transformation from floccules to particles.

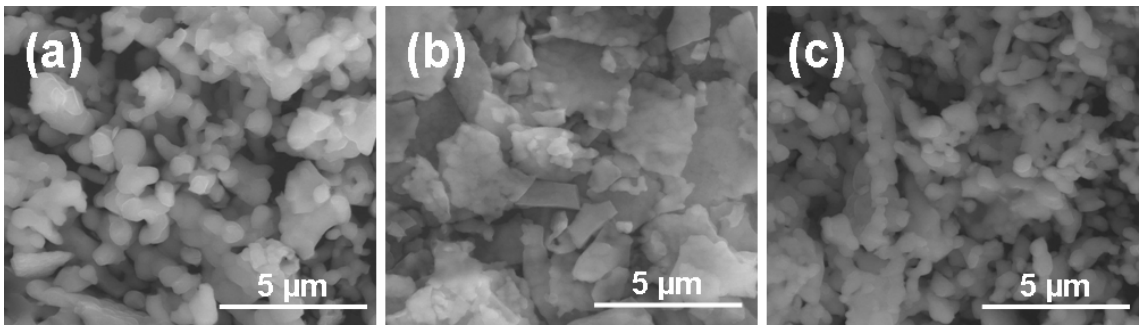


Figure 31. SEM images of the CLS precursors synthesized via various wet chemistry routes after sulfurization in a $CS_2$/Ar atmosphere at 1000 °C for 8 hours: (a) coprecipitation, (b) carbonate precipitation, and (c) combustion.

In order to investigate the feasibility of using the employed methods to effectively synthesize CLS powders, XRD was used to determine the phase compositions of the

sulfurized CLS precursors. Figure 32 shows the XRD patterns of the CLS precursors sulfurized in a $CS_2$/Ar atmosphere at 1000 °C for 8 hours. Analysis of the patterns reveals that all three samples are mainly composed of the cubic $Th_3P_4$ CLS phase (ICDD card no. 00-29-0339, $I\bar{4}3d$, a=8.6830 Å). Thus, it is concluded that the high-temperature sulfurization of the wet chemistry-processed precursors is effective in preparing CLS powders. For the precursor synthesized via carbonate precipitation, a small amount of CaS impurity phase is detected in the sample, which may be due to insufficient reaction during the carbonate precipitation process. Compared with the diffraction peaks of the as-synthesized precursor powders, the peaks of the sulfurized precursors are sharper and exhibit higher intensities, indicative of both crystallization and crystallite growth during the high-sulfurization treatments.

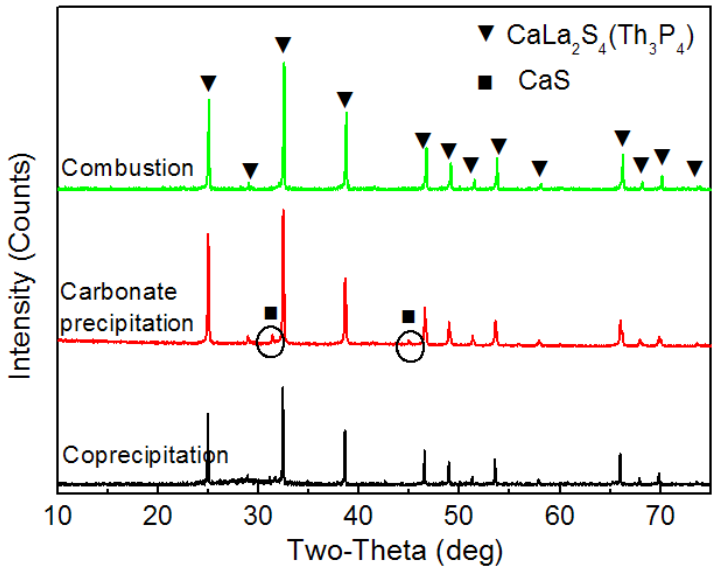


Figure 32. XRD patterns of the CLS precursors sulfurized at 1000 ºC in a $CS_2$/Ar atmosphere for 8 hours.

The elemental composition of select areas of the sulfurized CLS precursors synthesized via different routes is shown in the EDS spectra in Figure 33. For each sample, six areas were selected for measurements, and it was found that the six spectra for each sample are similar, indicative of relative elemental homogeneity throughout the sulfurized precursors. The presence of the primary elements (Ca, La and S) expected in CLS is

revealed by the EDS measurements. The presence of oxygen can be attributed to oxygen attached to the pores and surfaces of the sulfurized CLS precursors. The presence of a significant carbon peak indicates that some residual carbon, likely from the $CS_2$-sulfurization process, persists in the samples. It is important to note that, based on the peak intensities corresponding to Ca, La, and S, only the sulfurized CLS precursor processed via the combustion method exhibits a Ca/La/S stoichiometric ratio close to the expected theoretical value of CLS. Thus, the combustion method with citric acid as chelating agent is demonstrated to be the most effective method to obtain stoichiometric CLS. The other two samples are observed to be Ca-deficient, which is likely due to the difference in the ability of the chelating agents to bind Ca and La ions during wet chemistry synthesis. Due to the high similarity of the crystal structures of CLS and $La_2S_3$, the XRD patterns of the two materials are nearly identical, and the non-stoichiometric and Ca-deficient CLS fabricated in this study can alternately be considered to be Ca-doped $La_2S_3$, where Ca ions are doped to stabilize the cubic $Th_3P_4$ structure of $La_2S_3$. ($Ca_xLa_2S_{4-x}$, $0<x<1$).

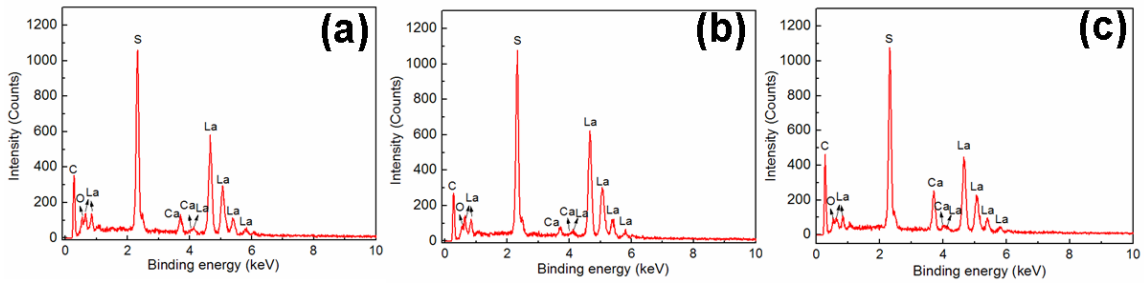


Figure 33. EDS spectra of the CLS precursors synthesized via varying wet chemistry routes after sulfurization in a $CS_2$/Ar atmosphere at 1000 °C for 8 hours: (a) coprecipitation, (b) carbonate precipitation, and (c) combustion.

Figure 34 (a) displays the UV-Vis spectra (300-700 nm) of the sulfurized CLS precursors in terms of absorbance versus wavelength. In this plot, the measured diffuse reflectance is converted to absorbance, and is shown along the y-axis. In order to determine the direct band gap of the obtained CLS powders, the curve can be replotted based on the equation for the Tauc relation, shown as follows: [263]

$$(\alpha h\nu)^m = A(h\nu - E_{bg}) \quad (6)$$

where $A$ is a constant and the band gap of the studied material is denoted as $E_{gn}$. The exponent $m$ depends upon the specific type of transition in which an electron is excited to the conduction band: $m$ may have values of 1/3, 2/3, 1/2 and 2, corresponding to the forbidden indirect, forbidden direct, allowed indirect and allowed direct transitions, respectively. The Tauc plots of the sulfurized precursors are shown in Figure 34 (b). An absorption energy can be determined by extrapolating the value of $h\upsilon$ to $\alpha$=0, which corresponds to the band gap energy $E_{bg}$. The band gap energies of the sulfurized precursors are estimated to be 2.04, 2.53 and 2.87 eV for the samples processed via coprecipitation, carbonate precipitation, and combustion, respectively. According to the aforementioned XRD and EDS results, the sulfurized precursor synthesized via the combustion method exhibits a stoichiometric CLS phase, while the sulfurized precursors synthesized via coprecipitation and carbonate precipitation are non-stoichiometric CLS, or Ca-doped $La_2S_3$. It has previously been reported that the theoretical band gaps of $La_2S_3$ and CLS are 2.00 and 2.70 eV, respectively. Here, it is revealed that the prepared CLS and Ca-doped $La_2S_3$ powders both have higher band gaps than predicted theoretically (2.70 eV for CLS and 2.00 eV for $La_2S_3$). This phenomenon is attributed to the nanometric scale of the crystallites composing the precursor agglomerates, which produces a pronounced quantum size confinement effect that leads to the apparent band gap enhancement in Ca-doped $La_2S_3$ and CLS.

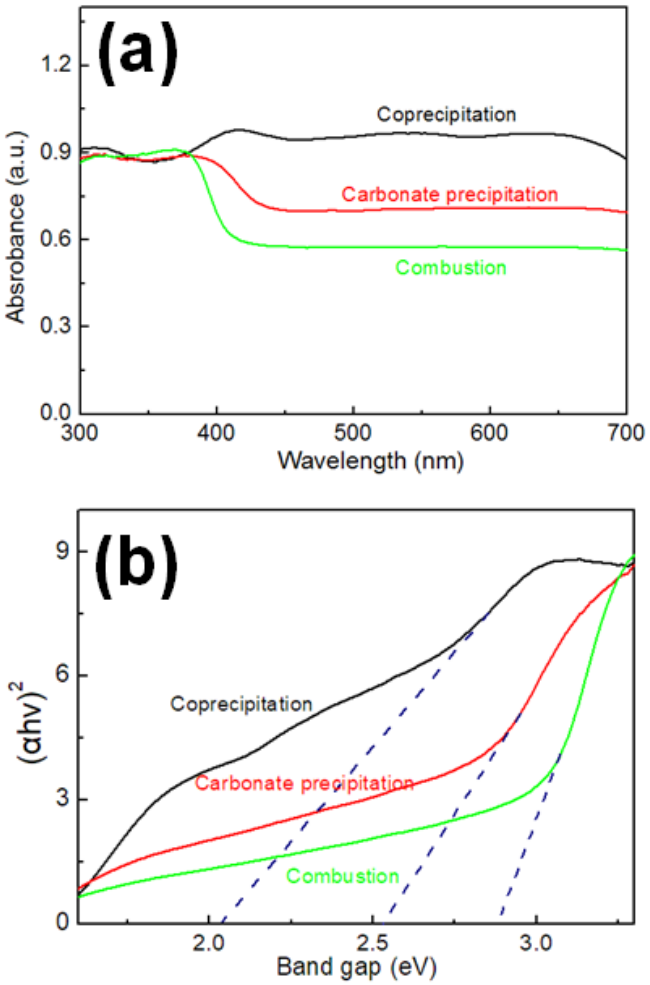


Figure 34. (a) UV-Vis absorption spectra and (b) Tauc plots of the sulfurized CLS precursors, with the UV-Vis diffuse reflectance spectra collected at 25 °C.

### 2. Synthesis without High-Temperature Sulfurization

Figure 35 shows the SEM images of the CLS precursors synthesized via wet chemical precipitation using different sulfur sources. It can be observed that all the synthesized precursors are composed of agglomerates of small nanoparticles, with the agglomerates exhibiting relatively similar morphology in all four samples. Figure 36 displays the SEM images of the precursors after thermal decomposition in an Ar atmosphere at 1000 °C for 5 hours. All the agglomerates experience apparent particle growth during heat treatment, but the thermally decomposed precursors have smaller particle sizes, compared with the sulfurized precursors. It is also observed that some

necklings have formed between particles in the samples processed using TAA and thiourea, which is likely due to the onset of sintering at high temperature.

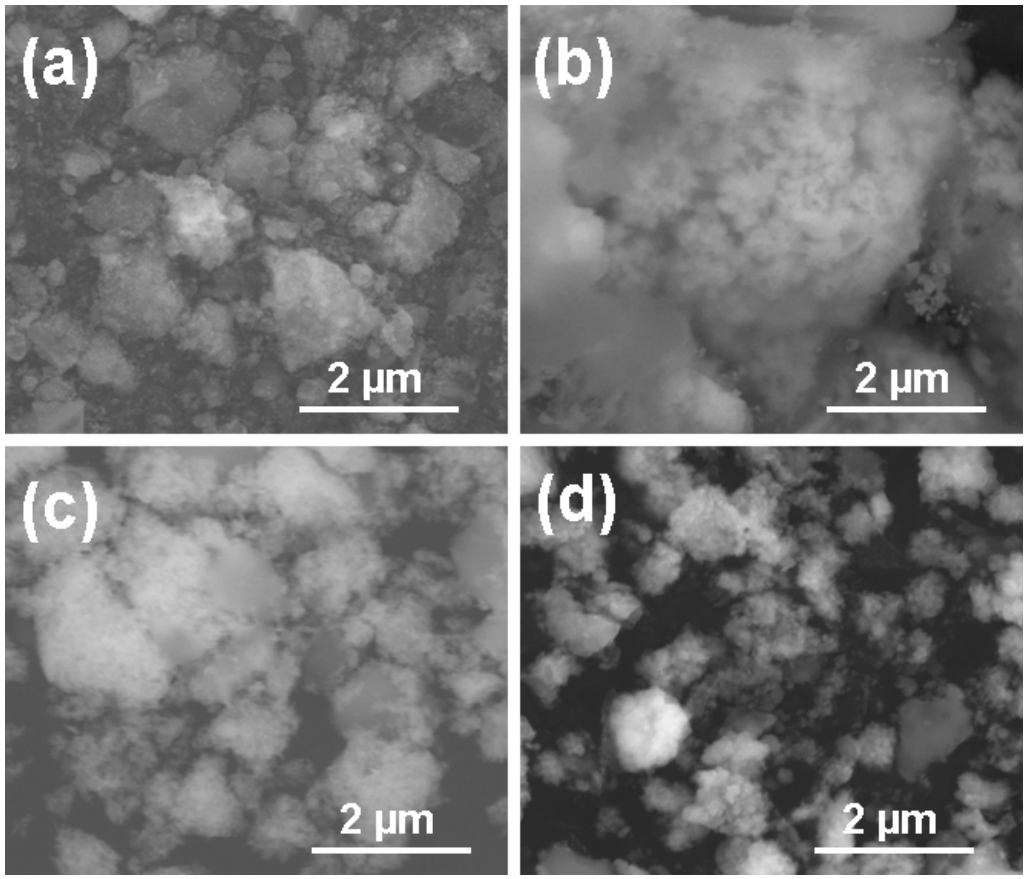


Figure 35. SEM images of the CLS precursors synthesized via wet chemical precipitation, using (a) TAA, (b) thiourea, (c) $(NH_4)_2S$, and (d) $Na_2S$ as sulfur sources.

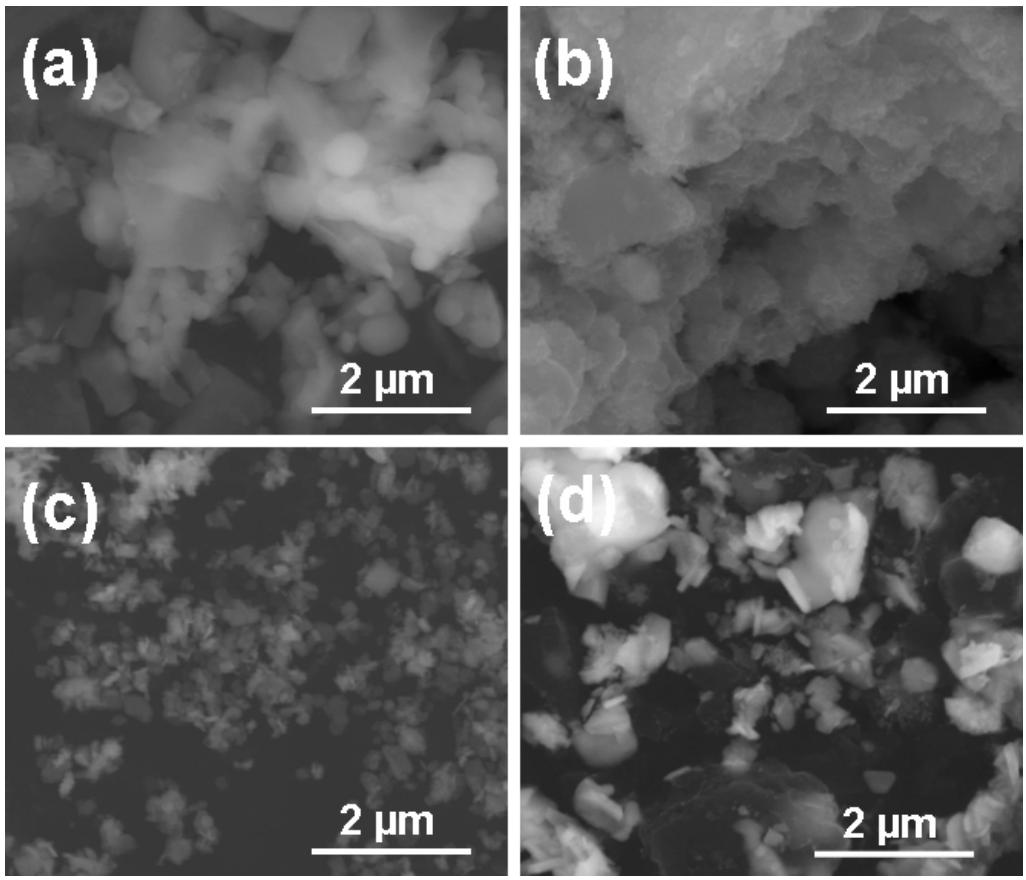


Figure 36. SEM images of the precursors synthesized via wet chemical precipitation after thermal decomposition in an Ar atmosphere at 1000 °C for 5 hours; using (a) TAA, (b) thiourea, (c) $(NH_4)_2S$, and (d) $Na_2S$ as sulfur sources.

Phase composition analysis was performed to investigate the feasibility of using the employed synthesis routes to fabricate CLS. Figure 37 shows the XRD patterns of the CLS precursors synthesized via wet chemistry precipitation after thermal decomposition in an Ar atmosphere at 1000 °C for 5 hours. Analysis of the patterns reveals that the use of different sulfur sources lead to different product phases after thermal decomposition. For the samples using TAA and $(NH_4)_2S$ as sulfur sources, the primary resulting phase is $La_2O_2(SO_4)$ (ICDD card no. 00-016-0501, *P*4/*mmm*, a=6.882 Å, c=12.300 Å). For the precursor synthesized using thiourea, the main phase is $La_2O_3$ (ICDD card no. 01-01056-0602, $P\bar{3}m1$, a=3.037 Å, c= 6.130 Å), while for the precursor synthesized using $Na_2S$ as sulfur source, the resulting main phase is $La_2O_2S$ (ICDD card no. 04-001-7885, $P\bar{3}1m$, a=4.052 Å, c=6.942 Å). It is revealed that the thermal decomposition of various CLS

precursors tends to generate oxides, oxysulfides, or oxysulfates as resulting main phases, rather than the $Th_3P_4$ phase of CLS. In addition, some minor peaks present in the XRD patterns of the thermally decomposed precursor products indicate the presence of $CaSO_4$. According to the Hard-Soft-Acid-Base theory,[264] the $La^{3+}$ and $Ca^{2+}$ ions are hard acid species, and thus have a tendency to react faster and form stronger bonds with $O^{2-}$, a hard base, compared with $S^{2-}$, a soft base. Thus, to effectively synthesize the ternary sulfide CLS, it is essential for the employed sulfur sources or chelating agents to have strong chelating ability, not only to bond La with Ca, but also to bond La/Ca complexes with S. The presence of oxygen-containing phases, and the segregation of La and Ca-containing phases can likely be attributed to the weak chelating ability of the employed sulfur sources/chelating agents to bind La and Ca ions together, and to bind La and Ca with S ions, during the wet chemistry precipitation process. This in turn leads to large inhomogeneities in the as-synthesized precursors and prevents the materials from forming the desired CLS phase upon high-temperature sulfurization.

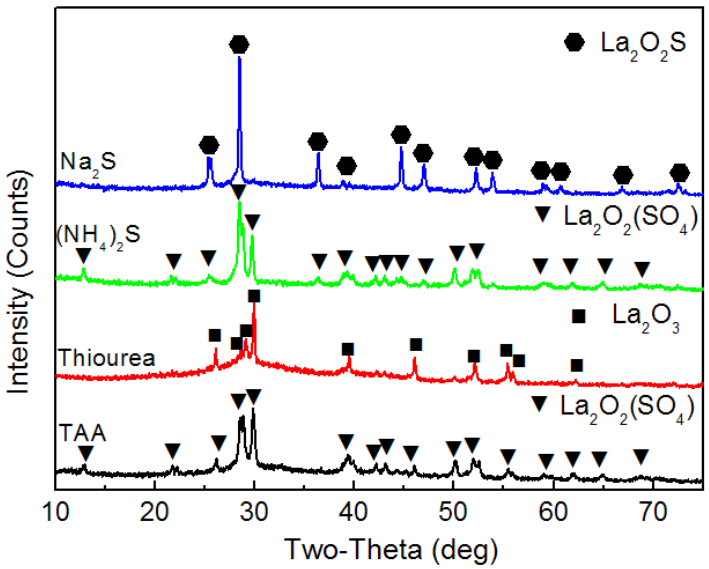


Figure 37. XRD patterns of the CLS precursors after thermal decomposition in an Ar atmosphere at 1000 °C for 5 hours.

Figure 38 displays the FTIR spectra of the precursors synthesized via wet chemical precipitation using different sulfur sources. The FTIR spectra show similar trends in the samples synthesized using $Na_2S$ and $(NH_4)_2S$. However, more absorption peaks are present

in the FTIR spectra of the precursors synthesized using TAA and thiourea, indicating the presence of more functional groups. Specifically, the broad absorption peaks in the 2900-3700 $cm^{-1}$ range and at ~1630 $cm^{-1}$ correspond to the $v_3$ asymmetric and $v_1$ symmetric stretching and bending modes of $H_2O$. The strong absorption peaks at 1380-1590 $cm^{-1}$ are due to the C=O stretching modes of carbonate groups. The absorption bands at 520-720 $cm^{-1}$ and 1000-1250 $cm^{-1}$ are attributed to the S-O vibrational bands of sulfate species.[188] For the samples synthesized using TAA and thiourea, the absorption bands at 2350-2850 $cm^{-1}$ correspond to the C=S and N-H stretching modes within the polymers composing the samples.

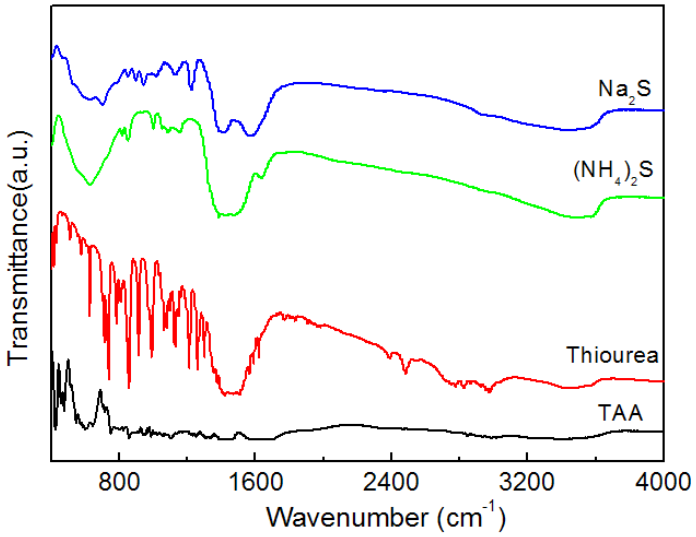


Figure 38. FTIR spectra of the precursors synthesized via wet chemical precipitation using different sulfur sources.

The TG/DTA curves of the precursors synthesized via wet chemical precipitation using different sulfur sources are shown in Figure 39, which illustrate the thermal behavior of the precursors during heat treatment. All the precursors experience weight loss with increasing temperature up to 1000 °C, with a maximum weight loss of ~80 % observed for the sample synthesized using thiourea. The broad exothermic peak accompanied by rapid weight loss over the entire temperature range corresponds to the thermal decomposition of polymers and raw materials in the samples. In the low temperature range below 400 °C, the present small endothermic peaks may be due to the release of water of hydration. As

temperature increases, the rate of weight loss gradually decreases. A number of endothermic peaks are present in the 400-1000 °C temperature range, which correspond to the formation of the oxide, oxysulfide and oxysulfate species identified previously by XRD.

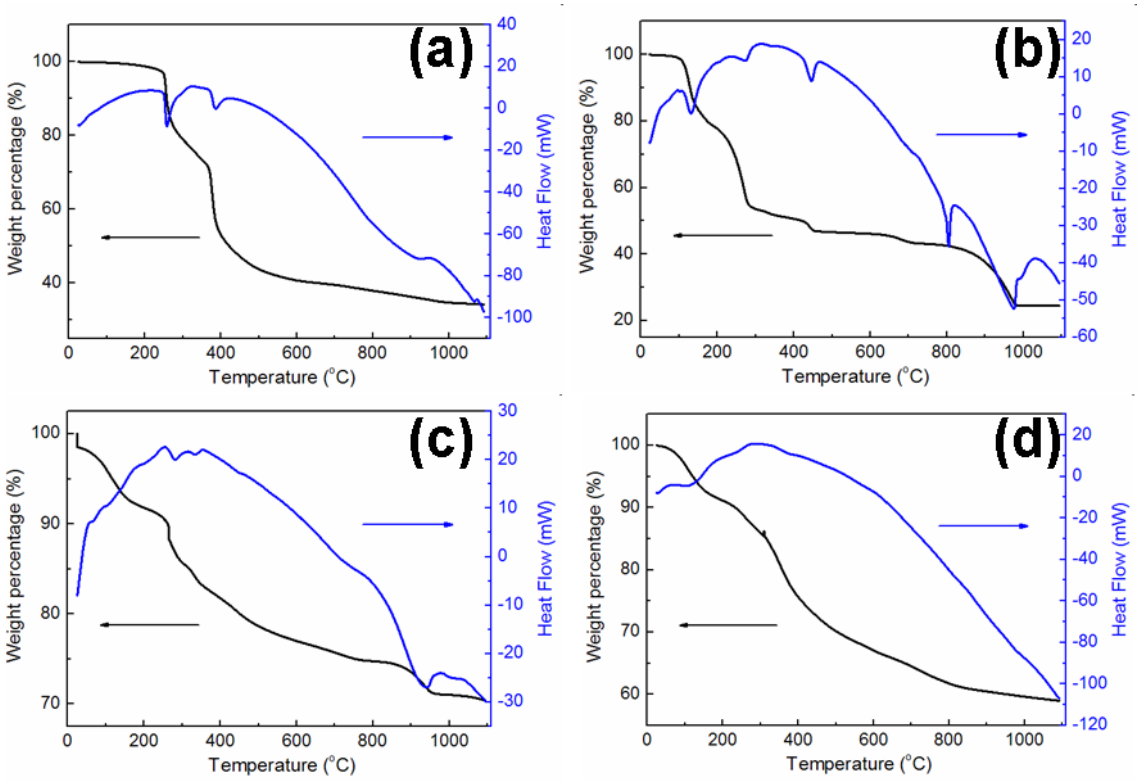


Figure 39. TG/DTA curves of the precursors synthesized via wet chemical precipitation, using (a) TAA, (b) thiourea, (c) $(NH_4)_2S$, and (d) $Na_2S$ as sulfur sources.

The product prepared via single-source precursor method followed by subsequent thermal decomposition was also characterized and investigated. Figure 40 shows the XRD pattern of the CLS precursor material after thermal decomposition and reaction at 1000 °C. The material is mostly single phase, with the main phase indexed to cubic calcium lanthanum sulfide (ICDD card no. 00-29-0339, $I\bar{4}3d$, a = 8.6830 Å). Through Rietveld refinement, the lattice parameter of the material is refined to be 8.6814 Å, which is very close to the standard PDF card data. In addition, it should be noted that some minor peaks exist in the XRD pattern, which correspond to residual carbon remaining in the powder

after thermal decomposition. The fact that the main phase of the powder is cubic CLS demonstrates that the route applied in this research is a feasible method to prepare CLS without the use of any long sulfurization treatments using sulfur-containing gases. It also suggests that Na(Ddtc) and Phen are effective at chelating the La and Ca ions with sulfur ions during wet chemical precipitation, with the schematic of the reaction is displayed in Figure 41. The effective chelation of the Ca, La, and S ions allows for the ternary sulfide CLS to be obtained using subsequent thermal decomposition and reaction of the precursor material. Due to the relatively high temperature at which the thermal decomposition and reaction is performed, the material experiences particle growth, and as such the crystallite size of the reaction products is relatively high, apparent as the narrow peaks observed in the XRD pattern in Figure 40.

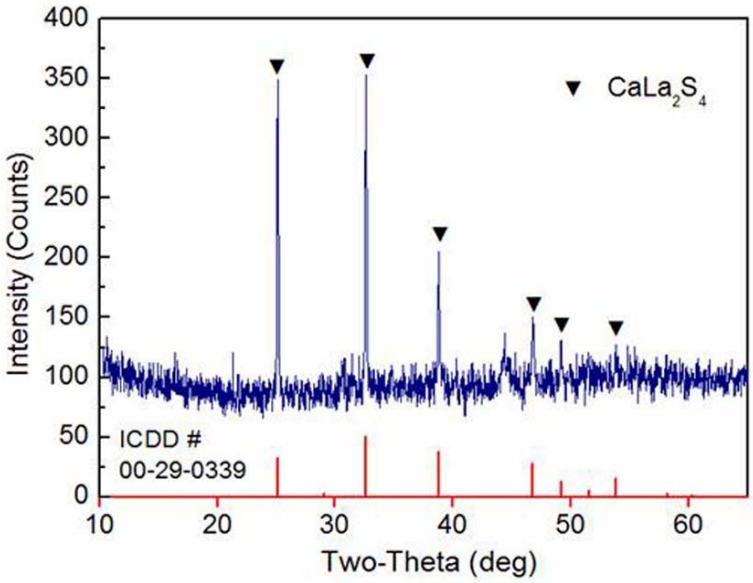


Figure 40. XRD pattern of the synthesized CLS powder after thermal decomposition at 1000 °C for 5 hours in flowing argon.

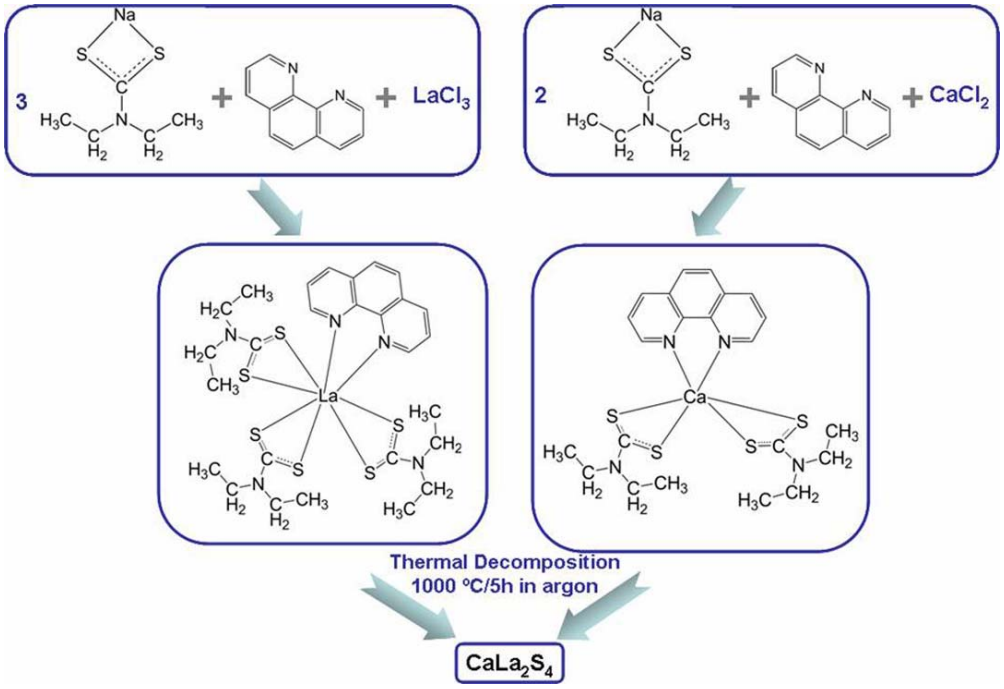


Figure 41. Schematic of the reaction to synthesize CLS via a wet chemistry method followed by thermal decomposition.

The TG/DTA curves of the CLS precursor material obtained via the wet chemistry route are displayed in Figure 42, which illustrates the various thermal reactions that the material goes through during the heat treatment in Ar. In the temperature range between room temperature and 400 °C, the broad exothermic peak accompanied by >50% weight loss corresponds to the rapid thermal decomposition of the polymers in the precursor. The two endothermic peaks in this range are likely due to the release of the waters of hydration from the hydrated nitrate raw materials used in the precursor. As temperature increases, the precursor material's rate of weight loss decreases. The weight loss of the CLS precursor becomes approximately stable with a total weight loss of 79%, at the final temperature of 1000 °C, with an endothermic peak at 1000 °C corresponding to the formation of CLS. The TG/DTA curves shown here provide a basic reference for the thermal decomposition profile of the precursor to synthesize CLS.

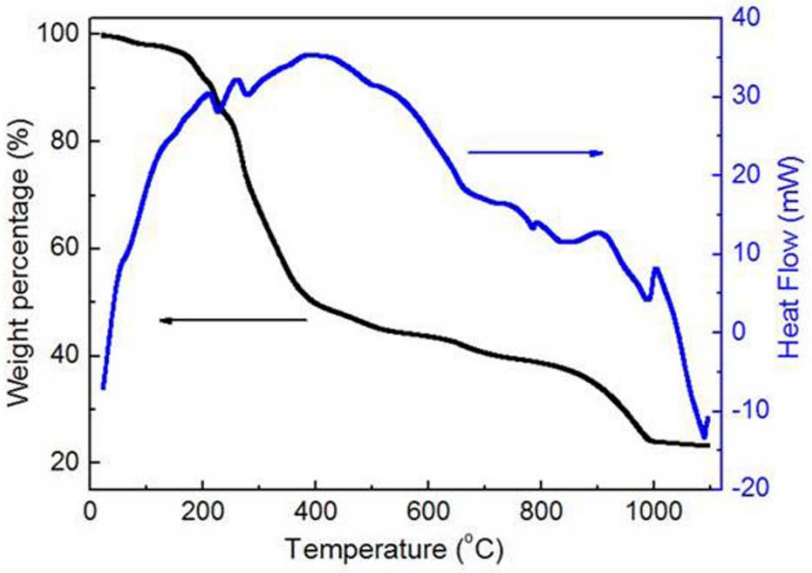


Figure 42. TG/DTA curves of the CLS precursors synthesized via the wet chemistry method.

The SEM image displayed in Figure 43 (a) shows that the CLS powder obtained by thermal decomposition of the precursor consists of inhomogeneous submicron-sized agglomerates of particles. It is further suggested by TEM (Figure 43 (b)) that the CLS particles are nanoscale, with an approximate average particle size of ~50 nm. Detailed observations of the powder reveal neckings between adjacent particles, which can be attributed to the powder beginning to sinter at the relatively high heat treatment temperature. In addition, EDS measurements of the powder (shown in Figure 43 (c)) reveal the presence of the main cations and anions expected in CLS. The oxygen peak is due to the oxygen attached to the pores and surface of the CLS powder. The presence of carbon indicates that some carbon species survive the thermal decomposition heat treatment of the CLS precursor. The powder needs to be further purified to remove carbon impurities for infrared optical ceramic applications.

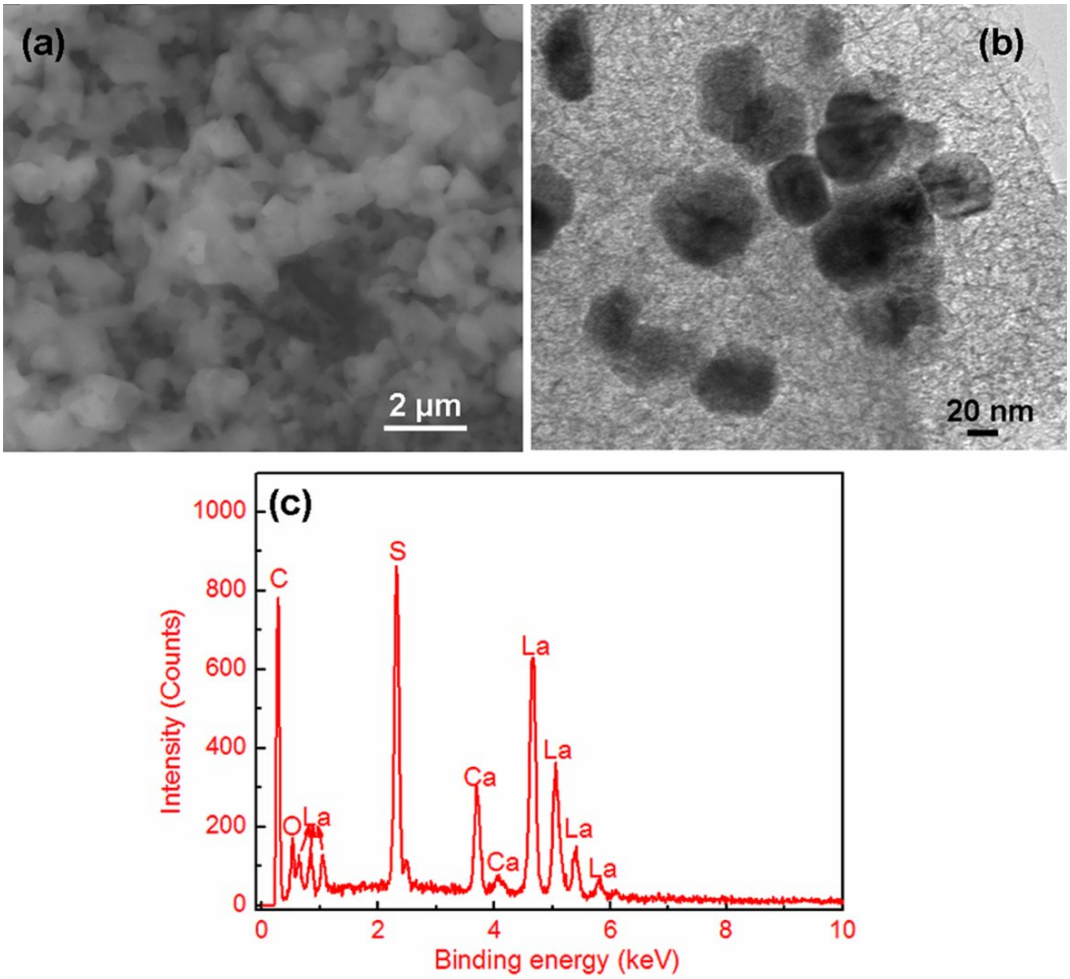


Figure 43. (a) SEM image, (b) TEM image, and (c) EDS spectrum of the CLS powder synthesized via a wet chemistry method followed by thermal decomposition.

Figure 44 (a) presents the $N_2$ adsorption-desorption isotherm curve of the synthesized CLS powder measured using the BJH method. The hysteresis loop shown in this typical irreversible type IV thermo curve is due to pore condensation,[265] suggesting the presence of mesopores within the CLS powder, which are believed to form primarily during the thermal decomposition of the CLS precursor. It is of interest to notice that no mesopores are shown in the particles in the TEM image. However, from the agglomerates observed in the SEM micrograph, we assume that the mesopores are due to interspaces within the small nano-sized particles during the process of particles' stackings and agglomerations. The BET specific surface area of the sample was measured to be 75.82±0.26 $m^2/g$, which is attributed to the submicron-scale agglomerates of the

nanoparticles, in combination with the effect of the mesopores. The pore size distribution curve displayed in Figure 44 (b) indicates that the sample has a narrow pore size distribution approximately at 23 nm, which also supports the notion that extensive mesopores exist within the sample.

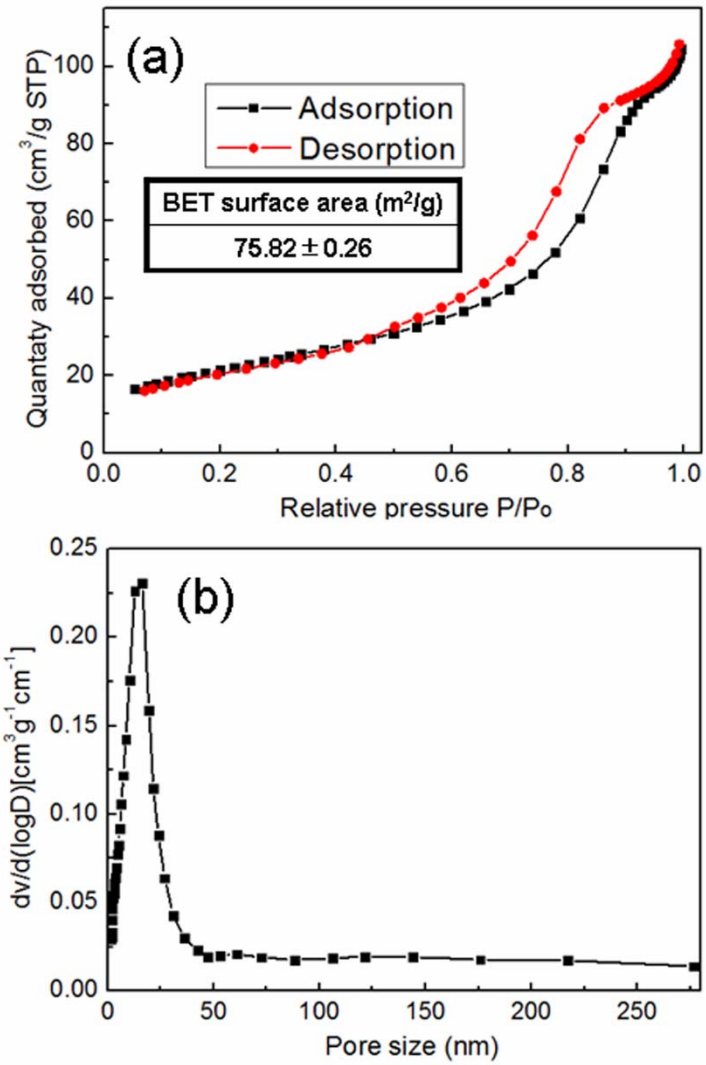


Figure 44. Adsorption-desorption isotherm curve (a) and pore size distribution curve (b) of the synthesized CLS powder.

The UV-Vis spectrum of the synthesized CLS powder is shown in terms of absorbance versus wavelength in Figure 45 (a). The measured diffuse reflectance is converted to absorbance in this plot. The maximum wavelength required to promote an

electron to the conduction band of the material is dependent on the material's band gap, and was estimated from the curve to be 429 nm. To determine the direct band gap of the CLS powder, the curve can be replotted based on the equation for the Tauc relation. Figure 45 (b) shows the Tauc plot of the synthesized CLS powder. An absorption energy can be determined by extrapolating the value of $h\upsilon$ to $\alpha$=0, which corresponds to the band gap energy $E_{gn}$. The band gap energy of the synthesized CLS powder is estimated to be 2.89 eV, higher than that measured for the bulk material (2.70 eV).[156,266] The small crystallites within the CLS powder result in quantum size confinement, which contributes to the apparent band gap enhancement of the synthesized powder.

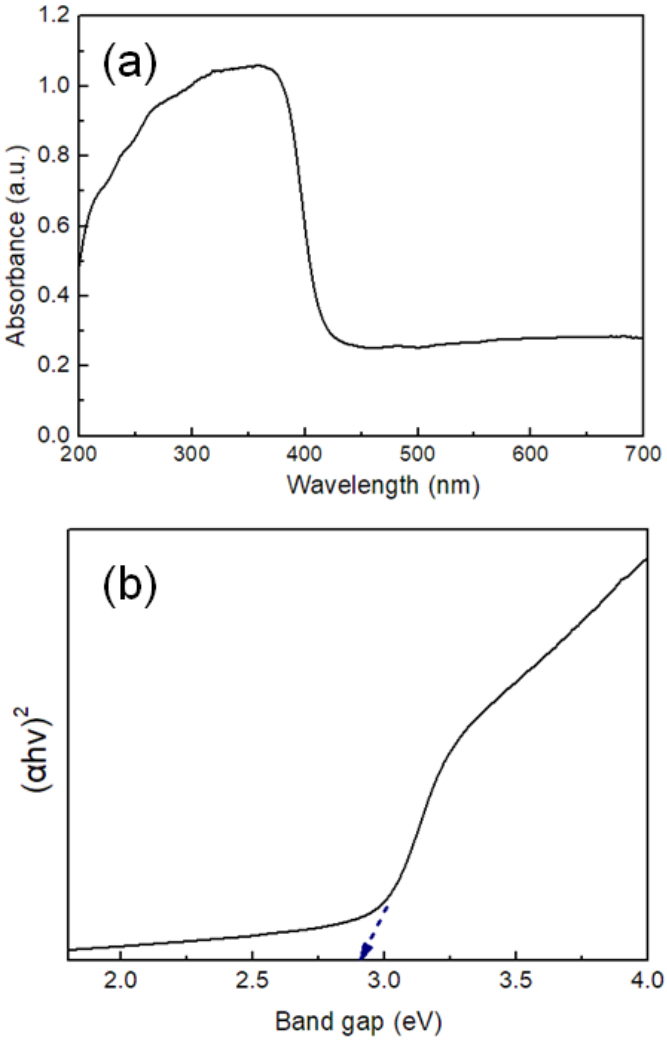


Figure 45. (a) UV-Vis absorption spectrum and (b) Tauc plot of the synthesized CLS powder, with the UV-Vis spectrum collected at 25 °C.

Figure 46 shows the photoluminescence emission spectrum (excitation wavelength: 365 nm) of the synthesized CLS powder measured with a xenon lamp as the light source. It was reported that the characteristic $Mn^{2+}$ peak, which originated from Mn impurities in the CaS impurity phase present in CLS, was observed in the photoluminescence spectra of CLS powder.[171] However, there are no such impurity peaks in the spectra measured in this study, likely due to the difference in the employed processing routes. Here, the sample shows an emission peak at approximately 454 nm, which is assumed to be due to the near-band-edge photoluminescence of the CLS semiconductor. It should be noted that the photoluminescence emission wavelength has a redshift compared with the estimated wavelength required for electron promotion through light absorption, as determined through UV-Vis spectroscopy (shown in Figure 45 (a)), which suggests that the emitted photon energy is lower than the absorbed photon energy. The energy degradation here can be ascribed to the Stokes shift in energy ($\Delta_{Stokes}$), which in semiconductors is attributed to the participation of phonons in the relaxation process.[267] In addition, it is believed that some sulfur defects are formed during the thermal decomposition process which forms the CLS powder. According to the semiquantitative analysis based on EDS spectra measured in different areas of the powder, we find that sulfur has an apparent deficiency compared with the supposed value in the stoichiometry of CLS. Furthermore, it has also been reported that sulfur losses and deficiencies were detected during hot pressing of CLS ceramics in vacuum and argon.[162,167] Thus, the broad peaks at 474 nm and 532 nm are assumed be due to the recombinations of electrons from conduction band and sulfur vacancy with holes in elemental sulfur species on surface, respectively.[268]

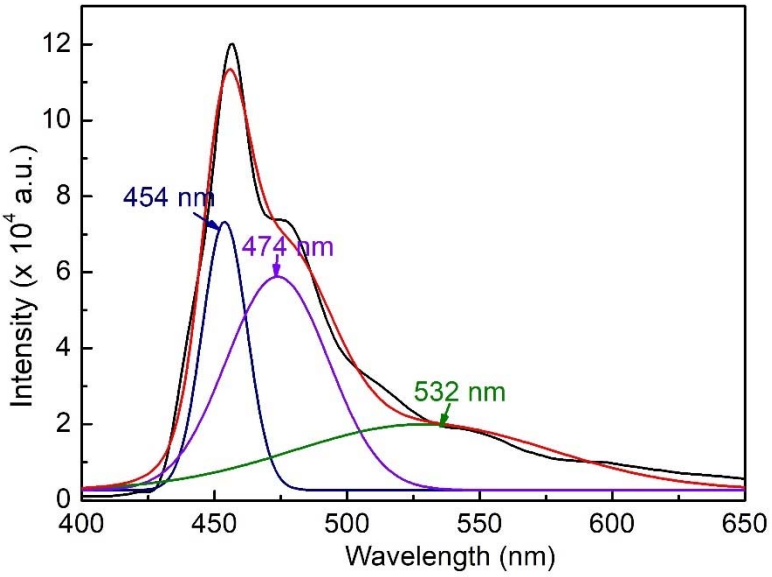


Figure 46. Photoluminescence emission spectrum of the synthesized CLS powder measured under excitation at a wavelength of 365 nm at 25 °C.

## D. Conclusions

In the current study, two processing routes were applied in an attempt to synthesize CLS: the wet chemistry processing of oxygen-containing precursors through coprecipitation, carbonate precipitation, and combustion methods, followed by high-temperature sulfurization in flowing $CS_2$/Ar gas; and preparation of sulfur-containing precursors via wet chemistry methods using different sulfur sources (TAA, thiourea, $(NH_4)_2S$ and $Na_2S$), followed by thermal decomposition in an Ar atmosphere. It was revealed that the sulfurization of wet chemistry-processed precursors could lead to the formation of CLS and Ca-doped $La_2S_3$ with the $Th_3P_4$ phase. The synthesized CLS and Ca-doped $La_2S_3$ powders were observed to exhibit band gap enhancement due to the nanometric size of the crystallites composing the powder agglomerates. It was demonstrated that the sulfurization of precursors synthesized via the combustion method is the most effective way to prepare stoichiometric CLS. In contrast, the approach involving the thermal decomposition of sulfur-containing precursors resulted in the formation of $La_2O_3$, $La_2O_2S$, and $La_2O_2(SO_4)$, rather than CLS, which was attributed to the weak chelating ability of the employed sulfur sources. It was further concluded that the optimum route to synthesize CLS without sulfurization was through the application of a wet-

chemistry method using a combination Na(Ddtc) and Phen, followed by thermal decomposition in an Ar atmosphere, due to the strong chelating ability of sulfur source and chelating agent. It appeared that the synthesized CLS powder exhibited the quantum size effect, which in turn led to band gap enhancement. Photoluminescence characterization indicated that the CLS powder exhibited a near-band-edge photoluminescence emission with a Stokes shift and two broad emission bands due to the sulfur defects.

# V. CONSOLIDATION OF $CaLa_2S_4$ INFRARED OPTICAL CERAMICS

## A. Introduction

The refractory ternary sulfide, $CaLa_2S_4$ (CLS), is considered to be a promising candidate for infrared optical ceramics for applications in harsh environments, for its good mechanical hardness and infrared transparency.[55,155,156] The material has seen extensive studies mainly focused on the preparation of CLS powders and the consolidation of CLS ceramics. It has been reported that pure CLS powders can be conventionally synthesized through high-temperature sulfurization of CLS precursors in $H_2S$ or $CS_2$ atmosphere over long time periods. Through hot pressing of synthesized CLS powders at 1346 ºC, K. Lewis et al. obtained CLS ceramics with 100% relative density, which were subsequently subjected to an annealing treatment at 1100 ºC in an Ar/$H_2S$ atmosphere, to compensate for sulfur losses during sintering. They then examined the infrared transmittance properties of the ceramics.[153] Later, M. Tsai et al. applied hot pressing (at 1050-1150 ºC) followed by resulfurization to fabricate infrared optical CLS ceramics, and subsequently investigated the influence of different La/Ca stoichiometric ratios on sintering behavior.[186,187] Furthermore, it was demonstrated that fully densified CLS ceramics with favorable optical properties could be achieved by HIPing of CLS ceramics initially sintered to closed porosity by hot pressing or by pressureless sintering in an $H_2S$ atmosphere. Through a study of the effects of sulfurization and sintering temperature on alkoxide-method-processed CLS powders, L. Wang et al. reported that 1400 ºC was the most suitable and promising pressureless sintering and HIPing temperature to obtain optimum infrared transmittance.[174] In contrast, J. Savage et al. investigated the sintering of CLS powders processed via evaporative decomposition of solutions, and suggested that infrared optical CLS ceramics with a composition of $Ca_{0.45}La_{1.1}S_{2.1}$ could be fabricated by pressureless sintering followed by HIPing, both at 1190 ºC.[155] Through investigation of the influence of three different La/Ca stoichiometries (2.2, 2.7 and 3.3) on sintering properties, M. Hills and K. Saunders revealed that $CaLa_2S_4$ ceramic the with a La/Ca ratio of 2.7, sintered in $H_2S$ at 1150 ºC and then HIPed at 990 ºC in argon under 200 MPa, showed the best optical performance.[55,169] In addition, W. White et al. proposed a two-stage consolidation process of hot pressing at

1450 ºC, followed by HIPing at 1400 ºC to prepare CLS infrared optical ceramics.[156] Researchers have also investigated the doping of $PbLa_2S_4$ and $La_2S_3$, precursors' dispersion characteristics, phase development, and sintering variables in order to provide insights into ways to optimize the sinterability of CLS powder, and improve the optical properties of the end ceramics.[163,179,182,269]

As a pressure-assisted and current-activated rapid sintering technique, FAST has been extensively researched in recent years as a method to process various materials, including metals, intermetallic compounds and ceramics. It has been shown that FAST can reduce sintering time, lower sintering temperature, accelerate the rate of superplastic deformation, and retard grain growth rates, all of which make it an effective and innovative route for materials synthesis and consolidation.[20,270] There have been some studies focused on field assisted sintering of sulfide-based materials, in the context of observing the influence of FAST on microstructural features and functional properties of these materials. J. Li et al. reported on the FAST consolidation of various sulfide polycrystals including $Bi_2S_3$, SnS, and $Cu_{1.8}S$, and observed enhanced thermoelectric efficiency in the FAST-processed materials.[271-274] FAST has been also demonstrated to be a suitable and viable route to fabricate electrochemically active sulfide electrodes for Li-ion battery applications.[275,276] V. Zestrea et al. investigated field assisted sintering of the ternary sulfide $FeCr_2S_4$, and revealed residual structural disorder in the samples consolidated by FAST.[277] In addition, it has been reported that ZnS optical ceramics can be consolidated at reduced temperatures, by applying FAST to both custom-synthesized and commercial ZnS powders.[126,133,138] However, few studies have been performed concerning the grain growth and densification behavior that occur during the field assisted sintering of CLS ceramics.

In this chapter, commercial CLS powders were sintered via FAST and hot pressing at different temperatures. Microstructural features of the CLS ceramics sintered via different sintering methods were compared. Through microstructural observations and sintering curve measurements, the densification behavior and grain growth kinetics during the sintering process were systematically investigated and discussed. In addition, the optical and mechanical properties of the CLS ceramics were correlated with the microstructural properties and densification of the ceramics.

## B. Experimental Procedures

Commercial CLS powders (Alfa Aesar, 99.9% (REO)) without any further purification were used in this study. The as-received CLS powders were loaded into a graphite die (I-85, Electrodes, Inc.) with a diameter of 18.75 mm, with graphite foils (thickness of 0.13 mm, Alfa Aesar) placed on the top and bottom of the sample to separate the sample from the graphite punches. An optical pyrometer was employed to measure the temperature on the outside wall of the graphite die. The powders were consolidated at 850 ºC, 900 ºC, 950 ºC, 1000 ºC, 1050 ºC and 1100 ºC for 10 min under a uniaxial pressure of 50 MPa, at a heating rate of 50 ºC/min, in a vacuum of $10^{-2}$ torr, under a direct current field by FAST (HP D 25, FCT Systeme GmbH, Germany). After the dwelling process, the sample was allowed to cool at an uncontrolled rate to room temperature, by immediately shutting down the power supply. In order to make a comparison, the CLS powders were also sintered via hot pressing in vacuum at 950 ºC, 1050 ºC, 1150 ºC and 1200 ºC under a uniaxial pressure of 50 MPa for 2 h, at a heating rate of 5 ºC/min with uncontrolled cooling to room temperature. Figures 47 and 48 display the schematics of the unit configuration of FAST and hot pressing, respectively.

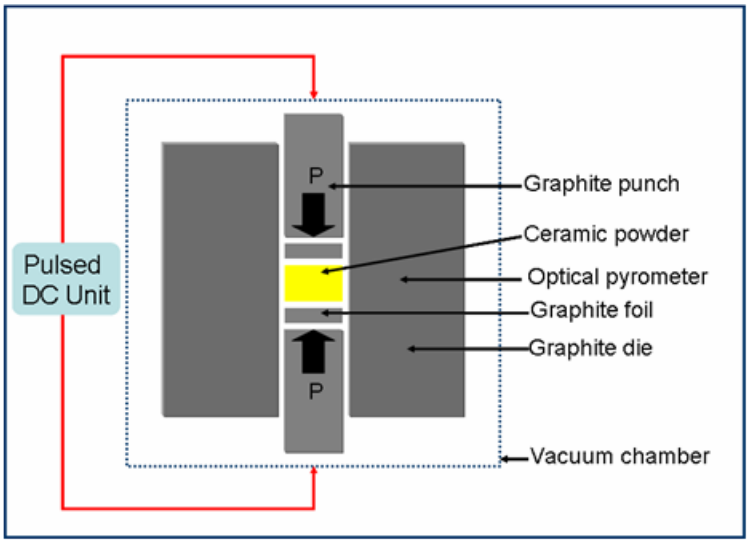


Figure 47. Schematic view of the FAST furnace configuration.

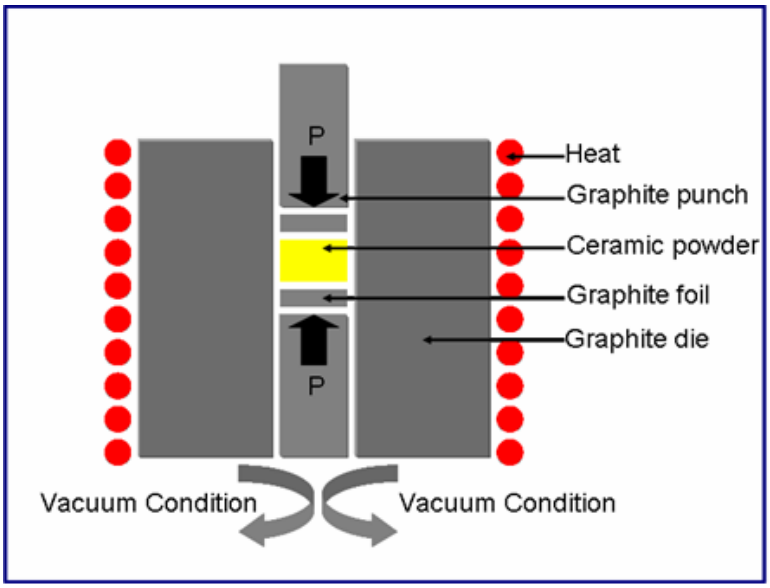


Figure 48. Schematic view of the vacuum hot pressing furnace configuration.

The phase compositions of the CLS powders and consolidated ceramics were measured with XRD with a Cu*Kα* (λ= 0.154 nm) radiation (D2 PHASER, Bruker), at a current of 10 mA and a voltage of 30 kV. Measurement conditions of 0.03 º2θ step size and 0.2 s count time were applied over a measurement range of 10-75 º2θ. Phase identification analysis was performed by using MDI Jade 9 integrated with the ICDD database. The morphological and microstructural features of the CLS powders and ceramics were investigated by SEM (Quanta 200, FEI). The surfaces of the CLS ceramics were observed after the ceramics were polished and thermally etched for 1 hour in an atmosphere of $CS_2$/Ar. Grain size analyses were performed by applying the line intercept method on over 300 grains per sample. During the field assisted sintering process, the height variation of the samples was recorded by the FAST instrumentation. The height variation data were then calibrated by subtracting the dimension change associated with the instrument. Archimedes's method was adopted to measure the density of the sintered CLS ceramics (theoretical density: 4.526 g/cm$^3$).[162] FTIR (Nicolet 6700, Thermo Fisher) was applied to measure the infrared transmittance of the polished CLS ceramics over a wavelength range of 2.5-21 μm. Vickers hardness measurements were performed on a micro-hardness tester (HMV-200, Shimadzu) with a load of 0.05 kgf and a loading time of 10 s.

## C. Results and Discussion

The XRD pattern and SEM image of the commercial CLS powders employed in this study are displayed in Figure 49. XRD analysis shows that the commercial powders have the main phase indexed to the cubic calcium lanthanum sulfide (ICDD card no. 00-29-0339, $I\bar{4}3d$, a = 8.6830 Å). It is also noted that several weak diffraction peaks at 22-23°, 35° and 41.7° in the XRD pattern may correspond to β-$La_2S_3$ (ICDD card no. 04-010-1841, $I4_1/acd$, a = 15.62 Å, c = 20.62 Å), and γ-$La_2S_3$ ($(La_2S_3)_{5.24}$, ICDD card no. 01-084-0231, $I\bar{4}3d$, a = 8.692 Å), which might be produced as impurity phases during the synthesis process of the commercial CLS powder. As can be observed from the SEM micrograph, the CLS powders are composed of submicron-sized and micron-sized agglomerates of CLS particles. Figure 50 shows the XRD patterns of the raw CLS powders and CLS ceramic samples sintered via FAST at different temperatures. All the ceramic samples are identified via XRD analysis to contain the main phase as the cubic thorium phosphate-structured phase of CLS. According to the Scherrer Equation,[278] peak broadening in XRD patterns occurs as crystallite size decreases. Here, it is noted that the CLS ceramics have sharper and narrower peaks than those of the raw CLS powders, which indicates grain growth during the sintering process. In addition, due to grain growth, the samples sintered at higher temperatures have narrower peaks than the ones sintered at lower temperatures.

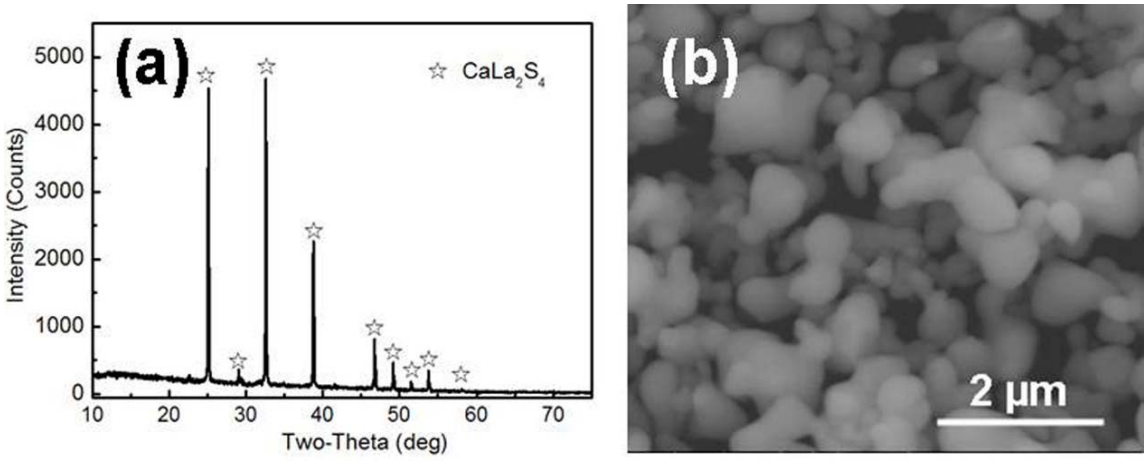


Figure 49. XRD pattern and SEM image of the commercial CLS powders employed in this study.

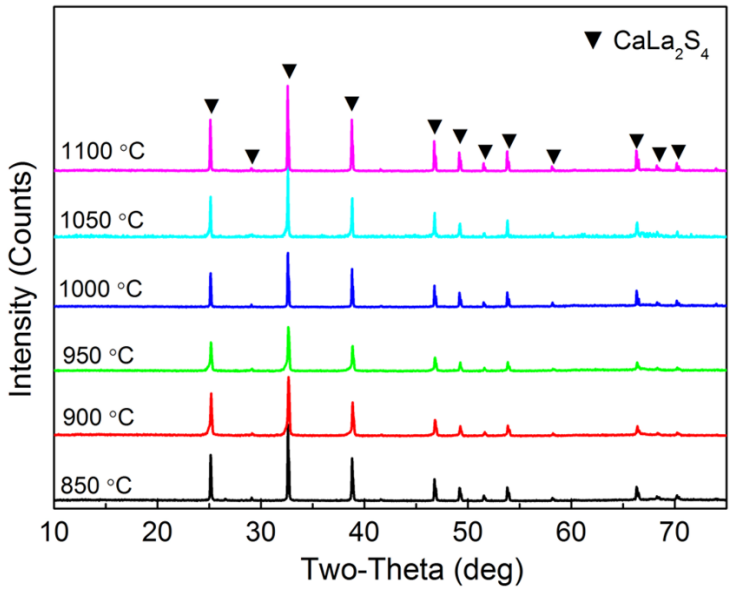


Figure 50. XRD patterns of the CLS ceramic samples sintered via FAST at different temperatures for 10 min under a uniaxial pressure of 50 MPa.

Figure 51 exhibits the temperature dependence of piston speed and relative density of the CLS ceramic sample sintered via FAST at 1200 ºC for 10 min under a pressure of 50 MPa. The instantaneous relative density of the CLS ceramic during sintering can be obtained by the equation:

$$D=(\frac{T_f}{T})D_f \qquad (7)$$

where $D$ is the instantaneous relative density, $D_f$ is the final relative density, $T_f$ is the final thickness, and $T$ is the instantaneous thickness, which is obtained through the height variation of the pressing piston recorded by the SPS equipment. Three sintering stages can be identified from the densification curve. The initial stage occurs below 810 ºC, where limited shrinkage, rearrangement of the CLS particles, and initial neck formation occur. During the intermediate stage over the temperature range between 810 ºC and 940 ºC, the sample experiences considerable densification and shrinkage, reflected by a rapid increase in relative density, with the highest densification rate occurring at approximately 890 ºC. In the intermediate stage, neck growth and grain boundary movement lead to grain growth through consumption of adjacent grains and reduction of porosity. As temperature increases above 940 ºC, densification is gradually completed, with a small increase in

relative density corresponding to the final removal of isolated porosity during the final stage of sintering.[19,279] Based on the densification curve of the sample sintered at 1200 ºC, six different temperatures (850 ºC, 900 ºC, 950 ºC, 1000 ºC, 1050 ºC and 1100 ºC) were chosen for the investigation of densification and grain growth of the CLS ceramics, while applied uniaxial pressure and dwell time were held constant for all temperatures at 50 MPa and 10 min, respectively.

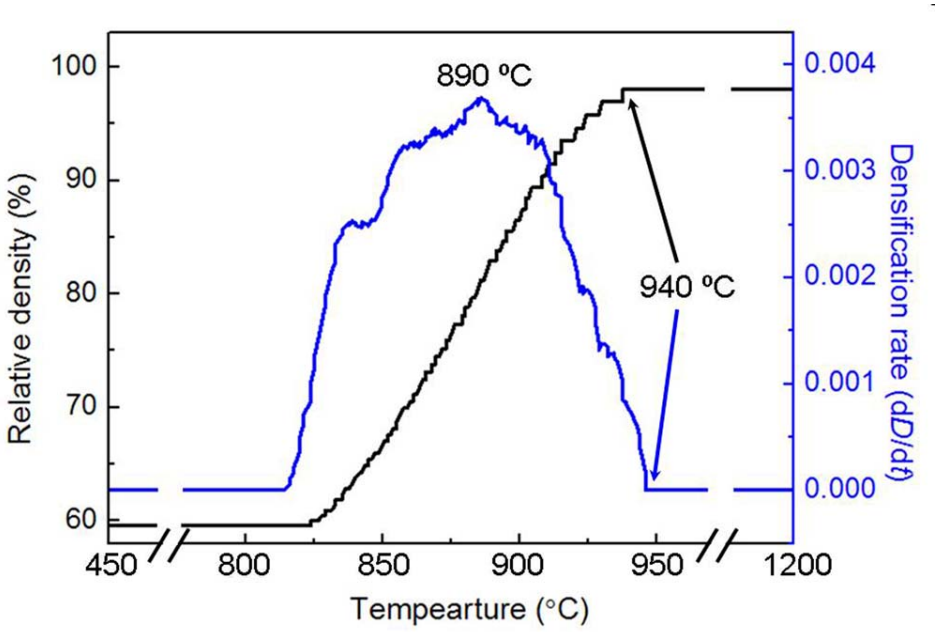


Figure 51. Densification curves as a function of temperature for the CLS ceramics sintered via FAST at 1200 ºC for 10 min under a uniaxial pressure of 50 MPa.

Figure 52 shows SEM images of the thermally etched surfaces and relative densities of the CLS ceramics sintered via FAST at different temperatures. It can be observed that all the CLS ceramics are composed of grains ranging from submicron-scale to micron-scale, with clear grain boundaries. The dependence of the samples' average grain size on sintering temperature is exhibited in Figure 53. As can be seen from the plot, the ceramics experience limited grain growth over the temperature range of 850-950 ºC, which corresponds to the rapid densification stage, according to the sintering curve shown in Figure 51. As temperature increases, the grains within the samples grow rapidly from submicron-sized to micron-sized, while relative density increases only slightly, indicating

that grain growth dominates between 950-1100 ºC. In addition, it is important to note that some residual isolated pores persist, and full densification still cannot be achieved by the end of the sintering cycle, which suggests that further densification process such as HIP is required to further improve the consolidation of the CLS ceramics.

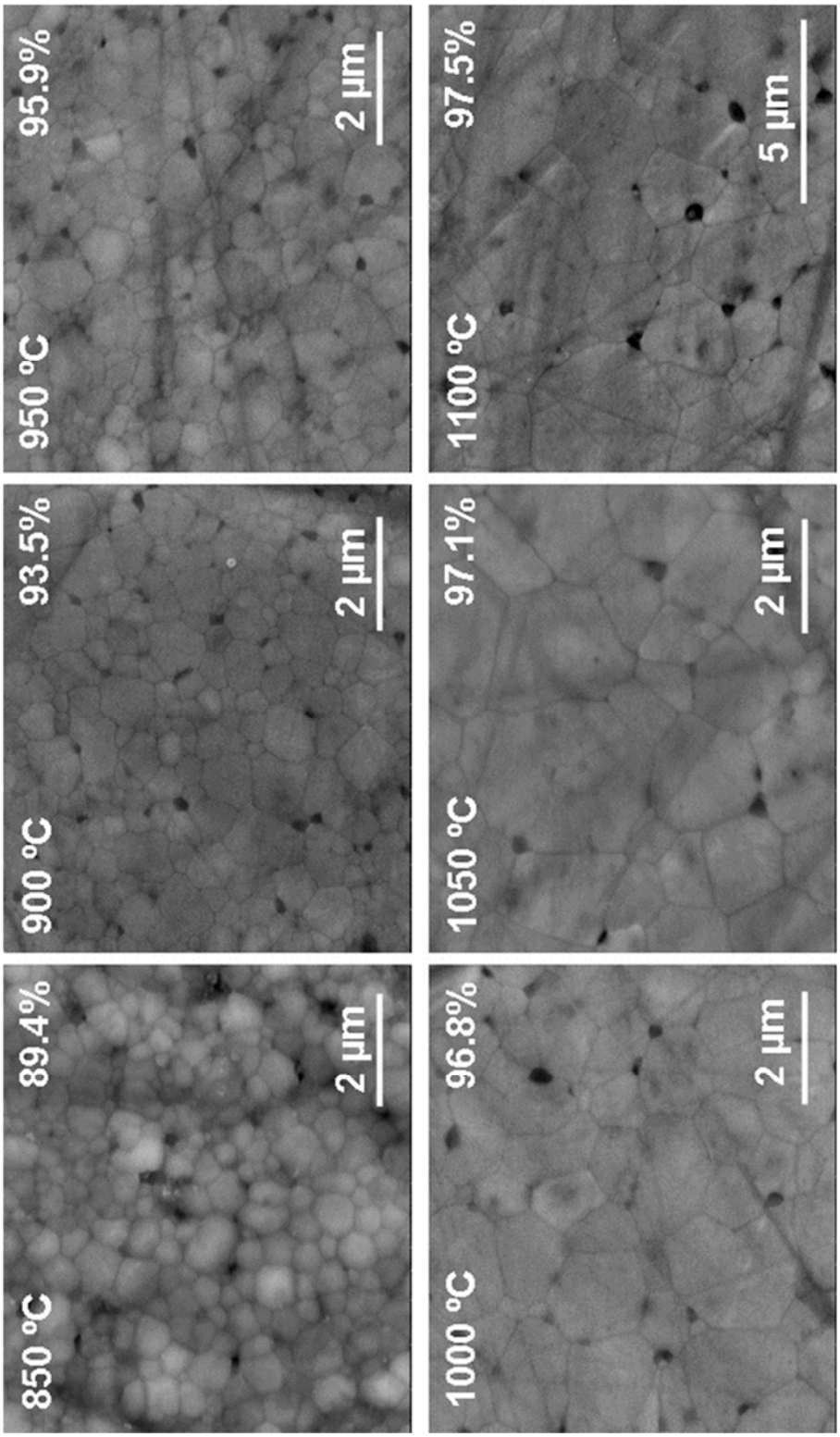


Figure 52. SEM images of the thermally etched surfaces and relative densities (shown in the inset) of the CLS ceramics sintered via FAST at different temperatures (850 ºC, 900 ºC, 950 ºC, 1000 ºC, 1050 ºC and 1100 ºC), under a uniaxial pressure of 50 MPa for 10 min.

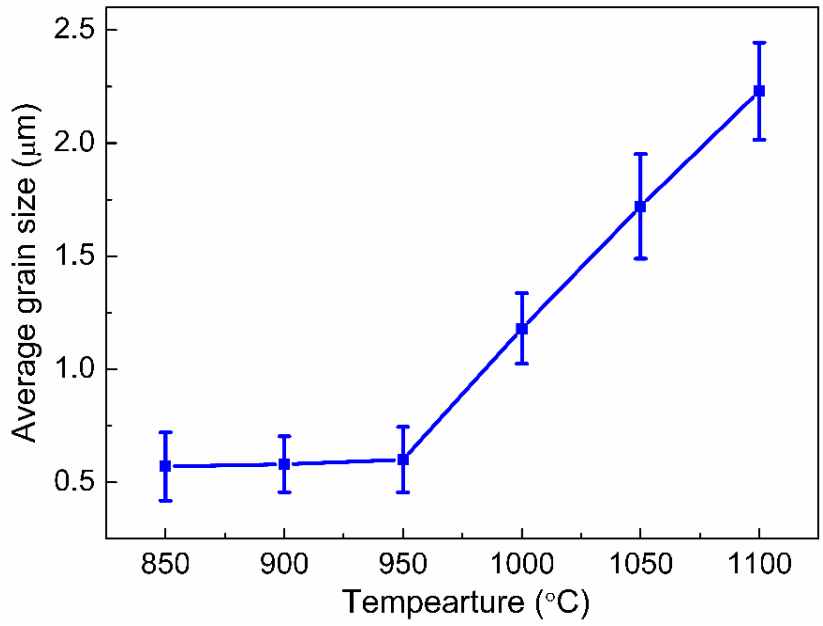


Figure 53. Temperature dependence of average grain size for ceramics sintered via FAST under a uniaxial pressure of 50 MPa for 10 min.

To further investigate the densification mechanism of the CLS ceramics during field assisted sintering, we applied the approach originally proposed by Bernard-Granger and Guizard on discussion of the field-assisted sintering behaviors of $Al_2O_3$ and $ZrO_2$.[280,281] During the sintering process, with or without an externally applied load, mass transport can be considered as analogous to that which occurs in high-temperature creep.[282,283] Thus, the FAST kinetics equation, which is assumed to be similar to that for hot pressing, can be simplified from the general steady-state creep strain equation by neglecting small thermodynamic driving forces.[284,285] The modified FAST kinetics equation can be expressed as:

$$\frac{1}{D}\frac{dD}{dt} = \frac{B\phi\mu_{eff}b}{kT}\left(\frac{b}{G}\right)^{p}\left(\frac{\sigma_{eff}}{\mu_{eff}}\right)^{n} \qquad (8)$$

where $D$ is the instantaneous relative density, $t$ is time, $B$ is a numerical constant, $k$ is the Boltzmann constant, $\phi$ is the diffusion coefficient, $T$ is the absolute temperature, $\sigma_{eff}$ is the instantaneous effective stress acting on the sample, $\mu_{eff}$ is the instantaneous effective

shear modulus of the sample, *b* is the Burgers vector, *G* is the grain size, *p* is the grain size exponent, and *n* is the stress exponent.

Based on the work performed by Helle et al.,[286] the effective stress can be expressed as:

$$\sigma_{eff} = \frac{1-D_0}{D^2(D-D_0)}\sigma_{mac} \tag{9}$$

where $\sigma_{mac}$ is the macroscopic compaction pressure (50 MPa) applied to the CLS sample, and $D_0$ is the starting green density. In addition, by applying the correlation between theoretical and effective Young's moduli, the effective shear modulus $\mu_{eff}$ can be obtained as follows:

$$\mu_{eff} = \frac{E_{th}}{2(1+\nu_{eff})}\frac{D-D_0}{1-D_0} \tag{10}$$

where $E_{th}$ is the theoretical Young's modulus (96.0 GPa), and $\nu_{eff}$ is the effective Poisson's ratio (0.26).

Thus, Equation (8) can be modified to:

$$\frac{1}{\mu_{eff}}\frac{1}{D}\frac{dD}{dt} = C_1\frac{e^{\frac{-Q_d}{RT}}}{T}(\frac{b}{G})^p(\frac{\sigma_{eff}}{\mu_{eff}})^n \tag{11}$$

where $C_1 = \frac{Bb\phi_0}{k}$ and is a constant ( $\phi_0$ is the pre-exponential factor of the diffusion coefficient $\phi$), R is the gas constant, and $Q_d$ is the activation energy of the mechanism controlling densification.

According to the aforementioned results of the grain size analyses, the average grain size changes little over the temperature range of 850-950 ºC. It is thus assumed that grain size is constant during sintering in this temperature range. With this assumption, Equation (11) can be transformed to:

$$\frac{1}{\mu_{eff}}\frac{1}{D}\frac{dD}{dt} = C_2\frac{e^{\frac{-Q_d}{RT}}}{T}(\frac{\sigma_{eff}}{\mu_{eff}})^n \tag{12}$$

where $C_2$ is a constant. In order to obtain the value of $n$, assuming that $Q_d$ is the only one constant, Equation (12) can be transformed into logarithmic form as:

$$\ln(\frac{1}{\mu_{eff}}\frac{1}{D}\frac{dD}{dt}) = n\ln(\frac{\sigma_{eff}}{\mu_{eff}}) + C_3 \quad (13)$$

where $C_3$ is a constant for a certain temperature. At last, the $n$ value can be obtained by determining the slope of the relation formed by a plot of $\ln(\frac{1}{\mu_{eff}}\frac{1}{D}\frac{dD}{dt})$ against $\ln(\frac{\sigma_{eff}}{\mu_{eff}})$.

Figure 54 (a) displays the densification curves of the CLS ceramics sintered via FAST at 850 ºC, 900 ºC and 950 ºC. For the samples sintered at lower temperatures (850 ºC and 900 ºC), the density is relatively low when the dwell temperature is reached, and continues to increase to a much higher final density during the dwelling step. In contrast, in the sample sintered at 950 ºC, densification is nearly completed at the beginning of the dwelling step, with only a limited density increase by the end of the dwelling step. Based on the data shown in Figure 54 (a), the logarithmic forms of $(\frac{1}{\mu_{eff}}\frac{1}{D}\frac{dD}{dt})$ and $(\frac{\sigma_{eff}}{\mu_{eff}})$ have been plotted in Figure 54 (b). As can be observed from the results of fitting the relations in this plot to determine $n$ values for samples sintered at different temperatures, $n$ is approximately in the range of 1-2, which suggests that in the 850-950 ºC temperature range, densification is likely controlled by a mixture of mechanisms. Different values of the stress exponent, $n$, correspond to different mechanisms controlling densification. It is known that lattice or grain boundary diffusion is the main mechanism when $n$ is equal to 1, while grain boundary sliding is the main mechanism when $n$ is equal to 2.[19,280] Thus, it is concluded that in this case (in the temperature range of 850-950 ºC), densification is likely controlled by a combination of lattice or grain boundary diffusion, and grain boundary sliding. The two mechanisms occur sequentially during the densification process, so that the slower mechanism controls the densification rate. Since the diameter of the graphite die employed in FAST is fixed, powder compaction occurs predominantly in the direction of the loaded pressure. Thus, it is reasonable to consider that sliding of the grains over one another, namely grain boundary sliding, is necessary to accommodate the diffusion-controlled shape changes that occur during the intermediate and final stages of the field assisted

sintering process.[19] Additionally, further studies on lattice or grain boundary diffusion and grain boundary sliding are required to provide supporting data to directly elucidate the densification mechanism of CLS ceramics in detail.

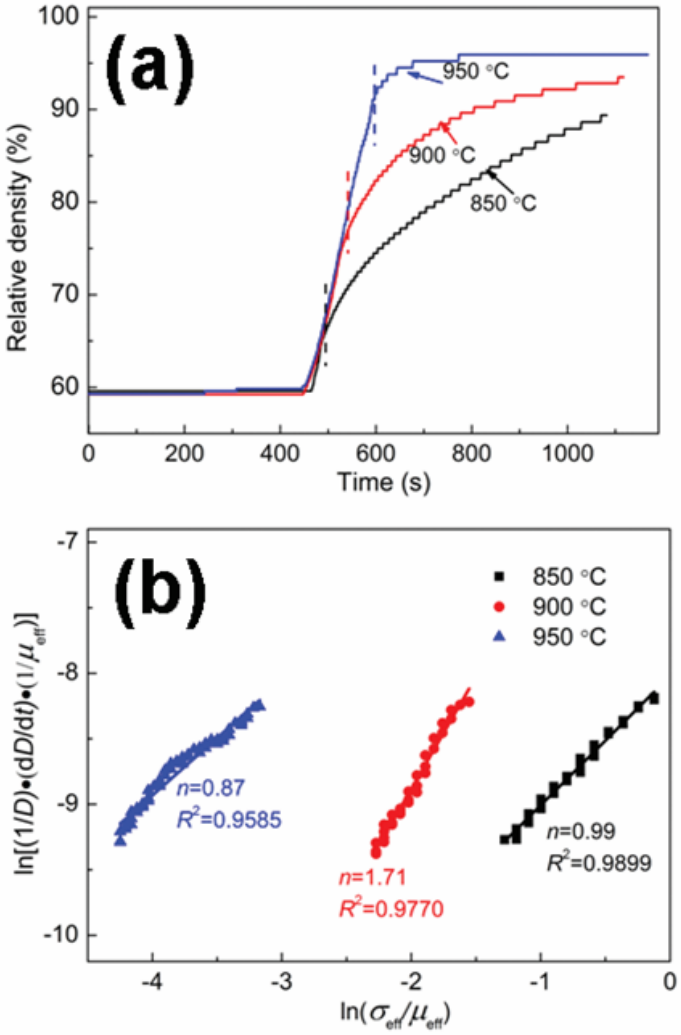


Figure 54. (a) Densification curves as a function of time for the CLS ceramics sintered via FAST at 850 ºC, 900 ºC and 950 ºC for 10 min under a uniaxial pressure of 50 MPa (dashed lines indicate the beginning of the dwelling step). (b) Plot of $\ln(\frac{1}{\mu_{eff}}\frac{1}{D}\frac{dD}{dt})$ as a function of $\ln(\frac{\sigma_{eff}}{\mu_{eff}})$, and $n$ values determined by fitting the slope of the relationship between $\ln(\frac{1}{\mu_{eff}}\frac{1}{D}\frac{dD}{dt})$ and $\ln(\frac{\sigma_{eff}}{\mu_{eff}})$ for each sintering temperature.

As mentioned previously, it is revealed that the CLS ceramics experience apparent grain growth with limited densification over the temperature range of 950-1100 ºC, based on density data and grain size analyses. As such, it is possible to investigate the grain growth kinetics by using the general grain growth equations for different atomistic mechanisms, described as follows:[287]

$$G_t^m - G_0^m = kt \tag{14}$$

$$k = k_0 \exp(-\frac{E_a}{RT}) \tag{15}$$

where $G_t$ and $G_0$ are the grain sizes at time $t$ and $t = 0$, respectively, $m$ is the grain growth exponent, $k_0$ is the pre-exponential constant of the diffusion coefficient, $E_a$ is the activation energy for grain growth, $T$ is the absolute temperature, and R is the gas constant.[288] Here, $G_0$ is taken as the average grain size for the CLS sample sintered at 950 ºC (0.60 μm).

Then, Equation (14) can be further transformed into logarithmic form (Arrhenius plot) as:

$$\ln(\frac{G_t^m - G_0^m}{t}) = -\frac{E_a}{R} \cdot \frac{1}{T} + C_4 \tag{16}$$

where $C_4$ is a constant. Both $m$ and $E_a$ can be obtained by plotting $\ln(\frac{G_t^m - G_0^m}{t})$ against $\frac{1}{T}$. Average grain sizes of the CLS ceramics sintered at 950 ºC, 1000 ºC, 1050 ºC, and 1100 ºC (as shown in Figure 53) are used for plotting to determine the grain growth mechanism. Figure 55 shows the plot of $\ln(\frac{G_t^m - G_0^m}{t})$ as a function of 1000/T for the CLS ceramics sintered at temperatures ranging from 950-1100 ºC. The value of the grain growth exponent $m$ is determined based on the fitting results of straight lines (obtained from the data at different sintering temperatures), by introducing three different integral values of $m$ into the Equation (16). Here, the $m$ value is determined to be 2, as it shows the best fitting to the data. It is acknowledged that different integral values of $m$ correspond to different mechanisms controlling grain growth.[19,287] When $m$ is equal to 2, grain growth is controlled by grain boundary diffusion. When $m$ equals 3, grain growth is controlled by lattice

diffusion. When *m* is equal to 4, surface diffusion is the primary mechanism controlling grain growth. Here, based on the determined *m* value, we conclude that grain boundary diffusion is the mechanism controlling grain growth mechanism associated with field assisted sintering of CLS ceramics, at temperatures between 950 ºC and 1100 ºC.[19] Thus, by calculating the slope of the straight line corresponding to *m*=2, the activation energy of grain growth can be calculated to be 57.97 kJ/mol.

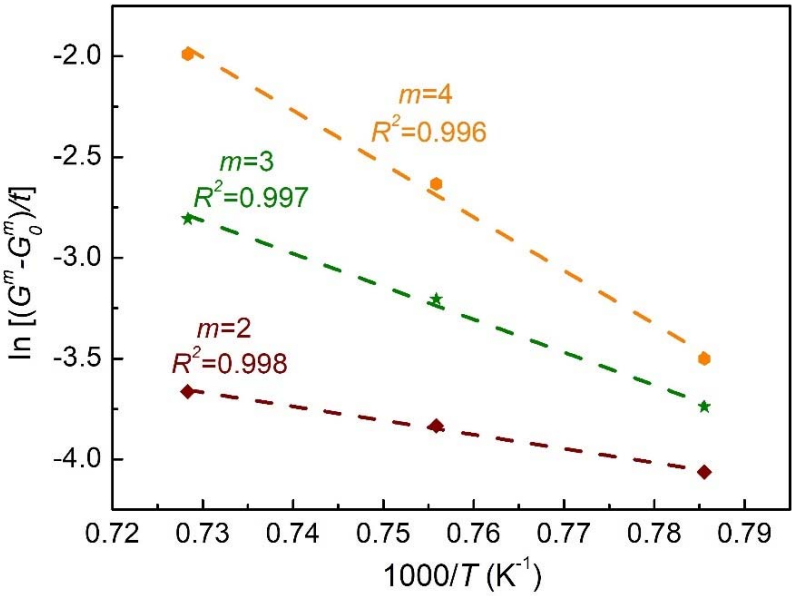


Figure 55. Plot of $\ln(\frac{G_t^m - G_0^m}{t})$ as a function of 1000/T for the CLS ceramics sintered via FAST at 1000 ºC, 1050 ºC and 1100 ºC for 10 min under a uniaxial pressure of 50 MPa.

Meanwhile, CLS ceramics were also consolidated via hot pressing to compare grain growth kinetics with the CLS ceramics sintered via FAST. Samples were hot-pressed at temperatures of 950 ºC, 1050 ºC, 1150 ºC and 1200 ºC under a uniaxial pressure of 50 MPa for 2 h, at a heating rate of 5 ºC/min with uncontrolled cooling to room temperature. In field assisted sintering, it has been reported that the actual temperature of sample within the graphite die is higher than the temperature measured on the exterior wall of the graphite die by optical pyrometer.[289] Thus, we chose samples sintered via hot pressing at temperatures between 950 ºC and 1200 ºC for comparison. It should be noted that the phase

composition analysis reveals that the all hot-pressed CLS ceramics also have the primary phase as the cubic CLS, similar to the results of the samples sintered via FAST. Figure 56 shows SEM images of the thermally etched surfaces of the hot-pressed CLS ceramics. Similar to samples sintered via FAST, the hot-pressed ceramics have some residual pores as well. Figure 57 (a) shows the grain size variation with consolidation temperature. It is interesting to note that the hot-pressed samples have smaller grain sizes at high temperatures, compared with the samples sintered via FAST, which is contrary to the well-acknowledged grain growth inhibition observed with FAST. It is assumed that a high defect concentration is generated within the CLS grains by the rapid heating during the FAST process. As proposed by Besson et al. and Murayama et al., rapid heating will induce an increase in defect concentration, which will enhance the grain growth rate.[290,291] However, a more comprehensive study is required to investigate the reason for the observed increase in grain growth rate during field assisted sintering of CLS ceramics. Figure 57 (b) shows the plot of $\ln(\frac{G_t^m - G_0^m}{t})$ as a function of 1000/T for the CLS ceramics sintered via hot pressing. In this case, average grain sizes of the CLS ceramics are used for plotting to determine the *m* value. $G_0$ is taken as the average grain size for the CLS sample sintered via hot pressing at 950 ºC (0.48 μm). Similarly, the *m* value is also determined to be 2, which suggests that in this sintering temperature range of hot pressing, grain growth is controlled by grain boundary diffusion, the same as in the field assisted sintering process at 950-1100 ºC. Thus, the activation energy of grain growth can be calculated to be 150.22 kJ/mol, which is much larger than that of the samples sintered via FAST, indicating that the grain growth is more difficult to be activated in the hot-pressed CLS ceramics.

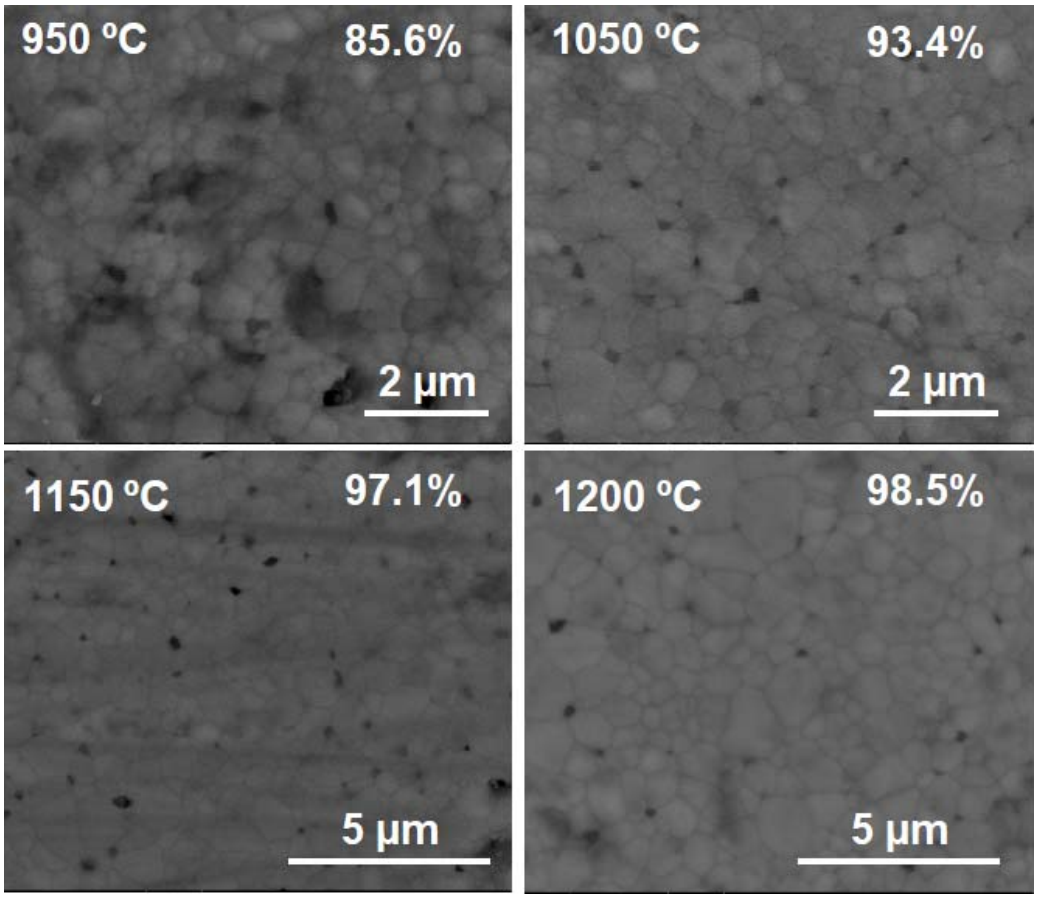


Figure 56. SEM images of the thermally etched surfaces and relative densities (shown in the inset) of the CLS ceramics sintered via hot pressing at different temperatures (950 ºC, 1050 ºC, 1150 ºC and 1200 ºC) under a uniaxial pressure of 50 MPa for 2 h.

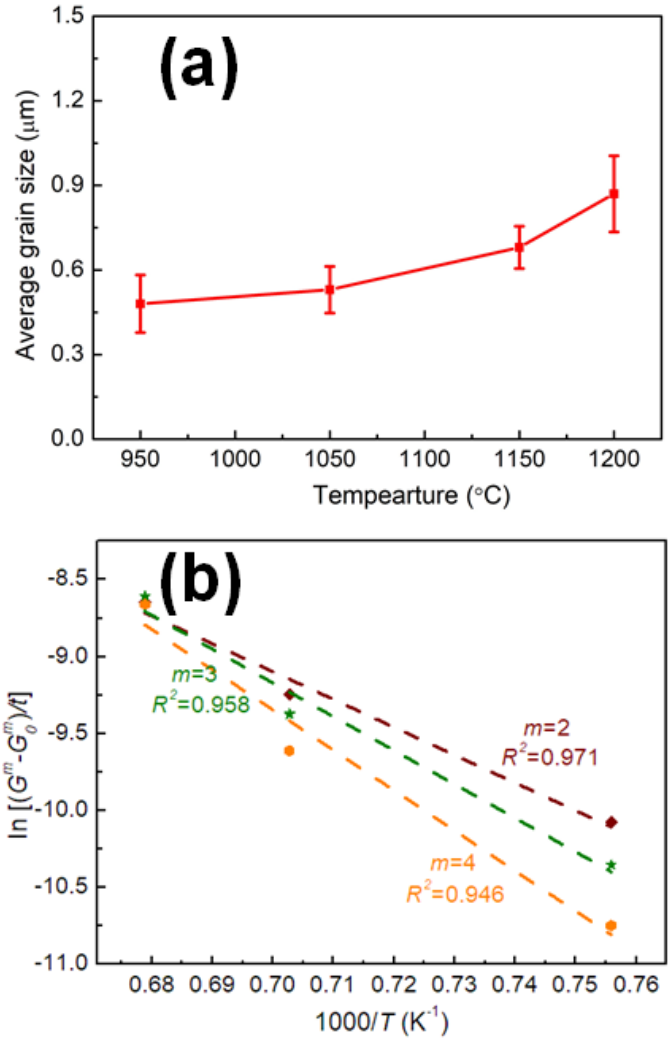


Figure 57. (a) Temperature dependence of the average grain size of the CLS ceramics sintered via hot pressing under a uniaxial pressure of 50 MPa for 2 h. (b) Plot of $\ln(\frac{G_t^m - G_0^m}{t})$ as a function of 1000/T for the CLS ceramics sintered via hot pressing at 1050 ºC, 1150 ºC and 1200 ºC under a uniaxial pressure of 50 MPa for 2 h.

Further investigation of the infrared optical transmittance of the CLS ceramics sintered via FAST was performed by FTIR measurements and analysis. It is important to note that the samples sintered at 1050 ºC and 1100 ºC exhibit dark black appearances, which is attributed to a sulfur deficiency induced by high sintering temperatures. Thus, no transmittance measurements are shown for these samples. In addition, the sample sintered at 850 ºC also exhibits very low infrared transmittance due to insufficient densification.

Figure 58 displays the infrared optical transmittance spectra of the polished CLS ceramics sintered at 900 ºC, 950 ºC and 1000 ºC. It is observed that the CLS sample sintered at 1000 ºC has the best optical performance, with a maximum transmittance of 48.1% at 9.2 μm, which is ascribed to higher densification and lower porosity than the other two samples, as shown in Figure 52. Based on a comparison of spectra from sample measurement and measurement of the ambient atmosphere, it is determined that the absorption peaks in the 3.2-4.2 μm range are due to atmospheric absorptions, with the absorption band at 3.2 μm attributed to water, and the peak at 4.2 μm due to $CO_2$.[133] The absorption peaks at 6.7 μm and 7.1 μm correspond to the C=O stretching modes in residual carbonates.[188,292] The minor absorption bands at 9.0 μm and 15.9 μm are assigned to $v_3$ and $v_4$ vibrational modes of molecular $SO_4$ complex species, respectively,[153,188] which originate from oxygen traces stabilizing the β-$La_2S_3$ ($La_{10}S_{14}O$).[188] The absorption bands at 10.8 μm and 18.4 μm are attributed to vibrational modes of the molecular $SO_3$ complex species. Specifically, the broad peak at 10.8 μm is due to the $v_3$ mode, and the 18.4 μm peak is ascribed to the $v_4$ vibrational mode of $SO_3$ species.[153] The presence of oxygen-containing species is assumed to be due to oxygen adsorbed onto the surface of the raw CLS powder prior to sintering, or the residual oxygen in chamber during the sintering process. In addition, small fractions of oxygen-containing impurities within the original commercial powders, which can not be detected by XRD due to the detection limit, may also contribute to the absorptions in the transmittance spectra. It is important to note that the three measured CLS ceramics exhibit brown appearances, which could be attributed to the carbon contamination from graphite during sintering.[133,293] It is also noted that the CLS ceramics sintered via hot pressing have the similar infrared optical transmittance (a maximum transmittance of 48.0% at 9.2 μm for the sample sintered at 1200 ℃) relative to samples sintered via FAST. The relatively inferior transmittance and apparent absorptions of the processed CLS ceramics significantly limit their applications in infrared windows and domes. Further studies on the densification enhancement and removal of impurities are necessary to improve the infrared optical properties of the CLS ceramics.

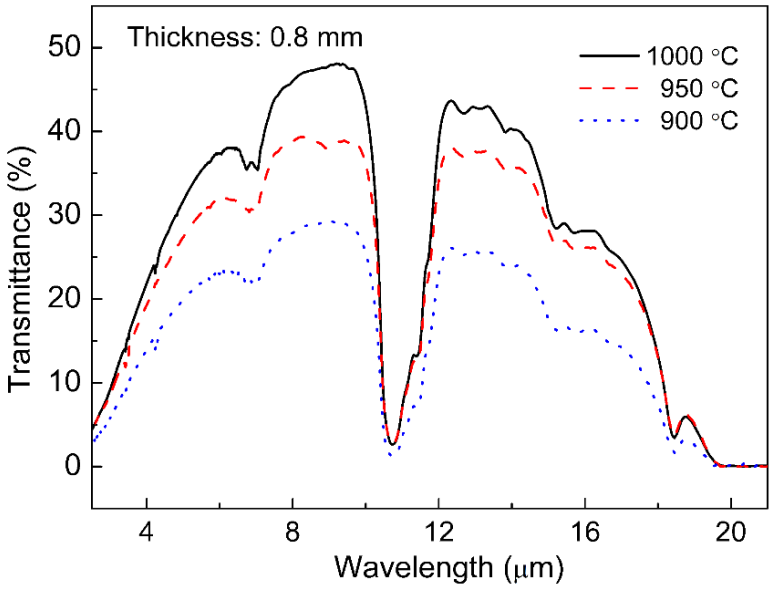


Figure 58. Infrared optical transmittance spectra of the polished CLS ceramics (thickness: 0.8 mm) sintered at 900 ºC, 950 ºC and 1000 ºC via FAST, under a uniaxial pressure of 50 MPa for 10 min.

The Vickers hardnesses of the CLS ceramics sintered via FAST are shown in Table IV. Vickers hardness ($H_v$) was calculated using Equation (17):

$$H_v = \frac{1.8544F}{d^2} \tag{17}$$

where $F$ is the indentation load and $d$ is the measured mean diagonal of the indentation. It is revealed that hardness increases with increasing sintering temperature from 850 ºC to 1050 ºC, due to the enhancement of densification,[294,295] as shown in Figure 52. However, as the sintering temperature reaches 1100 ºC, the hardness decreases sharply. It is assumed that dislocations are reduced due to a decrease in net grain boundary volume associated with the rapid increase of grain size within the CLS ceramics, which in turn leads to a reduction in hardness.[296]

Table IV. Vickers Hardness Data for the CLS Ceramics Sintered via FAST at 850-1100 ºC for 10 min under a Uniaxial Pressure of 50 MPa.

| CLS Samples | Vickers hardness (kgf/mm$^2$) |
|---|---|
| 850 ºC | 448.7 ± 44.7 |
| 900 ºC | 466.3 ± 80.4 |
| 950 ºC | 493.0 ± 61.3 |
| 1000 ºC | 535.3 ± 26.2 |
| 1050 ºC | 579.0 ± 30.0 |
| 1100 ºC | 480.3 ± 55.0 |

## D. Conclusions

In summary, CLS ceramics with submicron-sized and micron-sized grains were consolidated via FAST at 850-1100 ºC and hot pressing at 950-1200 ºC. Through phase identification, all the consolidated CLS ceramics were confirmed to have the cubic thorium phosphate-structured phase of CLS as the primary phase. Through microstructural and sintering analyses based on previously established model, it was revealed that in the temperature range of 850-950 ºC, the densification of the CLS ceramics sintered via FAST was controlled by a combination of lattice or grain boundary diffusion, and grain boundary sliding, with grain boundary diffusion determined to be the main mechanism controlling the grain growth between 950 ºC and 1100 ºC during FAST. The grain growth was determined to be controlled by grain boundary diffusion, with the activation energy calculated to be 57.97 kJ/mol and 150.22 kJ/mol, for samples sintered via FAST and hot pressing, respectively. The CLS ceramic sintered via FAST at 1000 ºC exhibited the highest infrared transmittance of all measured samples, of 48.1% at 9.2 μm, which might be further improved through further densification and impurity removal. It was also shown that the hardness of the CLS ceramics first increased with increasing sintering temperature, and then decreased due to densification and grain growth, respectively.

# VI. PRESSURE-ASSISTED CONSOLIDATION OF ZnS-$CaLa_2S_4$ COMPOSITE CERAMICS

## A. Introduction

As an extensively researched binary sulfide semiconductor with a wide band gap, ZnS has been widely applied, and is one of the most commonly used materials for infrared-imaging systems (IR windows) in the wavelength range of 8-12 μm.[1,97] As discussed previously, despite their wide application in many fields, due to their intrinsically weak chemical bonds and poor mechanical properties, ZnS infrared optical ceramics have low durability and resistance to erosion caused by rain and sand exposure, which limits their application as infrared windows and domes in harsh environments.[156] It is known that composite ceramics have the potential to provide mechanical properties over those of singe-phase materials through different hardening or strengthen mechanisms. Recently, 50vol% MgO-50vol% $Y_2O_3$ nanocomposite ceramics, sintered via various pressure-assisted sintering routes using different types of lab-processed powders, have been demonstrated to have superior mechanical properties than the two individual materials at no expense of the infrared optical performance.[192-195,199]

Extensive attempts have been made to enhance the mechanical strength of ZnS infrared optical ceramics by introducing a second phase with a similar refractive index and better mechanical properties, to form composite materials. R. Raj et al. proposed that the mechanical strength of ZnS could be improved through dispersion strengthening by embedding diamond particles into ZnS ceramics via hot pressing.[205-207] In that case, a combined shear mixing and freeze milling approach were found to be beneficial to achieving an effective diamond dispersion and to preserving favorable optical properties.[204] B. Dunn et al. investigated the equilibrium phase diagrams of ZnS-$Ga_2S_3$ and ZnS-CdS, and then further developed hot-pressed ZnS-$Ga_2S_3$ (8-16 vol% of $Ga_2S_3$) composites with considerably higher fracture toughness and hardness than pure ZnS, through solid-solution strengthening.[201-203] M. Akinc's group applied different synthesis routes, including flash pyrolysis and chemical vapor transport, to prepare ZnS-GaP nanocomposites, and succeeded in fabricating ZnS-GaP composite ceramics with enhanced mechanical properties through a combined cold isostatic pressing and HIPing approach.[210-

[212] In addition, through uniform mixing of ZnS with CLS, J. Wahl et al. from Raytheon Company managed to obtain layered ZnS-CLS nanocomposites by pressureless sintering, followed by HIPing.[213] They also employed magnetron radio frequency sputtering to generate nanocomposite coatings of ZnS-$Y_2S_3$ with improved hardness, for long-wave infrared optical window and coating applications.[213] In addition to ZnS-based optical materials,

With similar properties to ZnS, the refractory ternary sulfide CLS is also a desirable candidate for infrared optical windows and domes. In comparison with ZnS, CLS has superior mechanical strength, higher resistance to rain erosion, and a longer infrared transmittance cut-off wavelength. CLS has been developed as an infrared window material since the 1980s, as a promising material for applications in harsh environments.[54,156] Traditionally, ZnS and CLS infrared optical ceramics are consolidated by pressure-assisted sintering techniques.[107,108,126,127,133,137,138,141,142,156,188]

In this chapter, a study was performed to investigate the sintering, phase transition, and mechanical hardness behaviors of ZnS-CLS ceramics processed via field assisted sintering technique (FAST). Lab-processed homogeneous ZnS nanopowders were mixed with commercial CLS powders via high-energy ball milling. The mixed ZnS-CLS powders were subsequently consolidated by using FAST at different temperatures. Through microstructural observations and sintering curve measurements, the sintering behavior of the composite ceramics was investigated and discussed. The sphalerite-wurtzite phase transition of the ZnS component of the ceramics was also studied by phase composition analysis. Furthermore, the mechanical properties of the ZnS-CLS ceramics were correlated with densification behavior and microstructural properties.

## B. Experimental Procedures

ZnS powders were synthesized utilizing a facile colloidal processing route via precipitation in a hot-cold water bath under acidic conditions, using zinc nitrate hexahydrate (≥99.0%, Sigma Aldrich) as the zinc source, and thioacetamide (TAA, Sigma Aldrich, ≥99.0%) as the sulfur source, as reported in our previous research.[137] The as-synthesized ZnS powders were subsequently heat treated at 900 ºC for 4h in flowing argon in a tube furnace to remove impurities. Subsequently, commercial CLS powders (99.9%

(REO), Alfa Aesar) were mixed with the processed ZnS powders in ethanol, in a volume ratio of 50%:50% (0.5ZnS-0.5CLS) via high-energy planetary ball milling (Pulverisette 7, Fritsch, Germany), at a speed of 500 rpm for 1 h, with a ball: powder weight ratio of 5:1. The milling balls and jars were made of tungsten carbide. The ball-milled powders were then dried and loaded into a graphite die (I-85, Electrodes, Inc.) with a diameter of 18.75 mm, with graphite foils (thickness of 0.13 mm, Alfa Aesar) placed on the top and bottom of the sample to separate it from the graphite punches. An optical pyrometer was employed to measure the temperature on the outside wall of the graphite die. The powders were consolidated at 800 ºC, 850 ºC, 900 ºC, 950 ºC, 1000 ºC, and 1050 ºC for 20 min under a uniaxial pressure of 100 MPa, at a heating rate of 50 ºC/min, in a vacuum of $10^{-2}$ torr, under a direct current field generated by a FAST apparatus (HP D 25, FCT Systeme GmbH, Germany). An initial uniaxial pressure of 10 MPa was employed, and the loading pressure was increased to 100 MPa at 450 ºC and was maintained during the heating and dwelling processes. After dwelling at temperatures for 20 min, the samples were allowed to cool at an uncontrolled rate to room temperature and the pressure was released, by immediately shutting down the power supply. Alternatively, the 0.5ZnS-0.5CLS powders were also consolidated via vacuum hot pressing at 1000 ºC, 1100 ºC, 1200 ºC, and 1300 ºC for 2 h under a uniaxial pressure of 100 MPa, at a heating rate of 5 ºC/min.

The ZnS-CLS powders and ceramics were measured with XRD (D2 PHASER, Bruker) equipped with a CuKα radiation, operated at a current of 10 mA and voltage of 30 kV, in order to characterize phase composition. Phase identification analyses were performed using MDI Jade 9, integrated with the ICDD database. Diffraction peaks within the measured XRD patterns of the powders were fit using the Pseudo-Voigt function method in Topas profile and pattern analysis software (Bruker), in order to obtain the values of full width at half maximum (FWHM). The National Institute of Standards and Technology (NIST) standard reference material SRM660a $LaB_6$ was used to calibrate the instrumental broadening. Rietveld refinement was also performed in Topas to quantitatively determine the phase composition of the sintered ceramics. The microstructure and morphology of the composite powders and ceramics were observed by SEM (Quanta 200, FEI) at an acceleration voltage of 20 kV. The surfaces of the CLS ceramics were observed after the ceramics were polished and thermally etched in an

atmosphere of $CS_2$/Ar for 1 hour, in order to expose grains and grain boundaries. Grain size analyses were performed using NanoMeasurer 2.0 software, on over 300 grains per sample. TEM (2100F, JEOL) was also utilized at an acceleration voltage of 200 kV to investigate the ZnS phase transition in the composite ceramics. During the field assisted sintering process, the variation in piston displacement and speed were recorded as a function of time and temperature by the FAST instrumentation. The variation data were then calibrated by subtracting the dimension change associated with the instrument. Archimedes's method was adopted to measure the densities of the sintered 0.5ZnS-0.5CLS ceramics. The theoretical density of the composite ceramics was calculated based on the phase composition of the materials. Vickers hardness measurements were performed on a micro-hardness test apparatus (HMV-200, Shimadzu) with an applied load of 0.05 kgf and loading time of 10 s.

## C. Results and Discussion

Figure 59 shows SEM micrographs of the as-synthesized ZnS powders, commercial CLS powders, heat-treated ZnS powders, and ball-milled 0.5ZnS-0.5CLS composite powders employed in this study. It can be observed that the ZnS powders prepared by the colloidal processing route exhibits homogeneously-arranged submicron-scale (100-200 nm) particles with spherical morphology and narrow particle size distribution. The use of hot and cold water baths during the ZnS synthesis process is of significant importance to achieve better control over particle growth. In contrast, the commercial CLS powders are observed to be composed of inhomogeneous submicron-scale and micron-scale agglomerates of CLS particles. Through the heat treatment, the ZnS powders have pronounced particle growth, accompanied by some micron-scale agglomerations. Additionally, detailed observations reveal that necking occurred between the adjacent ZnS particles, indicative of beginning of sintering at relatively high temperature. The ball-milled composite 0.5ZnS-0.5CLS powders show fine nano-scale and submicron-scale particles, as shown in Figure 59 (d), which demonstrates that high-energy ball milling can effectively break up the agglomerates into individual fine particles, and mix the ZnS and CLS powders.

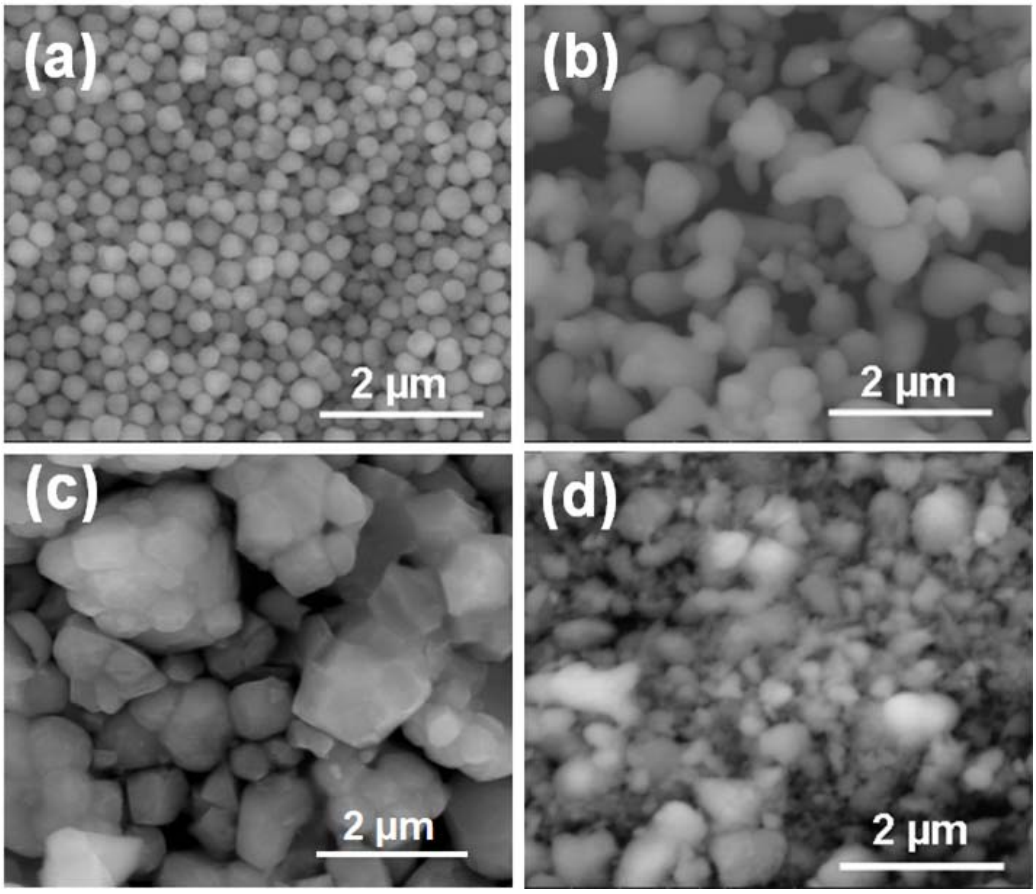


Figure 59. SEM images of the as-synthesized ZnS powders (a), commercial CLS powders (b), heat-treated ZnS powders (c), and ball-milled 0.5ZnS-0.5CLS powders (d).

The XRD patterns of the as-synthesized ZnS powders, commercial CLS powders, calcined ZnS powders, and ball milled 0.5ZnS-0.5CLS powders are displayed in Figure 60. The as-synthesized ZnS powders and commercial CLS powders are both determined to be single-phase, with phases that can be indexed to the cubic ZnS sphalerite phase (ICDD card no. 04-001-6857, $F\bar{4}3m$, a=5.40 Å) and the cubic thorium phosphate-structured phase of CLS (ICDD card no. 04-002-2117, $I\bar{4}3d$, a=8.68 Å), respectively. It is noted that peak broadening is strongly apparent in the XRD pattern of the synthesized ZnS powders, due to the small crystallite size of the powder. Peak broadening occurs as crystallite size decreases, according to the Scherrer Equation (Equation (1)). Through fitting primary peaks in the XRD patterns of the sample and standard material, the average crystallite size of the synthesized ZnS powders is calculated to be 17.3 ± 4.4 nm using the Scherrer

equation. It is interesting to note that the crystallite size is much smaller than the particle size observed via SEM. It is therefore concluded that the ZnS particles are actually composed of small nanocrystallites. Compared with the synthesized ZnS powders, the XRD pattern of the commercial CLS powders has much narrower peaks, resulting from the larger size of CLS crystallites that compose the agglomerates observed via SEM. XRD analysis also reveals that the heat treated ZnS powders consist of two phases. Besides the cubic ZnS phase as the primary phase, a small amount of the hexagonal ZnS wurtzite phase (ICDD card no. 04-008-7254, $P6_3mc$, a=3.82 Å, c=6.26 Å) is also present in the ZnS powders. This is likely due to an early phase transition from sphalerite ZnS to wurtzite ZnS, induced by heat treatment of the as-synthesized ZnS powders at 900 ºC in argon. The reduced particle size and correspondingly larger surface energy of small ZnS particles as compared with bulk ZnS leads to a reduction of the phase transition temperature, which is reported to be 1020 ºC for bulk ZnS.[124] Additionally, it is identified that the composite powders blended and milled by high energy ball milling are composed of three phases, sphalerite ZnS, wurtzite ZnS and thorium phosphate-structured CLS. It is noted that the CLS peaks in the XRD pattern of the composite powders have a larger FWHM than the peaks of the commercial CLS powders, due to the smaller particle and crystallite size generated by high energy ball milling.

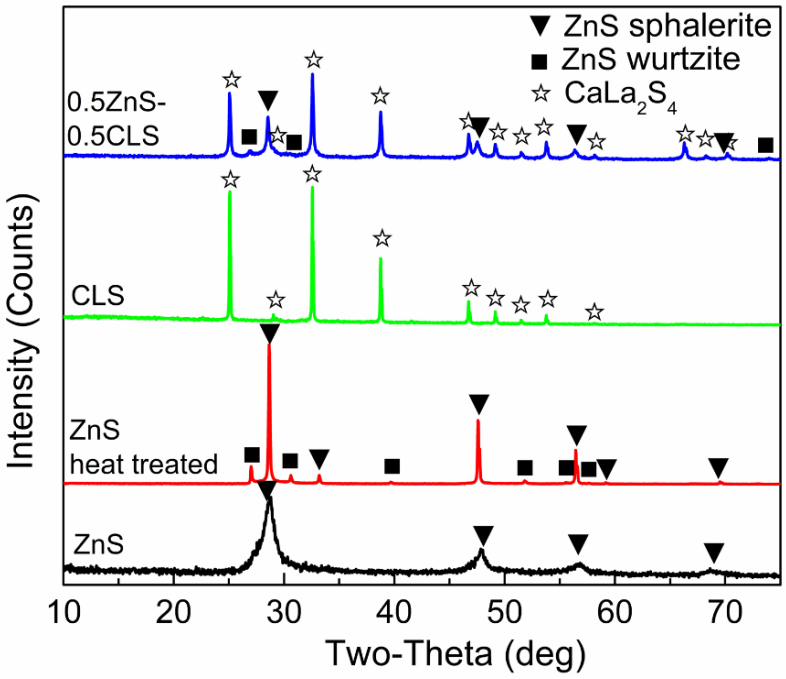


Figure 60. XRD patterns of the as-synthesized ZnS powders, heat treated ZnS powders, commercial CLS powders, and ball milled 0.5ZnS-0.5CLS powders.

Figure 61 depicts the microstructural evolution of the 0.5ZnS-0.5CLS ceramics, based on SEM images of the thermally etched microstructures of the composite ceramics sintered via FAST at 800-1050 ºC, under a uniaxial pressure of 100 MPa for 20 min. As is apparently indicated in the BSE images, two different phases are present, with a relatively homogeneous distribution throughout the ceramics. Based on the atomic number difference of the two phases, the darker phase corresponds to ZnS and the brighter phase to CLS, which is further demonstrated by EDS analysis. As can be observed from the SE images, the grains are connected to a grain boundary network. Table V shows the relative densities of the sintered 0.5ZnS-0.5CLS ceramics. According to the rule of mixtures, the relative density can be obtained by using the following equation:

$$\rho_r = \rho_m / \rho_t = \rho_m / (\sum \rho_i V_i) \qquad (18)$$

where $\rho_r$ is the relative density, $\rho_m$ is the measured density, $\rho_t$ is the theoretical density, $\rho_i$ is the theoretical density of individual phase (4.10 g/cm$^3$ for sphalerite ZnS, 3.98 g/cm$^3$ for wurtzite ZnS, and 4.53 g/cm$^3$ for thorium phosphate-structured CLS), and $V_i$ is the volume

fraction of each phase within the composite ceramics, which is obtained from the quantitative phase composition analysis (Table VI). All the samples exhibit relative densities higher than 90%, which is reflected in the well-densified microstructures observed via SEM. It is revealed that, over the sintering temperature range of 800-1000 ºC, the density of the composite ceramics increases with increasing sintering temperature. For samples sintered at lower temperatures of 800 ºC and 850 ºC, a few residual pores can still be detected within the ceramics. However, as sintering temperature increases, the composite ceramics become more consolidated and less apparent residual porosity can be detected. Overall, FAST is demonstrated to be an effective and rapid method to consolidate ZnS-CLS composite ceramics. In addition, it is observed that the ZnS and CLS grains within the 0.5ZnS-0.5CLS ceramics both experience apparent grain growth over the sintering temperature range of 800-1000 ºC. However, as the sintering temperature increases to 1050 ºC, the sample experiences an abrupt decrease in relative density and grains experience exaggerated grain growth, with some pores reappearing at the grain boundaries. This phenomenon is likely attributed to overheating, which results in chemical decomposition of the ceramic.

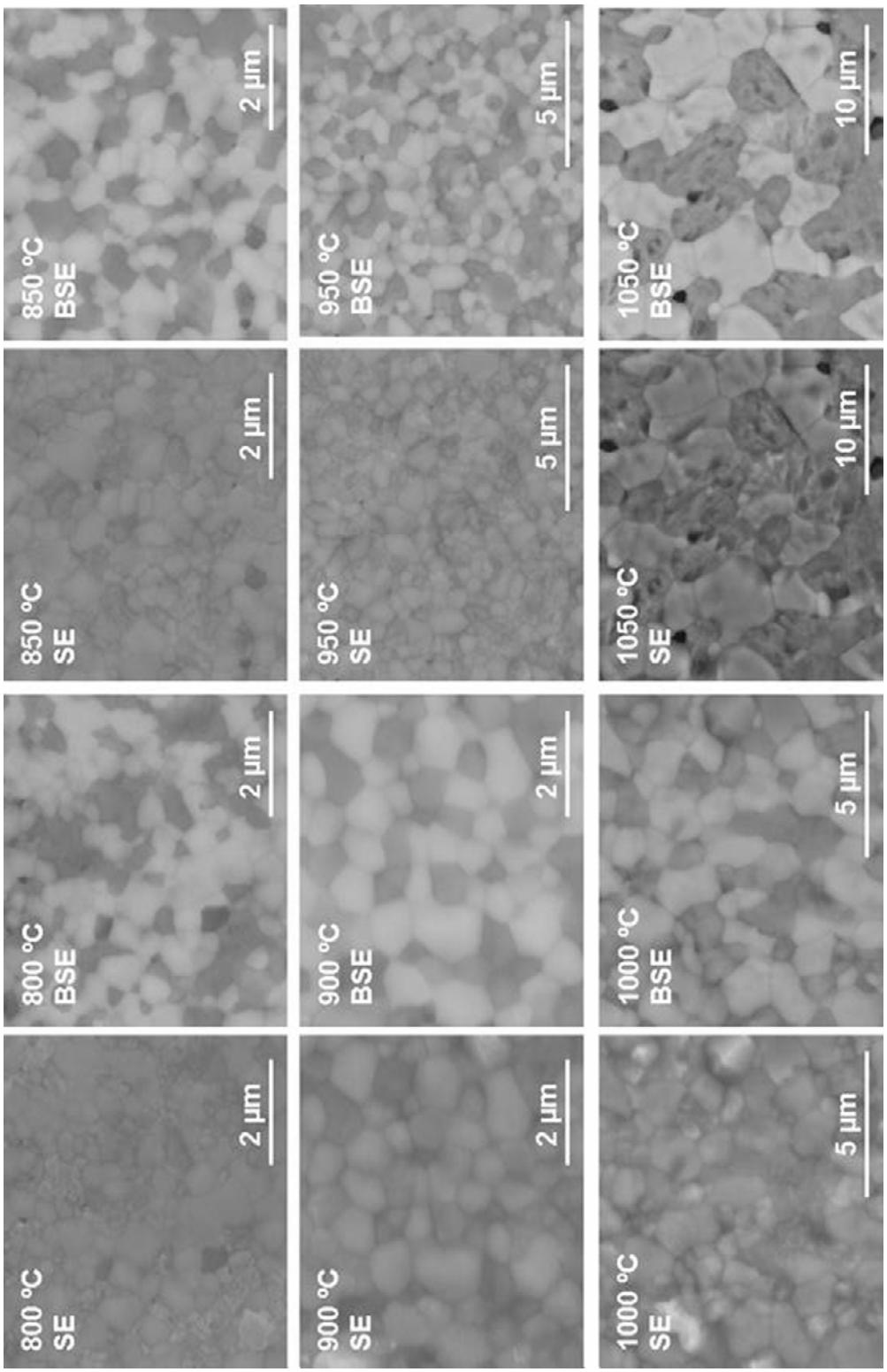


Figure 61. SEM images (secondary electron (SE) image and back scattering electron (BSE) image) of the thermally etched surfaces of the 0.5ZnS-0.5CLS ceramics sintered via FAST at 800 ºC, 850 ºC, 900 ºC, 950 ºC, 1000 ºC and 1050 ºC, under a uniaxial pressure of 100 MPa for 20 min.

Table V. Relative Densities of the 0.5ZnS-0.5CLS Ceramics Sintered via FAST at Different Temperatures.

| Sample | Relative density (%) |
|---|---|
| 800 ºC | 94.2 |
| 850 ºC | 95.7 |
| 900 ºC | 98.5 |
| 950 ºC | 99.1 |
| 1000 ºC | 99.4 |
| 1050 ºC | 92.5 |

To further investigate the observed sintering behavior, the temperature dependence of piston distance and speed during sintering is analyzed. Figure 62 shows a plot of actual piston distance and speed, measured during the field-assisted sintering of the ZnS-CLS composite ceramics at 1050 ºC under a uniaxial pressure of 100 MPa for 20 min. The variation of piston displacement reflects sample shrinkage and sample shrinkage rate during the pressure-assisted sintering process, parameters that are directly related to relative density and densification rate.[297] As shown in Figure 62, the sample experiences limited shrinkage below 700 ºC, where the initial stage of sintering occurs. Pronounced shrinkage and densification then occur during the intermediate sintering stage in the temperature range of 700 ºC to 855 ºC, reflected by a rapid increase in piston distance, with the highest piston speed occurring at approximately 785 ºC. As temperature increases above 855 ºC, shrinkage gradually decreases, with a small increase in density corresponding to the final removal of isolated porosity during the final stage of sintering. It is important to note that there is another abrupt increase in the piston distance and speed when the temperature increases above 1040 ºC. This is attributed to weight loss caused by chemical decomposition of the composite ceramic due to overheating, as previously discussed in the microstructural observation.

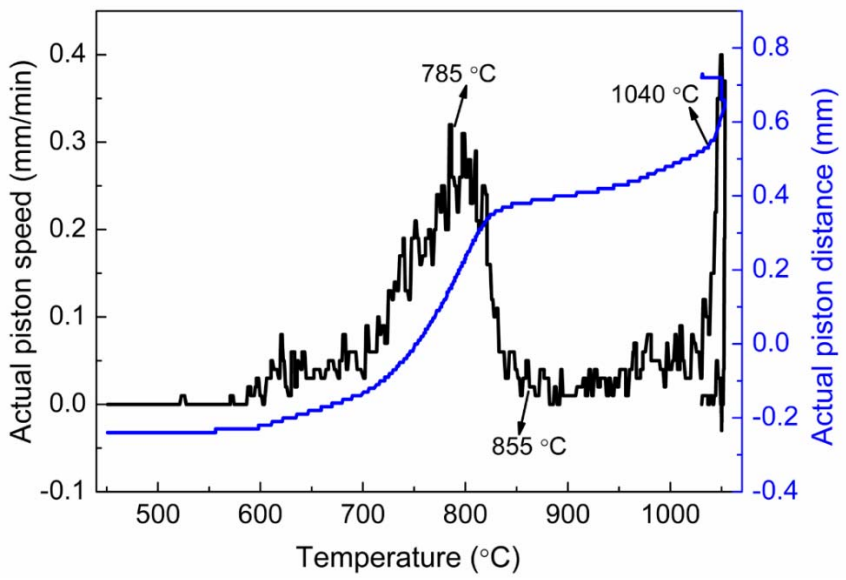


Figure 62. Temperature dependence of actual piston distance and speed, measured during the field-assisted sintering of the 0.5ZnS-0.5CLS composite ceramics at 1050 ºC, under a uniaxial pressure of 100 MPa for 20 min.

Detailed grain size analysis has been performed to investigate the grain growth of the 0.5ZnS-0.5CLS ceramics sintered in the temperature range of 800-1050 ºC. Figure 63 shows the grain size distributions of ZnS and CLS grains within the 0.5ZnS-0.5CLS ceramics sintered via FAST. It can be seen that the grains of both phases coarsen and grow simultaneously from submicron-scale to micron-scale with increasing sintering temperature. In addition, the ZnS grains are generally observed to be smaller than the CLS grains, except those that experience abrupt grain growth within the ceramic sintered at 1050 ºC. As such, it is possible to investigate the grain growth kinetics of the ZnS and CLS phases individually, by using the general equations (Equations (14-16)) for normal grain growth for different atomistic mechanisms. In this case, $G_0$ is taken as the grain sizes for the ZnS and CLS grains within the 0.5ZnS-0.5CLS sample sintered at 800 ºC (0.33 μm for ZnS and 0.44 μm for CLS). Then, both $m$ and $E_a$ can be obtained by plotting $\ln(\frac{G_t^m - G_0^m}{t})$ against $\frac{1}{T}$ and subsequent fitting the slope of the curve. Due to the fact that the sample sintered at 1050 ºC partially decomposes due to overheating, only grain growth in the sintering temperature range of 800 ºC to 1000 ºC is considered. Here, average grain sizes

of ZnS and CLS grains within the 0.5ZnS-0.5CLS ceramics (as shown in Figure 63) are used for plotting to determine the grain growth mechanism. Figure 64 shows the plot of $\ln(\frac{G_t^m - G_0^m}{t})$ as a function of 1000/T for both the ZnS and CLS grains within the composite ceramics sintered at temperatures ranging from 800-1000 ºC. The value of the grain growth exponent *m* is determined based on the fitting results of straight lines (obtained from the data at different sintering temperatures), by introducing three different integral values of *m* into the Equation (16). For both ZnS and CLS, the *m* values are determined to be 4, as they show the best fittings to the data. Different integral values of *m* correspond to different mechanisms controlling grain growth, and it should be emphasized that the situation for a two-phase system is different from that for a pure-phase system.[19] When the grain growth exponent *m* equals 2, grain growth is primarily interface-controlled. When the grain growth exponent *m* is equal to 3, grain growth is primarily controlled by bulk (lattice) diffusion. When *m* equals 4, it is grain boundary diffusion that controls grain growth.[298] Here, based on the fit *m* values, we conclude that for field-assisted sintering of 0.5ZnS-0.5CLS ceramics between 800 and 1000 ºC, grain boundary diffusion is the main mechanism controlling grain growth for both the ZnS and CLS phases within the composite ceramics. By calculating the slope of the straight line corresponding to *m*=4, the activation energy for grain growth of ZnS and CLS grains can be calculated to be 200.43 kJ/mol and 242.62 kJ/mol, respectively.

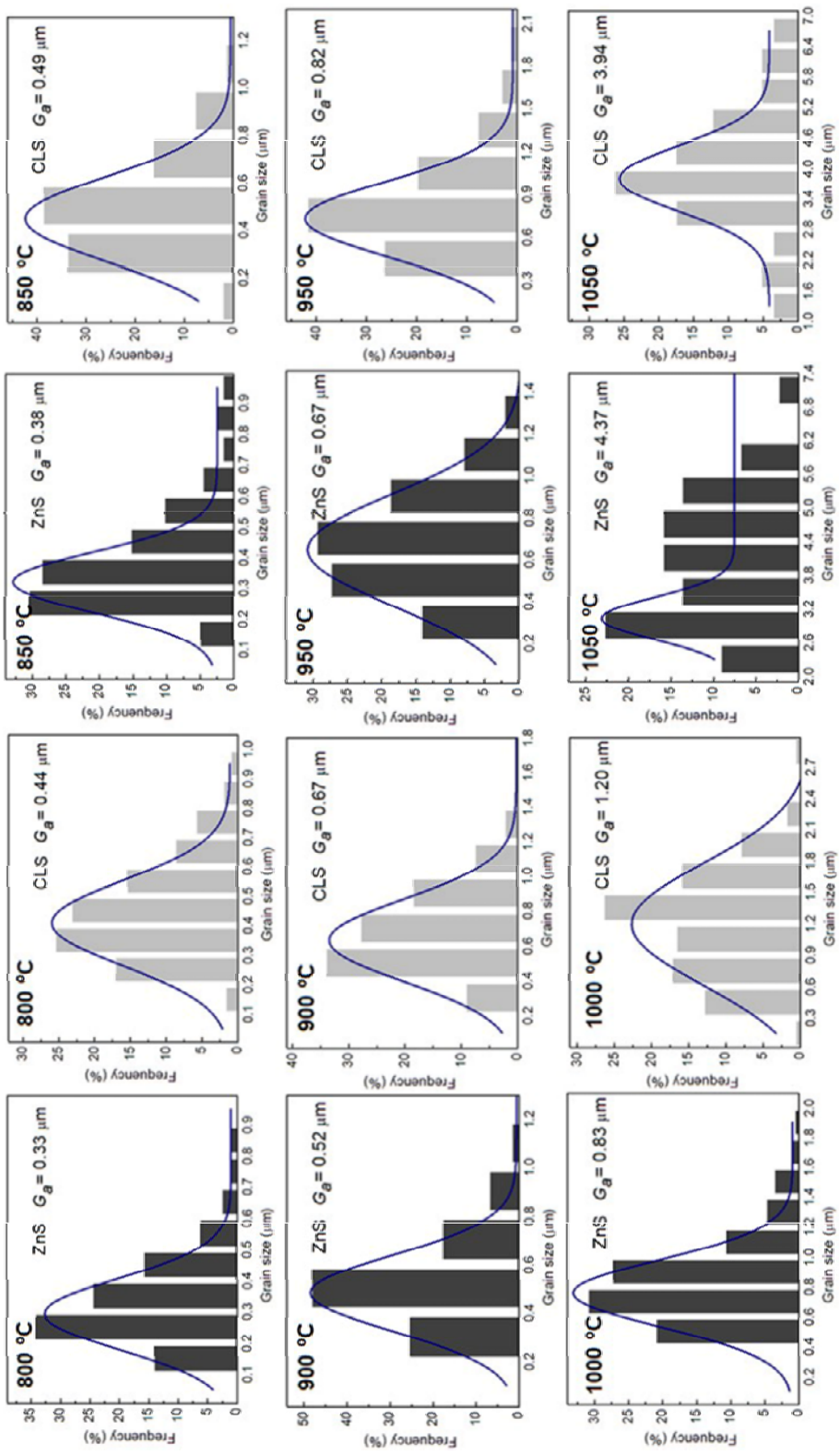


Figure 63. Grain size distributions of the ZnS and CLS grains within 0.5ZnS-0.5CLS ceramics sintered via FAST at different temperatures under a uniaxial pressure of 100 MPa for 20 min.

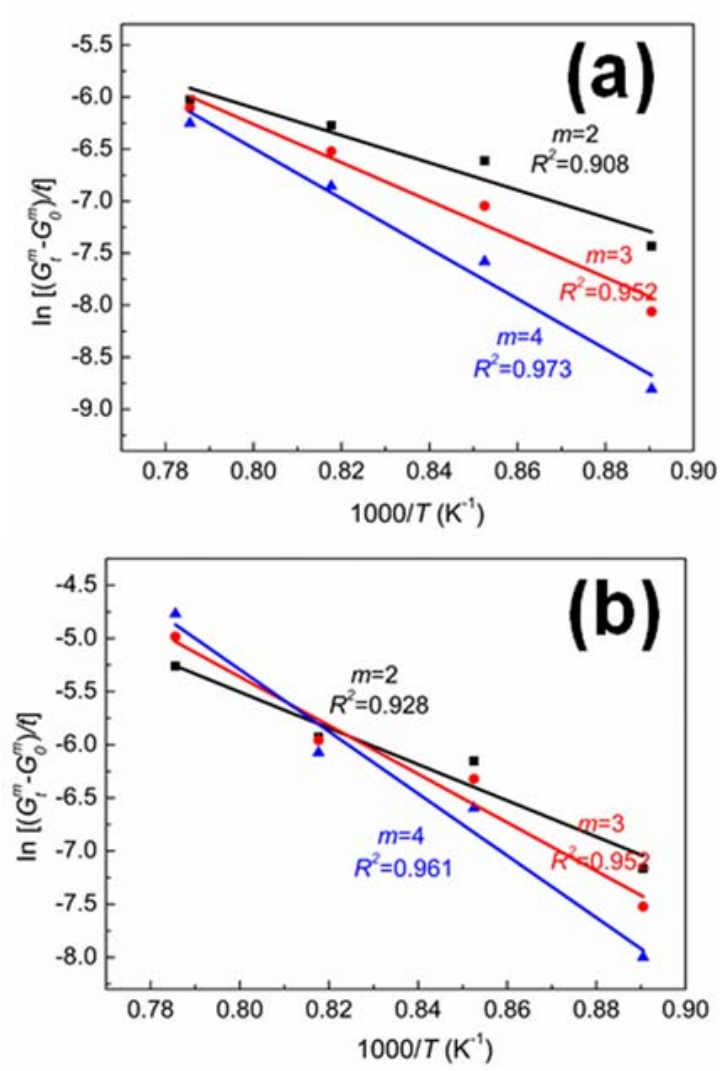


Figure 64. Plots of $\ln(\frac{G_t^m - G_0^m}{t})$ as a function of 1000/T for the ZnS (a) and CLS (b) grains within 0.5ZnS-0.5CLS ceramics sintered via FAST at 850 ºC, 900 ºC, 950 ºC and 1000 ºC for 20 min under a uniaxial pressure of 100 MPa.

Figure 65 shows the XRD patterns of the consolidated 0.5ZnS-0.5CLS ceramics sintered at 800-1050 ºC via FAST. It can be observed that peak broadening disappears after the ceramics are sintered, as particles grow and coarsen to larger grains during consolidation, resulting in much narrower peaks. Phase composition analysis reveals that all the samples are composed of three phases: sphalerite ZnS, wurtzite ZnS, and thorium phosphate-structured CLS. Table VI lists the quantitative phase composition (in vol%) of the 0.5ZnS-0.5CLS ceramics. As the sintering temperature increases, the peak intensity

corresponding to wurtzite ZnS increases, indicative of the formation of more wurtzite, which is also reflected in the quantitative phase composition analysis. Compared with the variation in the contents of the two different phases of ZnS, the cubic CLS phase remains stable with varying sintering temperature. It is acknowledged that, in bulk form at ambient pressure, ZnS experiences a phase transition from the low-temperature cubic sphalerite phase to the hexagonal wurtzite phase at 1020 ºC.[124] Here, the XRD results suggest a phase transition occurring earlier in the sintering process, at lower temperature, which is attributed to the small particle size of the ZnS powder, compared with that of bulk ZnS. The XRD results also demonstrate that increasing sintering temperature facilitates the phase transition from sphalerite to wurtzite. It has been reported that the activation energy for the sphalerite to wurtzite phase transition is dependent on particle size, and that wurtzite's stability can be increased by decreasing particle size, which lowers the effective transition temperature of the ZnS.[98,100-102] The kinetic mechanism by which the phase transition occurs during the sintering of powders with small particle size is likely different from that for bulk ZnS. The surface Gibbs free energy difference, which contributes to the energetic favorability of a phase transition, is also dependent on particle size.[101,220] In addition, a study which models the thermodynamics of the sphalerite-wurtzite phase transition in ZnS nanocrystals also suggests that the phase transition temperature drops as the ZnS particle size decreases.[214]

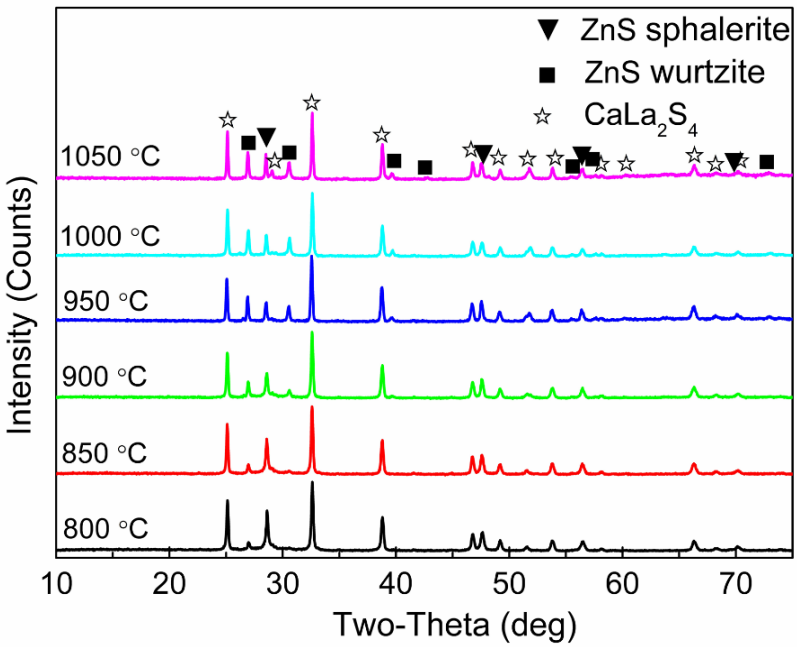


Figure 65. XRD patterns of the 0.5ZnS-0.5CLS ceramics sintered via FAST at different temperatures, under a uniaxial pressure of 100 MPa for 20 min.

Table VI. Quantitative Phase Composition of the 0.5ZnS-0.5CLS Ceramics Sintered at Different Temperatures via FAST.

| Sample | Sphalerite (vol%) | Wurtzite (vol%) | CLS (vol%) |
|---|---|---|---|
| 800 ºC | 42.3 | 4.4 | 54.3 |
| 850 ºC | 40.8 | 3.9 | 55.3 |
| 900 ºC | 44.0 | 8.1 | 47.9 |
| 950 ºC | 36.0 | 11.6 | 52.4 |
| 1000 ºC | 21.2 | 26.1 | 52.7 |
| 1050 ºC | 20.8 | 27.8 | 51.4 |

A TEM investigation provides detailed information on the sphalerite to wurtzite transition of the ZnS component within the composite ceramics. Figure 66 (a) shows the TEM image of the 0.5ZnS-0.5CLS ceramic sintered via FAST at 1000 ºC under a uniaxial pressure of 100 MPa for 20 min. As indicated, the ZnS and CLS grains are homogeneously distributed within the ceramics. It is noted that SEM imaging of the composite ceramic reveals that certain ZnS grains within the samples sintered at high temperatures appear to exhibit rough surfaces, while the surfaces of the CLS grains appear smooth, as shown in

the SE images in Figure 61. Here, it is detailed in TEM imaging that parallel stripes and bands are present in the ZnS grains, which in turn generate the rough surface observed via SEM. The HRTEM image shown in Figure 66 (b) further demonstrates the presence of bands and stripes in the ZnS grains. Figure 66 (c) reveals more details about the bands and stripes. It is observed that they are actually interfacial defects, including stacking faults and twins associated with the ZnS phase transition from sphalerite to wurtzite.[299] Both cubic sphalerite and hexagonal wurtzite are close-packed structures, with sphalerite possessing the close-packed ABCABC atomic arrangement on the {111} plane along the [110] axis, and wurtzite possessing the close-packed ABABAB atomic arrangement on the {0001} plane along the $[11\bar{2}0]$ axis.[87] It should be noted that the formation of these stacking faults between these two different stacking sequences is necessary for the solid state phase transition from sphalerite to wurtzite to occur.[92] The phase transition in bulk ZnS has been reported to be due to a periodic slip mechanism, involving the expansion of stacking faults around an axial screw dislocation.[93,300] In addition, twinning has been reported to occur in sphalerite ZnS along the [111] axis during the sphalerite-wurtzite phase transition,[112,301] which is demonstrated and indexed in the SAED pattern shown in Figure 66 (d). It is important to note that some dim diffraction spots not belonging to sphalerite are also shown in the pattern, which may be assigned to the ABAB layers of hexagonal ZnS wurtzite during the phase transition.[112]

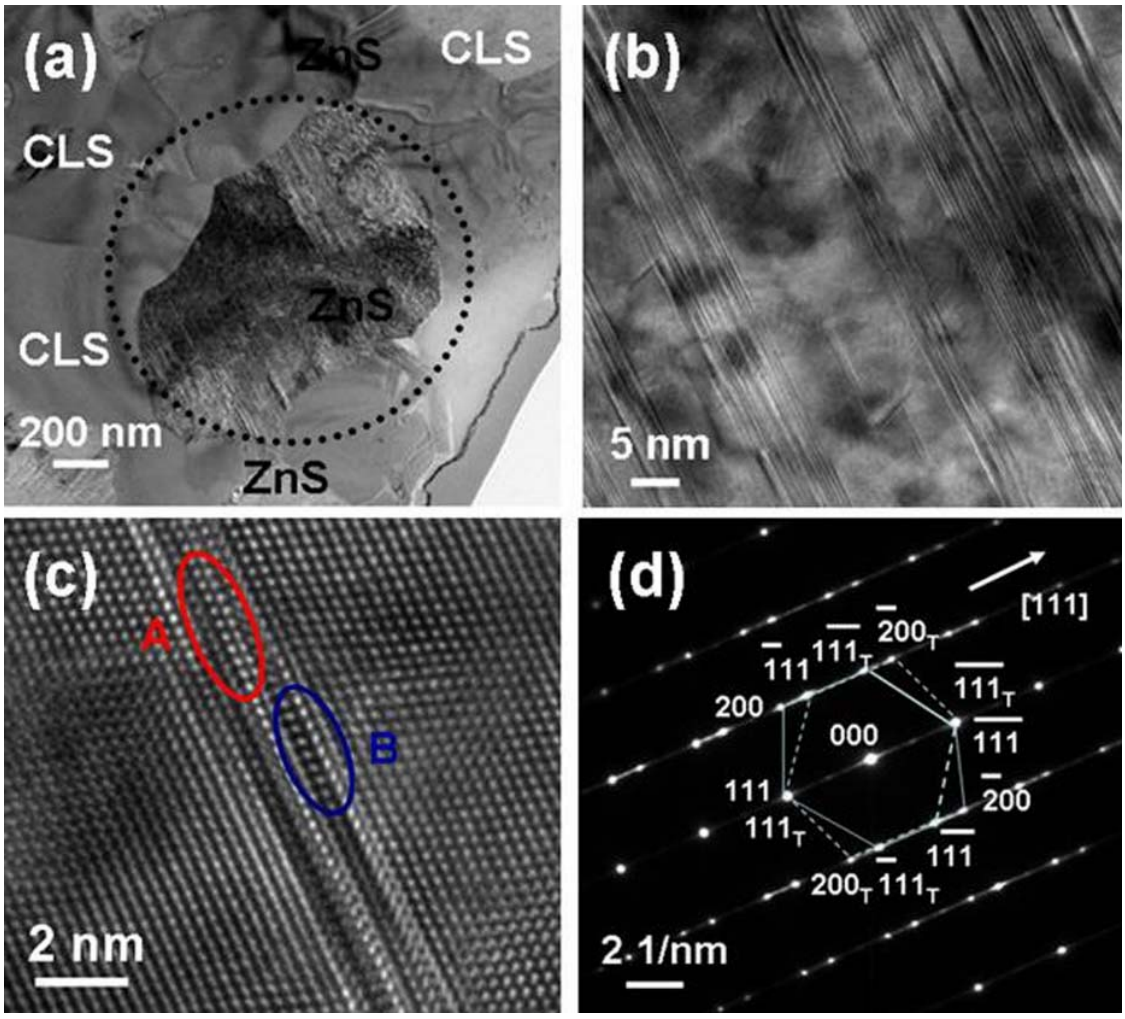


Figure 66. (a) TEM image of the 0.5ZnS-0.5CLS ceramic sintered via FAST at 1000 ºC under a uniaxial pressure of 100 MPa for 20 min; (b) High-resolution TEM (HRTEM) image showing the stripes present in a ZnS grain within the 0.5ZnS-0.5CLS ceramic sintered via FAST at 1000 ºC; (c) HRTEM image of a ZnS grain within the 0.5ZnS-0.5CLS ceramic sintered via FAST at 1000 ºC, showing stacking faults (A) and twins (B); (d) Selected area electron diffraction (SAED) pattern recorded from an area in ZnS within the 0.5ZnS-0.5CLS ceramic sintered via FAST at 1000 ºC, showing the presence of twinned sphalerite (the two hexagons).

Table VII shows the Vickers hardnesses of the 0.5ZnS-0.5CLS ceramics sintered via FAST at 800-1050 ºC. In addition, Vickers hardnesses of pure ZnS ceramics sintered under the same conditions using the aforementioned lab-processed powders are listed in Table VII for comparison. A typical Vickers hardness indentation of the composite ceramics is shown in the SEM image in Figure 67, with the specific indentation shown for

the sample sintered at 950 ºC. It is revealed that the addition of CLS phase can effectively increase the mechanical hardness of the composite material up to a maximum value of 5.11 GPa, which is much higher than that of pure ZnS. It is theorized that the composite 0.5ZnS-0.5CLS ceramics are also strengthened by the homogeneous dispersion of small ZnS and CLS grains. Since the sphalerite-wurtzite phase transition is accompanied by only a 0.2% volume expansion, stresses/strains due to the phase transition are not considered to significantly influence the hardness of the ceramics. It is also found that the hardness of the ceramics is dependent on the sintering temperature. An increase in hardness with increasing sintering temperature is observed over the temperature range of 800 ºC to 950 ºC, due to the enhancement of densification, as shown in Table V.[294] However, when the sintering temperature increases to 1000 ºC, the hardness decreases sharply. It is assumed that the number and density of dislocations are reduced by a decrease in net grain boundary volume, associated with the rapid increase in grain size of the ZnS and CLS phases, which in turn leads to a reduction in hardness.[296] In addition, due to the combined effect of large grain size and chemical decomposition, the sample sintered at 1050 ºC shows a significantly lower hardness than samples sintered at lower temperatures.

Table VII. Vickers Hardness Data for the Pure ZnS and 0.5ZnS-0.5CLS Ceramics Sintered via FAST at 800-1050 ºC, under a Uniaxial Pressure of 100 MPa for 20 min.

| Temperature | Vickers hardness (GPa) of ZnS | Vickers hardness (GPa) of ZnS-CLS |
|---|---|---|
| 800 ºC | 2.39 ± 0.22 | 3.63 ± 0.57 |
| 850 ºC | 2.59 ± 0.32 | 3.78 ± 0.12 |
| 900 ºC | 1.53 ± 0.60 | 4.21 ± 0.06 |
| 950 ºC | 1.41 ± 0.22 | 5.11 ± 0.31 |
| 1000 ºC | 1.37 ± 0.18 | 3.74 ± 0.66 |
| 1050 ºC | 1.39 ± 0.27 | 2.83 ± 0.13 |

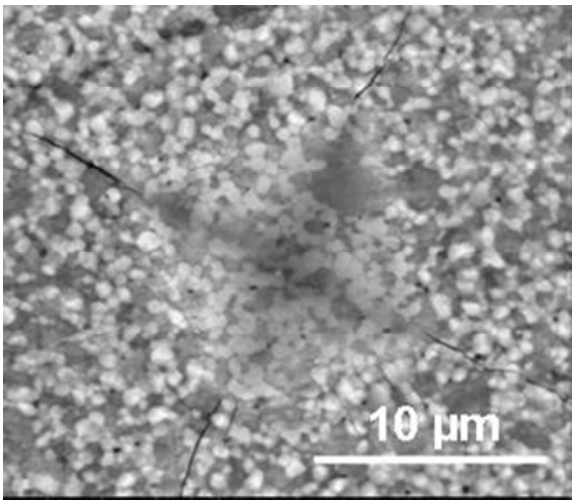


Figure 67. SEM image showing a typical Vickers hardness indentation for the 0.5ZnS-0.5CLS ceramic sintered at 950 ºC under a uniaxial pressure of 100 MPa for 20 min.

The 0.5ZnS-0.5CLS ceramics were also sintered via hot pressing at 1000 ºC, 1100 ºC, 1200 ºC, and 1300 ºC, under a uniaxial pressure of 100 MPa for 2 h, for comparison of microstructure, phase composition and hardness. Figure 68 shows the SEM images of thermally etched surfaces of samples sintered at various temperatures. It is observed that both ZnS and CLS grains experience pronounced grain growth with the increase in sintering temperature. The ceramic sintered at 1000 ºC well densified with little residual porosity. However, as the sintering temperature increases, the densification is somehow diminished, as some residual pores are observed at the grain boundaries between ZnS and CLS grains, which is hypothesized to be due to the chemical decomposition induced by the high surface energy or defects of the ZnS-CLS powders processed via high energy ball milling. Additionally, similar to the ceramics sintered via FAST, certain ZnS grains within the hot-pressed ceramics also appear to exhibit rough surfaces, while the surfaces of the CLS grains are smooth. This is attributed to formation of staking faults and twins, suggesting the ZnS phase transition between sphalerite and wurtzite.

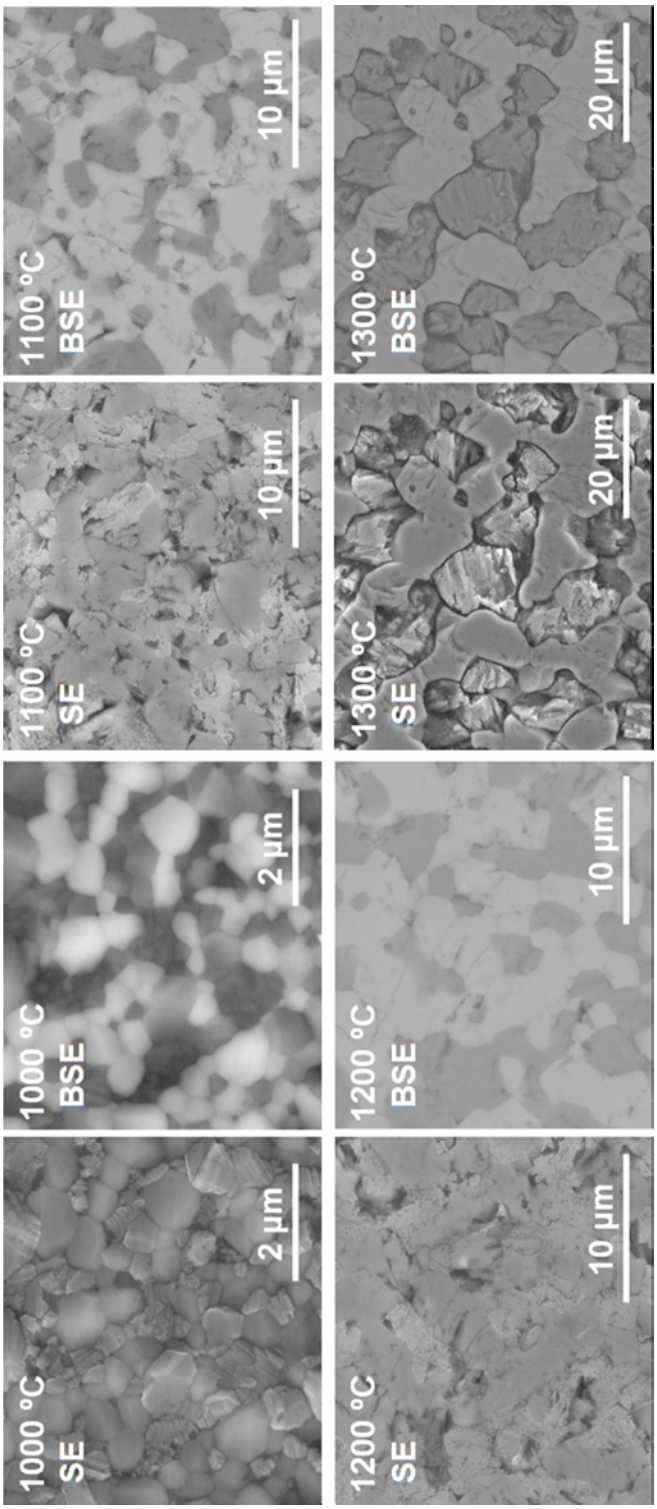


Figure 68. SEM images (SE image and BSE image) of thermally etched surfaces of the 0.5ZnS-0.5CLS ceramics sintered via hot pressing at 1000 ºC, 1100 ºC, 1200 ºC, and 1300 ºC, under a uniaxial pressure of 100 MPa for 2 h. In BSE images, the darker phase corresponds to ZnS, and the brighter phase corresponds to CLS.

The XRD patterns of the 0.5ZnS-0.5CLS ceramics sintered at different temperatures are displayed in Figure 69. It is identified by phase composition analysis that all the sintered 0.5ZnS-0.5CLS ceramics are composed of sphalerite ZnS, wurtzite ZnS, and thorium phosphate-structured CLS. The temperature-dependent phase transition from sphalerite to wurtzite is confirmed by qualitative assessment based on the examination of the relative intensities of wurtzite peaks. It is revealed that the fraction of wurtzite increases as the sintering temperature increases, suggesting the increase in the degree of the phase transition from sphalerite to wurtzite. In contrast, the cubic CLS phase is observed to remain stable with varying sintering temperature. TEM characterization was employed to further investigate into the ZnS phase transition between sphalerite and wurtzite in the composite ZnS-CLS ceramics. Figure 70 (a) shows the TEM image of the 0.5ZnS-0.5CLS ceramic sintered via hot pressing at 1100 ºC under a uniaxial pressure of 100 MPa for 2 h. Two different microstructures are observed on the surface of a ZnS grain, with a smooth surface shown in the circled region labeled 1, and a rough surface shown in the circled region labeled 2. The HRTEM image, shown in Figure 70 (b), reveals that the rough surface consists of bands and stripes, which are attributed to the stacking faults and twins associated with the phase transition between sphalerite and wurtzite. This discovery is in agreement with the aforementioned results of 0.5ZnS-0.5CLS ceramics sintered via FAST and pure ZnS ceramics sintered via hot pressing. The SAED patterns of the two circled areas labeled 1-2 are displayed in Figures 70 (c) and (d), respectively. The observed difference in SAED patterns further confirms the presence of staking faults or twins associated with the phase transition. Similar to 0.5ZnS-0.5CLS ceramics sintered via FAST, the composite ceramics sintered via hot pressing have the maximum indentation hardness of 4.70 ± 0.11 GPa (ceramic sintered at 1000 ºC), higher than that of pure ZnS ceramics, due to the addition and homogenous distribution of CLS phase.

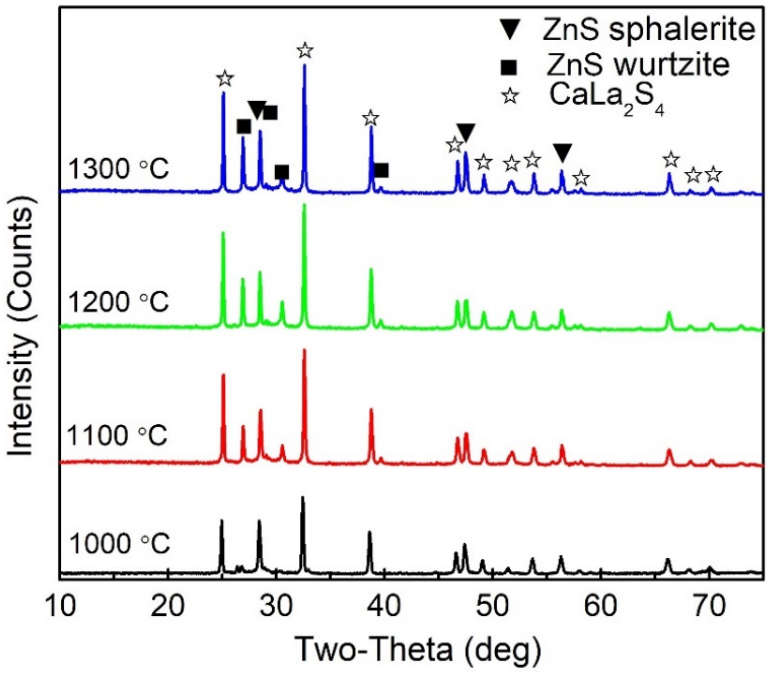


Figure 69. XRD patterns of the 0.5ZnS-0.5CLS ceramics sintered via hot pressing at different temperatures, under a uniaxial pressure of 100 MPa for 2 h.

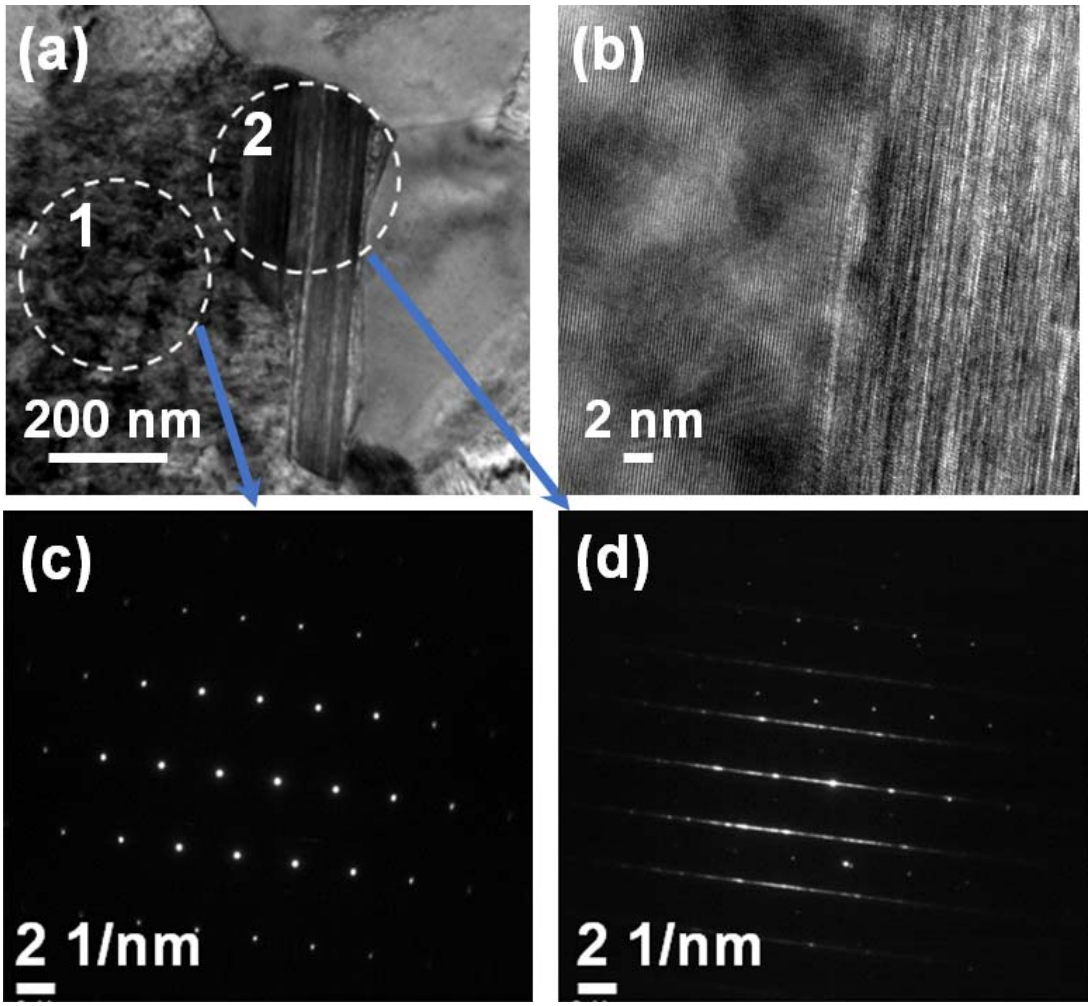


Figure 70. (a) TEM image of the 0.5ZnS-0.5CLS ceramic sintered via hot pressing at 1100 ºC under a uniaxial pressure of 100 MPa for 2 h; (b) HRTEM image showing the stripes (stacking faults and twins) present in a ZnS grain within the 0.5ZnS-0.5CLS ceramic sintered via hot pressing at 1100 ºC; (c) SAED pattern recorded from the circled area 1 in ZnS within the 0.5ZnS-0.5CLS ceramic sintered via hot pressing at 1100 ºC; (d) SAED pattern recorded from the circled area 2 in ZnS within the 0.5ZnS-0.5CLS ceramic sintered via hot pressing at 1100 ºC.

It is important to note that the 0.5ZnS-0.5CLS ceramics in this study have much lower infrared transmittances compared with the individual ZnS and CLS ceramics. This may be due to the relatively large grain size of both phases in the composite ceramics. The grain sizes are not small enough to eliminate the scattering effect caused by the difference in refractive index between the two phases.[193,199] Additionally, some minor impurities within ceramics that cannot be detected by XRD can cause a deterioration of the optical

performance. Further studies on adjustments of processing conditions and ZnS/CLS phase compositions will be performed to improve the infrared transmittance of the ZnS-CLS ceramics.

## D. Conclusions

In summary, ZnS-CLS composite ceramics with submicron-scale and micron-scale grains have been consolidated via field-assisted sintering of 0.5ZnS-0.5CLS (volume ratio) composite powders at 800-1050 ºC and hot pressing at 1000-1300 ºC, under a uniaxial pressure of 100 MPa. Through microstructural and sintering analyses, it has been revealed that in the sintering temperature range of 800-1000 ºC for sample sintered via FAST, the grain growths of both the ZnS and CLS components are controlled by grain boundary diffusion. The pressure-assisted sintered composite ceramics have been determined to consist of sphalerite ZnS, wurtzite ZnS and thorium phosphate-structured CLS, with the presence of wurtzite indicative of an early ZnS phase transition due to the small particle size of the starting ZnS powders. TEM investigation of the consolidated ceramics further reveals that the sphalerite-wurtzite phase transition of ZnS is accompanied by the formation of stacking faults and twins. In addition, it has been found that the mechanical hardness of the ceramics is improved with a maximum value of 5.11 GPa by the introduction of CLS and homogeneous dispersion of the ZnS and CLS fine grains. As sintering temperature increases, the hardness of the ZnS-CLS composite ceramics has been shown to first increase due to densification enhancement, and then decrease due to the initiation of exaggerated grain growth and thermal decomposition.

# VII. CONCLUSIONS

In summary, a detailed study has been carried out to investigate the effects of starting particle size and sintering pressure on the phase transition behaviour of ZnS ceramics. Through qualitative and quantitative phase composition analysis, the ceramics sintered using smaller starting particles experience an "earlier" phase transition at lower temperatures than the reported phase transition temperature (1020 °C) for ZnS bulks, which is attributed to both the increased surface energy and the smaller energy barrier for the propagation of a phase transition associated with decreasing particle size. The phase transition from wurtzite to sphalerite is promoted through the application of uniaxial pressure during hot pressing, due to the expansion of sphalerite deformation faults/twinning and the pressure-induced compressive effect on the crystal lattice. Moreover, the pressure-induced promotion of wurtzite-sphalerite phase transition, along with enhanced densification and twinning, contribute to the improved optical transmittance and mechanical hardness of the ZnS ceramics.

Highly dense $Cr^{2+}$:ZnS infrared transparent ceramics, with a maximum transmittance of 67% at 11.6 μm, have been successfully fabricated via vacuum hot pressing of colloidally processed ZnS powders mixed with commercial $Cr_2S_3$ powders. It has been determined that the $Cr^{2+}$:ZnS ceramics are composed of cubic ZnS sphalerite as a major phase and hexagonal ZnS wurtzite as a minor phase. Through infrared absorption analysis, $Cr^{2+}$ ions are demonstrated to be incorporated into the ZnS host lattice, and the concentration of $Cr^{2+}$ in the $Cr^{2+}$:ZnS ceramic is estimated to be $1.8 \cdot 10^{18}$ $cm^{-3}$. The characteristic $Cr^{2+}$ infrared photoluminescence band at 2000-2200 nm, with the measured decay time of 5.5 μm, corresponds to the $^5E \rightarrow {}^5T_2$ characteristic band of $Cr^{2+}$ in ZnS, which confirms that $Cr^{2+}$ is tetrahedrally coordinated in the ZnS lattice.

Two general processing routes (with and without sulfurization) have been investigated in an attempt to synthesize $CaLa_2S_4$. It has been revealed that the sulfurization of wet chemistry-processed oxygen-containing precursors could lead to the formation of CLS and Ca-doped $La_2S_3$ with the $Th_3P_4$ phase. In contrast, the optimum route to synthesize $CaLa_2S_4$ without sulfurization is through the application of a wet-chemistry method (single-source precursor method) using a combination Na(Ddtc) and Phen,

followed by thermal decomposition at 1000 ℃ in an Ar atmosphere, due to the strong chelating ability of sulfur source and chelating agent. Band gap enhancement is observed due to the nanometric nature of the crystallites composing the powder agglomerates.

A consolidation study has been performed on the pressure-assisted sintered $CaLa_2S_4$ infrared optical ceramics. Densification behavior and grain growth kinetics were studied through densification curves and microstructural characterizations. For the ceramics sintered via field-assisted sintering at 850-1100 ºC under 50 MPa, it has been determined that the densification in the 850-950 ºC temperature range is controlled by a mixture of lattice or grain boundary diffusion, and grain boundary sliding. It has been revealed that grain boundary diffusion is the main mechanism controlling the grain growth between 950 ºC and 1100 ºC. It has been proposed that the grain growth is controlled by grain boundary diffusion, with the activation energy of 57.97 kJ/mol and 150.22 kJ/mol, for samples sintered via FAST at 850-1100 ºC and hot pressing at 950-1200 ºC, respectively. The $CaLa_2S_4$ ceramic sintered via FAST at 1000 ºC displaythe highest infrared transmittance (48.1% at 9.2 μm) of all measured samples. It has been observed that the hardness of the $CaLa_2S_4$ ceramics first increases with increasing sintering temperature due to densification, and then decreases at higher sintering temperatures due to significant grain growth.

Furthermore, an investigation has been conducted into the sintering behavior, phase transition, and hardness of ZnS-$CaLa_2S_4$ composite ceramics, via pressure-assisted sintering of lab-processed ZnS nanopowders mixed with commercial $CaLa_2S_4$ powders by high-energy ball milling (50%:50% in volume ratio). For the ceramics sintered via field-assisted sintering at 800-1050 ºC under 100 MPa, it has been revealed that the grain growths of both the ZnS and $CaLa_2S_4$ components are controlled by grain boundary diffusion, in the sintering temperature range of 800-1000 ºC. XRD analysis has been used to determine that the pressure-assisted consolidated composite ceramics consist of sphalerite ZnS, wurtzite ZnS, and thorium phosphate-structured $CaLa_2S_4$, with the presence of wurtzite indicative of the early sphalerite-wurtzite phase transition. TEM investigations further suggest that the phase transition of ZnS is accompanied by the formation of stacking faults and twins. Additionally, by the introduction of $CaLa_2S_4$ and homogeneous dispersion of the ZnS and $CaLa_2S_4$ fine grains, the indentation hardness of

the ceramics is found to be improved up to a maximum value of 5.11 GPa. As sintering temperature increases, it is indicated that the hardness of the ZnS-$CaLa_2S_4$ composite ceramics first increases due to densification enhancement, and then decreases due to the initiation of exaggerated grain growth and effects of thermal decomposition.

# VIII. FUTURE WORK

Based on the present work on the consolidation of sulfide-based infrared optical ceramics, some future work is suggested as follows:

For the processing study, further investigation is required to be made into the purification process of starting $CaLa_2S_4$ powders in order to improve the infrared transmittance by removing the absorption peaks induced by carbon and oxygen impurities. Enhanced densification, including the application of ultra-high temperature consolidation and post-densification, will be of great help to increase infrared and visible transmittance at no expense of decreasing the mechanical properties of these sulfide-based infrared optical ceramics. With a view to improve the infrared transmittance of composite ZnS-$CaLa_2S_4$ ceramics, it is necessary to further adjust processing conditions for controlling grain growth and decreasing grain size.

For the study on fundamental mechanisms of phase transition and sintering, *in-situ* characterizations are required to observe the evolution of phase composition and microstructural features during the pressure-assisted sintering processes of the sulfide-based optical ceramics, so as to further elucidate the corresponding phenomena in detail. In addition, it will be interesting to modulate the consolidation of ZnS, $CaLa_2S_4$ and ZnS-$CaLa_2S_4$ ceramics, which will shed much new light on the phase transition kinetics of ZnS and the pressure-assisted sintering mechanisms of ceramics.

# IX. REFERENCES


1. D. C. Harris, *Materials for Infrared Windows and Domes: Properties and Performance*. SPIE Press, Bellingham, WA, 1999.

2. W. D. Callister, *Fundamentals of Materials Science and Engineering*; Ch. 19. John Wiley & Sons, New York, 2001.

3. C. B. Carter and M. G. Norton, *Ceramic Materials: Science and Engineering*; Ch. 32. Springer Science & Business Media, New York, 2007.

4. A. Krell, T. Hutzler, and J. Klimke, "Transmission Physics and Consequences for Materials Selection, Manufacturing, and Applications," *J. Eur. Ceram. Soc.,* **29** [2] 207-21 (2009).

5. S. Wang, J. Zhang, D. Luo, F. Gu, D. Tang, Z. Dong, G. E. Tan, W. Que, T. Zhang, and S. Li, "Transparent Ceramics: Processing, Materials and Applications," *Prog. Solid State Chem.,* **41** [1] 20-54 (2013).

6. A. D'Amico, C. Di Natale, F. L. Castro, S. Iarossi, A. Catini, and E. Martinelli, "Volatile Compounds Detection by IR Acousto-Optic Detectors"; pp. 21-59 in *Unexploded Ordnance Detection and Mitigation*. Edited by J. Byrnes. Springer Science & Business Media, Dordrecht, Netherlands, 2008.

7. A. J. Marker III, and N. Neuroth, "Overview: Opitcal Glass - An Engineered Material"; pp. 1-17 in *The Properties of Optical Glass*. Edited by H. Bach and N. Neuroth. Springer-Verlag Berlin Heidelberg, New York, 1998.

8. J. Li, Y. Pan, Y. Zeng, W. Liu, B. Jiang, and J. Guo, "The History, Development, and Future Prospects for Laser Ceramics: A Review," *Int. J. Refract. Met. Hard Mater.,* **39**, 44-52 (2013).

9. L. B. Kong, Y. Huang, W. Que, T. Zhang, S. Li, J. Zhang, Z. Dong, and D. Tang, *Transparent Ceramics*; Ch. 1-2. Springer, New York, 2015.

10. M. Suárez, A. Fernández, J. L. Menéndez, and R. Torrecillas, "Sintering to Transparency of Polycrystalline Ceramic Materials"; pp. 527-52 in *Sintering of Ceramics - New Emerging Techniques*. Edited by A. Lakshmanan. InTechOpen, London, 2012.

11. G. Wei, "Transparent Ceramics for Lighting," *J. Eur. Ceram. Soc.,* **29** [2] 237-44 (2009).

12. A. J. Stevenson, H. Serier-Brault, P. Gredin, and M. Mortier, "Fluoride Materials for Optical Applications: Single Crystals, Ceramics, Glasses, and Glass–Ceramics," *J. Fluorine Chem.,* **132** [12] 1165-73 (2011).

13. C. Lin, C. Rüssel, and S. Dai, "Chalcogenide Glass-Ceramics: Functional Design and Crystallization Mechanism," *Prog. Mater. Sci.,* **93**, 1-44 (2018).

14. L. Calvez, "Chalcogenide Glasses and Glass-Ceramics: Transparent Materials in the Infrared for Dual Applications," *C. R. Phys.,* **18** [5-6] 314-22 (2017).

15. A. Ikesue and Y. L. Aung, "Ceramic Laser Materials," *Nature Photon.,* **2** [12] 721-7 (2008).

16. A. Ikesue, Y. L. Aung, T. Taira, T. Kamimura, K. Yoshida, and G. L. Messing, "Progress in Ceramic Lasers," *Annu. Rev. Mater. Res.,* **36**, 397-429 (2006).

17. J. Peelen and R. Metselaar, "Light Scattering by Pores in Polycrystalline Materials: Transmission Properties of Alumina," *J. Appl. Phys.,* **45** [1] 216-20 (1974).

18. Y. Wu, "Nanostructured Transparent Ceramics with an Anisotropic Crystalline Structure," *Opt. Mater. Express,* **4** [10] 2026-31 (2014).

19. M. N. Rahaman, *Ceramic Processing and Sintering*, 2nd ed. CRC Press, Boca Raton, FL, 2003.

20. Z. Munir, U. Anselmi-Tamburini, and M. Ohyanagi, "The Effect of Electric Field and Pressure on the Synthesis and Consolidation of Materials: A Review of the Spark Plasma Sintering Method," *J. Mater. Sci.,* **41** [3] 763-77 (2006).

21. E. Carnall Jr, S. E. Hatch, L. S. Ladd, and W. F. Parsons, "Magnesium Fluoride Optical Element," U.S. Pat. 3,365,271, January 1968.

22. E. Carnall Jr, S. E. Hatch, S. L. Le Roy, and W. F. Parsons, "Method of Molding Magnesium Fluoride," U.S. Pat. 3,294,878, December 1966.

23. E. Carnall Jr, P. B. Mauer, W. F. Parsons, and D. W. Roy, "Process for Molding Zinc Sulfide," U.S. Pat. 3,131,238, April 1964.

24. E. Carnall Jr, P. B. Mauer, W. F. Parsons, and D. W. Roy, "Zinc Sulfide Optical Element," U.S. Pat. 3,131,025, April 1964.

25. E. Carnall Jr, "Hot-Pressing of ZnS and CdTe," *J. Am. Ceram. Soc.,* **55** [11] 582-3 (1972).

26. D. W. Roy and W. F. Parsons, "Method of Forming Zinc Selenide Infrared Transmitting Optical Elements," U.S. Pat. 3,454,685 July 1969.

27. S. E. Hatch and R. J. Weagley, "Calcium Fluoride Optical Elements and Method for Making Same," U.S. Pat. 3,359,066, December 1967.

28. E. Carnall Jr, S. E. Hatch, W. F. Parsons, and R. J. Weagley, "Hot Pressed Polycrystalline Laser Material," U.S. Pat. 3,453,215, July 1969.

29. S. Hatch, W. Parsons, and R. Weagley, "Hot-Pressed Polycrystalline $CaF_2$:$Dy^{2+}$ Laser," *Appl. Phys. Lett.,* **5** [8] 153-4 (1964).

30. R. E. Clark, "Plurality Optical Element Pressing Process," U.S. Pat. 3,589,880, June 1971.

31. E. Carnall Jr and W. Parsons, "Cadmium Sulfide Infrared Transmitting Optical Elements," U.S. Pat. 3,824,301, July 1974.

32. E. Carnall Jr, "Lanthanum Fluoride Infrared Transmitting Optical Elements," U.S. Pat. 3,206,279, September 1965.

33. E. Carnall Jr and S. E. Hatch, "Process of Hot Pressing Magnesium Oxide Infrared Transmitting Optical Elements," U.S. Pat. 3,402,226, September 1968.

34. E. Carnall Jr and D. W. Roy, "Method of Forming Zinc Oxide Infrared Transmitting Optical Element," U.S. Pat. 3,416,907, December 1968.

35. E. Carnall Jr, W. F. Parsons, and D. W. Roy, "Hot Pressed Cadmium Telluride," U.S. Pat. 3,475,116, October 1969.

36. D. W. Roy and W. F. Parsons, "Hot Pressing Titanium Dioxide," U.S. Pat. 3,459,503, August 1969.

37. D. A. Buckner, H. C. Hafner, and N. J. Kreidl, "Hot-Pressing Magnesium Fluoride," *J. Am. Ceram. Soc.,* **45** [9] 435-8 (1962).

38. W. Stollar and H. Moss, "Pressure Sintering of Gallium Arsenide," *J. Am. Ceram. Soc.,* **52** [4] 204-9 (1969).

39. M. W. Benecke, N. E. Olson, and J. A. Pask, "Effect of LiF on Hot-Pressing of MgO," *J. Am. Ceram. Soc.,* **50** [7] 365-8 (1967).

40. R. C. Anderson, "Transparent Yttria-Based Ceramics and Method for Producing Same," U.S. Pat. 3,545,987, December 1970.

41. S. Dutta and G. Gazza, "Transparent $Y_2O_3$ by Hot-Pressing," *Mater. Res. Bull.,* **4** [11] 791-6 (1969).

42. R. Lefever and J. Matsko, "Transparent Yttrium Oxide Ceramics," *Mater. Res. Bull.,* **2** [9] 865-9 (1967).

43. L. Brissette, P. Burnett, R. Spriggs, and T. Vasilos, "Thermomechanically Deformed $Y_2O_3$," *J. Am. Ceram. Soc.,* **49** [3] 165-6 (1966).

44. R. L. Coble, "Transparent Alumina and Method of Preparation," U.S. Pat. 3,026,210, March 1962.

45. D. W. Roy and F. J. Stermole, "Method for Manufacturing a Transparent Ceramic Body," U.S. Pat. 3,974,249, August 1976.

46. K. Mazdiyasni, C. Lynch, and J. S. Smith II, "Cubic Phase Stabilization of Translucent Yttria-Zirconia at Very Low Temperatures," *J. Am. Ceram. Soc.,* **50** [10] 532-7 (1967).

47. K. S. Mazdiyasni, C. Lynch, and J. S. Smith, "Transparent Zirconia Composition and Process for Making Same," U.S., Pat. 3,432,314, March 1969.

48. K. S. Mazdiyasni, C. T. Lynch, and J. S. Smith, "Transparent Zirconia and Process for Making Same," U.S. Pat. 3,525,597, August 1970.

49. J. W. McCauley and N. D. Corbin, "Phase Relations and Reaction Sintering of Transparent Cubic Aluminum Oxynitride Spinel (ALON)," *J. Am. Ceram. Soc.,* **62** [9-10] 476-9 (1979).

50. S. R. Steele and J. Pappis, "Chemical Vapor Deposition of IR Materials," DTIC Document AFAL-TR-71-200, Raytheon Co. Research Division, Waltham, MA, August 1971.

51. D. C. Harris, "Development of Hot-Pressed and Chemical-Vapor-Deposited Zinc Sulfide and Zinc Selenide in the United States for Optical Windows"; pp. 654502-1-27 in *Proc. SPIE 6545, Window and Dome Technologies and Materials X*. Edited by R. W. Tustison. International Society for Optics and Photonics, Orlando, FL, 2007.

52. N. Kuramoto and H. Taniguchi, "Transparent AlN Ceramics," *J. Mater. Sci. Lett.,* **3** [6] 471-4 (1984).

53. M. Mitomo, Y. Moriyoshi, T. Sakai, T. Ohsaka, and M. Kobayashi, "Translucent β-sialon Ceramics," *J. Mater. Sci. Lett.,* **1** [1] 25-6 (1982).

54. J. Savage and K. Marsh, "A Materials Study to Find an Advanced Optical Window Material for 8 to 12 μm Airborne Applications"; pp. 35-7 in *Proc. SPIE 0297, Emerging Optical Materials*. Edited by S. Musikant. International Society for Optics and Photonics, San Diego, CA, 1982.

55. K. Saunders, T. Wong, T. Hartnett, R. Tustison, and R. Gentilman, "Current and Future Development of Calcium Lanthanum Sulfide"; pp. 72-8 in *Proc. SPIE 0683, Infrared and Optical Transmitting Materials*. Edited by R. W. Schwartz. International Society for Optics and Photonics, San Diego, CA, 1986.

56. H. Van Dijk, "Translucent $Y_3Al_5O_{12}$ Ceramics," *Mater. Res. Bull.,* **19** [12] 1669-74 (1984).

57. A. Ikesue, I. Furusato, and K. Kamata, "Fabrication of Polycrystal Line, Transparent YAG Ceramics by a Solid-State Reaction Method," *J. Am. Ceram. Soc.,* **78** [1] 225-8 (1995).

58. A. Ikesue, T. Kinoshita, K. Kamata, and K. Yoshida, "Fabrication and Optical Properties of High-Performance Polycrystalline Nd: YAG Ceramics for Solid-State Lasers," *J. Am. Ceram. Soc.,* **78** [4] 1033-40 (1995).

59. A. Bertrand, J. Carreaud, S. Chenu, M. Allix, E. Véron, J. R. Duclère, Y. Launay, T. Hayakawa, C. Genevois, and F. Brisset, "Scalable and Formable Tellurite-Based Transparent Ceramics for Near Infrared Applications," *Adv. Opt. Mater.,* **4** [10] 1482-6 (2016).

60. M. Dolhen, M. Tanaka, V. Couderc, S. Chenu, G. Delaizir, T. Hayakawa, J. Cornette, F. Brisset, M. Colas, and P. Thomas, "$Nd^{3+}$-Doped Transparent Tellurite Ceramics Bulk Lasers," *Sci. Rep.,* **8** [1] 4640 (2018).

61. Y. Jiang, B. Jiang, N. Jiang, P. Zhang, S. Chen, Q. Gan, G. Zhang, J. Fan, X. Mao, and L. Su, "Perfectly Transparent Pore-Free $Nd^{3+}$-Doped $Sr_9GdF_{21}$ Polycrystalline Ceramics Elaborated from Single-Crystal Ceramization," *J. Eur. Ceram. Soc.,* **37** [15] 4912-8 (2017).

62. A. Gallian, V. V. Fedorov, S. B. Mirov, V. V. Badikov, S. N. Galkin, E. F. Voronkin, and A. I. Lalayants, "Hot-Pressed Ceramic $Cr^{2+}$:ZnSe Gain-Switched Laser," *Opt. Express,* **14** [24] 11694-701 (2006).

63. N. Nishiyama, R. Ishikawa, H. Ohfuji, H. Marquardt, A. Kurnosov, T. Taniguchi, B. N. Kim, H. Yoshida, A. Masuno, and J. Bednarcik, "Transparent Polycrystalline Cubic Silicon Nitride," *Sci. Rep.,* **7**, 44755-1-8 (2017).

64. W. Kim, G. Villalobos, C. Baker, J. Frantz, B. Shaw, S. Bayya, B. Sadowski, M. Hunt, B. Rock, and I. Aggarwal, "Overview of Transparent Optical Ceramics for High-Energy Lasers at NRL," *Appl. Optics,* **54** [31] F210-21 (2015).

65. W. Kim, G. R. Villalobos, C. Baker, J. A. Frantz, B. Shaw, S. S. Bayya, B. Sadowski, I. D. Aggarwal, M. Hunt, and J. Sanghera, "Ceramic Windows and Gain Media for High-Energy Lasers," *Opt. Eng.,* **52** [2] 021003 (2012).

66. S. Bayya, G. Villalobos, W. Kim, J. Sanghera, M. Hunt, and I. D. Aggarwal, "Rugged Sensor Window Materials for Harsh Environments"; pp. 92021D-1-9 in *Proc. SPIE 9202, Photonics Applications for Aviation, Aerospace, Commercial, and Harsh Environments V*. Edited by A. A. Kazemi, B. C. Kress, and E. A. Mendoza. International Society for Optics and Photonics, San Diego, CA, 2014.

67. J. Cheng, D. Agrawal, Y. Zhang, and R. Roy, "Microwave Reactive Sintering to Fully Transparent Aluminum Oxynitride (ALON) Ceramics," *J. Mater. Sci. Lett.,* **20** [1] 77-9 (2001).

68. X. Mao, S. Wang, S. Shimai, and J. Guo, "Transparent Polycrystalline Alumina Ceramics with Orientated Optical Axes," *J. Am. Ceram. Soc.,* **91** [10] 3431-3 (2008).

69. R. Apetz and M. P. Van Bruggen, "Transparent Alumina: A Light-Scattering Model," *J. Am. Ceram. Soc.,* **86** [3] 480-6 (2003).

70. D. Jiang, D. M. Hulbert, U. Anselmi-Tamburini, T. Ng, D. Land, and A. K. Mukherjee, "Optically Transparent Polycrystalline $Al_2O_3$ Produced by Spark Plasma Sintering," *J. Am. Ceram. Soc.,* **91** [1] 151-4 (2008).

71. S. Grasso, B. N. Kim, C. Hu, G. Maizza, and Y. Sakka, "Highly Transparent Pure Alumina Fabricated by High-Pressure Spark Plasma Sintering," *J. Am. Ceram. Soc.,* **93** [9] 2460-2 (2010).

72. H. Zhang, Z. Li, B. N. Kim, K. Morita, H. Yoshida, K. Hiraga, and Y. Sakka, "Highly Infrared Transparent Nanometric Tetragonal Zirconia Prepared by High-Pressure Spark Plasma Sintering," *J. Am. Ceram. Soc.,* **94** [9] 2739-41 (2011).

73. S. Chen, Y. Wu, and Y. Yang, "Spark Plasma Sintering of Hexagonal Structure $Yb^{3+}$-Doped $Sr_5(PO_4)_3F$ Transparent Ceramics," *J. Am. Ceram. Soc.,* **96** [6] 1694-7 (2013).

74. T. Lu, X. Chang, J. Qi, X. Luo, Q. Wei, S. Zhu, K. Sun, J. Lian, and L. Wang, "Low-Temperature High-Pressure Preparation of Transparent Nanocrystalline $MgAl_2O_4$ Ceramics," *Appl. Phys. Lett.,* **88** [21] 213120-1-3 (2006).

75. M. Sokol, S. Kalabukhov, M. Dariel, and N. Frage, "High-Pressure Spark Plasma Sintering (SPS) of Transparent Polycrystalline Magnesium Aluminate Spinel (PMAS)," *J. Eur. Ceram. Soc.,* **34** [16] 4305-10 (2014).

76. D. N. Muche, J. W. Drazin, J. Mardinly, S. Dey, and R. H. Castro, "Colossal Grain Boundary Strengthening in Ultrafine Nanocrystalline Oxides," *Mater. Lett.,* **186**, 298-300 (2017).

77. B. H. Kear, R. Sadangi, V. Shukla, T. Stefanik, and R. Gentilman, "Submicron-Grained Transparent Yttria Composites"; pp. 227-34 in *Proc. SPIE 5786, Window and Dome Technologies and Materials IX*. Edited by R. W. Tustison. International Society for Optics and Photonics, Orlando, FL, 2005.

78. T. Stefanik, R. Gentilman, and P. Hogan, "Nanocomposite Optical Ceramics for Infrared Windows and Domes"; pp. 65450A-1-5 in *Proc. SPIE 6545, Window and Dome Technologies and Materials X*. Edited by R. W. Tustison. International Society for Optics and Photonics, Orlando, FL, 2007.

79. K. Morita, B.-N. Kim, H. Yoshida, K. Hiraga, and Y. Sakka, "Spectroscopic Study of the Discoloration of Transparent $MgAl_2O_4$ Spinel Fabricated by Spark-Plasma-Sintering (SPS) Processing," *Acta Mater.,* **84**, 9-19 (2015).

80. I. Reimanis and H. J. Kleebe, "A Review on the Sintering and Microstructure Development of Transparent Spinel ($MgAl_2O_4$)," *J. Am. Ceram. Soc.,* **92** [7] 1472-80 (2009).

81. D. C. Harris, "Durable 3–5 μm Transmitting Infrared Window Materials," *Infrared. Phys. Technol.,* **39** [4] 185-201 (1998).

82. J. McCloy, "International Development of Chemical Vapor Deposited Zinc Sulfide"; pp. 654503-1-12 in *Proc. SPIE 6545, Window and Dome Technologies and Materials X*. Edited by R. W. Tustison. International Society for Optics and Photonics, Orlando, FL, 2007.

83. X. R. Chen, X. F. Li, L. C. Cai, and J. Zhu, "Pressure Induced Phase Transition in ZnS," *Solid State Commun.,* **139** [5] 246-9 (2006).

84. Y. Zhou, A. J. Campbell, and D. L. Heinz, "Equations of State and Optical Properties of the High Pressure Phase of Zinc Sulfide," *J. Phys. Chem. Solids,* **52** [6] 821-5 (1991).

85. Y. Pan, S. Qu, S. Dong, Q. Cui, W. Zhang, X. Liu, J. Liu, B. Liu, C. Gao, and G. Zou, "An Investigation on the Pressure-Induced Phase Transition of Nanocrystalline ZnS," *J. Phys. Condens. Matter,* **14** [44] 10487 (2002).

86. A. Nazzal and A. Qteish, "Ab Initio Pseudopotential Study of the Structural Phase Transformations of ZnS under High Pressure," *Phys. Rev. B,* **53** [13] 8262 (1996).

87. M. Fleet, "Structural Transformations in Natural ZnS," *Am. Mineral.,* **62** [5-6] 540-6 (1977).

88. D. Pandey and S. Lele, "On the Study of the F.C.C.-H.C.P. Martensitic Transformation Using a Diffraction Approach—I. F.C.C.→H.C.P. Transformation," *Acta Metall.,* **34** [3] 405-13 (1986).

89. D. Pandey and S. Lele, "On the Study of the F.C.C.-H.C.P. Martensitic Transformation Using a Diffraction Approach—II. H.C.P.→F.C.C. Transformation," *Acta Metall.,* **34** [3] 415-24 (1986).

90. E. T. Allen, J. L. Crenshaw, and H. E. Merwin, "The Sulphides of Zinc, Cadmium, and Mercury; Their Crystalline Forms and Genetic Conditions; Microscopic Study by H.E. Merwin," *Am. J. Sci.,* **34** [202] 341-96 (1912).

91. S. Scott and H. Barnes, "Sphalerite-Wurtzite Equilibria and Stoichiometry," *Geochim. Cosmochim. Ac,* **36** [11] 1275-95 (1972).

92. M. Akizuki, "Investigation of Phase Transition of Natural ZnS Minerals by High Resolution Electron Microscopy," *Am. Mineral.,* **66** [9-10] 1006-12 (1981).

93. M. Sebastian and P. Krishna, "Mechanism of Phase Transformations in ZnS," *Pramana-J. Phys.,* **23** [3] 395-403 (1984).

94. P. W. Bridgman, "The High Pressure Behavior of Miscellaneous Minerals," *Am. J. Sci.,* **237** [1] 7-18 (1938).

95. S. Omel'chenko and M. Bulanyi, "Reversible Changes in the Structure of Zinc Sulfide Crystals During Elastic Deformation," *Phys. Solid State,* **39** [7] 1091-3 (1997).

96. M. Kulakov and S. Shmurak, "Structural Changes in ZnS Crystals on Account of Partial Dislocation Movement," *Phys. Status Solidi A,* **59** [1] 147-53 (1980).

97. X. S. Fang, T. Y. Zhai, U. K. Gautam, L. Li, L. M. Wu, Y. Bando, and D. Golberg, "ZnS Nanostructures: From Synthesis to Applications," *Prog. Mater. Sci.,* **56** [2] 175-287 (2011).

98. F. Huang and J. F. Banfield, "Size-Dependent Phase Transformation Kinetics in Nanocrystalline ZnS," *J. Am. Chem. Soc.,* **127** [12] 4523-9 (2005).

99. S. Qadri, E. Skelton, A. Dinsmore, J. Hu, W. Kim, C. Nelson, and B. Ratna, "The Effect of Particle Size on the Structural Transitions in Zinc Sulfide," *J. Appl. Phys.,* **89** [1] 115-9 (2001).

100. S. Qadri, E. Skelton, D. Hsu, A. Dinsmore, J. Yang, H. Gray, and B. Ratna, "Size-Induced Transition-Temperature Reduction in Nanoparticles of ZnS," *Phys. Rev. B,* **60** [13] 9191 (1999).

101. Z. Wang, L. L. Daemen, Y. Zhao, C. Zha, R. T. Downs, X. Wang, Z. L. Wang, and R. J. Hemley, "Morphology-Tuned Wurtzite-Type ZnS Nanobelts," *Nature Mater.,* **4** [12] 922-7 (2005).

102. Y. Zhao, Y. Zhang, H. Zhu, G. C. Hadjipanayis, and J. Q. Xiao, "Low-Temperature Synthesis of Hexagonal (Wurtzite) ZnS Nanocrystals," *J. Am. Chem. Soc.,* **126** [22] 6874-5 (2004).

103. S. H. Yu and M. Yoshimura, "Shape and Phase Control of ZnS Nanocrystals: Template Fabrication of Wurtzite ZnS Single-Crystal Nanosheets and ZnO Flake-Like Dendrites from a Lamellar Molecular Precursor $ZnS{\cdot}(NH_2CH_2CH_2NH_2)_{0.5}$," *Adv. Mater.,* **14** [4] 296-300 (2002).

104. F. Huang, B. Gilbert, H. Zhang, and J. F. Banfield, "Reversible, Surface-Controlled Structure Transformation in Nanoparticles Induced by an Aggregation State," *Phys. Rev. Lett.,* **92** [15] 155501-1-4 (2004).

105. A. Tiwari and S. Dhoble, "Critical Analysis of Phase Evolution, Morphological Control, Growth Mechanism and Photophysical Applications of ZnS

Nanostructures (Zero-Dimensional to Three-Dimensional): A Review," *Cryst. Growth Des.,* **17** [1] 381-407 (2016).

106. N. S. Karan, S. Sarkar, D. Sarma, P. Kundu, N. Ravishankar, and N. Pradhan, "Thermally Controlled Cyclic Insertion/Ejection of Dopant Ions and Reversible Zinc Blende/Wurtzite Phase Changes in ZnS Nanostructures," *J. Am. Chem. Soc.,* **133** [6] 1666-9 (2011).

107. J. S. McCloy and R. W. Tustison, *Chemical Vapor Deposited Zinc Sulfide*. SPIE Press, Bellingham, WA, 2013.

108. F. Zhenyi, C. Yichao, H. Yongliang, Y. Yaoyuan, D. Yanping, Y. Zewu, T. Hongchang, X. Hongtao, and W. Heming, "CVD Growth of Bulk Polycrystalline ZnS and Its Optical Properties," *J. Cryst. Growth,* **237** 1707-10 (2002).

109. Y. Drezner, S. Berger, and M. Hefetz, "A Correlation between Microstructure, Composition and Optical Transparency of CVD-ZnS," *Mater. Sci. Eng. B,* **87** [1] 59-65 (2001).

110. P. Biswas, R. S. Kumar, P. Ramavath, V. Mahendar, G. Rao, U. Hareesh, and R. Johnson, "Effect of Post-CVD Thermal Treatments on Crystallographic Orientation, Microstructure, Mechanical and Optical Properties of ZnS Ceramics," *J. Alloy. Compd.,* **496** [1-2] 273-7 (2010).

111. E. V. Karaksina, V. B. Ikonnikov, and E. M. Gavrishchuk, "Recrystallization Behavior of ZnS During Hot Isostatic Pressing," *Inorg. Mater.,* **43** [5] 452-4 (2007).

112. J. S. McCloy, R. Korenstein, and B. Zelinski, "Effects of Temperature, Pressure, and Metal Promoter on the Recrystallized Structure and Optical Transmission of Chemical Vapor Deposited Zinc Sulfide," *J. Am. Ceram. Soc.,* **92** [8] 1725-31 (2009).

113. T. Zscheckel, W. Wisniewski, A. Gebhardt, and C. Rüssel, "Recrystallization of CVD-ZnS During Thermal Treatment," *Opt. Mater. Express,* **4** [9] 1885-94 (2014).

114. T. Zscheckel, W. Wisniewski, A. Gebhardt, and C. Rüssel, "Mechanisms Counteracting the Growth of Large Grains in Industrial ZnS Grown by Chemical Vapor Deposition," *ACS Appl. Mater. Interfaces,* **6** [1] 394-400 (2013).

115. T. Zscheckel, W. Wisniewski, and C. Rüssel, "Microstructure and Texture of Polycrystalline CVD-ZnS Analyzed Via EBSD," *Adv. Funct. Mater.,* **22** [23] 4969-74 (2012).

116. X. Wang, H. Huang, B. Liang, Z. Liu, D. Chen, and G. Shen, "ZnS Nanostructures: Synthesis, Properties, and Applications," *Crit. Rev. Solid State,* **38** [1] 57-90 (2013).

117. A. Celikkaya and M. Akinc, "Morphology of Zinc Sulfide Particles Produced from Various Zinc Salts by Homogeneous Precipitation," *J. Am. Ceram. Soc.,* **73** [2] 245-50 (1990).

118. A. Celikkaya and M. Akinc, "Preparation and Mechanism of Formation of Spherical Submicrometer Zinc Sulfide Powders," *J. Am. Ceram. Soc.,* **73** [8] 2360-5 (1990).

119. M. Akinc and A. Celikkaya, "Synthesis and Hot Pressing of ZnS Powders"; pp. 60-8 in *Proc. SPIE 1112, Window and Dome Technologies and Materials*. Edited by P. Klocek. International Society for Optics and Photonics, Orlando, FL, 1989.

120. A. Celikkaya, "Preparation and Processing of ZnS Powders with Spherical Submicron Particles"; M.S. Thesis. Iowa State University, Ames, IA, 1989.

121. Y. D. Kim, K. Sonezaki, H. Maeda, and A. Kato, "Sintering Behaviour of Monodispersed ZnS Powders," *J. Mater. Sci.,* **32** [19] 5101-6 (1997).

122. L. A. Xue and R. Raj, "Effect of Hot-Pressing Temperature on the Optical Transmission of Zinc Sulfide," *Appl. Phys. Lett.,* **58** [5] 441-3 (1991).

123. L. A. Xue and R. Raj, "Deformation-Induced Phase Transformation in Zinc Sulphide," *J. Mater. Sci. Lett.,* **9** [7] 818-9 (1990).

124. L. A. Xue and R. Raj, "Superplastic Deformation of Zinc Sulfide Near Its Transformation Temperature [1020°]," *J. Am. Ceram. Soc.,* **72** [10] 1792-6 (1989).

125. Z. Shizen, M. Hongli, R. Jean, M. Odile, A. Jean-Luc, L. Jacques, and Z. Xianghua, "Preparation and Hot Pressing of ZnS Nano Powders for Producing Transparent Ceramics," *Optoelectron. Adv. Mater., Rapid Commun.,* **1** [12] 667-71 (2007).

126. C. Chlique, G. Delaizir, O. Merdrignac-Conanec, C. Roucau, M. Dollé, P. Rozier, V. Bouquet, and X. H. Zhang, "A Comparative Study of ZnS Powders Sintering by Hot Uniaxial Pressing (HUP) and Spark Plasma Sintering (SPS)," *Opt. Mater.,* **33** [5] 706-12 (2011).

127. C. Chlique, O. Merdrignac-Conanec, N. Hakmeh, X. H. Zhang, and J. L. Adam, "Transparent ZnS Ceramics by Sintering of High Purity Monodisperse Nanopowders," *J. Am. Ceram. Soc.,* **96** [10] 3070-4 (2013).

128. D. Gao and T. S. Stefanik, "Transparent Zinc Sulfide Processed from Nanocrystalline Powders"; pp. 87080L-1-7 in *Proc. SPIE 8708, Window and Dome Technologies and Materials XIII*. Edited by R. W. Tustison and B. Zelinski. International Society for Optics and Photonics, Baltimore, MD, 2013.

129. K. G. Rozenburg and E. H. Urruti, "Polycrystalline Chalcogenide Ceramic Material," U.S. Pat. Application No. 14/958,360, March 2016.

130. T. Ueno, M. Hasegawa, M. Yoshimura, H. Okada, T. Nishioka, K. Teraoka, A. Fujii, and S. Nakayama, "Development of ZnS Lenses for FIR Cameras," *SEI Tech. Rev.,* **69**, 48-53 (2009).

131. D. Ravichandran and D. Balachari, "Monodispersed and Spherical ZnS for Nano-Grain Optical Windows," U.S. Pat. 8,426,817, April 2012.

132. D. Ravichandran and Y. Shi, "Polycrystalline Sintered Nano-Grain Zinc Sulfide Ceramics for Optical Windows," U.S. Pat. 8,803,088, August 2014.

133. Y. Chen, L. Zhang, J. Zhang, P. Liu, T. Zhou, H. Zhang, D. Gong, D. Tang, and D. Shen, "Fabrication of Transparent ZnS Ceramic by Optimizing the Heating Rate in Spark Plasma Sintering Process," *Opt. Mater.,* **50**, 36-9 (2015).

134. M. Isogai and M. Sano, "Development of Optical Ceramic Materials for Infrared Applications by Optimizing Sintering Conditions"; pp. 101790L-1-10 in *Proc. SPIE 10179, Window and Dome Technologies and Materials XV*. Edited by B. Zelinski. International Society for Optics and Photonics, Anaheim, CA, 2017.

135. H. Y. Ahn, W. J. Choi, S. Y. Lee, B. K. Ju, and S. H. Cho, "Mechanochemical Synthesis of ZnS for Fabrication of Transparent Ceramics," *Res. Chem. Intermediat,* **44** [8] 4721-31 (2018).

136. Y. Li, "Photoluminescent Zinc Sulfide Optical Ceramics"; M.S. Thesis. New York State College of Ceramics at Alfred University. Kazuo Inamori School of Engineering, Alfred, NY, 2015.

137. Y. Li and Y. Wu, "Transparent and Luminescent ZnS Ceramics Consolidated by Vacuum Hot Pressing Method," *J. Am. Ceram. Soc.,* **98** [10] 2972-5 (2015).

138. Y. Li, L. Zhang, K. Kisslinger, and Y. Wu, "Green Phosphorescence of Zinc Sulfide Optical Ceramics," *Opt. Mater. Express,* **4** [6] 1140-50 (2014).

139. J. S. McCloy, M. Bliss, B. Miller, Z. Wang, and S. Stave, "Scintillation and Luminescence in Transparent Colorless Single and Polycrystalline Bulk Ceramic ZnS," *J. Lumin.,* **157**, 416-23 (2015).

140. J. S. McCloy and B. G. Potter, "Photoluminescence in Chemical Vapor Deposited ZnS: Insight into Electronic Defects," *Opt. Mater. Express,* **3** [9] 1273-8 (2013).

141. C. Li, Y. Pan, H. Kou, H. Chen, W. Wang, T. Xie, and J. Li, "Densification Behavior, Phase Transition, and Preferred Orientation of Hot-Pressed ZnS Ceramics from Precipitated Nanopowders," *J. Am. Ceram. Soc.,* **99** [9] 3060-6 (2016).

142. C. Li, T. Xie, H. Kou, Y. Pan, and J. Li, "Hot-Pressing and Post-HIP Treatment of $Fe^{2+}$: ZnS Transparent Ceramics from Co-Precipitated Powders," *J. Eur. Ceram. Soc.,* **37** [5] 2253-7 (2017).

143. C. Li, T. Xie, J. Dai, H. Kou, Y. Pan, and J. Li, "Hot-Pressing of Zinc Sulfide Infrared Transparent Ceramics from Nanopowders Synthesized by the Solvothermal Method," *Ceram. Int.,* **44** [1] 747-52 (2018).

144. K. T. Lee, B. H. Choi, J. U. Woo, J. S. Kang, J. H. Paik, B. U. Chu, and S. Nahm, "Microstructural and Optical Properties of the ZnS Ceramics Sintered by Vacuum Hot-Pressing Using Hydrothermally Synthesized ZnS Powders," *J. Eur. Ceram. Soc.,* **38** [12] 4237-44 (2018).

145. S. Y. Yeo, T. H. Kwon, C. S. Park, C. I. Kim, J. S. Yun, Y. H. Jeong, Y. W. Hong, J. H. Cho, and J. H. Paik, "Sintering and Optical Properties of Transparent ZnS Ceramics by Pre-Heating Treatment Temperature," *J. Electroceram.,* **41** [1-4] 1-8 (2018).

146. X. Mao, B. Chai, L. Zhang, B. Jiang, Q. Yuan, and J. Xie, "Method for Producing Infrared ZnS Domes," U.S. Pat. 9,559.411, January 2017.

147. S. B. Mirov, V. V. Fedorov, I. S. Moskalev, and D. V. Martyshkin, "Recent Progress in Transition-Metal-Doped II–VI Mid-IR Lasers," *IEEE J. Sel. Top. Quantum Electron.,* **13** [3] 810-22 (2007).

148. S. Mirov, V. Fedorov, D. Martyshkin, I. Moskalev, M. Mirov, and V. Gapontsev, "Progress in Mid-IR $Cr^{2+}$ and $Fe^{2+}$ Doped II-VI Materials and Lasers [Invited]," *Opt. Mater. Express,* **1** [5] 898-910 (2011).

149. K. Graham, S. B. Mirov, V. V. Fedorov, M. E. Zvanut, A. G. Avanesov, V. V. Badikov, B. Ignat'ev, V. Panutin, and G. S. Shevyrdayeva, "Laser Performance of $Cr^{2+}$-Doped ZnS"; pp. 81-8 in *Proc. SPIE 4267, Solid State Lasers X*. Edited by R. Scheps. International Society for Optics and Photonics, San Jose, CA, 2001.

150. S. B. Mirov, V. V. Fedorov, D. Martyshkin, I. S. Moskalev, M. Mirov, and S. Vasilyev, "Progress in Mid-IR Lasers Based on Cr and Fe-Doped II–VI Chalcogenides," *IEEE J. Sel. Top. Quantum Electron.,* **21** [1] 292-310 (2015).

151. S. Mirov, V. Fedorov, K. Graham, I. Moskalev, I. Sorokina, E. Sorokin, V. Gapontsev, D. Gapontsev, V. Badikov, and V. Panyutin, "Diode and Fibre Pumped $Cr^{2+}$:ZnS Mid-Infrared External Cavity and Microchip Lasers," *IEE Proc. Optoelectron.,* **150** [4] 340 (2003).

152. S. B. Mirov and V. V. Fedorov, "Mid-IR Microchip Laser: ZnS: $Cr^{2+}$ Laser with Saturable Absorber Material," U.S. Pat. 6,960,486, November 2005.

153. K. Lewis, J. Savage, K. Marsh, and A. Jones, "Recent Developments in the Fabrication of Rare-Earth Chalcogenide Materials for Infra-Red Optical Applications"; pp. 21-8 in *Proc. SPIE 0400, New Optical Materials*. Edited by S. Musikant and J. Dupuy. International Society for Optics and Photonics, Geneva, Switzerland, 1983.

154. D. L. Chess, C. A. Chess, and W. B. White, "Physical Properties of Ternary Sulfide Ceramics," *Mater. Res. Bull.,* **19** [12] 1551-8 (1984).

155. J. Savage, K. Lewis, and R. Whitehouse, "Recent Progress in the Synthesis of Calcium Lanthanum Sulphide Optical Ceramic"; pp. 127-32 in *Proc. SPIE 0588, Recent Developments in Materials & Detectors for the Infrared*. Edited by J. S. Seeley. International Society for Optics and Photonics, Cannes, France, 1986.

156. W. B. White, D. Chess, C. A. Chess, and J. V. Biggers, "$CaLa_2S_4$: Ceramic Window Material for the 8 to 14 μm Region"; pp. 38-43 in *Proc. SPIE 0297, Emerging Optical Materials*. Edited by S. Musikant. International Society for Optics and Photonics, San Diego, CA, 1982.

157. J. S. McCloy, B. J. Riley, D. A. Pierce, B. R. Johnson, and A. Qiao, "Infrared-Transmitting Glass-Ceramics: A Review"; pp. 87080N-1-20 in *Proc. SPIE 8708, Window and Dome Technologies and Materials XIII*. Edited by R. W. Tustison and B. Zelinski. International Society for Optics and Photonics, Baltimore, MD, 2013.

158. M. J. Weber, *Handbook of Optical Materials*. CRC Press, Boca Raton, FL, 2002.

159. A. W. Sleight and C. T. Prewitt, "Crystal Chemistry of the Rare Earth Sesquisulfides," *Inorg. Chem.,* **7** [11] 2282-8 (1968).

160. P. Kumta and S. Risbud, "Rare-Earth Chalcogenides—An Emerging Class of Optical Materials," *J. Mater. Sci.,* **29** [5] 1135-58 (1994).

161. S. Musikant, "Development of a New Family of Improved Infrared (Ir) Dome Ceramics"; pp. 2-13 in *Proc. SPIE 0297, Emerging Optical Materials*. Edited by S. Musikant. International Society for Optics and Photonics, San Diego, CA, 1982.

162. J. Beswick, D. Pedder, J. Lewis, and F. Ainger, "New Infra-Red Window Materials"; pp. 12-20 in *Proc. SPIE 0400, New Optical Materials*. Edited by S. Musikant and J. Dupuy. International Society for Optics and Photonics, Geneva, Switzerland, 1983.

163. J. Savage, K. Lewis, B. Kinsman, A. Wilson, and R. Riddle, "Fabrication of Infrared Optical Ceramics in the $CaLa_2S_4$-$La_2S_3$ Solid Solution System"; pp. 79-84 in *Proc. SPIE 0683, Infrared and Optical Transmitting Materials*. Edited by R. W. Schwartz. International Society for Optics and Photonics, San Diego, CA, 1986.

164. D. L. Chess, C. A. Chess, J. V. Biggers, and W. B. White, "Processing Ternary Sulfide Ceramics: Powder Preparation, Sintering, and Hot-Pressing," *J. Am. Ceram. Soc.,* **66** [1] 18-22 (1983).

165. D. L. Chess, C. A. Chess, and W. B. White, "Precursor Powders for Sulfide Ceramics Prepared by Evaporative Decomposition of Solutions," *J. Am. Ceram. Soc.,* **66** [11] c205-7 (1983).

166. D. L. Chess, C. A. Chess, J. A. Marks, and W. B. White, "Phase Equilibria and Processing of Infrared Optical Ceramics on the Join $CaLa_2S_4$-$La_2S_3$," *J. Ceram. Process. Res,* **11** [4] 465-70 (2010).

167. D. W. Roy, "Progress in the Development of Ternary Sulfides for Use from 8 to 14 μm"; pp. 24-35 in *Proc. SPIE 0297, Emerging Optical Materials*. Edited by S. Musikant. International Society for Optics and Photonics, San Diego, CA, 1982.

168. R. L. Gentilman, M. B. Dekosky, T. Y. Wong, R. W. Tustison, and M. E. Hills, "Calcium Lanthanum Sulfide as a Long Wavelength IR Material"; pp. 57-65 in *Proc. SPIE 0929, Infrared Optical Materials IV*. Edited by S. Musikant. International Society for Optics and Photonics, Orlando, FL, 1988.

169. M. E. Hills, "Preparation, Properties, and Development of Calcium Lanthanum Sulfide as an 8- to 12-Micrometer Transmitting Ceramic," DTIC Document NWC-TP-7037, Naval Weapons Center, China Lake, CA, September 1989.

170. K. J. Saunders and R. L. Gentilman, "Optical Material and Process for Making the Same," U.S. Pat. 4,765,931, August 1988.

171. J. Covino, D. C. Harris, M. E. Hills, R. T. Loda, and R. W. Schwartz, "Development of Calcium Lanthanum Sulfide as an 8-12μm Transmitting Ceramic"; pp. 42-6 in *Proc. SPIE 0505, Advances in Optical Materials*. Edited by S. Musikant. International Society for Optics and Photonics, San Diego, CA, 1984.

172. D. C. Harris, M. E. Hills, R. L. Gentilman, K. Saunders, and T. Wong, "Fabrication and ESR Characterization of Transparent $CaLa_2S_4$," *Adv. Ceram. Mater.,* **2**, 74-8 (1987).

173. Y. Han and M. Akinc, "Preparation of Calcium Lanthanum Sulfide Powders Via Alkoxide Sulfurization," *J. Am. Ceram. Soc.,* **74** [11] 2815-9 (1991).

174. L. H. Wang and M. H. Hon, "Effects of Sulfidization and Sintering Temperatures of $CaLa_2S_4$ Powder on Its Optical Property," *Jpn. J. Appl. Phys.,* **31** [7R] 2177-80 (1992).

175. L. H. Wang, M. H. Hon, W. L. Huang, and W. Y. Lin, "Formation and Densification of $CaLa_2S_4$ Powders by Sulfidization of Metal Alkoxides," *Mater. Sci. Eng. B,* **7** [3] 237-42 (1990).

176. L. H. Wang, M. H. Hon, W. L. Huang, and W. Y. Lin, "Processing and Densification of $CaLa_2S_4$ Powder through Alkoxide Route," *Mater. Res. Bull.,* **26** [7] 649-58 (1991).

177. L. H. Wang and M. H. Hon, "Investigation of $CaLa_2S_4$ Powder Prepared by Sulphurization of Coprecipitated Carbonates," *J. Mater. Sci.,* **28** [9] 2304-10 (1993).

178. L. H. Wang, M. H. Hon, W. L. Huang, and W. Y. Lin, "Sulphurization of Coprecipitated Carbonates for Formation of $CaLa_2S_4$," *J. Mater. Sci.,* **26** [18] 5013-8 (1991).

179. L. H. Wang, M. S. Tsai, and M. H. Hon, "Dispersion of Precursors for Improving the Homogeneity and Sinterability of $CaLa_2S_4$ Powders," *Mater. Chem. Phys.,* **35** [1] 64-70 (1993).

180. L. H. Wang, "Processing and Densification of $CaLa_2S_4$ Powder by the Acetates Route," *J. Mater. Sci. Lett.,* **12** [4] 212-4 (1993).

181. L. H. Wang and M. H. Hon, "Powder and Pellet Fabrication of $CaLa_2S_4$-$PbLa_2S_4$ Solid Solution," *Scripta Mater.,* **26** [3] 455-9 (1992).

182. B. J. Tsay, L. H. Wang, and M. H. Hon, "Formation and Densification of $Pb_{0.1}Ca_{0.9}La_2S_4$ Powders by Sulfidization of Modified Metal Alkoxides," *Ceram. Int.,* **25** [4] 303-8 (1999).

183. B. J. Tsay, L. H. Wang, and M. H. Hon, "Formation and Densification of $CaLa_2S_4$ Powders by Sulfidization of Modified Metal Alkoxides in Different Atmospheres," *Mater. Sci. Eng. B,* **72** [1] 31-5 (2000).

184. M. S. Tsai and M. H. Hon, "The Effects of Sulphurizing Agent on the Formation of Calcium Lanthanum Sulphide," *Mater. Sci. Eng. B,* **26** [1] 29-33 (1994).

185. M. S. Tsai, L. H. Wang, and M. H. Hon, "Formation of Calcium Lanthanum Sulfide by Carbonate Coprecipitation and $CS_2$ Sulfurization," *J. Am. Ceram. Soc.,* **78** [5] 1185-90 (1995).

186. M. S. Tsai and M. H. Hon, "Hot-Press Sintering and the Properties of Lanthanum-Rich Calcium Lanthanum Sulfide Ceramic," *J. Mater. Res.,* **9** [11] 2939-43 (1994).

187. M. S. Tsai and M. H. Hon, "Fabrication of Calcium Lanthanum Sulfide Ceramic by Carbonate Coprecipitating Method," *Scripta Mater.,* **32** [5] 713-8 (1995).

188. O. Merdrignac-Conanec, G. Durand, S. Walfort, N. Hakmeh, and X. Zhang, "Elaboration of $CaLa_2S_4$ Transparent Ceramics from Novel Precursor Powders Route," *Ceram. Int.,* **43** [8] 5984-9 (2017).

189. S. S. Bayya, W. Kim, J. S. Sanghera, G. R. Villalobos, and I. D. Aggarwal, "Calcium Lanthanoid Sulfide Powders, Methods of Making, and Ceramic Bodies Formed Therefrom," U.S. Pat. 9,809,501, November 2017.

190. B. Shaw, M. Hunt, W. Kiim, S. Bayya, D. Boyd, C. Brown, S. Bowman, and J. Sanghera, "Fabrication and Spectroscopy $Pr^{3+}$ Doped Ceramic Calcium Lanthanum Sulfide for Mid-IR Laser Gain Material"; pp. MM3C.5 in *Mid-Infrared Coherent Sources in Proceedings High-Brightness Sources and Light-Driven Interactions*. Optical Society of America, Strasbourg, France, 2018.

191. L. B. Shaw, M. Hunt, W. Kim, S. Bayya, C. Brown, S. Bowman, and J. S. Sanghera, "$Pr^{3+}$ Doped Ceramic Calcium Lanthanum Sulfide for Mid-IR Laser Gain Material"; pp. JTu5A.114 in *CLEO: Science and Innovations in Proceedings Conference on Lasers and Electro-Optics*. Optical Society of America, San Jose, CA, 2017.

192. D. Jiang and A. K. Mukherjee, "Spark Plasma Sintering of an Infrared-Transparent $Y_2O_3$–MgO Nanocomposite," *J. Am. Ceram. Soc.,* **93** [3] 769-73 (2010).

193. H. J. Ma, W. K. Jung, C. Baek, and D. K. Kim, "Influence of Microstructure Control on Optical and Mechanical Properties of Infrared Transparent $Y_2O_3$-MgO Nanocomposite," *J. Eur. Ceram. Soc.,* **37** [15] 4902-11 (2017).

194. J. Wang, D. Chen, E. H. Jordan, and M. Gell, "Infrared-Transparent $Y_2O_3$–MgO Nanocomposites Using Sol–Gel Combustion Synthesized Powder," *J. Am. Ceram. Soc.,* **93** [11] 3535-8 (2010).

195. S. Xu, J. Li, H. Kou, Y. Shi, Y. Pan, and J. Guo, "Spark Plasma Sintering of $Y_2O_3$–MgO Composite Nanopowder Synthesized by the Esterification Sol–Gel Route," *Ceram. Int.,* **41** [2] 3312-7 (2015).

196. S. Xu, J. Li, C. Li, Y. Pan, and J. Guo, "Infrared-Transparent $Y_2O_3$–MgO Nanocomposites Fabricated by the Glucose Sol–Gel Combustion and Hot-Pressing Technique," *J. Am. Ceram. Soc.,* **98** [9] 2796-802 (2015).

197. H. J. Ma, W. K. Jung, Y. Park, and D. K. Kim, "A Novel Approach of an Infrared Transparent Er:$Y_2O_3$–MgO Nanocomposite for Eye-Safe Laser Ceramics," *Journal of Materials Chemistry C,* **6** [41] 11096-103 (2018).

198. V. L. Blair, Z. D. Fleischman, L. D. Merkle, N. Ku, and C. A. Moorehead, "Co-Precipitation of Rare-Earth-Doped $Y_2O_3$ and MgO Nanocomposites for Mid-Infrared Solid-State Lasers," *Appl. Optics,* **56** [3] B154-8 (2017).

199. D. C. Harris, L. R. Cambrea, L. F. Johnson, R. T. Seaver, M. Baronowski, R. Gentilman, C. Scott Nordahl, T. Gattuso, S. Silberstein, and P. Rogan, "Properties of an Infrared-Transparent MgO:$Y_2O_3$ Nanocomposite," *J. Am. Ceram. Soc.,* **96** [12] 3828-35 (2013).

200. A. D. Gledhill, D. Li, T. Mroz, L. M. Goldman, and N. P. Padture, "Strengthening of Transparent Spinel/$Si_3N_4$ Nanocomposites," *Acta Mater.,* **60** [4] 1570-5 (2012).

201. J. Zhang, W. W. Chen, A. J. Ardell, and B. Dunn, "Solid-State Phase Equilibria in the ZnS-$Ga_2S_3$ System," *J. Am. Ceram. Soc.,* **73** [6] 1544-7 (1990).

202. W. Chen, J. Zhang, A. Ardell, and B. Dunn, "Solid-State Phase Equilibria in the ZnS-CdS System," *Mater. Res. Bull.,* **23** [11] 1667-73 (1988).

203. J. Zhang, W. W. Chen, and A. J. Ardell, "Solid Solution Strengthening of ZnS"; pp. 93-8 in *Proc. SPIE 1326, Window and Dome Technologies and Materials II*. Edited by P. Klocek. International Society for Optics and Photonics, San Diego, CA, 1990.

204. L. A. Xue and R. Raj, "Influence of Green State Processing on the Properties of Diamond/Zinc Sulphide Composites," *J. Mater. Sci.,* **27** [11] 3021-5 (1992).

205. L. A. Xue and R. Raj, "Effect of Diamond Dispersion on the Superplastic Rheology of Zinc Sulfide," *J. Am. Ceram. Soc.,* **73** [8] 2213-6 (1990).

206. L. Xue, T. Noh, A. Sievers, and R. Raj, "Optical Properties of ZnS/Diamond Composites"; pp. 183-96 in *Proc. SPIE 1534, Diamond Optics IV*. Edited by A. Feldman and S. Holly. International Society for Optics and Photonics, San Diego, CA, 1991.

207. D. S. Farquhar, R. Raj, and S. L. Phoenix, "Fracture and Stiffness Characteristics of Particulate Composites of Diamond in Zinc Sulfide," *J. Am. Ceram. Soc.,* **73** [10] 3074-80 (1990).

208. L. Xue, D. Farquhar, T. Noh, A. Sievers, and R. Raj, "Optical and Mechanical Properties of Zinc Sulphide Diamond Composites," *Acta Metall. Mater.,* **38** [9] 1743-52 (1990).

209. A. Fujii, H. Wada, K.-I. Shibata, S. Nakayama, and M. Hasegawa, "Diamond-ZnS Composite Infrared Window"; pp. 206-17 in *Proc. SPIE 4375, Window and Dome Technologies and Materials VII*. Edited by R. W. Tustison. International Society for Optics and Photonics, Orlando, FL, 2001.

210. Y. Han and M. Akinc, "Zinc Sulfide/Gallium Phosphide Composites by Chemical Vapor Transport," *J. Am. Ceram. Soc.,* **78** [7] 1834-40 (1995).

211. Y. Han, E. T. Voiles, L. S. Chumbley, M. Akinc, A. A. Naiini, and J. G. Verkade, "Synthesis and Characterization of Zinc Sulfide/Gallium Phosphide Nanocomposite Powders," *J. Am. Ceram. Soc.,* **77** [12] 3153-60 (1994).

212. M. Akinc and Y. Han, "Synthesis and Consolidation of ZnS/Gap Powders"; pp. 533-42 in *Fine Particles Science and Technology.* Edited by E. Pelizzetti. Kluwer Academic Publishers, Norwell, MA, 1996.

213. J. M. Wahl, R. L. Gentilman, R. W. Tustison, C. S. Nordahl, H. Q. Nguyen, and R. Korenstein, "Long Wave Infrared Transparent Window and Coating Materials," U.S. Pat. Application No. 15/979,920, September 2018.

214. S. Li, J. Lian, and Q. Jiang, "Modeling Size and Surface Effects on ZnS Phase Selection," *Chem. Phys. Lett.,* **455** [4] 202-6 (2008).

215. C. S. Tiwary, S. Saha, P. Kumbhakar, and K. Chattopadhyay, "Observation of Combined Effect of Temperature and Pressure on Cubic to Hexagonal Phase

Transformation in ZnS at the Nanoscale," *Crystal Growth & Design,* **14** [9] 4240-6 (2014).

216. S. Chen and Y. Wu, "New Opportunities for Transparent Ceramics," *Am. Ceram. Soc. Bull.,* **92** [2] 32-7 (2013).

217. H. P. Klug and L. E. Alexander, *X-Ray Diffraction Procedures: For Polycrystalline and Amorphous Materials*, 2nd ed.; Ch. 9. John Wiley & Sons, New York, 1974.

218. C. S. Tiwary, C. Srivastava, and P. Kumbhakar, "Onset of Sphalerite to Wurtzite Transformation in ZnS Nanoparticles," *J. Appl. Phys.,* **110** [3] 034908-1-7 (2011).

219. B. Gilbert, H. Zhang, F. Huang, M. P. Finnegan, G. A. Waychunas, and J. F. Banfield, "Special Phase Transformation and Crystal Growth Pathways Observed in Nanoparticles," *Geochem. Trans,* **4** [4] 20-7 (2003).

220. R. Dingreville, J. Qu, and M. Cherkaoui, "Surface Free Energy and Its Effect on the Elastic Behavior of Nano-Sized Particles, Wires and Films," *J. Mech. Phys. Solids,* **53** [8] 1827-54 (2005).

221. F. Lee and K. J. Bowman, "Texture and Anisotropy in Silicon Nitride," *J. Am. Ceram. Soc.,* **75** [7] 1748-55 (1992).

222. M. S. Jensen, M. A. Einarsrud, and T. Grande, "Preferential Grain Orientation in Hot Pressed $TiB_2$," *J. Am. Ceram. Soc.,* **90** [4] 1339-41 (2007).

223. I. Steinberger, I. Kiflawi, Z. Kalman, and S. Mardix, "The Stacking Faults and Partial Dislocations Involved in Structure Transformations of ZnS Crystals," *Philos. Mag.,* **27** [1] 159-75 (1973).

224. R. W. Balluffi, S. Allen, and W. C. Carter, *Kinetics of Materials*. John Wiley & Sons, Hoboken, NJ, 2005.

225. H. Blank, P. Delavignette, and S. Amelinckx, "Dislocations and Wide Stacking Faults in Wurtzite Type Crystals: Zinc Sulfide and Aluminium Nitride," *Phys. Status Solidi B,* **2** [12] 1660-9 (1962).

226. C. Borchers, D. Stichtenoth, S. Müller, D. Schwen, and C. Ronning, "Catalyst–Nanostructure Interaction and Growth of ZnS Nanobelts," *Nanotechnology,* **17**, [4] 1067-71 (2006).

227. S. Takeuchi, K. Suzuki, K. Maeda, and H. Iwanaga, "Stacking-Fault Energy of II–VI Compounds," *Philos. Mag. A,* **50** [2] 171-8 (1985).

228. R. W. Rice, *Mechanical Properties of Ceramics and Composites: Grain and Particle Effects*. Marcel Dekker, New York, 2000.

229. A. G. Evans and R. Cannon, "Overview No. 48: Toughening of Brittle Solids by Martensitic Transformations," *Acta Metall.,* **34** [5] 761-800 (1986).

230. J. H. Song, T. Atay, S. Shi, H. Urabe, and A. V. Nurmikko, "Large Enhancement of Fluorescence Efficiency from CdSe/ZnS Quantum Dots Induced by Resonant Coupling to Spatially Controlled Surface Plasmons," *Nano Lett.,* **5** [8] 1557-61 (2005).

231. A. Kudo and M. Sekizawa, "Photocatalytic $H_2$ Evolution under Visible Light Irradiation on Ni-Doped ZnS Photocatalyst," *Chem. Commun.,* [15] 1371-2 (2000).

232. H. Hu and W. Zhang, "Synthesis and Properties of Transition Metals and Rare-Earth Metals Doped ZnS Nanoparticles," *Opt. Mater.,* **28** [5] 536-50 (2006).

233. A. A. Khosravi, M. Kundu, L. Jatwa, S. Deshpande, U. Bhagwat, M. Sastry, and S. Kulkarni, "Green Luminescence from Copper Doped Zinc Sulphide Quantum Particles," *Appl. Phys. Lett.,* **67** [18] 2702-4 (1995).

234. P. Yang, M. Lü, D. Xü, D. Yuan, J. Chang, G. Zhou, and M. Pan, "Strong Green Luminescence of $Ni^{2+}$-Doped ZnS Nanocrystals," *Appl. Phys. A Mater. Sci. Process.,* **74** [2] 257-9 (2002).

235. Y. Li and Y. Wu, "Spectroscopic Characteristics of ($Mn^{2+}$, $Nd^{3+}$) Co-Doped Zinc Sulfide Nanocrystals," *Opt. Mater.,* **49**, 100-4 (2015).

236. S. Ummartyotin, N. Bunnak, J. Juntaro, M. Sain, and H. Manuspiya, "Synthesis and Luminescence Properties of ZnS and Metal (Mn, Cu)-Doped-ZnS Ceramic Powder," *Solid State Sci.,* **14** [3] 299-304 (2012).

237. L. D. DeLoach, R. H. Page, G. D. Wilke, S. Payne, and W. F. Krupke, "Transition Metal-Doped Zinc Chalcogenides: Spectroscopy and Laser Demonstration of a New Class of Gain Media," *IEEE. J. Quantum. Elect.,* **32** [6] 885-95 (1996).

238. I. Moskalev, V. Fedorov, and S. Mirov, "10-Watt, Pure Continuous-Wave, Polycrystalline $Cr^{2+}$:ZnS Laser," *Opt. Express,* **17** [4] 2048-56 (2009).

239. S. Wang, S. B. Mirov, V. V. Fedorov, and R. P. Camata, "Synthesis and Spectroscopic Properties of Cr-Doped ZnS Crystalline Thin Films"; pp. 13-20 in *Proc. SPIE 5332, Solid State Lasers XIII: Technology and Devices*. Edited by R. Scheps and H. J. Hoffman. International Society for Optics and Photonics, San Jose, CA, 2004.

240. D. Martyshkin, V. Fedorov, C. Kim, I. Moskalev, and S. Mirov, "Mid-IR Random Lasing of Cr-Doped ZnS Nanocrystals," *J. Opt.,* **12** [2] 024005-1-5 (2010).

241. N. Tolstik, E. Sorokin, and I. T. Sorokina, "Kerr-Lens Mode-Locked Cr:ZnS Laser," *Opt. Lett.,* **38** [3] 299-301 (2013).

242. E. Sorokin, N. Tolstik, and I. T. Sorokina, "1 Watt Femtosecond Mid-IR Cr:ZnS Laser"; pp. 859916-1-7 in *Proc. SPIE 8599, Solid State Lasers XXII: Technology and Devices*. Edited by W. A. Clarkson and R. Shori. International Society for Optics and Photonics, San Francisco, CA, 2013.

243. S. Vasilyev, M. Mirov, and V. Gapontsev, "Kerr-Lens Mode-Locked Femtosecond Polycrystalline $Cr^{2+}$:ZnS and $Cr^{2+}$:ZnSe Lasers," *Opt. Express,* **22** [5] 5118-23 (2014).

244. S. Vasilyev, I. Moskalev, M. Mirov, S. Mirov, and V. Gapontsev, "Three Optical Cycle Mid-IR Kerr-Lens Mode-Locked Polycrystalline $Cr^{2+}$:ZnS Laser," *Opt. Lett.,* **40** [21] 5054-7 (2015).

245. S. Vasilyev, I. Moskalev, M. Mirov, S. Mirov, and V. Gapontsev, "Multi-Watt Mid-IR Femtosecond Polycrystalline $Cr^{2+}$:ZnS and $Cr^{2+}$:ZnSe Laser Amplifiers with the Spectrum Spanning 2.0–2.6 μm," *Opt. Express,* **24** [2] 1616-23 (2016).

246. N. Vlasenko, P. Oleksenko, M. Mukhlyo, L. Veligura, and Z. Denisova, "Stimulated Emission of $Cr^{2+}$ Ions in ZnS:Cr Thin–Film Electroluminescent Structures," *Semicond. Phys. Quantum Electron. Optoelectron.,* **12** [4] 362-5 (2009).

247. M. Nematollahi, X. Yang, L. M. S. Aas, Z. Ghadyani, M. Kildemo, U. J. Gibson, and T. W. Reenaas, "Molecular Beam and Pulsed Laser Deposition of ZnS:Cr for Intermediate Band Solar Cells," *Sol. Energ. Mater. Sol. C.,* **141**, 322-30 (2015).

248. T. Xiao-Ming, K. Xiao-Yu, and Z. Kang-Wei, "EPR Theoretical Study of Local Lattice Structure in ZnS:$Cr^{2+}$ System," *Solid State Commun.,* **136** [7] 395-9 (2005).

249. M. Brik, "First-Principles Calculations of Crystal Field Effects and Absorption Spectra for 3d Ions in Laser Crystals"; pp. 203-50 in *Optical Properties of 3d-Ions in Crystals: Spectroscopy and Crystal Field Analysis.* Edited by N. M. Avram and M. G. Brik. Springer-Verlag Berlin Heidelberg, New York, 2013.

250. M. Chen, H. Cui, W. Li, H. Kou, J. Li, Y. Pan, and B. Jiang, "Reparative Effect of Diffusion Process on Host Defects in $Cr^{2+}$ Doped ZnS/ZnSe," *J. Alloy. Compd.,* **597**, 124-8 (2014).

251. L. Esposito, A. Piancastelli, and S. Martelli, "Production and Characterization of Transparent $MgAl_2O_4$ Prepared by Hot Pressing," *J. Eur. Ceram. Soc.,* **33** [4] 737-47 (2013).

252. Z. Liu, B. Mei, J. Song, and W. Li, "Optical Characterizations of Hot-Pressed Erbium-Doped Calcium Fluoride Transparent Ceramic," *J. Am. Ceram. Soc.,* **97** [8] 2506-10 (2014).

253. W. Kim, C. Baker, S. Bowman, C. Florea, G. Villalobos, B. Shaw, B. Sadowski, M. Hunt, I. Aggarwal, and J. Sanghera, "Laser Oscillation from $Ho^{3+}$ Doped $Lu_2O_3$ Ceramics," *Opt. Mater. Express,* **3** [7] 913-9 (2013).

254. W. Kim, C. Baker, G. Villalobos, J. Frantz, B. Shaw, J. Sanghera, B. Sadowski, and I. Aggarwal, "Laser Based on Highly Doped $Lu_2O_3$ Ceramics," *J. Dir. Energy,* **5** [1] 93-104 (2013).

255. G. Grebe and H. J. Schulz, "Luminescence of $Cr^{2+}$ Centres and Related Optical Interactions Involving Crystal Field Levels of Chromium Ions in Zinc Sulfide," *Z. Naturforsch. A Phys. Sci.,* **29** [12] 1803-19 (1974).

256. H. Nelkowski and G. Grebe, "IR-Luminescence of ZnS:Cr," *J. Lumin.,* **1**, 88-93 (1970).

257. B. Henderson and R. H. Bartram, *Crystal-Field Engineering of Solid-State Laser Materials*. Cambridge University Press, Cambridge, UK, 2005.

258. I. T. Sorokina, E. Sorokin, S. Mirov, V. Fedorov, V. Badikov, V. Panyutin, A. Di Lieto, and M. Tonelli, "Continuous-Wave Tunable $Cr^{2+}$:ZnS Laser," *Appl. Phys. B: Lasers Opt.,* **74** [6] 607-11 (2002).

259. C. S. Kelley and F. Williams, "Optical Absorption Spectra of Chromium-Doped Zinc Sulfide Crystals," *Phys. Rev. B,* **2** [1] 3 (1970).

260. T. Trindade, P. O'Brien, X. M. Zhang, and M. Motevalli, "Synthesis of PbS Nanocrystallites Using a Novel Single Moleculeprecursors Approach: X-Ray Single-Crystal Structure of $Pb(S_2CNEtPr^i)_2$," *J. Mater. Chem.,* **7** [6] 1011-6 (1997).

261. S. L. Castro, S. G. Bailey, R. P. Raffaelle, K. K. Banger, and A. F. Hepp, "Synthesis and Characterization of Colloidal $CuInS_2$ Nanoparticles from a Molecular Single-Source Precursor," *J. Phys. Chem. B,* **108** [33] 12429-35 (2004).

262. T. Duan, W. Lou, X. Wang, and Q. Xue, "Size-Controlled Synthesis of Orderly Organized Cube-Shaped Lead Sulfide Nanocrystals via a Solvothermal Single-Source Precursor Method," *Colloids Surf. A,* **310** [1] 86-93 (2007).

263. J. Tauc, R. Grigorovici, and A. Vancu, "Optical Properties and Electronic Structure of Amorphous Germanium," *Phys. Status. Solidi. B,* **15** [2] 627-37 (1966).

264. R. G. Pearson, "Hard and Soft Acids and Bases," *J. Am. Chem. Soc.,* **85** [22] 3533-9 (1963).

265. S. Lowell, J. E. Shields, M. A. Thomas, and M. Thommes, *Characterization of Porous Solids and Powders: Surface Area, Pore Size and Density*. Springer Science & Business Media, Norwell, MA, 2012.

266. C. Lowe-Ma, "Characterization of Rare Earth Sulfides"; pp. 267-79 in Materials Science and Research, Vol. 15, *Advances in Materials Characterization*. Edited by D. R. Rossington, R. A. Condrate, and R. L. Snyder. Springer Science & Business Media, New York, 1983.

267. B. Ullrich, D. Ariza-Flores, and M. Bhowmick, "Intrinsic Photoluminescence Stokes Shift in Semiconductors Demonstrated by Thin-Film CdS Formed with Pulsed-Laser Deposition," *Thin Solid Films,* **558**, 24-6 (2014).

268. C. H. Ye, X. S. Fang, M. Wang, and L. D. Zhang, "Temperature-Dependent Photoluminescence from Elemental Sulfur Species on ZnS Nanobelts," *J. Appl. Phys.,* **99** [6] 063504-1-4 (2006).

269. L. H. Wang, M. H. Hon, W. L. Huang, and W. Y. Lin, "Phase Development in the Formation of $CaLa_2S_4$ Powder and Pellet," *Ceram. Int.,* **18** [1] 27-33 (1992).

270. O. Guillon, J. Gonzalez-Julian, B. Dargatz, T. Kessel, G. Schierning, J. Räthel, and M. Herrmann, "Field-Assisted Sintering Technology/Spark Plasma Sintering: Mechanisms, Materials, and Technology Developments," *Adv. Eng. Mater.,* **16** [7] 830-49 (2014).

271. Z. H. Ge, B. P. Zhang, P. P. Shang, and J. F. Li, "Control of Anisotropic Electrical Transport Property of $Bi_2S_3$ Thermoelectric Polycrystals," *J. Mater. Chem.,* **21** [25] 9194-200 (2011).

272. L. D. Zhao, B. P. Zhang, W. S. Liu, H. L. Zhang, and J. F. Li, "Enhanced Thermoelectric Properties of Bismuth Sulfide Polycrystals Prepared by Mechanical Alloying and Spark Plasma Sintering," *J. Solid State Chem.,* **181** [12] 3278-82 (2008).

273. Q. Tan and J. F. Li, "Thermoelectric Properties of Sn-S Bulk Materials Prepared by Mechanical Alloying and Spark Plasma Sintering," *J. Electron. Mater.,* **43** [6] 2435-9 (2014).

274. Z. H. Ge, B. P. Zhang, Y. X. Chen, Z. X. Yu, Y. Liu, and J. F. Li, "Synthesis and Transport Property of $Cu_{1.8}S$ as a Promising Thermoelectric Compound," *Chem. Commun.,* **47** [47] 12697-9 (2011).

275. X. Xu, Z. Wen, X. Yang, and L. Chen, "Dense Nanostructured Solid Electrolyte with High Li-Ion Conductivity by Spark Plasma Sintering Technique," *Mater. Res. Bull.,* **43** [8] 2334-41 (2008).

276. T. Takeuchi, H. Kageyama, K. Nakanishi, M. Tabuchi, H. Sakaebe, T. Ohta, H. Senoh, T. Sakai, and K. Tatsumi, "All-Solid-State Lithium Secondary Battery with $Li_2S$-C Composite Positive Electrode Prepared by Spark-Plasma-Sintering Process," *J. Electrochem. Soc.,* **157** [11] A1196-201 (2010).

277. V. Zestrea, V. Kodash, V. Felea, P. Petrenco, D. Quach, J. R. Groza, and V. Tsurkan, "Structural and Magnetic Properties of $FeCr_2S_4$ Spinel Prepared by Field-Activated Sintering and Conventional Solid-State Synthesis," *J. Mater. Sci.,* **43** [2] 660-4 (2008).

278. B. E. Warren, *X-Ray Diffraction*; Ch. 13. Dover Publications, New York, 1990.

279. D. Richerson, D. W. Richerson, and W. E. Lee, *Modern Ceramic Engineering: Properties, Processing, and Use in Design*, 3rd ed.; Ch. 14. CRC Press, Boca Raton, FL, 2005.

280. G. Bernard-Granger and C. Guizard, "Spark Plasma Sintering of a Commercially Available Granulated Zirconia Powder: I. Sintering Path and Hypotheses about the Mechanism(s) Controlling Densification," *Acta Mater.,* **55** [10] 3493-504 (2007).

281. G. Bernard-Granger, A. Addad, G. Fantozzi, G. Bonnefont, C. Guizard, and D. Vernat, "Spark Plasma Sintering of a Commercially Available Granulated Zirconia Powder: Comparison with Hot-Pressing," *Acta Mater.,* **58** [9] 3390-9 (2010).

282. R. L. Coble, "Diffusion Models for Hot Pressing with Surface Energy and Pressure Effects as Driving Forces," *J. Appl. Phys.,* **41** [12] 4798-807 (1970).

283. R. J. Brook, E. Gilbert, D. Hind, and J. M. Vieira, "Hot-Pressing Dilatometry in the Study of Sintering Mechanisms"; pp. 585-90 in *Sintering-Theory and Practice: Proceedings of the 5th International Round Table Conference on Sintering*. Edited by D. Kolar, S. Pejovnik, and M. M. Ristić. Elsevier, Amsterdam, Netherlands, 1982.

284. R. K. Bordia and R. Raj, "Sintering of $TiO_2$–$Al_2O_3$ Composites: A Model Experimental Investigation," *J. Am. Ceram. Soc.,* **71** [4] 302-10 (1988).

285. A. K. Mukherjee, J. E. Bird, and J. E. Dorn, "Experimental Correlations for High-Temperature Creep," Tech. Rept. UCRL-18526, University of California, Berkeley, Lawrence Radiation Lab, Berkeley, CA, October 1968.

286. A. Helle, K. E. Easterling, and M. Ashby, "Hot-Isostatic Pressing Diagrams: New Developments," *Acta Metall.,* **33** [12] 2163-74 (1985).

287. R. Chaim, "Densification Mechanisms in Spark Plasma Sintering of Nanocrystalline Ceramics," *Mater. Sci. Eng. A,* **443** [1] 25-32 (2007).

288. J. G. Santanach, A. Weibel, C. Estournès, Q. Yang, C. Laurent, and A. Peigney, "Spark Plasma Sintering of Alumina: Study of Parameters, Formal Sintering Analysis and Hypotheses on the Mechanism(s) Involved in Densification and Grain Growth," *Acta Mater.,* **59** [4] 1400-8 (2011).

289. U. Anselmi-Tamburini, S. Gennari, J. Garay, and Z. A. Munir, "Fundamental Investigations on the Spark Plasma Sintering/Synthesis Process: II. Modeling of Current and Temperature Distributions," *Mater. Sci. Eng. A,* **394** [1] 139-48 (2005).

290. J. Besson and M. Abouaf, "Grain Growth Enhancement in Alumina During Hot Isostatic Pressing," *Acta Metall. Mater.,* **39** [10] 2225-34 (1991).

291. N. Murayama and W. Shin, "Effect of Rapid Heating on Densification and Grain Growth in Hot Pressed Alumina," *J. Ceram. Soc. Jpn.,* **108** [1261] 799-802 (2000).

292. Y. Gotoh, J. Akimoto, M. Goto, Y. Oosawa, and M. Onoda, "The Layered Composite Crystal Structure of the Ternary Sulfide $(BiS)_{1.11}NbS_2$," *J. Solid State Chem.,* **116** [1] 61-7 (1995).

293. G. Bernard-Granger, N. Benameur, C. Guizard, and M. Nygren, "Influence of Graphite Contamination on the Optical Properties of Transparent Spinel Obtained by Spark Plasma Sintering," *Scripta Mater.,* **60** [3] 164-7 (2009).

294. N. Tamari, T. Tanaka, K. Tanaka, I. Kondoh, M. Kawahara, and M. Tokita, "Effect of Spark Plasma Sintering on Densification and Mechanical Properties of Silicon Carbide," *J. Ceram. Soc. Jpn.,* **103** [1199] 740-2 (1995).

295. A. L. Chamberlain, W. G. Fahrenholtz, and G. E. Hilmas, "Low-Temperature Densification of Zirconium Diboride Ceramics by Reactive Hot Pressing," *J. Am. Ceram. Soc.,* **89** [12] 3638-45 (2006).

296. R. W. Rice, C. C. Wu, and F. Boichelt, "Hardness-Grain-Size Relations in Ceramics," *J. Am. Ceram. Soc.,* **77** [10] 2539-53 (1994).

297. M. K. Mani, G. Viola, M. J. Reece, J. P. Hall, and S. L. Evans, "Fabrication of Carbon Nanotube Reinforced Iron Based Magnetic Alloy Composites by Spark Plasma Sintering," *J. Alloy. Compd.,* **601**, 146-53 (2014).

298. K. B. Alexander, P. F. Becher, S. B. Waters, and A. Bleier, "Grain Growth Kinetics in Alumina–Zirconia (CeZTA) Composites," *J. Am. Ceram. Soc.,* **77** [4] 939-46 (1994).

299. X. L. Wang, J. Y. Shi, Z. C. Feng, M. R. Li, and C. Li, "Visible Emission Characteristics from Different Defects of ZnS Nanocrystals," *Phys. Chem. Chem. Phys.,* **13** [10] 4715-23 (2011).

300. S. Mardix, Z. Kalman, and I. Steinberger, "Periodic Slip Processes and the Formation of Polytypes in Zinc Sulphide Crystals," *Acta Cryst. A,* **24** [4] 464-9 (1968).

301. C. Ma, D. Moore, J. Li, and Z. L. Wang, "Nanobelts, Nanocombs, and Nanowindmills of Wurtzite ZnS," *Adv. Mater.,* **15** [3] 228-31 (2003).

# PUBLICATION LIST

**Sulfide-Based Optical Ceramics:**

**Y. Li**, L. Zhang, K. Kisslinger, and Y. Wu, "Field-Assisted Sintering and Phase Transition of ZnS-$CaLa_2S_4$ Composite Ceramics," *J. Eur. Ceram. Soc.,* **37** [15] 4741-9 (2017) (feature article).

**Y. Li**, and Y. Wu, "Sintering Behavior of Calcium Lanthanum Sulfide Ceramics in Field Assisted Consolidation," *J. Am. Ceram. Soc.,* **100** [11] 5011-9 (2017).

**Y. Li**, Y. Liu, V.V. Fedorov, S.B. Mirov, and Y. Wu, "Hot-Pressed Chromium Doped Zinc Sulfide Infrared Transparent Ceramics," *Scr. Mater.,* **125**, 15-8 (2016).

**Y. Li**, L. Zhang, and Y. Wu, "Synthesis and Characterization of Calcium Lanthanum Sulfide via a Wet Chemistry Route Followed by Thermal Decomposition," *RSC Adv.,* **6** [41] 34935-9 (2016).

**Y. Li**, and Y. Wu, "Spectroscopic Characteristics of ($Mn^{2+}$, $Nd^{3+}$) Co-Doped Zinc Sulfide Nanocrystals," *Opt. Mater.,* **49**, 100-4 (2015).

**Y. Li**, and Y. Wu, "Transparent and Luminescent ZnS Ceramics Consolidated by Vacuum Hot Pressing Method," *J. Am. Ceram. Soc.,* **98** [10] 2972-5 (2015).

**Y. Li**, L. Zhang, K. Kisslinger, and Y. Wu, "Green Phosphorescence of Zinc Sulfide Optical Ceramics," *Opt. Mater. Express,* **4** [6] 1140-50 (2014).

J. Yin, **Y. Li**, and Y. Wu, "Near-Net-Shape Processed ZnS Ceramics by Aqueous Casting and Pressureless Sintering," *Ceram. Int.,* **42** [9] 11504-8 (2016).

**Y. Li**, W. Tan, and Y. Wu, "Phase Transition between Sphalerite and Wurtzite in ZnS Optical Ceramic Materials," to be submitted.

**Y. Li**, and Y. Wu, "Investigation into Syntheses of Calcium Lanthanum Sulfide with and without High-Temperature Sulfurization," to be submitted.

**Other Optical and Electronic Ceramics:**

Y. Liu, **Y. Li**, and Y. Wu, "Low-Temperature Crystal Growth of Yb:$Sr_5F(PO_4)_3$ without Evident Thermal Runaway," *J. Am. Ceram. Soc.,* **100** [6] 2402-6 (2017).

J. Li, X. Chen, L. Tang, **Y. Li**, and Y. Wu, "Fabrication and Properties of Transparent Nd-Doped $BaF_2$ Ceramics," *J. Am. Ceram. Soc.,* **102** [1] 178-84 (2019).

X, Chen, Y. Wu, N. Wei, J. Qi, **Y. Li**, Q. Zhang, T. Hua, W. Zhang, Z. Lu, B. Ma, and T. Lu, "Fabrication and Spectroscopic Properties of Yb/Er: YAG and Yb, Er: YAG Transparent Ceramics by Co-Precipitation Synthesis Route," *J. Lumin.,* **188**, 533-40 (2017).

B. Zhang, Q. Zhao, A. Chang, Y. Liu, **Y. Li**, and Y. Wu, "Synthesis of $YCrO_3$ Ceramics through a Field-Assisted Sintering Technique," *J. Mater. Sci. Mater. Electron.,* **25** [3] 1400-3 (2014).

B. Zhang, Q. Zhao, A. Chang, **Y. Li**, Y. Liu, and Y. Wu, "Electrical Conductivity Anomaly and X-Ray Photoelectron Spectroscopy Investigation of $YCr_{1-x}Mn_xO_3$ NTC Ceramics," *Appl. Phys. Lett.,* **104** [10] 102109-1-4 (2014).

B. Zhang, Q. Zhao, A. Chang, **Y. Li**, Y. Liu, and Y. Wu, "Spark Plasma Sintering of $MgAl_2O_4$-$YCr_{0.5}Mn_{0.5}O_3$ Composite NTC Ceramics," *J. Eur. Ceram. Soc.,* **34** [12] 2989-95 (2014).